Modelling of borehole heat exchangers and heat transfer along horizontal connection pipes

Von der Fakultät für Bauingenieurwesen
der Rheinisch-Westfälischen Technischen Hochschule Aachen
zur Erlangung des akademischen Grades eines Doktors
der Ingenieurwissenschaften genehmigte Dissertation

vorgelegt von
Stephan Düber

Berichter: Univ.-Prof. Dr. Raul Fuentes
Prof. Dr. Phil Vardon

Tag der mündlichen Prüfung: 04.10.2024

Contents

List of Figures

List of Tables

Acronyms

BHE	borehole heat exchanger
BMS	building management system
CDS	central difference scheme
CFL	Courant-Friedrichs-Lewy number
COP	coefficient of performance
FFT	fast Fourier transform
FLS	finite line source
FVM	finite volume method
GSHP	ground source heat pump
HDPE	high density polyethylene
HFLS	horizontal finite line source
ICS	infinite cylinder source
ILS	infinite line source
MAE	mean absolute error
MFLS	moving finite line source
MLR	multiple linear regression
PC	personal computer
SP	(temperature) set point
TMY	typical meteorological year
TRCM	thermal resistance capacitance model
VIF	variance inflation factor

Abstract

The use of geothermal energy with shallow borehole heat exchangers (BHEs) is growing steadily. BHEs are the underground components of heat pump systems that uses the ground as source or sink of thermal energy for conditioning of buildings. Larger systems with tens to hundreds of boreholes are being built. Analytical calculation approaches are successfully used for the design of such systems and mechanical plants. To simulate and optimise the actual operating conditions, more complex models that take into account transient conditions may be required. In addition, large BHE fields often require hundreds of meters of horizontal connection pipes to connect the BHE to the manifolds and the building. Heat transfer along these pipes is often neglected.

This thesis presents a hybrid simulation approach for BHEs based on a novel combination of existing solutions for the simulation of heat transfer processes within the borehole and the surrounding ground. Heat transfer is modelled using a combination of analytically determined g-functions and a borehole thermal resistance capacity model. The computational efficiency of long-term simulations is drastically increased by dividing the simulation time into multiple periods, where the influence of past periods on future periods is calculated using the Fast Fourier Transform.

Based on monitoring data from a BHE field with 40 BHEs and a combined connection pipe length of 900 m, heat transfer along connection pipes is investigated. The heat transfer along the connection pipes is correlated with parameters such as surface types or solar radiation above the pipes using multiple linear regression analysis, showing that solar radiation above the pipes has the greatest effect.

A comparison of three soil and three pipe models of varying complexity is carried out to investigate their suitability in the context of connection pipes and BHE simulation. Based on the results, a computationally efficient approach is proposed using a novel combination of established steady-state models for the BHE and the connection pipes. The model is used to investigate the effect of horizontal connection pipes attached to a BHE for the 25 most representative climate zones. The consideration of the connection pipes leads to the biggest BHE load reduction in tropical climates, followed by temperate, arid and continental climates.

In the case of existing BHE fields where the connection pipes have not been considered in the design, various options for the subsequent use of heat gains along the pipes are investigated.

The study explores the potential of extended operation, increased loads and an optimised operating strategy to exploit the idle capacity gain from the horizontal connection pipes.

Finally, a simple and fast methodology to account for changing thermal properties by using the g-function method is presented. The simulation time is divided into periods according to the changes in thermal properties. By transforming the temperature response from one period to the next and subsequent superposition, any changes in the thermal conductivity properties can be taken into account. The computational time is significantly shorter than comparable numerical simulations.

Kurzfassung

Die Nutzung der geothermischen Energie mit Erdwärmesonden (EWS) nimmt stetig zu. Es werden immer größere Anlagen mit Dutzenden bis Hunderten von EWS gebaut. Die Dimensionierung solcher Anlagen erfolgt zuverlässig auf Grundlage analytischer Berechnungsansätze. Für die Simulation und Optimierung der tatsächlichen Betriebsbedingungen können komplexere Modelle erforderlich sein, die auch instationäre Zustände berücksichtigen. Außerdem sind bei großen EWS-Feldern in der Regel horizontale Verbindungsleitungen mit einer Gesamtlänge von mehreren Hundert Metern erforderlich, um die EWS mit Verteilerschächten und dem Gebäude zu verbinden. Die Wärmeübertragung entlang dieser Verbindungsleitungen wird oft nicht berücksichtigt.

In dieser Arbeit wird ein hybrider Simulationsansatz für Erdwärmesonden (EWS) vorgestellt. Dieser Ansatz kombiniert bestehende Lösungen zur Simulation des Wärmetransports innerhalb des Bohrlochs und im umliegenden Erdreich. Der Wärmetransport wird dabei mithilfe analytisch ermittelter g-Funktionen und eines Widerstandskapazitätsmodells für die EWS modelliert. Ein neuer Algorithmus verbessert die Berechnungsdauer von Langzeitsimulationen erheblich. Dabei wird der Simulationszeitraum in mehrere Perioden unterteilt, und der Einfluss vergangener Perioden auf zukünftige Perioden wird basierend auf dem Faltungssatz mit der schnellen Fourier-Transformation berechnet.

Auf der Grundlage von Monitoringdaten einer EWS-Anlage mit 40 Erdwärmesonden und einer Gesamtlänge der Verbindungsleitungen von 900 m Metern wird der Wärmetransport entlang der Verbindungsleitungen untersucht. In einer multiplen linearen Regressionsanalyse werden Parameter wie die Oberflächenart und die Sonneneinstrahlung über den Leitungen berücksichtigt. Die Analyse zeigt, dass die Sonneneinstrahlung den größten Einfluss auf den Wärmetransport entlang der Verbindungsleitungen hat.

Im Kontext der kombinierten Simulation von Verbindungsleitungen und Erdwärmesonden (EWS) wird ein Vergleich von drei Untergrund- und drei Rohrmodellen unterschiedlicher Komplexität durchgeführt. Basierend auf den Ergebnissen wird ein rechnerisch effizienter Ansatz vorgeschlagen, der eine neuartige Kombination etablierter stationärer Modelle für die EWS und die Verbindungsleitungen verwendet. Mit diesem Modell werden die Auswirkungen horizontaler Verbindungsleitungen auf den EWS-Betrieb in 25 Klimazonen untersucht. Es zeigt sich, dass die Berücksichtigung der Verbindungsleitungen zur größten Reduktion der Sondenlast in tropischen Klimazonen führt, gefolgt von gemäßigten, ariden und kontinentalen Klimazonen.

Für bestehende EWS-Felder, bei denen die Verbindungsleitungen bei der Auslegung nicht berücksichtigt wurden, werden verschiedene Möglichkeiten zur Nutzung der Wärmegewinne entlang der Leitungen untersucht. Die Studie analysiert das Potenzial eines verlängerten Betriebs, erhöhter Lasten und einer optimierten Betriebsstrategie, um die Kapazitätsgewinne aus den horizontalen Verbindungsleitungen zu nutzen.

Schließlich wird ein einfaches und schnelles Verfahren zur Berücksichtigung variabler thermischer Eigenschaften mittels der g-Funktion-Methode vorgestellt. Der Simulationszeitraum wird in mehrere Abschnitte unterteilt, die den Änderungen der thermischen Eigenschaften entsprechen. Durch die Transformation der Temperaturantwort von einem Abschnitt zum nächsten und die anschließende Überlagerung können beliebige Variationen der Wärmeleitfähigkeitsparameter berücksichtigt werden. Die Berechnungszeit ist dabei deutlich kürzer als bei vergleichbaren numerischen Simulationen.

Chapter 1

Introduction

1.1 Motivation and objective

As part of the research project *GeTIS - Geothermal information system for dimensioning, modelling, evaluation and approval of linked geothermal energy systems on building and urban district level* (Treeck et al., 2020), various analytical and numerical calculation approaches for the design and simulation of borehole heat exchangers (BHEs) were implemented in a web-based information and design tool. BHEs are deep, vertical boreholes housing a plastic pipe, usually made of high density polyethylene (HDPE) or cross linked polyethylene (PEX), through which a heat transfer fluid is pumped to exchange heat with the ground. In combination with a heat pump, they can be used to heat or cool buildings (Figure 1.1).

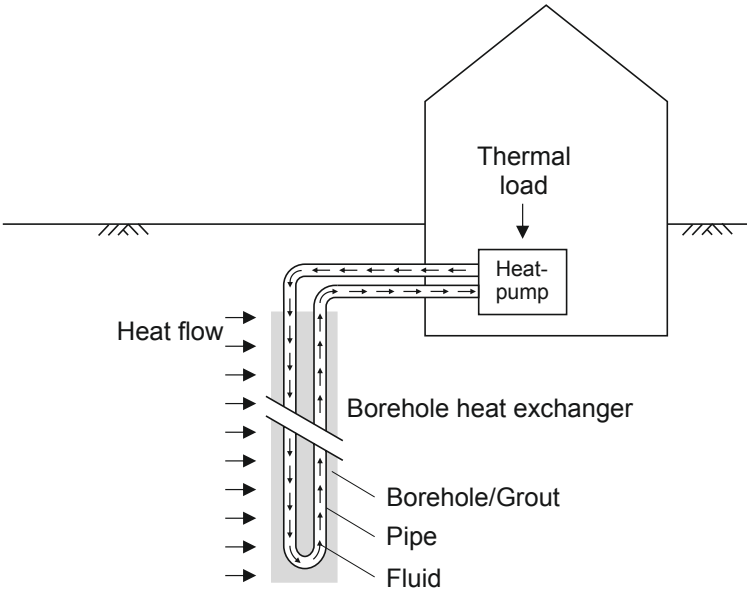

Figure 1.1 Working principle of a borehole heat exchanger.

The implemented calculation codes should be validated using monitoring data from the BHE field at the EON.ERC building located in Aachen, Germany. The building is supplied with energy for heating and cooling via 40 BHEs. The boreholes are grouped in three manifolds and are arranged around the building as shown in Figure 1.2. All BHEs have in-depth

measurement monitoring. The supply and return temperatures of the fluid, as well as fluid flow rate, are measured in the manifolds and recorded with a time step of 30 s - over an operating period of several years, covering a wide range of operating conditions (Clauser et al., 2017).

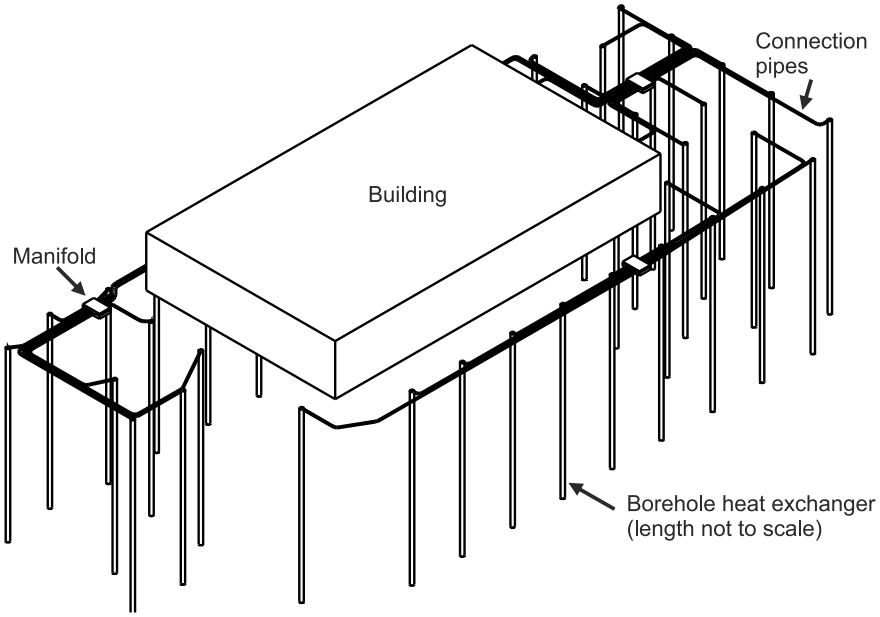

Figure 1.2 BHE field at the E.ON ERC.

During the validation process of the GeTIS tools, it became clear that neither the exisiting analytical nor the numerical calculation models could satisfactorily represent the behaviour of the entire BHE field under all conditions. While the numerical simulation is theoretically capable of fully representing the dynamics and thermal interaction of all BHEs, the modelling and especially the computational effort is enormous and results in unacceptable computation times. The analytical calculation models, on the other hand, although efficient, were not able to represent the operation of the BHEs with sufficient accuracy under all conditions. For example, short cycling times of the heat pump would violate the steady-state assumption within the boreholes, and response functions representing the whole field could not account for the on/off switching of individual BHEs.

In addition, it was unclear how the horizontal connection pipes, with a total length of about 900 m in that case, affected the BHE operation and how they could be included in a model. Based on this, the following research questions were defined:

1. How can large fields of borehole heat exchangers be efficiently modelled for multi-year periods in small time steps?
2. What are the effects of the near-surface horizontal connection pipes on the operation of the geothermal system?
3. Which models are suitable for the connection pipe network in combination with the borehole heat exchanger simulation?

4. Can the operation strategy be optimised based on the heat gains and losses along the horizontal connection pipes?

This thesis answers these and other questions that arose during the course of the PhD journey. To this end, a variety of computational models have been developed, implemented and published.

1.2 Structure

The structure of the thesis corresponds to its genesis. Chapter 2 deals with the basics of thermal modelling of borehole heat exchangers and connection pipes. The first research question is then answered in Chapter 3. In the corresponding article, a hybrid calculation model is developed, implemented and validated. The computational efficiency of long-term simulations is improved by sub-dividing the time scale into multiple periods, where the influence of past periods on future periods is calculated using the Fast Fourier Transform (FFT). The method achieves computational time reductions of over 90 % in some cases, with greater improvements as the simulation time increases.

Chapter 4 answers the second research question by analysing the monitoring data of the BHE field at the E.ON ERC. The monitoring data are compared with results from an analytical calculation approach, showing good agreement in some cases and deviations of more than 100 % in others. To gain further insight into the governing parameters, a multiple linear regression is performed to correlate the observed deviations with additional information, such as the surface types above the connection pipes. Finally, it was shown that the connection pipes can have both positive and negative effects depending on the season and the operating condition.

Chapter 5 answers research question 3 and investigates different approaches to modelling the horizontal connection pipes. The models investigated include numerical and analytical models for both the ground and the pipes. All model combinations are coupled with the hybrid BHE model from Chapter 3. Based on the results, a computationally efficient approach is proposed using a novel combination of established steady-state models for the BHE and connection pipes.

Chapter 6 uses the model derived in the previous chapter to continue to answer the second research question, this time in a global context. The effect of the horizontal connection pipes is investigated for the 25 most representative climate zones. In the reference scenario studied, the consideration of the connection pipes leads to an average reduction in BHE load of 34 % in tropical climates, 19 % in temperate climates, 11 % in arid climates and 4 % in continental climates, resulting in a potentially significant reduction in drilling costs.

Chapter 7 finally answers the last research question. The analysis considers load profiles with different heating to cooling ratios and finds that the effect of horizontal pipes becomes

more significant with unbalanced load profiles. The study explores the potential of extended operation and increased loads to exploit the capacity gain from the horizontal connection pipes. In addition, the study highlights the potential of an optimised operating strategy involving adjustments to the number of BHEs in operation to reduce power consumption and therefore reducing operating costs in existing systems by exploiting heat gains from the horizontal connection pipes.

The analytical models for the ground used in Chapter 5 and 6 have some limitations, one of which is that the thermal properties of the near-surface ground are assumed to be constant. This limitation is overcome in Chapter 8 where a simple and fast method to account for changing thermal properties by using thermal response factors is presented. The simulation period is divided into several periods according to the changes in thermal properties. By transforming the temperature response from one period to the next and subsequent superposition, any changes in the thermal conductivity properties of the media through which heat travels can be accounted for. The method is verified by numerical simulation and its efficiency is demonstrated in an application example. Finally, the entire thesis is discussed and summarised in chapter 9.

Chapter 2

Literature review

2.1 Borehole exchanger modelling

The simulation of borehole heat exchangers is challenging due to the three-dimensional heat transfer processes in the ground and in the heat exchanger, the large spatial scale differences and the long operating times (e.g. M. Li et al., 2014). The scale-distributed geometries and transient transfer processes lead to high computational costs when using numerical models. For example, traditional design periods of 50 years mean that, such models are not often used in engineering practice (Spitler and Bernier, 2016). Simplified solutions with some limitations are widely preferred due to their ease of use and short computational times. In many common solutions, the spatial domain is divided into two parts: the domain inside the borehole and the domain outside the borehole. One advantage of this approach is that different simulation methods can be used for each domain. The structure of this chapter follows this scheme, where solutions for the domain outside the borehole are presented in section 2.1.1 and inside the borehole in section 2.1.2.

2.1.1 Outside borehole - ground

A common objective of thermal simulation of borehole heat exchangers, especially in the design phase of such systems, is to calculate the fluid temperatures within the BHE for a defined thermal load. Considering the separation of the domains inside and outside the borehole, the wall defines the interface between the two domains. The domains can be coupled by the borehole wall temperature T_b and the heat flux. The heat flux is usually related to the length of the BHE and is denoted as q in $\mathrm{W\,m^{-1}}$ in the following. Different methods of calculating the borehole wall temperature are presented below, and the correlation with the fluid temperatures inside the BHE is shown in section 2.1.2.

The simplest geometric representation of a BHE, or more precisely, the borehole, is the infinite line source (ILS), also referred to as Kelvin's line source (Carslaw and Jaeger, 1959; Ingersoll, 1948). It reduces the three-dimensional problem to one dimension and conductive heat transfer:

$$\Delta T_\mathrm{b}(r,t) = \frac{q}{4\pi\lambda}\int_{\frac{r^2}{4\alpha t}}^{\infty}\frac{\exp(-u)}{u}du = \frac{q}{4\pi\lambda}E_1\left(\frac{r^2}{4\alpha t}\right). \tag{2.1}$$

Here, λ is the thermal conductivity of the ground, α is its thermal diffusivity and r is the radial distance from the line source at which the temperature is evaluated. E_1 is the exponential integral (Gautschi and Cahill, 1964).

The simplification of the BHE geometry as an infinite line source leads to inaccuracies for long periods and short BHEs (Philippe et al., 2009). The finite line source (FLS) overcomes this simplification and considers the finite length and a ground surface boundary condition (Claesson and Eskilson, 1987; N. R. Diao et al., 2004; Lamarche and Beauchamp, 2007; Zeng et al., 2002):

$$\Delta T_\mathrm{b}(r,z,t) = \frac{q}{4\pi\lambda}\int_{D}^{D+H}\left\{\frac{\operatorname{erfc}\left(\frac{\sqrt{r^2+(z-h)^2}}{2\sqrt{at}}\right)}{\sqrt{r^2+(z-h)^2}} - \frac{\operatorname{erfc}\left(\frac{\sqrt{r^2+(z+h)^2}}{2\sqrt{at}}\right)}{\sqrt{r^2+(z+h)^2}}\right\}dh. \tag{2.2}$$

Here, z is the depth at which the temperature is evaluated, H is the length of the line source and D is its burial depth which is the distance between the top of the line source and the ground surface. The method of images (Thomson and Kelvin, 1872) leading to the FLS was proposed for vertical boreholes by Claesson and Eskilson (1987) and coupled with a solution for the domain inside the borehole (section 2.1.2) by N. R. Diao et al. (2004). Lamarche and Beauchamp (2007) presented a formulation to evaluate the mean temperature along the line source computationally more efficient for the case where $D = 0$. The formulation used in this work was presented by Claesson and Javed (2011) and solves for the mean temperature and is valid for $D \geq 0$ while maintaining computational efficiency:

$$\Delta T_\mathrm{b}(r,t) = \frac{q}{4\pi\lambda}\int_{\frac{1}{\sqrt{4\alpha t}}}^{\infty}\exp\left(-r^2s^2\right)\frac{Y(Hs,Ds)}{Hs^2}ds \tag{2.3}$$

with

$$Y(h,d) = 2\,\mathrm{ierf}(h) + 2\,\mathrm{ierf}(h+2d) - \mathrm{ierf}(2h+2d) - \mathrm{ierf}(2d), \tag{2.4}$$

$$\mathrm{ierf}(X) = X\operatorname{erf}(X) - \frac{1}{\sqrt{\pi}}\left(1-\exp\left(-X^2\right)\right). \tag{2.5}$$

The simplification of the BHE geometry to a one-dimensional line is justified by the small diameter of the BHE compared to its length. However, there are also analytical solutions, such as the cylinder source theory, which allow the diameter of the BHE to be taken into account. Carslaw and Jaeger (1959) presented three different solutions for the treatment of the region inside a cylindrical heat source: a form where the inside of the cylinder is empty and all heat flow is going outward from the cylinder, a form where the inside of the cylinder is a perfect conductor with a defined capacity, and one where the inside of the cylinder has

different thermal properties to the outside (Spitler and Bernier, 2016). The extent to which the use of the cylinder source is useful for simulating BHEs depends on how the area within the borehole (Section 2.1.2) is taken into account. As the line source approaches neglect the domain inside the borehole, Eskilson and others (Eskilson, 1987; Ingersoll et al., 1954; M. Li and Lai, 2012; Philippe et al., 2009) defined application limits depending on thermal properties and the borehole geometry. Philippe et al. (2009) concluded in their intermodel comparison of the ILS, FLS and infinite cylinder source (ICS) that the ICS is recommended for times less than 34 h. In contrast, Lamarche (2013) showed with numerical reference models that the ICS is no better than the ILS when the inside of the borehole is represented by a borehole thermal resistance (see Section 2.1.2). However, in the model presented in Chapter 3, a thermal resistance capacity model is used for the area inside the borehole so that the use of the ICS improves the accuracy in that case. Due to the strict separation of the areas inside and outside the borehole in the model in Chapter 3, the formulation of Carslaw and Jaeger (1959) for an empty cylinder corresponds to the underlying model concept. As this formulation is difficult to solve (Bernier, 2001; Philippe et al., 2009), the formulation derived from the ILS presented by Man et al. (2010) is used:

$$\Delta T_{\mathrm{b}}(r,t) = \frac{q}{4\pi\lambda}\int_0^{\pi}\frac{1}{\pi}\,\mathrm{Ei}\left(\frac{r^2+r_0^2-2rr_0\cos\varphi'}{4\alpha t}\right)d\varphi' \tag{2.6}$$

where r_0 is the radius of the cylinder and Ei is the exponential integral. This solution corresponds to a solid cylinder with identical thermal properties as the surrounding ground.

The solutions presented so far only consider heat transfer by conduction. In the presence of moving groundwater, the temperature field around the BHE is additionally determined by heat transfer due to forced convection. This phenomenon can be considered using several approaches to moving heat sources. These include the moving infinite line source (N. Diao et al., 2004; Pasquier and Lamarche, 2022; Sutton et al., 2003; Zubair and Chaudhry, 1996), the moving finite line source (MFLS) presented by Molina-Giraldo et al. (2011) and the moving cylindrical source (Al-Khoury et al., 2020). In addition, the analytical approaches only take into account time-constant and homogeneous properties of the ground. The problem of time-variable thermal properties will be solved in Chapter 8, while several authors have proposed solutions for inhomogeneous ground based on the FLS and MFLS (Abdelaziz et al., 2014; Erol and François, 2018; Pan et al., 2020).

A further constraint appears to be the constant thermal load q in Equations 2.1-2.6. This limitation is solved by applying Duhamel's theorem, presented in the context of heat conduction in the book of Carslaw and Jaeger (1959). The application of Duhamel's theorem, henceforth referred to as the superposition principle, is presented in detail for buried pipes in the work of Claesson and Dunand (1983). For the application, a time-varying load $q(t)$ (Figure 2.1, (a)) is divided into load increments $\Delta q = q_i - q_{i-1}$ (Figure 2.1, (b)). Finally, the temperature

changes due to each load increment are determined using e.g. Equation 6 (Figure 2.1, (c)) and are superimposed to give the total temperature change (Figure 2.1, (d)) due to $q(t)$.

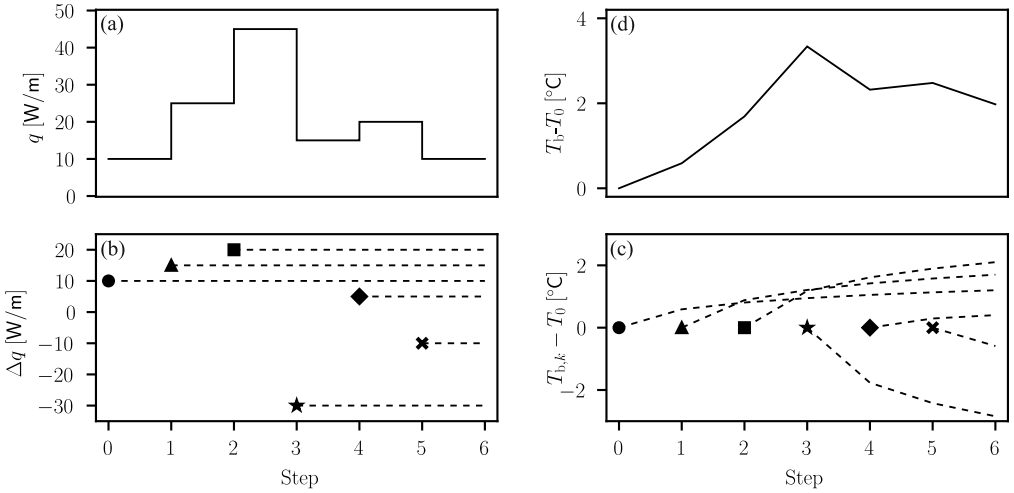

Figure 2.1 Application of the superposition principle for time-varying loads: Decomposition of the load (a) as load increments (b) and superposition of the temperature responses (c) to construct the solution (d). After Marcotte and Pasquier (2008) and Lazzarotto (2015).

Figure 2.1 (c) shows that when applying the superposition principle for each load increment, the temperature response has to be calculated for all subsequent time steps, i.e. the computational effort increases exponentially with linearly increasing number of time steps. This can lead to a significant computational burden when using hourly load profiles in combination with the usual design periods of several decades. To solve this problem, various authors have proposed load aggregation schemes of varying complexity (Bernier et al., 2004; Claesson and Javed, 2012; Liu, 2005; Yavuzturk and Spitler, 1999). In these algorithms, past loads are lumped into larger blocks of time to reduce the number of calculation steps. While achieving computational time reductions of up to 99 % (Yavuzturk and Spitler, 1999), the accuracy always depends on the chosen block sizes and number of blocks. A more elegant solution was proposed by Marcotte and Pasquier (2008), who solved the problem by applying the convolution theorem and the Fast Fourier Transform. Unlike the load aggregation methods, the Marcotte and Pasquier (2008) approach provides the exact solution. The summation of temperature responses (Figure 2.1, (c)) can be replaced by a simple array multiplication in the Fourier domain. This reduces the computation time by several orders of magnitude, depending on the number of time steps.

In addition to the time domain, the superposition principle can also be applied in the spatial domain to account for multiple, thermally interacting boreholes. However, this poses a problem for analytical solutions defined as a function of the borehole load q (e.g. Equation 2.6). Multiple BHEs arranged in a field are usually operated in parallel and connected to a common heat pump so that all BHEs receive the same inlet temperature. Depending on the geometric arrangement, the thermal interference will result in different extraction capacities.

There is a greater volume of thermally undisturbed ground available at the perimeter of the borehole field compared to the inner boreholes. Accordingly, the edge boreholes have higher extraction rates. This problem was solved by Eskilson, who introduced the concept of numerically calculated response functions, called *g-functions*, for BHE fields with thermally interacting BHEs (Eskilson, 1987; Eskilson and Claesson, 1988). In the numerical model an equal borehole wall temperature, serving as a surrogate for equal inlet temperatures, is assumed for all boreholes. The concept of g-functions is defined as:

$$\Delta T_\mathrm{b} = \frac{q}{2\pi\lambda} \cdot g\left(\frac{t}{t_\mathrm{s}}, \frac{r_\mathrm{b}}{H}, \frac{B}{H}, \frac{D}{H}\right) \tag{2.7}$$

where t_s is a characteristic time defined by Eskilson (1987) as $t_\mathrm{s} = \frac{H^2}{9\alpha}$ and B is the horizontal spacing in regularly spaced BHE fields. It is easy to see that the analytical equations shown so far (Eq. 2.1-2.6) can be used to calculate g-functions for individual BHEs. By introducing the dimensionless time t/t_s and moving the thermal conductivity to the left term of the right hand side of Equation 2.7, the g-function depends only on the geometry of the BHE (field). This means that once calculated, the g-function for a given geometry can be used for any thermal properties of the ground, which is what makes the concept so popular and used in many established design tools like EED, EWS, GLHEPRO and others (Hellström and Sanner, 1994; Huber, 2005; Spitler, 2000). Eskilson and others used numerical models to calculate the g-functions for a variety of borefield layouts, which were then stored in the computer programs (Eskilson, 1987; Monzó et al., 2015; Naldi and Zanchini, 2019; Priarone and Fossa, 2016). While interpolation between different layouts is possible, the approach of tabulated g-functions is clearly limited by the predefined layouts. Cimmino and Bernier (2014) presented a semi-analytical model based on the FLS for the computationally efficient calculation of any borefield layout g-functions. By dividing the boreholes into segments, the variation in heat extraction along each borehole and between multiple boreholes is considered, resulting in deviations of less than 5 % compared to the numerical approach. A Python implementation is available within the *pygfunction* toolbox (Cimmino and Cook, 2022).

The use of analytical or numerical g-functions is the basis of many design tools due to their efficiency and ease of use. However, as the application of the superposition principle requires linear boundary conditions, phenomena that generate non-linear terms cannot be considered (Spitler and Bernier, 2016). In this context, freeze-thaw processes and time-varying groundwater flows may be relevant to the simulation of BHEs. Accurate results taking these processes into account can only be obtained using numerical models. The relevant heat transfer processes in the ground, conduction and convection, can be solved using numerous numerical codes based on the finite element, finite difference or finite volume methods. Programs that also have integrated models for the BHE itself are suitable for the simulation of borehole heat exchangers. For example the finite element programs FEFLOW (Diersch, 2013) and OpenGeoSys (Bilke et al., 2022) have integrated models for coaxial,

single-U and double-U type BHEs. The finite difference solver SHEMAT-Suite (Keller et al., 2020) also has models for coaxial and double-U BHEs (Mottaghy and Dijkshoorn, 2012). These programs are not specifically designed to simulate BHEs, but to simulate heat and mass transport in the ground, and are therefore particularly flexible. The simulation platform COMSOL Multiphysics (COMSOL AB, Stockholm, Sweden, n.d.) has integrated pipe flow modules that can be used to simulate the flow within the pipes of a BHE (e.g. Ozudogru et al., 2014). However, the borehole and grout material must be discretised, which requires small elements and therefore long computation times. Other, more BHE design-oriented tools, use numerical ground models with limited capabilities. BASIMO (Schulte et al., 2016) is specifically designed for the optimisation of borehole thermal energy storage systems and uses the MATLAB FEM implementation (Alberty et al., 1999) for the heat transfer in the ground. As the use case is energy storage, convective heat transport is neglected.

Even if simplified models are used for the BHE, linking a BHE model to a numerical ground model is not trivial. In FEFLOW, for example, the interfaces between the BHE model and the ground model are nodes of the finite element mesh. These nodes act as the wall of the borehole: on the one hand, the node temperature corresponds to the ground temperature at the borehole wall as an input parameter for the borehole model, and on the other hand, the thermal energy is introduced into the ground model via the nodes. To obtain accurate results, spatial discretisation close to the BHE nodes must follow specific rules (Diersch et al., 2010).

Since the simulation and design of borehole heat exchangers has been the subject of research for multiple decades, there are several comprehensive review articles providing additional information (Christodoulides et al., 2020; M. Li et al., 2016; Spitler and Bernier, 2016; Zhao et al., 2022).

2.1.2 Inside the borehole - grout, pipes, circulating fluid

While the heat transport processes in the ground depend on the site specific hydrogeological conditions, heat transport in the BHE is always a combination of convection in the circulating fluid and conduction in the pipes and grout. The models for the area inside the borehole can be grouped into steady-state and transient models. The steady-state models assume that the components of the BHE (fluid, pipes and grout) are in thermal equilibrium. This assumption is justified in many cases and can be checked with the borehole time according to Eskilson (1987):

$$t_\mathrm{b} = \frac{5 r_\mathrm{b}^2}{\alpha} + \pi r_\mathrm{p}^2 \frac{2H}{V_\mathrm{f}} \tag{2.8}$$

where r_b is the radius of the borehole, r_p is the inner radius of the fluid pipe and V_f is the fluid flow rate per U-loop. Thermal equilibrium within the borehole can be assumed for times greater than t_b.

The conventional method of modelling the BHE under steady-state conditions is to use a single thermal resistance. This borehole resistance can be defined locally as

$$R_\mathrm{b} = \frac{T_\mathrm{f,l} - T_\mathrm{b}}{q}, \tag{2.9}$$

or globally, denoted as the effective borehole resistance, as

$$R_\mathrm{b}^* = \frac{T_\mathrm{f} - T_\mathrm{b}}{q}. \tag{2.10}$$

It allows the fluid temperatures to be calculated based on the temperature of the borehole wall T_b and the thermal load q. Here, $T_\mathrm{f,l}$ is the average between the inlet and outlet fluid temperatures at a cross section of the BHE at an any depth, while T_f is the average of the inlet and outlet temperatures at the head of the BHE. The effective borehole resistance R_b^* differs from the local borehole resistance R_b by taking into account the thermal short circuiting between the inlet and outlet. Relationships between R_b^* and R_b can be found in the work of Hellström (1991). While the thermal response test allows the calculation of R_b^* for existing BHEs (Mogensen, 1983), a variety of models exist to calculate R_b and R_b^* based on the BHE properties. These models use the multipole method (Claesson and Javed, 2011) or thermal resistance circuits that simplify the heat transport in the horizontal plane. An overview and comparison of the relevant models is presented in the review paper of Javed and Spitler (2017).

The simplest thermal resistance circuit for a single-U BHE is the delta circuit shown in Figure 2.2.

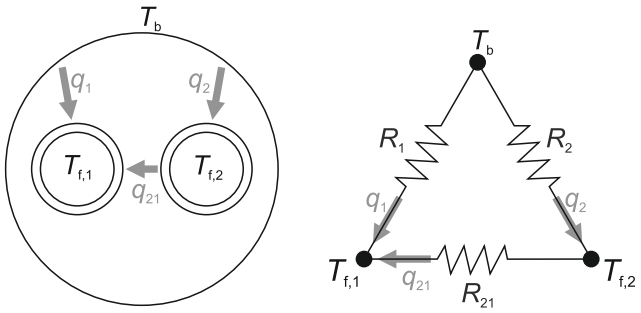

Figure 2.2 Cross section of the borehole and the resistance circuit. After Eskilson (1987).

Here, the temperatures of the borehole wall T_b and the fluid temperatures in the inlet and outlet pipe $T_\mathrm{f,1}$ and $T_\mathrm{f,2}$ are represented as temperature nodes which are connected through thermal resistances R_i. The heat flux q_i between the nodes can then simply be described

by the one-dimensional conduction Equation, e.g. $q_1 = (T_b - T_{f,1})/R_1$. It is apparent that the resistances from the fluid to the ground R_1 and R_2 in Figure 2.2 are actually serial connections of several resistances: the convective resistance from the fluid to the inner wall of the pipe, the conductive resistance of the pipe and the conductive resistance of the grout material. The convective resistance from the fluid to the pipe can be calculated using empirical formulae (Gnielinski, 2013; Nusselt, 1916; Prandtl, 1905; Reynolds, 1883) while the conductive resistance of the pipe can be calculated analytically (Carslaw and Jaeger, 1959). The main challenge is to calculate the resistance of the grout. Due to the geometry, there is no general analytical solution. To get around this, various researchers have used and improved the equivalent diameter method, where the two fluid pipes are replaced by a single concentric pipe (e.g. Bose, 1985; Claesson and Dunand, 1983; Claesson and Javed, 2011; Lamarche and Beauchamp, 2007; Shirazi and Bernier, 2013). However, in the case of symmetrically arranged tubes of a single U BHE, there is a direct analytical solution based on zero and first order multipole expansions (Hellström, 1991). A comparison of eight other approaches for grout resistance calculation with the higher order multipole method, which is considered to be the state of the art, shows that most approaches give reliable results within certain limits. However, for extreme configurations, such as pipes touching the borehole wall, they may lead to double digit relative errors (Javed and Spitler, 2017).

For deep boreholes, low flow rates or short time periods, the steady-state assumption within the borehole may not be valid (see Equation 2.8). The two most common solutions to this problem are short-term response functions and hybrid thermal resistance capacitance models. In the latter, the the heat transfer along the borehole axis, often limited to the fluid, is solved numerically, while the horizontal heat transfer is determined using thermal resistance circuits.

In the Wetter and Huber (1997) model, the fluid flow in the pipes is calculated using a finite volume model with explicit time stepping and an upwind scheme. All pipes are connected through a thermal resistance to a single grout node per axial layer representing the grout capacity and temperature. The Al-Khoury and Bonnier (2006) model uses the finite element method for heat transfer in vertical direction. Again, the grout is represented by a single node per layer in the axial direction and the heat flow between the fluid in the pipes and the grout is solved using thermal resistances based on the equivalent diameter method. Unlike the Wetter and Huber (1997) model, the heat conduction in the grout material along the borehole axis is taken into account.

The use of a single node for grout capacitance and temperature assumes a uniform grout temperature, which is a significant simplification. The Oppelt et al. (2010) model divides the grout cross-section of a double-U BHE into three zones with individual temperatures and capacities. It is combined with the Wetter and Huber (1997) model to solve the heat transfer in the fluid along the borehole axis. Vertical conduction in the grout is neglected. Wołoszyn

and Gołaś (2013) used three zones for the grout of a single-U BHE and the finite element method to solve the heat transfer in the vertical direction.

Zarrella et al. (2011) divided the grout material of a double-U BHE into two zones: a core zone and an outer shell zone with corresponding temperatures and capacities. In the thermal network, all fluid temperature nodes are connected to both the core and shell nodes. In addition, there are direct connections between adjacent pipes. The heat transfer along the borehole axis is again limited to the fluid and solved using the finite volume method.

In the Bauer et al. (2011) model, the grout is divided into one zone per pipe for single- and double-U BHEs and one grout zone for the coaxial type BHE. In contrast to the the previous model, the resistances are connected in such a way that the heat exchange from one pipe to the other can only take place through the grout material, considering its capacity. This gives a better representation of the short-term behaviour. However, the model is sensitive to the location of the thermal center of the grout area and can be inaccurate in extreme configurations, such as where the pipes touch the borehole wall (Javed and Spitler, 2017).

The concept was further improved by Pasquier and Marcotte (2012), who also considered the pipe capacitance and subdivided the grout into more zones leading to significant accuracy improvements. The Pasquier and Marcotte (2012) model is only presented for a single slice, i.e. two-dimensional. When extended to three dimensions, the computational effort increases accordingly due to the additional nodes. In the three-dimensional extension presented later, the authors restricted the heat transfer in vertical direction to the fluid to reduce the computational effort (Pasquier and Marcotte, 2014). The simplified Minaei and Maerefat (2017a) TRCM uses again just one grout node for each U-loop. There are also direct connections between the fluid temperature nodes of all the pipes. The model was extended to three dimensions by Minaei and Maerefat (2017b). A more detailed overview with further information on 2D and 3D BHE models can be found in the review paper by Y. Cui et al. (2018).

The hybrid resistance capacity models described above need to be coupled with numerical (e.g. Bauer et al., 2011; Al-Khoury and Bonnier, 2006; Oppelt et al., 2010; Wetter and Huber, 1997) or analytical (e.g. Laferrière et al., 2020; Minaei and Maerefat, 2017a; Ruiz-Calvo et al., 2016) models for the area outside the borehole. This is not trivial with numerical ground models, but also allows phenomena such as transient groundwater flow to be taken into account. Short-term g-functions, on the other hand, provide an *all-in-one* solution. In principle, short-term g-functions can be calculated with all hybrid thermal resistance capacitance models mentioned so far, but there are others worth mentioning.

Javed and Claesson (2011) presented an analytical model based on the equivalent diameter method and the Laplace transform, which was used by Claesson and Javed (2011) to calculate short-term g-functions. These were then combined with the finite line source solution for the long-term to generate g-functions valid for time scales from minutes to decades. Lamarche (2015) presented a closed form for the Javed and Claesson (2011) model and discussed the

choice of the equivalent radius. M. Li et al. (2014) presented a short-term g-function based on the composite medium line source theory (M. Li and Lai, 2013). In contrast to the equivalent diameter approach, the composite-medium line-source theory accounts for the thermal interaction of multiple pipes within the borehole. Their short-term g-function is also combined with the finite line source to produce a full-scale g-function (M. Li et al., 2014). A simplified, more easily implemented version of the composite medium line source theory was presented by Wei et al. (2016). Also with the aim of making it easier to use, Pasquier et al. (2018) trained an artificial neural network to generate short-term g-functions. The training data was generated using their previous model (Pasquier and Marcotte, 2012, 2014).
Similar to the modeling of the ground outside the borehole, there are a large number of models of varying complexity and functionality for the BHE itself. The choice of the appropriate model should always be based on the objective and the specific boundary conditions.

2.2 Horizontal connection pipe modelling

Horizontal connection pipes are required to connect the vertical BHEs to the heat pump or manifolds. The modelling of heat transfer in and around these pipes has many overlaps with the modelling of borehole heat exchangers. For example, the same empirical and analytical approaches can be used to calculate the advective resistance from the fluid to the inner wall of the pipe (Gnielinski, 2013; Nusselt, 1916; Prandtl, 1905; Reynolds, 1883) and the thermal resistance of the pipe (Carslaw and Jaeger, 1959). There are differences for the area outside the pipe: the supply and return pipe can be much further apart, the trenches are backfilled rather than grouted, and heat transport mechanisms other than conduction may be involved. Again, both analytical and numerical approaches have been proposed in different contexts, such as buried power cables, oil or steam pipelines, pipes used in district heating networks and, more recently, horizontal geothermal collectors.

2.2.1 Outside the pipe

Similar to the vertical boreholes, the analytical solutions are based on the line or cylinder source theory, while the method of images takes into account the ground surface (e.g. Ingersoll, 1948; Ingersoll et al., 1954). Instead of calculating the temperature change at the borehole wall ΔT_b, they are now used to calculate the temperature change at the outer wall of a single pipe, denoted as ΔT_p. The same temporal and spatial superposition methods are used as for the vertical heat sources.

Applying the method of images to the infinite line source (Eq. 2.1) leads to

$$\Delta T_\mathrm{p}(r,t,D) = \frac{q}{4\pi\lambda}\left\{E_1\left(\frac{r^2}{4\alpha t}\right) - E_1\left(\frac{(2D)^2}{4\alpha t}\right)\right\} \tag{2.11}$$

where D is the burial depth of the line source and r is the outer radius of the pipe. The general solution for an arbitrarily oriented finite line source in a semi-infinite body was presented by Marcotte and Pasquier (2009), reading as

$$\Delta T_{\mathrm{w}}(t) = \frac{q}{4\pi k S} \int_{\mathrm{wall}} \int_{x_1}^{x_2} \frac{\operatorname{erfc}\left(d\left(x, x_{\mathrm{w}}\right)/2\sqrt{\alpha t}\right)}{d\left(x, x_{\mathrm{w}}\right)} dx - \int_{y_1}^{y_2} \frac{\operatorname{erfc}\left(d\left(y, x_{\mathrm{w}}\right)/2\sqrt{\alpha t}\right)}{d\left(y, x_{\mathrm{w}}\right)} dy dx_{\mathrm{w}} \quad (2.12)$$

where $S = 2\pi r H$ and x_1, x_2 are the points defining the line source while y_1, y_2 define the image of the line source as shown in Figure 2.3. The index w defines points that are located on the outer wall of the pipe, while d is the distance between two points, e.g. $d(x, x_{\mathrm{w}})$ is the distance between a point on the line source and a point on the pipe wall, leading to $d(x, x_{\mathrm{w}}) = r$ in that case.

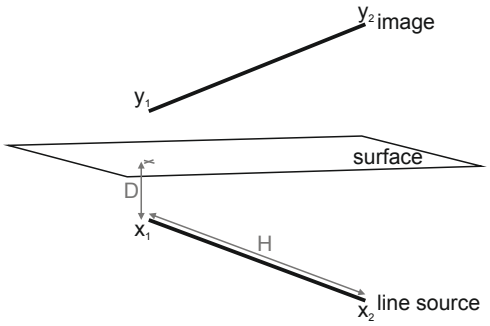

Figure 2.3 Real and image inclined finite line source. After Marcotte and Pasquier (2009).

Following the work of Claesson and Javed (2011) and Cimmino and Bernier (2014) on vertical boreholes, Lamarche (2019) presented the general form for the segment-to-segment response for horizontal pipes, which eliminates the double integral in Equation 2.12. Reduced to a single segment, we get

$$\Delta T_{\mathrm{p}}(r, t, D) = \frac{q}{4\pi\lambda} \int_{\frac{1}{\sqrt{4\alpha t}}}^{\infty} \frac{2\left(e^{-r^2 s^2} - e^{-(2D)^2 s^2}\right)}{s^2} \left[Hs \operatorname{erf}(Hs) - \frac{1}{\sqrt{\pi}}\left(1 - e^{-H^2 s^2}\right)\right] ds. \quad (2.13)$$

To account for the radius of the heat source, the same procedure as for the line source can be applied to the cylinder source: the solutions for the vertical cylinder sources are extended by a sink term using the method of images to account for the ground surface (e.g. Ioffe, 1972; Martin and Sadhal, 1978). For example, for the infinite cylinder source (Eq. 2.6) we get:

$$\Delta T_\mathrm{b}(r,t,D) = \frac{q}{4\pi\lambda}\int_0^\pi \frac{1}{\pi}\Bigg\{ \mathrm{Ei}\left(\frac{r^2+r_0^2-2rr_0\cos\varphi'}{4\alpha t}\right) - \mathrm{Ei}\left(\frac{(2D)^2+r_0^2-4D)r_0\cos\varphi'}{4\alpha t}\right)\Bigg\} d\varphi'. \quad (2.14)$$

Analytical solutions for heat transport around horizontal heat sources are generally subject to the same limitations as those for vertical heat sources. One extension is the work from Bau (1984), presenting an analytical solution for steady-state low Rayleigh number convection induced by a pipe buried in a saturated, semi-infinite, permeable medium. To cover a wider range of Rayleigh numbers, Farouk and Shayer (1988) used a finite difference model on the same problem. More recent works on horizontal ground heat exchangers also consider other transfer mechanisms using numerical models. The Piechowski (1999) finite difference model and the Gan (2019) finite volume model include mass transfer due to moisture content. The Gan (2013) finite volume model includes freezing. Another aspect that is more relevant for horizontal pipes than for vertical borehole heat exchangers is the boundary condition at the ground surface. The Gan (2013) model accounts for convection at the surface, while the Gan (2019) model includes condensation, evaporation, freezing, thawing, precipitation and diffusion for moisture transfer, wind and buoyancy-induced natural convection, radiation, heat conversion from precipitation and evaporation/condensation.

2.2.2 Inside the pipe

With a diameter of a few centimetres, the horizontal connection pipes in BHE fields are similar in size to the fluid pipes within the BHEs. This means that, unlike oil pipelines, for example, turbulent flow and a homogeneous temperature profile of the fluid can be assumed across the cross-section of the pipe. The temperature profile in the fluid can thus be regarded as one-dimensional and is described by Eq. 2.15. The heat capacity of the pipe wall is neglected, and heat is exchanged with the surrounding ground (Diersch et al., 2010):

$$\frac{\partial T_\mathrm{f}}{\partial t} + u_\mathrm{f}\frac{\partial T_\mathrm{f}}{\partial x} - \alpha_\mathrm{f}\frac{\partial^2 T_\mathrm{f}}{\partial x^2} + \phi\,(T_\mathrm{f}-T_\mathrm{s}) = 0. \quad (2.15)$$

T_f and T_s are the temperatures of the fluid and the soil, u_f is the velocity of the fluid and α_f is its thermal diffusivity. The specific heat transfer coefficient ϕ is calculated based on the thermal resistance between fluid and soil R_fs, the volumetric heat capacity of the fluid ρc_f and the inner cross-sectional area of the pipe A_i:

$$\phi = \frac{1}{R_\mathrm{fs} A_\mathrm{i} \rho c_\mathrm{f}}. \quad (2.16)$$

The thermal resistance between the fluid and the soil is the sum of the advective resistance from the fluid to the inner wall of the pipe and the conductive resistance of the pipe (see Chapter 5 for more details).

An analytical solution for Eq. 2.15 was presented by Van Genuchten (1981, 1982) for specific initial and boundary conditions in the context of solute transport. For $T(x,0) = T_\mathrm{s}$, $T(0,t) = T_\mathrm{in}$ and $\frac{\partial T_\mathrm{f}}{\partial x}(\infty, 0) = 0$ it is

$$T(x,t) = T_\mathrm{s} + \frac{(T_\mathrm{in} - T_\mathrm{s})}{2} \Bigg\{ \exp\left[\frac{(u_\mathrm{f} - v)x}{2\alpha_\mathrm{f}}\right] \operatorname{erfc}\left(\frac{x - vt}{2\sqrt{\alpha_\mathrm{f} t}}\right) + \exp\left[\frac{(u_\mathrm{f} + v)x}{2\alpha_\mathrm{f}}\right] \operatorname{erfc}\left(\frac{x + vt}{2\sqrt{\alpha_\mathrm{f} t}}\right) \Bigg\} \quad (2.17)$$

with

$$v = u_\mathrm{f} \sqrt{1 + \frac{4\phi\alpha_\mathrm{f}}{u_\mathrm{f}^2}}. \quad (2.18)$$

Inserting $t = \infty$ results in the solution for the steady state:

$$T(x) = T_\mathrm{s} + (T_\mathrm{f,in} - T_\mathrm{s}) \exp\left[\frac{(u_\mathrm{f} - v)x}{2\alpha_\mathrm{f}}\right]. \quad (2.19)$$

In Eq. 2.17 and 2.19 the temperature at the outside of the pipe T_s is constant along the pipe. This results in an exponentially decaying heat flux and temperature profile in the fluid. On the other hand, if a linear temperature profile is assumed in the fluid, this corresponds to a constant heat flux along the pipe:

$$T(x) = T_\mathrm{s} + (T_\mathrm{f,in} - T_\mathrm{s})(1 - \frac{x}{R_\mathrm{fs} V \rho c_\mathrm{f}}). \quad (2.20)$$

Both approaches, linear and exponential temperature profiles are used in the literature. Claesson and Dunand (1983) derived the formula for the exponential decay and defined limits in which the linear approximation can be used with good accuracy. Bahmani and Hakkaki-Fard (2022), Habibi and Hakkaki-Fard (2018), and Rezaei et al. (2012) and Kayaci and Demir (2018) used the exponential decay in their horizontal ground heat exchangers models. Xiong et al. (2015) assumed a linear temperature profile in their slinky ground heat exchanger model. Kavanaugh and K. D. Rafferty (2014) used the linear approximation to calculate temperature changes along header pipes. In the work of Fontaine et al. (2011) and Lamarche (2019) on horizontal ground heat exchangers, the pipe is divided into multiple

segments and the solutions for linear and exponential temperature profile per segment are considered.

Dividing the pipe into several segments and then coupling the segments is a form of discretisation. Other authors use different numerical methods to discretise Eq. 2.15. Usually the same methods are then used to discretise the surrounding ground. The finite difference method has often been used in earlier work. For example, Negiz et al. (1993) used the finite difference method to simulate the three-dimensional transient heat transfer from a buried pipe on a supercomputer. Piechowski (1999) uses the same method for his model of a ground heat exchanger. In more recent work, the finite difference method is used less frequently. Dasare and Saha (2015) used the finite volume method to investigate influencing factors on horizontal ground heat exchanger performance. C. F. Li et al. (2019) used the finite element method to investigate the influence of ground surface boundary conditions on horizontal ground-source heat pump systems and Dinh et al. (2021) used it to study the effect of groundwater level drop with soil–water thermal characteristics. The COMSOL Multiphysics software package is often used in conjunction with the *Pipe Flow Module*, which can simulate flow, heat and mass transfer in pipes (e.g. Dinh et al., 2021; Kim et al., 2018; Lamarche, 2019; Shi et al., 2022; Tang and Nowamooz, 2020; Yang et al., 2020).

2.3 Heat transfer along connection pipes in geothermal bore fields

Research on heat transfer along horizontal connection pipes of BHEs is limited. Luo et al. (2013) analysed the heat transfer along horizontal connection pipes in a BHE field located in Nuremberg, Germany. The field is grouped into three manifolds, each connected to six BHEs. Fluid temperatures were measured along the supply pipes to the manifolds with two monitoring points in one pipe spaced 18 m apart. The pipe is buried at a depth of 1 m without insulation. During the heating operation in January the measurements indicated a temperature drop of about 1 K between the monitoring points when the fluid was circulating. The heat pump operated intermittently, with cycle times between 30 and 60 min. The inlet temperature of the BHE field during that time was around 7 °C which can be considered high for the maximum heating loads that occur during that time. In summer, the system is used for passive cooling with a more continuous operation. Here, the inlet temperature of the BHE field was 17 °C and no temperature differences could be observed between the monitoring points.

The authors also investigated the effect of burial depth and pipe insulation using a 3D finite element model and concluded that the soil temperature is influenced by the ambient (air) temperature and that increasing burial depth reduces heat loss in winter. The temperature drop in or along the pipe was investigated in two scenarios: stagnant fluid and circulating fluid. However, it is not clear from the results presented which scenario they refer to. Based on the temperature losses, the energy loss (kW h) was calculated and directly converted into

monetary costs. It is questionable whether this analysis is valid. Instead, the whole system of heat pump, horizontal pipes and BHEs should be considered. Depending on the building load, the heat pump imposes a defined thermal load on the system of connection pipes and BHE, as long as the temperature limits of the heat pump are maintained. If there is heat loss in the connection pipes, this is compensated by increased extraction along the BHE. However, this may result in lower fluid temperatures. To convert this temperature drop into a cost, the power consumption of the heat pump must be taken into account according to the temperature dependent coefficient of performance (COP).

Tian et al. (2022) performed an experimental study on heat transfer along horizontal header pipes with a sandbox experiment. The test setup was a 1 m deep U-loop connected to a 2 m long connection pipe. The reason for this unusual length ratio is not explained. The connection pipe was then covered with limestone, dolomite and sandstone with thicknesses of 20, 40 and 60 mm to investigate the effect of burial depth and covering material. The photos indicate that the covering material is crushed with a grain size of around 10 mm for the dolomite and limestone, while for the sandstone the material seems to be much finer. This results in different bulk densities, so the reported rock thermal conductivities are unlikely to be the same as in the experiments. The initial average temperature of sandbox was around 15 °C, the surface of the covering layer was heated to 30, 35 or 40 °C and the pipe was flowed through with 24 °C warm water for 30 min in each experiment. With these thermal boundary conditions the fluid temperature rose along the supply connection pipe, dropped in the BHE, and rose again in the return connection pipe. It should be noted the reported temperature differences between the monitoring points (inlet supply connection pipe, inlet and outlet vertical U-loop and outlet connection pipe) are often < 0.1 K. Finally, the results are all common sense and to be expected.

2.4 Summary of research gaps

The literature review on borehole heat exchanger simulation shows that the available solutions fall into two categories. On the one hand, there are tools such as EED (Hellström and Sanner, 1994) and EWS (Huber, 2005) that designers and engineers use every day to design geothermal systems. These software packages are easy to use and provide fast results, but are primarily intended for layout and design purposes and lack flexibility for other applications. On the other hand, simulation platforms such as COMSOL Multiphysics (COMSOL AB, Stockholm, Sweden, n.d.) are mainly used in research and development. These tools can address almost any problem, but require significant expertise and modelling effort. Even with this expertise, simulations often have high computational times. In addition to these directly available tools, there are numerous publications on other computational models in research. However, as shown above, much of this work is limited to one of the areas, either inside or outside

the borehole. Furthermore, the models are often only published as papers; ready-to-use implementations such as *pygfunction* (Cimmino and Cook, 2022) are the exception rather than the rule. In summary, there is a lack of a model that combines the flexibility of research and development software with the efficiency of common design tools. This gap will be addressed by answering the research question *How can large fields of borehole heat exchangers be efficiently modelled for multi-year periods in small time steps?*.

The effects of horizontal connection pipes in BHE fields have been largely neglected in research and practice. This is often justified for smaller systems with short connection pipe lengths, but as the EON.ERC example shows, larger systems require connection pipes that can quickly equal several additional BHEs in length. The two publications cited on this subject leave many questions unanswered. In the Luo et al. (2013) work, only the horizontal pipes are simulated, without consideration of the BHEs. The Tian et al. (2022) paper is purely experimental, without any calculations. This indicates that there is a lack of a holistic calculation approach for horizontal pipes and borehole heat exchangers. By answering the research question *Which models are suitable for the loop network in combination with the borehole heat exchanger simulation?*, this gap will be filled.

The Luo et al. (2013) work is limited to the Nuremberg site. The heat transfer along the horizontal connection pipes is primarily driven by the temperature difference between the fluid in the pipes and the surrounding ground, making it directly dependent on climatic conditions and the thermal load profile. This is addressed by answering the research question *What are the effects of the near-surface horizontal connection pipes on the operation of the geothermal system?* in a global context considering several climate zones.

The potential to exploit positive effects or avoid negative effects of horizontal connection pipes has been completely ignored until now. Addressing the research question, *Can the operating strategy be optimized based on the heat gains and losses along the horizontal connection pipes?* represents the first step into this previously unexplored field.

Chapter 3

Hybrid borehole heat exchanger model

Published as:

Düber S., Ziegler M., Fuentes R. (2022): Development and validation of a computationally efficient hybrid model for temporal high-resolution simulations of geothermal bore fields. *International Journal for Numerical and Analytical Methods in Geomechanics*, 46 (14), pp. 2792 - 2813.

Düber S.: Conceptualization, Methodology, Software, Validation, Writing - Original Draft **Ziegler M.:** Writing - Review & Editing, Supervision **Fuentes R.:** Writing - Review & Editing, Supervision.

Abstract

This paper presents a hybrid simulation approach for 1U-, 2U- and coaxial single, and field of, borehole heat exchangers. We implement a novel combination of existing solutions for the simulation of heat transfer processes within the borehole and the surrounding ground. The heat transfer in the ground is modelled with a combination of analytically determined g-functions, the borehole models utilize thermal resistance capacity models and the finite volume method. Critically, we improve the computational efficiency of long-term simulations by sub-dividing the time scale into multiple periods, where the influence of past periods on future periods is calculated using the Fast Fourier Transform. The accuracy and efficiency of the proposed method is validated against single borehole numerical models and a 40 bore field case study. The method achieves computational times reductions of over 90 % in some cases, with greater improvement as the simulation time increases.

3.1 Introduction

The design and simulation of geothermal systems with borehole heat exchangers can be challenging due to the three-dimensional heat transfer processes in the ground and the heat exchanger, the large spatial scale differences and the long operational periods. The scale-distributed geometries and transient transfer processes lead to high computational costs when using numerical models. For example, traditional design periods of 50 years mean that, such models are not often used in practice (Spitler and Bernier, 2016). Simplified solutions with some limitations are widely preferred due to their simpler handling and short computational times. In most common solutions, the spatial domain is divided into two parts, the domain inside the borehole and the domain outside the borehole (see Figure 3.1, left). One advantage of this approach is that different simulation methods can be used for both areas.

A computationally efficient method for the area outside the borehole is the g-function approach introduced by Eskilson (1987). G-functions are thermal response functions that can be used to calculate the temperature response at the borehole wall or any other point in the ground for an imposed constant load. For time varying loads, as they occur in reality, Duhamel's theorem, from now on referred to as superposition principle, is typically applied (Carslaw and Jaeger, 1959). To speed up computational time for high-resolution time variable loads, Marcotte and Pasquier (2008) proposed to solve the problem in the Fourier domain using the convolution theorem.

G-functions depend on the borehole geometry and the characteristic time $t_s = H^2/9\alpha_s$ where H is the length of the borehole and α_s the thermal diffusivity of the ground and can be derived with numerical or analytical methods (Eskilson, 1987). While Eskilson (1987) and others (Yavuzturk et al., 1999) determine g-functions numerically, a variety of analytical

solutions exist. One key element is the geometry used to model the borehole in a simplified way. While the infinite line source (ILS) considers the borehole as an infinite one-dimensional heat source in infinite space (Carslaw and Jaeger, 1959; Ingersoll, 1948), the finite line source (FLS) considers the finite length of the borehole in semi-infinite space (Zeng et al., 2002). In contrast to line sources models, cylinder source models consider the actual radius of the borehole (Bernier, 2001; Carslaw and Jaeger, 1959; Ingersoll et al., 1954; Man et al., 2010). Philippe et al.Philippe et al. (2009) show the different validity ranges in the time domain of the mentioned solutions. While the FLS provides better results for short boreholes or long observation periods, the cylinder source models lead to more accurate results for short-term observations because of the relative importance of the borehole geometry initially in the short-term. M. Li et al. (2014) combine the different models and derive a g-function that produces accurate results over the entire time scale and call it *fullscale* g-function.

To account for groundwater flow in homogeneous soil, the borehole can be modelled as a moving line (Carslaw and Jaeger, 1959; Molina-Giraldo et al., 2011; Sutton et al., 2003) or cylinder sources (W. Zhang et al., 2013). Other extensions of the finite line source consider inhomogeneous soil structure (Abdelaziz et al., 2014) and horizontal groundwater flow through sequences of permeable and impermeable soil layers (Erol and François, 2018).

By dividing the borehole into multiple segments, Cimmino and Bernier (2014) developed a method based on the FLS for determining the g-function of BHE fields with different boundary conditions, such as equal borehole wall temperature in all boreholes.

While the approaches mentioned above are used to calculate temperatures outside and at the borehole wall, others also include the heat exchanger itself (Cimmino, 2015; Claesson and Javed, 2011; Loveridge and Powrie, 2013; Pasquier et al., 2018; Yavuzturk and Spitler, 1999; Yavuzturk et al., 1999).

An alternative method to cover the processes inside the borehole are models based on thermal resistances and capacities (Bauer et al., 2011; Y. Gu and O'Neal, 1998; Hellström, 1991; Liao et al., 2012; Pasquier and Marcotte, 2012; Sharqawy et al., 2009; Zarrella et al., 2011). In this approach, the horizontal heat flows are modelled with a circuit of coupled thermal resistances (see Figure 3.1, middle). The convective heat flows in the circulating fluid can be solved analytically with a few simplifications by coupled partial differential equations (Eskilson and Claesson, 1988) or numerical methods (Kavanaugh, 1985; Al-Khoury and Bonnier, 2006). Models that use thermal resistance capacitance models (TRCM) for the horizontal heat transfer and numerical methods for the vertical heat transfer within the fluid are referred to as numerical borehole models here on. Combining both approaches explained above, various simulation tools use a combination of numerical borehole models and g-functions. The simulation tool *EWS* couples a TRCM with numerical or analytical derived g-functions (Huber, 2005). Ruiz-Calvo et al. (2016) include the near ground effects in the numerical BHE model and couple it with a g-function for the far-field and a load aggregation scheme. The model presented by Düber (2018) combines TRCM with a fullscale analytical g-function.

Laferrière et al. (2020) also use a fullscale analytical g-function coupled to a TRCM and combine it with a load aggregation scheme. All of the above report accurate results against different conditions. However, their efficiency in terms of computational time when not using a load aggregation scheme could be improved. This is of particular importance when the number of boreholes in a field is large or when the modelled times are long, as in the real-life operation of such systems, e.g. 100 years or longer.

This paper presents an extension to the model from Düber (2018), incorporating the application of the fast Fourier transformation to perform high temporal resolution simulations of multiple BHE in a computationally efficient manner. By using this method, the calculation time could be reduced significantly without the use of a load aggregation scheme. The paper starts with a description of the model in Section 3.2, followed by a validation and demonstration in Section 3.3 using single borehole with 1U-, 2U- and coaxial type heat exchangers, and a borehole field consisting of 40 2U-BHEs. Finally a discussion and conclusions are presented. All models are implemented in Python and are available through a GitHub repository (Düber, 2022).

3.2 Model

3.2.1 Model structure and simulation process

The presented model has several components: the simulation methods for the domains inside and outside the borehole; the coupling of the two and; the integration of the FFT model for the domain outside the borehole. Furthermore, a method for the determination of model specific parameters is presented to demonstrate its use.

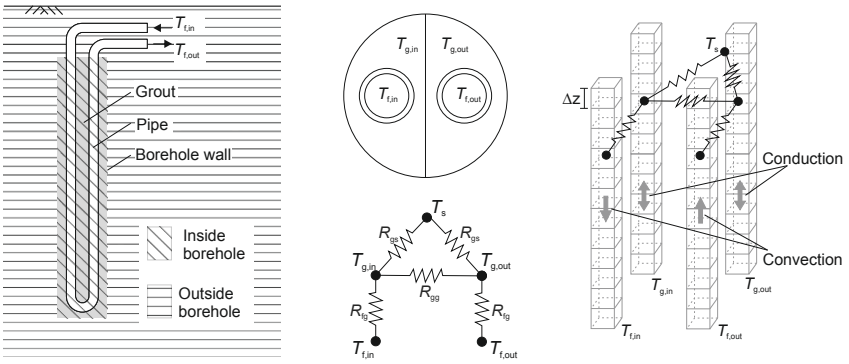

Figure 3.1 Schematic illustrations of a 1U-BHE model: longitudinal section (left); cross section and resistance model with temperature nodes (middle); vertical discretisation and transfer processes,the resistances and temperature nodes are shown exemplary for one horizontal plane (right).

3.2.1.1 Heat transfer inside the borehole

Here we use the implementation of Bauer et al. (2011) for the thermal resistances and the spatial division of the grout material for 1U-, 2U-, and Coaxial-BHE with an annular inlet.

The heat transfer in the vertical direction is a combination of heat conduction in the grout material and convection in the fluid and is governed by the transient convection-diffusion equation

$$\varrho c \frac{\partial T}{\partial t} = \boldsymbol{\nabla} \cdot (\lambda \boldsymbol{\nabla} T - \upsilon \varrho c T) + q_{\mathrm{h}} \tag{3.1}$$

which is discretised using the finite volume method. In Eq.3.1 T denotes the temperature, t the time, ϱc the volumetric heat capacity, λ the thermal conductivity, υ the fluid velocity and q_{h} the source term. As shown in Figure 3.1 on the right, the equation is discretised and solved in 1D for each temperature node within the borehole. For the grout material this results in:

$$\varrho c \frac{\partial T}{\partial t} = \boldsymbol{\nabla} \cdot (\lambda \boldsymbol{\nabla} T) + q_{\mathrm{h}} \tag{3.2}$$

and for the temperatures in the fluid, neglecting conduction:

$$\varrho c \frac{\partial T}{\partial t} = \boldsymbol{\nabla} \cdot (-\upsilon \varrho c T) + q_{\mathrm{h}}. \tag{3.3}$$

Different numerical interpolation schemes are used for Eq. 3.2 and Eq. 3.3. The diffusion term (Eq. 3.2) is interpolated with the central difference scheme (CDS) whereas the convective term (Eq. 3.3) is approximated with the upwind scheme to prevent oscillating solutions for high Péclet numbers. Besides being computationally efficient, the upwind scheme does not produce any non-physical solutions (e.g. oscillations), which may produce problems when coupling the model with other system component models. On the other hand the upwind scheme can introduce numerical diffusion, which can be controlled by adequate spatial and time discretisation, depending on the numerical integration method.

The heat transfer in the horizontal direction is solved with analytical equations based on Fourier's law. The horizontal heat flows q_{h} are integrated as a source term in Eq.3.1, and they depend on the total thermal resistance R_{th} (e.g. the resistance between fluid and grout R_{fg}, or the resistance between grout and soil R_{gs}), the cell height Δz and are driven by the temperature gradient ΔT between two temperature nodes (e.g. $T_{\mathrm{f,in}} - T_{\mathrm{g,in}}$ or $T_{\mathrm{g,in}} - T_{\mathrm{s}}$, as shown in the nodes-resistance model in Figure 3.1):

$$q_{\mathrm{h}} = \frac{\Delta z \cdot \Delta T}{R_{\mathrm{th}}}. \tag{3.4}$$

The total thermal resistances R_{th} are serial connections of convective and diffusive resistances. For example, the resistance between the fluid and the grout is a serial connection of the convective resistance between the fluid and the inner wall of the pipe R_{conv}, the conductive

resistance of the pipe R_{pipe} and the conductive resistance between the outer wall of the pipe and the thermal center of the grout $R_{\text{pipe-grout}}$ (Figure 3.2). While the conductive resistances are calculated based on the geometry and thermal properties of the material, the convective resistance is based on the dimensionless flow coefficients *Reynolds*, *Nusselt* and *Prandtl*. Detailed compilations of all equations are given in Diersch et al. (2010) and Bauer et al. (2011).

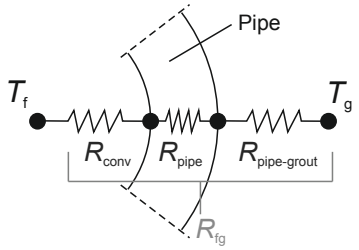

Figure 3.2 Exemplary illustration of the elements of the thermal resistance between fluid and grout.

For the numerical integration of Eq. 3.1 the forward and backward Euler methods are implemented and compared. The Euler method was chosen for its simplicity and efficiency. Depending on fluid velocity, spatial and temporal discretization or desired accuracy, one of the methods may be advantageous over the other. While the backward scheme is preferred in general due to its robustness and unconditional stability, the forward scheme can be more computationally efficient for certain conditions. It is also easier to reduce the numerical diffusion caused by the upwind method in the forward scheme by choosing a Courant-Friedrichs-Lewy (CFL) number close to 1, while for the backward method the spatial and temporal discretisation have to be refined. Figure 3.3 shows the computational time per timestep for the 2U-BHE model. The computational times of the BHE models are driven only by the number of cells, as no internal iteration is required for the forward models and a direct solver (*scipy.sparse.linalg.spsolve*, Virtanen et al., 2020) is used for the backward models. For a model with 100 cells for each temperature node the Forward Euler implementation is about 5 times faster than the backward Euler model. With increasing number of cells the difference between the two schemes also increases linearly. Despite these results, it cannot be concluded that the forward scheme will always be the best choice in terms of computational effort as it depends on the timestep. The maximum timestep that can be used depends on cell size and fluid velocity, according to Fichter (Treeck et al., 2020) it can be calculated using the CFL condition as

$$\Delta t_{\max} = \left(\frac{v}{\Delta z} + \frac{2\alpha}{(\Delta z)^2} + \sum_i \frac{\Delta z}{\varrho c R_{\text{th}} \Delta V} \right)^{-1}. \tag{3.5}$$

The first term of Eq. 3.5 accounts for the convection, the second term with the thermal diffusivity α for conduction in vertical direction and the last term with the cell volume ΔV for the horizontal heat transfer. The total thermal resistance R_{th} is calculated according

to the pipe configuration (Bauer et al., 2011; Diersch et al., 2010) and the cell type. To obtain the overall maximum timestep size for the forward implementation, Eq. 3.5 has to be solved for the grout and the fluid cells. Accordingly, the following results for a 1U-BHE configuration as shown in Figure 3.1 with the thermal resistances between fluid and grout R_{fg}, between the two grout sections R_{gg}, and between grout and soil R_{gs}:

$$\Delta t_{\mathrm{max,fluid}} = \left(\frac{\upsilon}{\Delta z} + \frac{\Delta z}{\varrho c_{\mathrm{f}} R_{\mathrm{fg}} \Delta V} \right)^{-1} \tag{3.6}$$

and

$$\Delta t_{\mathrm{max,grout}} = \left(\frac{2\alpha}{(\Delta z)^2} + \frac{\Delta z}{\varrho c_{\mathrm{g}} R_{\mathrm{fg}} \Delta V} + \frac{\Delta z}{\varrho c_{\mathrm{g}} R_{\mathrm{gg}} \Delta V} + \frac{\Delta z}{\varrho c_{\mathrm{g}} R_{\mathrm{gs}} \Delta V} \right)^{-1}. \tag{3.7}$$

The minimum of $\Delta t_{\mathrm{max,fluid}}$ and $\Delta t_{\mathrm{max,grout}}$ is the decisive timestep for the simulation.

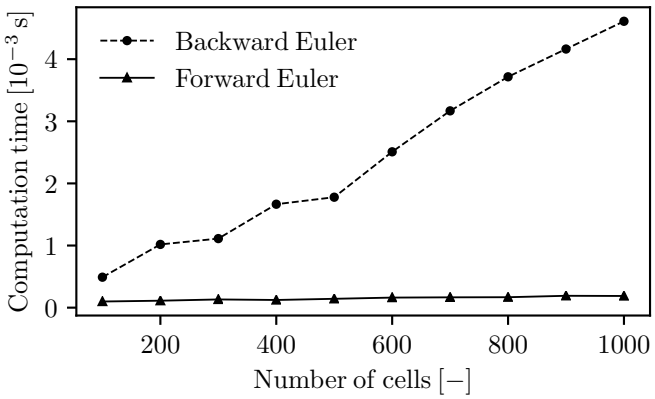

Figure 3.3 Computational time per step for forward and backward Euler BHE models depending on vertical discretization. Processing unit is an Intel i7-7700K processor at 4200 MHz, 16 GB of RAM, Windows version 10.

3.2.1.2 Heat transfer outside the borehole

For the domain outside the borehole, the g-function approach introduced by Eskilson (1987) is used. The temperature at the borehole wall T_{b} due to an imposed load q is calculated as follows:

$$T_{\mathrm{b}} = T_0 + \frac{q}{2\pi\lambda_{\mathrm{s}}} \cdot g\left(\frac{t}{t_{\mathrm{s}}}, \frac{r_{\mathrm{b}}}{H}, \frac{D}{H}\right). \tag{3.8}$$

The second term of Eq. 3.8 represents the temperature change due to the imposed load, where T_0 is the undisturbed ground temperature. Here λ_{s} denotes the thermal conductivity of the soil, r_{b} the borehole radius and D the buried depth.

Three of the main analytical solutions to calculate g to date are the infinite cylinder source (ICS) (Man et al., 2010), the finite line source (FLS) (Zeng et al., 2002) and the infinite line source (ILS) (Carslaw and Jaeger, 1959). As shown by Philippe et al. (2009), the ICS works most accurately for the shortest dimensionless time, whereas the ILS is only accurate for the medium term and the FLS for the longer term. Inspired by the work of M. Li et al. (2014) we use a combination of different analytical derived g-functions to cover the full-time range (Düber, 2018; Laferrière et al., 2020):

$$g_{\text{fullscale}} = g_{\text{ICS}} + g_{\text{FLS}} - g_{\text{ILS}}. \tag{3.9}$$

While for the short term and medium term ILS and FLS overlap, the same is true for the medium term and long term for ICS and ILS. This allows us to intersect the different approaches according to Eq. 3.9 and thus calculate a combined *fullscale* g-function that is valid for the entire time range. We use the FLS formulation proposed by Claesson and Javed (2011) to calculate the integral mean temperature along the borehole. For the ICS we favour the easy to evaluate formulation proposed by Man et al. (2010).

For multiple boreholes, the spatial superposition principle (Carslaw and Jaeger, 1959) can be used to account for thermal interaction:

$$\Delta T_{\text{b},i} = \sum_{j=1}^{n_\text{b}} \frac{q_j}{2\pi\lambda_\text{s}} g_j(d_{ji}) \tag{3.10}$$

$$d_{ji} = \begin{cases} r_{\text{b},i} & \text{for } i = j \\ \sqrt{(x_i - x_j)^2 + (y_i - y_j)^2} & \text{for } i \neq j \end{cases} \tag{3.11}$$

This means the temperature change ΔT_b at the borehole i is the sum of the temperature changes due to all considered boreholes with coordinates (x_j, y_j) and their associated loads q_j. For the consideration of time variable loads, temporal superposition can be applied where $q(t)$ (Figure 3.4, (1)) is divided into load increments $\Delta q(t_k) = q(t_k) - q(t_{k-1})$ (Figure 3.4, (2)). The temperature change at any step k (Figure 3.4, (4)) is the sum of all past temperature responses (Figure 3.4, (3)) at their respective load increments. Including the summation over time into Eq. 3.10 leads to:

$$\Delta T_{\text{b},i,k} = \sum_{l=1}^{k} \sum_{j=1}^{n_\text{b}} \frac{\Delta q_{j,l}}{2\pi\lambda_\text{s}} g_{j,k-l+1}(d_{ji}). \tag{3.12}$$

3.2.1.3 Coupling of borehole and underground model

The coupling parameter between the numerical borehole model and the g-function model is the soil temperature at the borehole wall T_b. Based on the soil temperature and the fluid

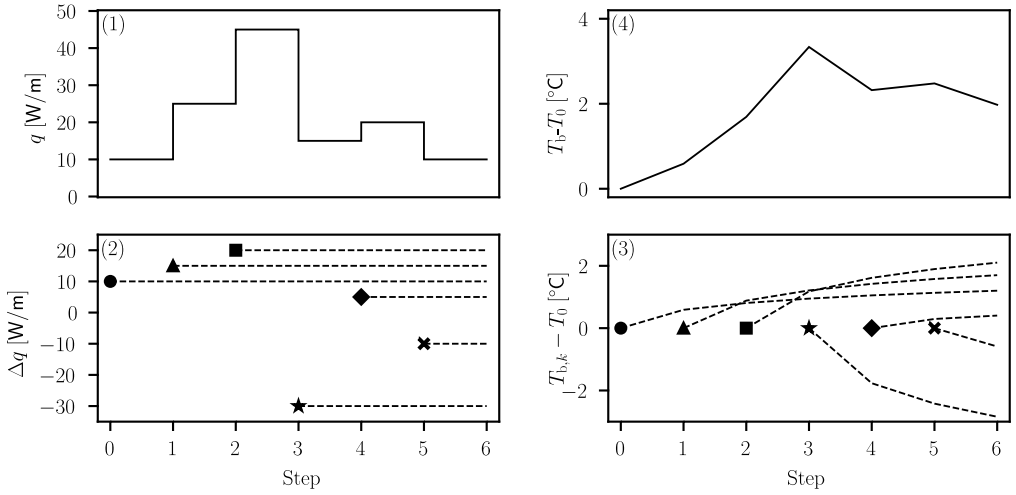

Figure 3.4 Application of the superposition principle for time-varying loads: Decomposition of the load (1) as load increments (2) and superposition of the temperature responses (3) to construct the solution (4). After Marcotte and Pasquier (2008) and (Lazzarotto, 2015).

inlet temperature, the borehole model calculates new temperatures for all BHE components. The difference between the mean grout temperature $\overline{T}_\mathrm{g}$ and the soil temperature T_b and the thermal resistance between grout and soil R_gs determine the ground load:

$$q = \frac{T_\mathrm{b} - \overline{T}_\mathrm{g}}{R_\mathrm{gs}}. \tag{3.13}$$

The ground load serves as input for the g-function model to calculate the soil temperature at the borehole wall. As the borehole wall temperature depends on the grout temperature which also depends on the borehole wall temperature, this problem requires an iterative scheme as shown in Figure 3.5. As a first guess of the soil temperature, we use the value at the previous timestep $i-1$. After calculating a new ground temperature, this process is repeated, until an error tolerance criterion is fulfilled. The deviation of the outlet fluid temperature between 2 iterations is used as error criterion:

$$e = \left| \frac{T_\mathrm{f,out}^\mathrm{new} - T_\mathrm{f,out}^\mathrm{old}}{T_\mathrm{f,out}^\mathrm{old}} \right|. \tag{3.14}$$

The error tolerance has a negligible influence as long as sufficient iterations are allowed. After the error criterion is met, the g-function model is used to calculate the temperature change according to the ground load increment $\Delta q(t_k) = q(t_k) - q(t_{k-1})$ for all future timesteps.

3.2.1.4 Integration of Fast Fourier transform

A disadvantage of the previously presented model, from now on referred to as *semi-analytical model*, is that the computational time increases exponentially with increasing simulation steps

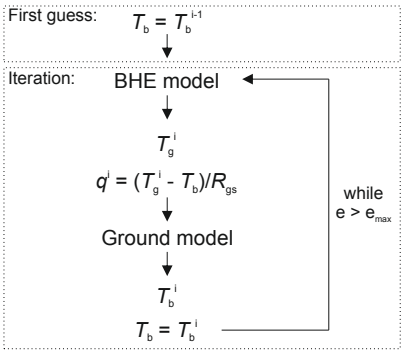

Figure 3.5 Scheme of the coupling process between borehole and ground model.

as the ground temperatures have to be calculated for all future timesteps in each timestep. For example, in the case shown in Figure 3.4, the temperatures due to the first load increment (marked with a circle) must be calculated for timesteps $1-6$. For the second increment (marked wit a triangle) for steps $2-6$ and so on. However, Marcotte and Pasquier (2008) have shown that the computation of the ground temperature can be seen as a convolution in the time domain that can be efficiently evaluated by using the fast Fourier transform (FFT). Applying the FFT to Eq. 3.12 leads to:

$$\Delta T_{\mathrm{b},i} = \sum_{j=1}^{n_\mathrm{b}} \mathscr{F}^{-1}\left(\mathscr{F}(\frac{\Delta q_j}{2\pi\lambda_\mathrm{s}}) * \mathscr{F}(g_j(d_{ji}))\right) \tag{3.15}$$

where $\mathscr{F}$ is the direct and $\mathscr{F}^{-1}$ the inverse FFT. Here we use the *scipy.fft* module (Virtanen et al., 2020) to calculate $\mathscr{F}$ and $\mathscr{F}^{-1}$.

Replacing Eq. 3.12 by Eq. 3.15 can reduce the computational time by several orders of magnitude, depending on the number of timesteps. To make use of Eq.3.15, the load increments Δq for all timesteps have to be known which means it cannot be used directly in the semi-analytical model. However, if we divide the simulation time into multiple time periods (see Figure 3.6) and use the FFT, each of these periods can be simulated using the semi-analytical model. After a period is simulated, all load increments of this period are passed to a second model, from now on referred to as *FFT model*, which uses Eq. 3.15 to calculate the ground temperatures for the following period. These temperatures become the initial temperatures T_0 for the next period.

To give a more practical example let us assume a simulation with 26 time steps with a known inlet temperature as boundary condition. The simulation time is divided into four periods with six time steps each (Figure 3.7). The undisturbed ground temperature is 12 °C. With the undisturbed ground temperature and the fluid inlet temperature, the semi-analytical model is used to simulate the first period. Results of the simulation are, among others, the outlet fluid temperature and the corresponding ground load (Figure 3.8, left). This ground load is now passed to the FFT model. According to the number of time steps of the next period, zeros are appended to the load vector. With this load vector (Figure 3.8,

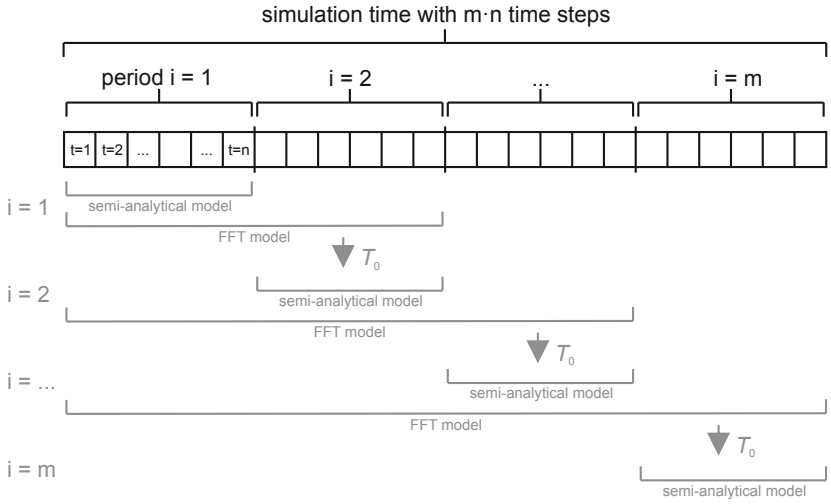

Figure 3.6 Simulation setup with periods (black) and simulation process (grey).

right), the FFT model calculates the ground temperature at the borehole wall for the time steps of the first two periods (Figure 3.8, right). The temperatures for the first period are a by-product and already known from the simulation with the semi-analytical model, while the temperatures for the second period serve as inputs for the simulation of the second period with the semi-analytical model. While for the simulation of the first period with the semi-analytical model the undisturbed ground temperature was initialized with 12 °C, it is now set to the values calculated by the FFT model for the time steps of the second period as shown in Figure 3.8 on the right.

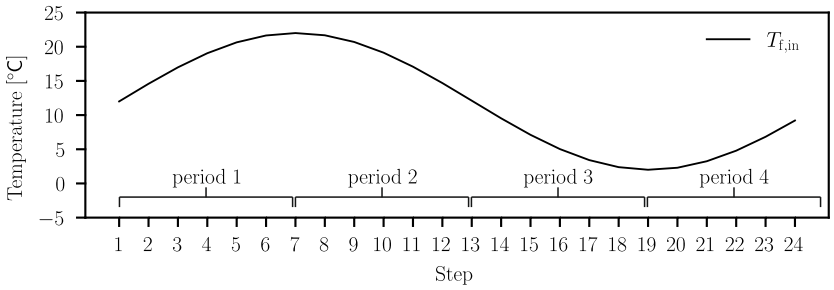

Figure 3.7 Inlet temperature and simulation setup for an exemplary simulation.

Finally, this procedure is repeated for all further periods. The semi-analytical model is used to determine the outlet temperature and the load for the second period (Figure 3.9, left). Using the loads from the first two periods, the FFT model is used again to calculate the ground temperatures for simulation of the third period with the semi-analytical model (Figure 3.9, left). The procedure is repeated until all periods are calculated (Figure 3.10). The simulation of the last period with the semi-analytical model is not shown here, but Figure 3.11 shows the overall result of the simulation.

In the semi-analytical model the g-function model has to be solved at each timestep for all following timesteps of the period (Eq. 3.12). The FFT model however, needs to be computed

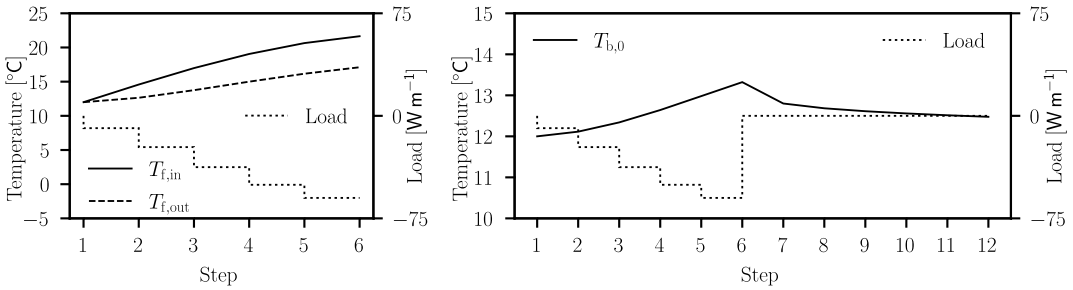

Figure 3.8 Results of the semi-analytical model (left) and the FFT model (right) for the first iteration i according to Figure 3.6.

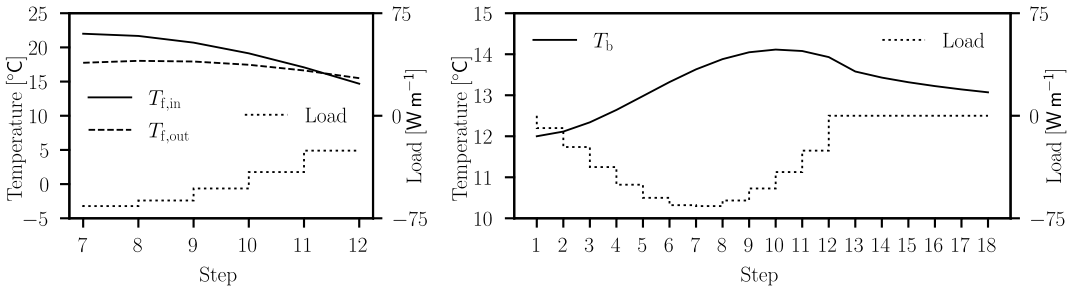

Figure 3.9 Results of the semi-analytical model (left) and the FFT model (right) for the second iteration i according to Figure 3.6.

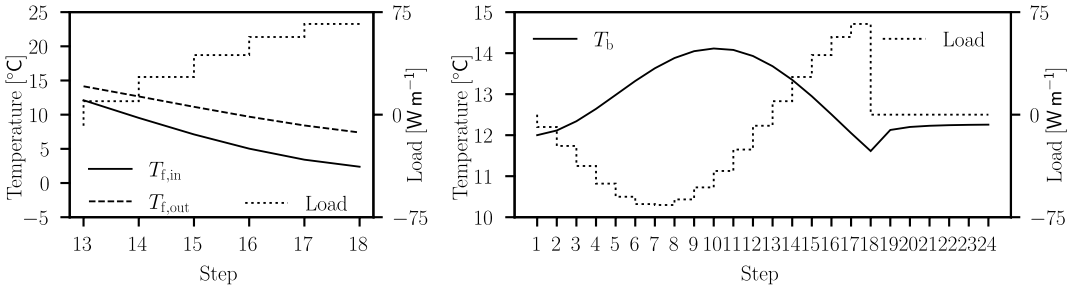

Figure 3.10 Results of the semi-analytical model (left) and the FFT model (right) for the third iteration i according to Figure 3.6.

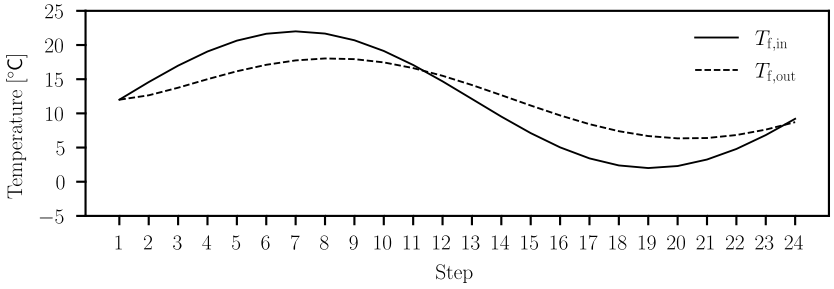

Figure 3.11 Final result of the exemplary simulation.

only once for each period, as the temperature responses for all timesteps are obtained simultaneously by solving Eq.3.15. This procedure reduces the effect of the exponential growth of the computational time as a function of the timesteps. For example, if the

computational time is defined as $\Delta t = \psi n_\mathrm{s}^2$ where n_s is the number of timesteps for the full modelling time, this leads to a computational time of $\Delta t = \psi 100^2$. With the sub-division in periods and FFT, the time becomes $\Delta t = 10 \cdot \psi 10^2$ which is 10 times shorter. Both the computational time of the semi-analytical model and the FFT model depend on the number of timesteps per period. This analysis aims to determine the optimal number of periods depending on the total number of timesteps.

3.2.2 Division of the simulation time

The procedure shown in Figure 3.6 leads to the question though of how many periods the simulation time must be divided into for the most efficient simulation, which we solve in this Section. To provide a more application-oriented view and include memory access times, it was decided to base the analysis on measured process times.

Considering one period with the semi-analytical model, the computational time for the temperature response of each load increment decreases with progressing simulation time, as the temperature response has to be calculated only for the remaining timesteps n_r.

Due to the linear time complexity of the operations involved, the computational time for a timestep Δt_step can then be defined, in general, as a linear function of the remaining timesteps n_r times a constant factor ψ_sa as follows plus a constant c_sa that accounts for setup and memory access time:

$$\Delta t_\mathrm{step} = \psi_\mathrm{sa} n_\mathrm{r} + c_\mathrm{sa}. \tag{3.16}$$

This becomes clear when determining ψ_sa by measuring the computational time for different n_r as shown in Figure 3.12. The line has two sections separated at a breakpoint of $n_\mathrm{bp} = 130\,000$. This breakpoint occurs because of the way the data is handled within the PC. Its location will change depending on the data types, operating system, compilers, etc. Hence, it needs to be calculated for each hardware and software set-up individually. The same applies to the other parameters derived from measured computational times. Since the calculation is only an array multiplication and subtraction, the only relevant parameter is the number of elements n_r. The linear fit leads to:

$$\psi_\mathrm{sa} = \begin{cases} 5.8 \times 10^{-10} & \text{for } n_\mathrm{r} < 130000 \\ 3.7 \times 10^{-9} & \text{for } n_\mathrm{r} \geq 130000 \end{cases} \tag{3.17}$$

and:

$$c_\mathrm{sa} = \begin{cases} 5.4 \times 10^{-6} & \text{for } n_\mathrm{r} < 130000 \\ -9.1 \times 10^{-5} & \text{for } n_\mathrm{r} \geq 130000 \end{cases} \tag{3.18}$$

These values depend on the computer used, the operating system and other factors and are not generally valid. A script for determining the values for any other setup is included in the repository (Düber, 2022).

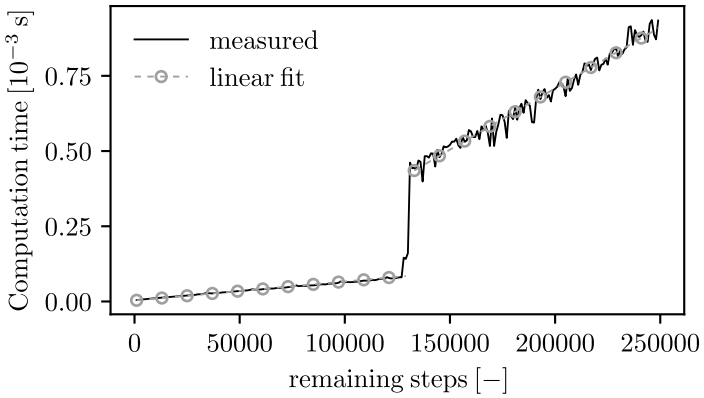

Figure 3.12 Computational time per timestep of the ground model in the semi-analytical model depending on the number of remaining steps. The calculation consists of multiplying the load increment by the g-function for the remaining time steps, and adding the calculated temperature change to the previous temperature.

The fitted line though allows predicting the total computational time of the entire period Δt_{per} which is defined as a function of the number of steps per period n_{sp}:

$$\Delta t_{\mathrm{per}} = \sum_{i=0}^{n_{\mathrm{sp}}-1} \psi_{\mathrm{sa}}(n_{\mathrm{sp}} - i) + c_{\mathrm{sa}} = \frac{\psi_{\mathrm{sa}}}{2}({n_{\mathrm{sp}}}^2 + n_{\mathrm{sp}}) + c_{\mathrm{sa}} n_{\mathrm{sp}}. \tag{3.19}$$

When resolving the summation in Eq. 3.19, it should be noted that different values of ψ_{sa} and c_{sa} apply depending on the side of the breakpoint at which the function is evaluated. When n_{sp} is bigger than n_{bp}, new values $\bar{\psi}_{\mathrm{sa}}$ and $\bar{c}_{\mathrm{sa}}$ are necessary. By introducing $\psi_{\mathrm{sa}} = \psi^{<}_{\mathrm{sa}}$ for $n_{\mathrm{r}} < n_{\mathrm{bp}}$ and $\psi_{\mathrm{sa}} = \psi^{>}_{\mathrm{sa}}$ for $n_{\mathrm{r}} \geq n_{\mathrm{bp}}$ and applying the same for c_{sa} we can calculate weighted parameters (see Appendix 3.5.2 for more details on $\bar{\psi}_{\mathrm{sa}}$):

$$\bar{\psi}_{\mathrm{sa}} = \frac{n_{\mathrm{bp}}^2(\psi^{<}_{\mathrm{sa}} - \psi^{>}_{\mathrm{sa}}) + n_{\mathrm{bp}}(\psi^{>}_{\mathrm{sa}} - \psi^{<}_{\mathrm{sa}}) + \psi^{>}_{\mathrm{sa}}(n_{\mathrm{sp}}^2 + n_{\mathrm{sp}})}{n_{\mathrm{sp}}^2 - n_{\mathrm{sp}}} \tag{3.20}$$

$$\bar{c}_{\mathrm{sa}} = \frac{n_{\mathrm{sp}} - (n_{\mathrm{bp}} - 1)}{n_{\mathrm{sp}}} c^{>}_{\mathrm{sa}} + \frac{n_{\mathrm{bp}} - 1}{n_{\mathrm{sp}}} c^{<}_{\mathrm{sa}} \tag{3.21}$$

However, the implementation of the FFT has a linearithmic time complexity which is linearly approximated for simplicity. This will lead to a negative ordinate intersection for an unconstrained linear fit. Since this does not correspond to reality, and also leads to problems in the following calculations, we will constrain the ordinate intersection to zero for the linear

approximation, so that the relation between the computational time and the number of steps n for the FFT model can be defined as:

$$\Delta t = \psi_{\mathrm{FFT}} n. \tag{3.22}$$

Figure 3.13 shows the computational time of the FFT model depending on the number of steps measured with the model. The linear approximation leads to $\psi_{\mathrm{FFT}} = 1.58 \times 10^{-6}$.

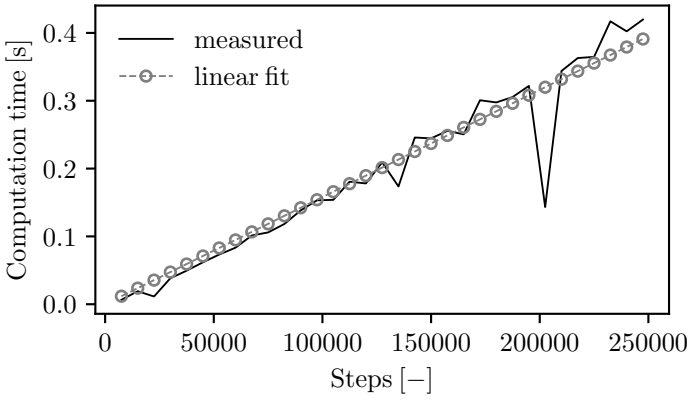

Figure 3.13 Computational time of the FFT model depending on the number of steps.

The total computational time for the FFT model for all periods is

$$\Delta t_{\mathrm{FFT}} = \sum_{i=1}^{n_{\mathrm{per}}-1} (i+1) n_{\mathrm{sp}} \psi_{\mathrm{FFT}} = \frac{\psi_{\mathrm{FFT}}}{2} n_{\mathrm{sp}} ({n_{\mathrm{per}}}^2 + n_{\mathrm{per}} - 2), \tag{3.23}$$

leading to the total computational time for the ground model:

$$\Delta t_{\mathrm{t}} = \frac{1}{2} \left(n_{\mathrm{per}} \psi_{\mathrm{sa}} (\frac{n_{\mathrm{t}}}{n_{\mathrm{per}}}^2 + \frac{n_{\mathrm{t}}}{n_{\mathrm{per}}}) + \frac{n_{\mathrm{t}}}{n_{\mathrm{per}}} c_{\mathrm{sa}} + \psi_{\mathrm{FFT}} \frac{n_{\mathrm{t}}}{n_{\mathrm{per}}} ({n_{\mathrm{per}}}^2 + n_{\mathrm{per}} - 2) \right). \tag{3.24}$$

To find the optimal number of periods depending on the overall number of steps Eq. 3.24 can be minimized (derivation in Appendix 3.5.1), leading to:

$$n_{\mathrm{per}} = \frac{\sqrt{\psi_{\mathrm{sa}} n_{\mathrm{t}} + c_{\mathrm{sa}} - 2\psi_{\mathrm{FFT}}}}{\sqrt{\psi_{\mathrm{FFT}}}}. \tag{3.25}$$

If the number of steps per period n_{sp} is bigger than the n_{bp}, Eq. 3.25 has to be solved iteratively incorporating Eq. 3.20 and Eq. 3.21. Figure 3.14 shows the computational time of the ground model according to Eq. 3.24 and Eq. 3.20-3.21 with the optimal number of periods according to Eq. 3.25 and just one period. While the model expects integer period numbers, Eq. 3.25 also returns floating point numbers, which have to be rounded accordingly. Depending on the total number of steps the reduction is several orders of magnitude. A value

of timesteps equal to approx. 3.4×10^6 represents the break point up to which the equations can be solved with $\psi^{<}_{\mathrm{sa}}$ and $c^{<}_{\mathrm{sa}}$.

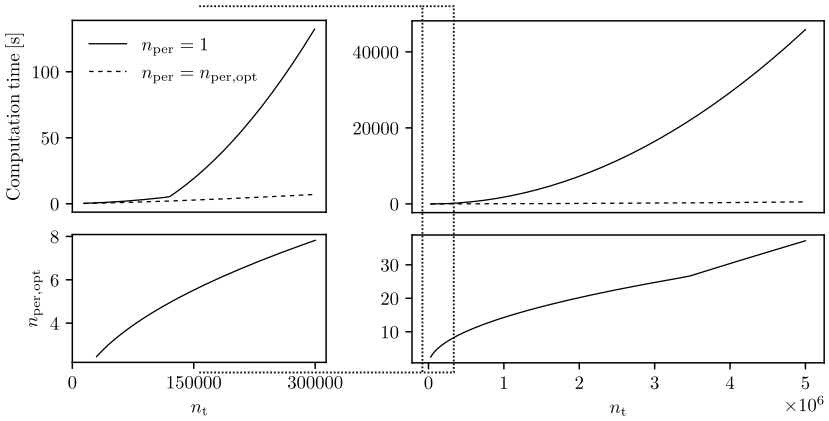

Figure 3.14 Computational time of the ground model according to Eq. 3.24 for one period and the optimal number of periods according to Eq. 3.25 over the total number of timesteps (top); optimal number of periods over the total number of timesteps (bottom).

3.3 Results

3.3.1 Verification of the borehole models

To validate the modelling approach, we compare our results to those obtained using the finite element software FEFLOW. The TRCMs used here are also implemented in FEFLOW by default, so that the same implementation can be compared. The boundary conditions are inspired by Diersch et al. (2010) and have no physical relevance. Nevertheless, they are suitable to confirm the correct implementation. For the the borehole models, the temperature at the borehole wall is set to a constant value of 10 °C. The inlet temperature is set to 0 °C for the first 1800 s and then switched to 20 °C for another 1800 s. The time period of 1800 s was chosen because a steady state is reached relatively quickly due to the constant borehole wall temperature. The temperatures are chosen arbitrarily within the range of a real operation as the validation of equations and methodology is independent of the chosen temperatures. The same applies to any other parameters with the exception of the flow rate, which is why they are not shown here. Depending on the Reynolds number, different equations (Bauer et al., 2011; Diersch et al., 2010) are used for the Nusselt numbers which are used to calculate the convective resistances, for a laminar, turbulent or transition flow. In the examples shown here, the flow rate was set to $41\,\mathrm{m^3\,d^{-1}}$, leading to flow in the transition region for all pipes except for the outlet pipe of the Coax-BHE where the flow is turbulent due to the geometry and cross-sectional area. We have checked the implementation for other flow conditions with equally satisfying results. Figures 3.15 to 3.17 show the results for all 3 BHE models. Both

the forward and backward Euler implementations show a very good agreement with the FEFLOW simulations.

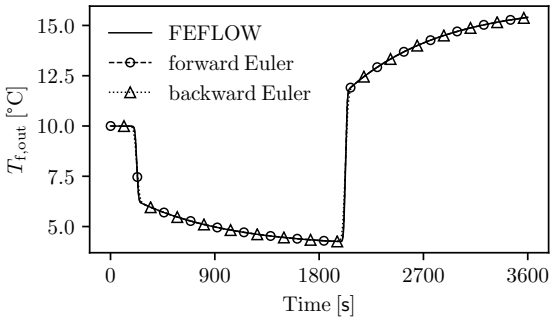

Figure 3.15 Comparison between the presented model and FEFLOW for a 1U-BHE.

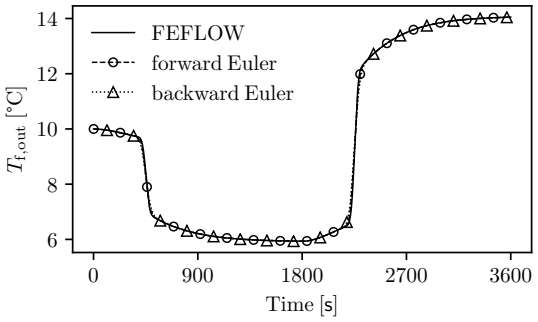

Figure 3.16 Comparison between the presented model and FEFLOW for a 2U-BHE.

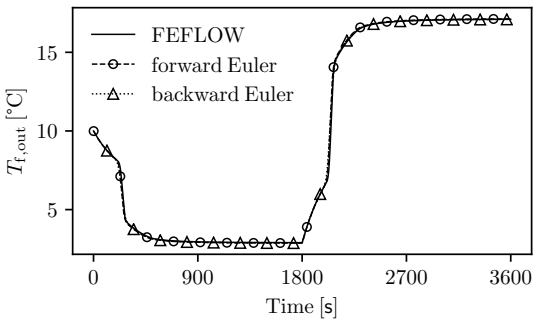

Figure 3.17 Comparison between the presented model and FEFLOW for a Coax-BHE.

3.3.2 Comparison with monitored field data

This section shows a comparison with a real bore field consisting of 40 2U-BHEs that provides heating and cooling energy for the office building of the E.ON Energy Research Centre (E.ON ERC) at RWTH Aachen University. The entire supply system of the building is monitored in

the framework of a research project of the E.ON ERC. In addition to the monitoring data, there is a high-quality ground model, which was created using outcrops, logging measurements, enhanced thermal response tests and measurements with temperature sensor modules. A detailed description of the bore field and related parameters can be found in Clauser et al. (2017). The ground consists of various soil types with varying thermal properties. For the calculations here, however, the smeared properties obtained from a thermal response test were used as listed in Table 3.1 together with all other parameters.

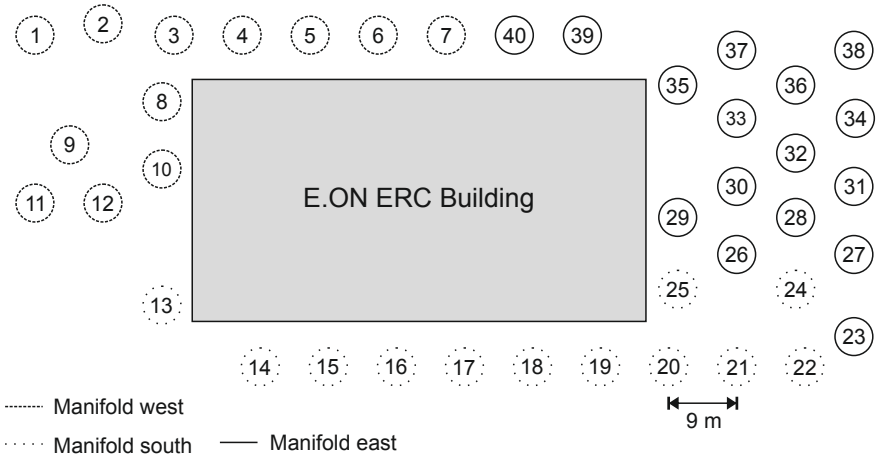

Figure 3.18 Schematic representation of the BHE arrangement at E.ON ERC building.

Fluid inlet and outlet temperatures as well as flow rate were recorded for each borehole individually at an interval of 30 s from July 2018 to June 2019. The BHE field is divided into 3 manifolds (Figure 3.18). The manifolds are connected in parallel to the heat pump. Within the manifolds, the associated BHEs are then connected in parallel with the same flow rate and inlet temperature. The measuring units are installed in the manifolds. The horizontal supply pipes between the manifolds and the top of the BHEs are up to 60 m long. Any heat losses or heat gains along these supply pipes are not considered in our model. This simplification still allows obtaining satisfactory results against the measured data and does not detract from the objective of showing the efficiency of our proposed algorithm. A first comparison is made with a single BHE, and then for the entire BHE field. However, the large distances between the BHEs and the thermal properties of the ground prevent any significant thermal interactions between the BHEs for the investigated periods.

3.3.2.1 Modeling of a single BHE

BHE 18 was chosen for the single BHE comparison, as the length of the supply pipe between the BHE head and the measuring point is only 3 m. Multiple scenarios are to be investigated with respect to computational time and accuracy. These include a coarse and a fine vertical discretization as well as simulations with constant and time-variable flow rates. The simulations are carried out with both the forward and backward Euler borehole models.

Table 3.1 BHE and ground properties of the BHE field.

Parameter	**Value**	**Units**
Fuild properties		
Thermal conductivity	0.43	$\mathrm{W\,m^{-1}\,K^{-1}}$
Density	1054	$\mathrm{kg\,m^{-3}}$
Volumetric heat capacity	3 800 000	$\mathrm{J\,m^{-3}\,K^{-1}}$
Dynamic Viscosity	0.0035	$\mathrm{Pa\,s}$
BHE geometry		
Length	100	m
Diameter	0.152	m
Shank space	0.04	m
Outer diameter pipes	0.032	m
Pipe wall thickness	0.0029	m
BHE-properties		
Thermal conductivity grout	2.0	$\mathrm{W\,m^{-1}\,K^{-1}}$
Volumetric heat capacity grout	1 000 000	$\mathrm{J\,m^{-3}\,K^{-1}}$
Thermal conductivity pipe	0.3	$\mathrm{W\,m^{-1}\,K^{-1}}$
Ground properties		
Average thermal conductivity	2.3	$\mathrm{W\,m^{-1}\,K^{-1}}$
Average volumetric heat capacity	2 300 000	$\mathrm{J\,m^{-3}\,K^{-1}}$
Undisturbed ground temperature	12.0[1]	°C

[1] increased from 10.7 to 12 °C to account for the predominant cooling operation of the past 6 years of operation.

Table 3.2 Computational time per timestep for different discretizations (BHE models).

$\dot{\mathbf{V}}$	**BHE model**	$\mathbf{n_c}$ [-]	$\mathbf{\Delta t}$ [s]	**comp. time per step** $[\mathbf{10^{-5}\,s}]$	**comp. time for** $\mathbf{\Delta t = 30\,s}$ $[\mathbf{10^{-5}\,s}]$
const.	Forward	5	30	4.4	4.4
	Backward	5	1.5 / 30	6.6	6.6
	Forward	100	1.5	4.7	$20 \cdot 4.7 = 94$
	Backward	100	1.5 / 30	24.7	24.7
variable	Forward	5	30	4.8	4.8
	Backward	5	1.5 / 30	24.5	24.5
	Forward	100	1.5	5.2	$20 \cdot 5.2 = 104$
	Backward	100	1.5 / 30	244	244

The maximum measured flow rate of the fluid in the entire field is $52.4\,\mathrm{m^3\,d^{-1}}$. Applying Eq. 3.5 to this flow rate and the BHE properties in Tab. 3.1 leads to a minimum cell height of 18.51 m for the recorded 30 s timestep or to a maximum timestep of 1.77 s if the cell height is set to 1 m. For the 30 s timestep we choose 5 cells with a height of 20 m. Both cases are considered below as examples of a coarse and a fine vertical discretization. The chosen timestep for the fine discretization is 1.5 s, leading to 20 timesteps for each measured timestep of 30 s.

Table 3.2 shows the computational time of the borehole models. These are the times required by the BHE models to calculate the new temperatures within the BHE. Further steps, such as reading the ground temperature and setting it as a boundary condition at the borehole wall, are not considered as they are independent of the Euler scheme or discretization. The computational times per timestep are independent of the timestep size Δt. Looking at scenarios with constant flow rates, the forward implementation is faster for both cases and rather independent of the vertical discretization. However, if the goal is to simulate a BHE with 100 cells which corresponds to a vertical cell height of 1 m for this case and a timestep of $\Delta t = 30\,\mathrm{s}$ and a constant flow rate, the backward implementation is faster as 20 timesteps with the forward model would correspond to one timestep with the backward model ($20 \cdot 4.7 = 94 < 1 \cdot 24.7$, note that the computational time for $\Delta t = 30\,\mathrm{s}$ equal to the computational time for $\Delta t = 1.5\,\mathrm{s}$). For the scenarios with time-variable flow rates, the forward implementation is superior in terms of computational time for both discretizations. Unlike the backward model, where the entire BHE matrix needs to be rebuilt, only the flow rate dependent coefficients have to be recalculated. Even for the fine discretization it would be twice as fast to compute 20 timesteps at 1.5 s with the forward model compared to one 30 s timestep with the backward model. The vertical discretization must be chosen according to the stability criterion as a function of the maximum flow rate. For any lower flow rates the numerical diffusion increases due to the chosen upwind scheme, which may result in decreasing accuracy.

Table 3.3 Computational time for varying periods and 89 280 timesteps (forward model, $n_c = 5$, $\Delta t = 30\,\text{s}$, $\dot{V}$=const.).

$\mathbf{n}_{per}$	$\mathbf{n}_{sp}$	**comp. time [s]**
1	89 280	15.05
2	44 640	14.03
4	22 320	13.52
5	17 856	13.27
6	14 880	13.05
10	8928	13.26
20	4464	13.74
30	2976	14.40
40	2232	15.31

July 2018 was chosen for the first simulation, containing 89280 values of each measured quantity. Applying Eq. 3.25 leads to an optimal number of 5.8 periods for this simulation. To verify the presented hybrid approach and Eq. 3.25, multiple simulations with different number of periods as listed in Tab. 3.3 are carried out. The minimum measured calculation time is at 6 periods as projected, although the variations between all simulations are rather small.

Figure 3.19 shows the observed total computational times as listed in Table 3.3 compared to the calculated computational times using Eq. 3.24. The curves have the same shape with an offset of around 13 s between both values. An offset is expected as the calculated computational time neglects the computational time for the BHE model and any framework around the models, e.g caching the initial state of the BHE model, setting the boundary conditions or calculating the ground load increments. Critically, the comparison shows that the chosen approach predicts the relative computational time improvements for different periods correctly. For the given example the computational time can be reduced by 13 % by increasing n_{per} from 1 to 6. With further increasing n_{per} the computational time increases rather slowly as indicated by Eq. 3.24.

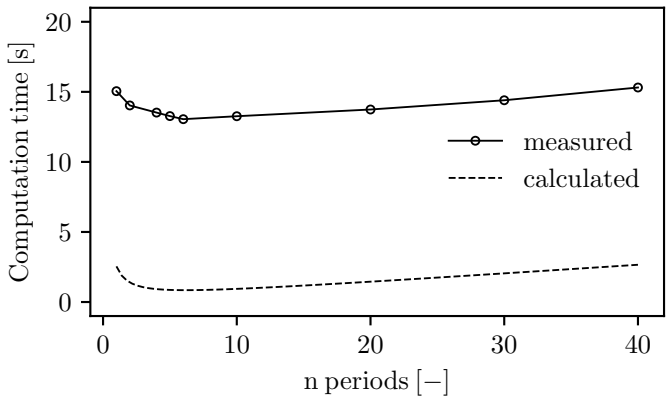

Figure 3.19 Measured total computational time and calculated computational time for the ground model for a simulation period with 89280 steps.

Based on these results, all of the following models are simulated with 6 periods. Table 3.4 summarizes the results in terms of computational time and accuracy. The use of a constant flow rate averaged over time has no effect on the accuracy for the period investigated. This was to be expected, as the flow rate fluctuates only slightly around a constant value (Figure 3.20, middle).

Figure 3.20 shows the results for the backward model with 100 cells and a time variable flow rate. While the top and middle part of Figure 3.20 show the measured values, the bottom part shows the difference between the measured and simulated outlet temperatures. The figure shows that the difference is decreasing within the first 100 h. The deviation at the start of the simulation is due to the thermal impact of the past operation of the BHE, which was not considered in the simulation. Figure 3.21 shows a 2 h period extracted from Figure 3.20. The influence of the time variable flow rate is so small that the curves for the 100 cell backward model overlap and are indistinguishable. The deviations between measurement and simulation are caused by 3 components shown in Figure 3.22. All models have a slight offset in the simulated return temperatures (e_1). Furthermore, all models have a slight offset along the time axis (e_2). The third type of error e_3 is a smeared reaction to rapidly changing fluid inlet temperatures. In Figure 3.22 this can be seen clearly for the backward model. This error is caused by the numerical diffusion due to the upwind scheme and can be reduced with finer discretizations for the backward model. For the forward model, it can be completely eliminated by forcing the CFL number to 1. However, a CFL number of 1 does not necessarily lead to the most accurate result, as the model does not consider natural diffusion that occurs in reality. For the forward model in Figure 3.22, the CFL number is approximately 0.6 which coincidentally matches the slope of the measured curve quite well. While error types e_1 and e_2 are rather independent of the BHE model type and discretization, error type e_3 can be influenced accordingly. Figure 3.22 also shows the problems that arise when using the mean absolute error (MAE). Although the forward model generally represents the characteristic of the curve better, the deviations for the backward model are smaller overall due to smearing. The MAEs are therefore only given to show that the models basically work; they are unsuitable for comparing the models with each other without further consideration which is not the focus of this paper.

Next the simulation period is extended to a full year consisting of 1051200 timesteps at 30 s. Applying Eq. 3.25 results in an optimal number of 19.7 periods for this simulation. To incorporate the small influence of the variable flow rate, the flow rate in the following simulations is only adjusted if it changes by more than ±5 % between different consecutive timesteps. All simulations are performed with the 5 cell forward model, leading to a MAE of 0.032 K. Table 3.5 and Figure 3.23 show the results for different n_{per}. In this case, the calculated optimum of $n_{\mathrm{per}} = 19.7$ does not lead to the lowest computational time which is at 16. Although the calculated optimum is 4 periods off, the computational times in this range differ only slightly. By increasing the number of periods from 1 to 16, the computational time

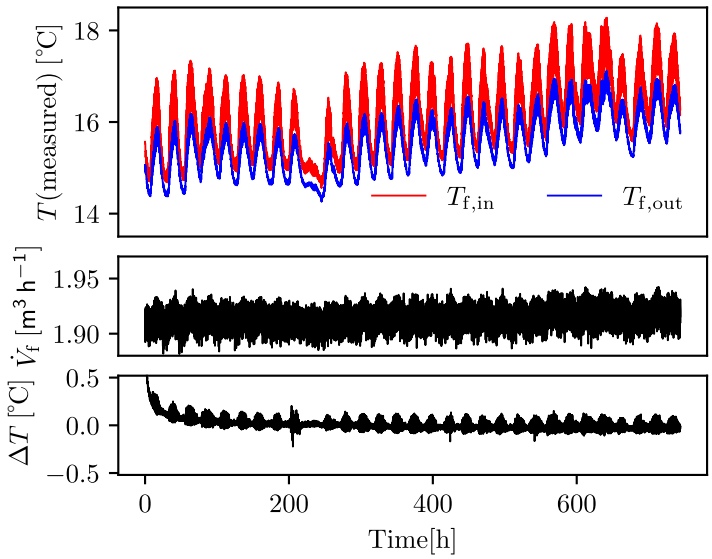

Figure 3.20 Measured fluid temperatures (top), flow rate (middle) and difference between measured and simulated outlet temperatures (bottom) for the one-month simulation.

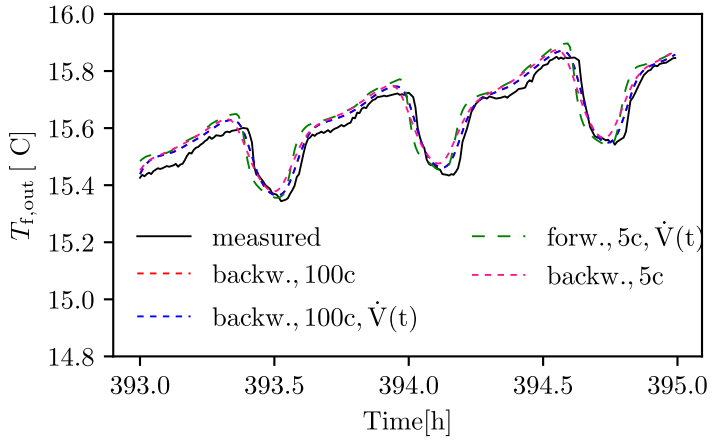

Figure 3.21 Two-hour segment of the one-month simulation. Comparison of the measured and simulated outlet temperatures.

could be reduced by 90 % while the difference between $n_{per} = 20$ and $n_{per} = 16$ in relation to $n_{per} = 1$ is less than 1 %. It shows nevertheless that Eq. 3.25 is only an approximation.

Figure 3.24 shows the results analogue to Figure 3.20 for the one year simulation. The increasing deviation between calculated and measured outlet temperatures towards the end of the simulation period is related to the short cycle times of the circulation pump, which are sometimes less than 30 min. Every time the circulation pump is switched on again, there are briefly larger deviations due to the fluid stagnating in the supply line, which is not considered in the simulation.

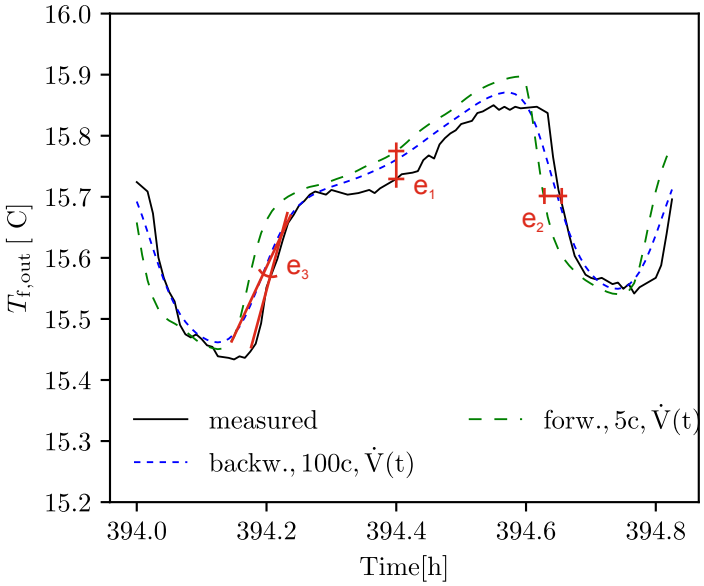

Figure 3.22 Different types of deviation between measured and simulated outlet temperatures.

Table 3.4 Computational time per timestep for different discretizations.

$\dot{V}$	BHE model	n_c [-]	Δt [s]	comp. time [s]	MAE [K]
const.	Forward	5	30	13.3	0.049
	Backward	5	30	17.5	0.044
	Forward	100	1.5	217.2	0.042
	Backward	100	30	51.6	0.039
variable	Forward	5	30	13.8	0.049
	Backward	5	30	37.1	0.044
	Forward	100	1.5	222.6	0.042
	Backward	100	30	276.2	0.039

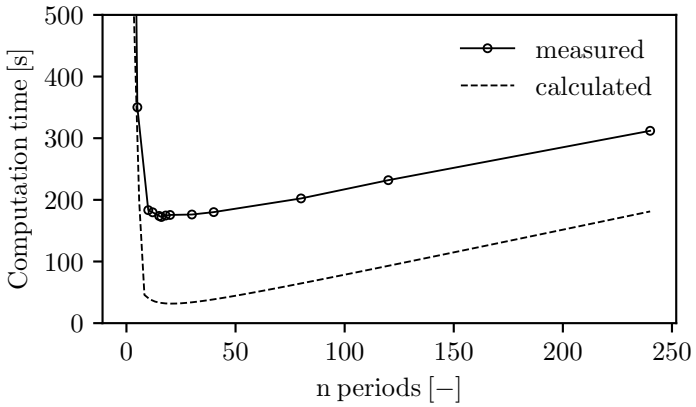

Figure 3.23 Measured total computational time and calculated computational time for the ground model for a simulation period with 1051200 steps.

Table 3.5 Computational time for varying periods and 1 051 200 timesteps (forward model, $n_c = 5$, $\Delta t = 30$ s).

$\mathbf{n}_{\mathrm{per}}$	$\mathbf{n}_{\mathrm{sp}}$	comp. time [s]
1	1 051 200	1726.6
5	210 240	350.2
10	105 120	183.3
16	65 700	172.2
18	58 400	174.6
20	52 560	175.5
30	35 040	176.2
40	26 280	180.1
80	13 140	202.3
120	8760	231.9
240	4380	312.0

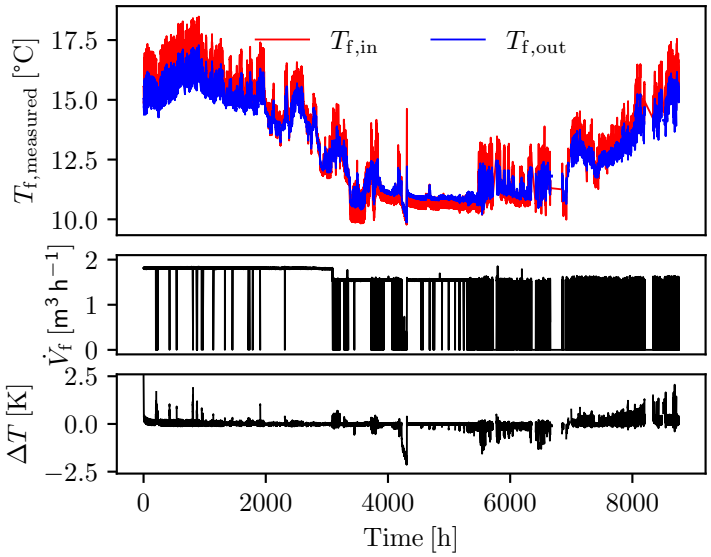

Figure 3.24 Measured fluid temperatures (top), flow rate (middle) and difference between measured and simulated outlet temperatures (bottom) for the one-year simulation.

3.3.2.2 Modelling the whole field

For the simulation of multiple BHEs, the effort of the ground simulation increases theoretically quadratically to the number of boreholes, as the temperature change for each borehole has to be calculated not just for the borehole itself but for the rest. For further reduction of the computational time, the calculation of the FFT model for the simulation of multiple BHEs is parallelised. Accordingly, the time reduction potential when using the hybrid model should be even greater than for the single BHE. To illustrate this, all 40 BHE are simulated as one bore field over a simulation period of one year corresponding to 1051200 timesteps of 30 s. With consideration of the parallelisation, ψ_{FFT} was redetermined to 7.8×10^{-4} which is one order of magnitude smaller than $1.58 \times 10^{-6} \cdot 40^2 = 2.53 \times 10^{-3}$. To check for possible scaling effects in the semi-analytical model, its parameters were also redetermined for the simulation of 40 BHE, leading to:

Table 3.6 Computational time for varying periods for all 40 BHE (forward model, $n_c = 5$, $\Delta t = 30\,\mathrm{s}$).

$\mathbf{n_{per}}$	$\mathbf{n_{sp}}$	**comp. time [h]**
1	1 051 200	873.1
10	105 120	40.3
20	52 560	22.3
30	35 040	17.8
40	26 280	16.6
50	21 024	14.1
60	17 520	16.2
80	13 140	17.1

$$\psi_{sa} = \begin{cases} 1.9 \times 10^{-6} & \text{for } n_r < 130000 \\ 5.3 \times 10^{-6} & \text{for } n_r \geq 130000 \end{cases} \tag{3.26}$$

and:

$$c_{sa} = \begin{cases} 3.4 \times 10^{-3} & \text{for } n_r < 130000 \\ -5.5 \times 10^{-2} & \text{for } n_r \geq 130000 \end{cases} \tag{3.27}$$

The newly determined values are partly above, below or in the range of the old values multiplied by 40^2, indicating some scaling effects, and showing the uncertainties associated with the measurement of the computational times. Applying Eq. 3.25 with these parameters leads to an optimal number of 50.6 periods.

The computational times for different numbers of periods are listed in Tab. 3.6 and displayed in Figure 3.25. By increasing the number of periods from 1 to 50, the computational time could be reduced by 98.4 %. In this case the optimal number of periods coincides with the measured computational times. Figure 3.26 shows the MAE for all BHE for the full year simulation. Some of the BHEs have only been in operation towards the end of the investigated period when the short cycle times of the heat pump started or had measurement problems. These BHEs are displayed as empty circles. Excluding these, the MAE of all BHEs is within the accuracy of the sensors which is $\pm 0.1\,\mathrm{K}$ for both inlet and outlet temperatures in the given temperature range.

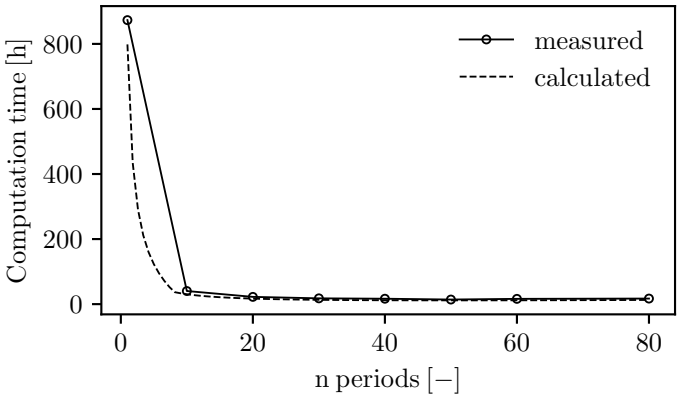

Figure 3.25 Measured total computational time and calculated computational time for the ground model for a simulation period with 1051200 steps and 40 BHE.

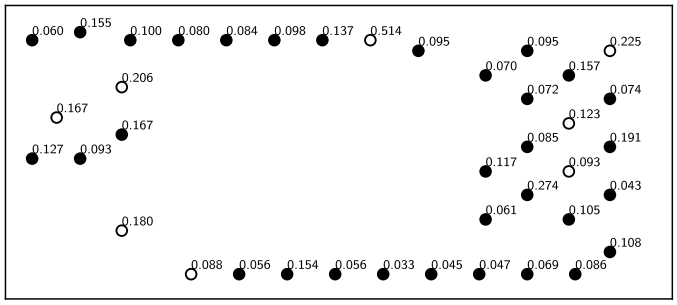

Figure 3.26 BHE layout with MAE for the one year simulation. BHEs with measurement problems as empty circles.

3.4 Discussion and conclusions

By extending a semi-analytical simulation model for BHE with the FFT approach, the computational time of the model could be reduced significantly. As the reduction occurs in the simulation of the ground, the extent depends on the share of the ground simulation in the total simulation. Furthermore, it was shown that the computational efficiency becomes especially significant for high numbers of timesteps, since the calculation time of the original model grows exponentially with the number of timesteps. While the time reduction for a simulation of a single BHE with 89280 timesteps was only 13 %, the reduction for a simulation with 1051200 timesteps increased to 90 %. When simulating the entire field with 40 BHEs, the reduction was in fact 98 %. By integrating the FFT into the model, real operating periods of several years can now be simulated efficiently with high temporal resolution without the use of a load aggregation scheme. This can be particularly interesting for cases where the BHE simulation is coupled with other models that require high temporal resolutions. A simple equation based on measured computational times of the model was derived for the determination of the optimal number of periods depending on the total number of timesteps of a simulation period. Increasing the number of periods initially leads to a

considerable improvement up to this optimal. After reaching the optimal number of periods, the computational time increases only moderately with further increasing number of periods. It is therefore rather advisable to round up the number of selected periods. The simplified assumption of a linear relation between timesteps and computational time for the ground models can introduce a mismatch between the projected optimal number of periods and the actual number of periods with the lowest computational time in some cases. However, the deviations are negligible compared to the improvement achieved by the hybrid approach.

Furthermore, the forward and backward Euler implementations were compared for different use cases. Depending on the use case, one or the other model is superior with respect to computational time as summarised below:

- The forward Euler model has a much lower computational time per timestep and is comparatively independent of the spatial discretization.
- Depending on the discretization, time-variable flow rates lead to a multiplication of the computing time for the backward Euler model.
- The forward Euler model must be discretized according to the CFL criteria for the maximum volume flow rate for time-variable flow rates. For all smaller flow rates the numerical diffusion increases which can lead to a accuracy reduction.
- The backward model is advantageous for larger timesteps or high flow rates.

By implementing and publishing the model in Python, easy adaptation and further development are possible. In future work, the model will be coupled with other system models such as heat pumps or solar collectors.

3.5 Appendix

3.5.1 Determination of the optimal number of periods

$$\frac{\partial}{\partial n_{\mathrm{per}}}\left(\frac{1}{2}\left(n_{\mathrm{per}}\psi_{\mathrm{sa}}(\frac{n_{\mathrm{t}}}{n_{\mathrm{per}}}^{2}+\frac{n_{\mathrm{t}}}{n_{\mathrm{per}}})+\frac{n_{\mathrm{t}}}{n_{\mathrm{per}}}c_{\mathrm{sa}}+\psi_{\mathrm{FFT}}\frac{n_{\mathrm{t}}}{n_{\mathrm{per}}}({n_{\mathrm{per}}}^{2}+n_{\mathrm{per}}-2)\right)\right) = \frac{n_{\mathrm{t}}}{n_{\mathrm{per}}^{2}}\left(-0.5\psi_{\mathrm{sa}}n_{\mathrm{t}}-0.5c_{\mathrm{sa}}+\psi_{\mathrm{FFT}}(0.5n_{\mathrm{per}}^{2}+1)\right) \quad (3.28)$$

$$\frac{n_{\mathrm{t}}}{n_{\mathrm{per}}^{2}}\left(-0.5\psi_{\mathrm{sa}}n_{\mathrm{t}}-0.5c_{\mathrm{sa}}+\psi_{\mathrm{FFT}}(0.5n_{\mathrm{per}}^{2}+1)\right)=0 \quad (3.29)$$

$$n_{\mathrm{per}}=\pm\frac{\sqrt{\psi_{\mathrm{sa}}n_{\mathrm{t}}+c_{\mathrm{sa}}-2\psi_{\mathrm{FFT}}}}{\sqrt{\psi_{\mathrm{FFT}}}} \quad (3.30)$$

3.5.2 Determination of the weighted parameters

$$\Delta t(\psi_{\mathrm{sa}}) = \sum_{i=0}^{n_{\mathrm{sp}-1}} \psi_{\mathrm{sa}}(n_{\mathrm{sp}} - i) = \sum_{i=1}^{n_{\mathrm{sp}}} \psi_{\mathrm{sa}} i \tag{3.31}$$

$$\Delta t(\psi_{\mathrm{sa}}^{<}, \psi_{\mathrm{sa}}^{>}) = \sum_{i=1}^{n_{\mathrm{b}}-1} \psi_{\mathrm{sa}}^{<} i + \sum_{i=n_{\mathrm{b}}}^{n_{\mathrm{sp}}} \psi_{\mathrm{sa}}^{>} i = \frac{1}{2}\left(\psi_{\mathrm{sa}}^{<}(n_{\mathrm{bp}}^2 - n_{\mathrm{bp}}) - \psi_{\mathrm{sa}}^{>}(n_{\mathrm{bp}}^2 - n_{\mathrm{sp}}^2 - n_{\mathrm{b}} - n_{\mathrm{sp}})\right) \tag{3.32}$$

$$\frac{\bar{\psi}_{\mathrm{sa}}}{2}(n_{\mathrm{sp}}^2 + n_{\mathrm{sp}}) = \frac{1}{2}\left(\psi_{\mathrm{sa}}^{<}(n_{\mathrm{bp}}^2 - n_{\mathrm{bp}}) - \psi_{\mathrm{sa}}^{>}(n_{\mathrm{bp}}^2 - n_{\mathrm{sp}}^2 - n_{\mathrm{b}} - n_{\mathrm{sp}})\right) \tag{3.33}$$

$$\bar{\psi}_{\mathrm{sa}} = \frac{n_{\mathrm{bp}}^2(\psi_{\mathrm{sa}}^{<} - \psi_{\mathrm{sa}}^{>}) + n_{\mathrm{bp}}(\psi_{\mathrm{sa}}^{>} - \psi_{\mathrm{sa}}^{<}) + \psi_{\mathrm{sa}}^{>}(n_{\mathrm{sp}}^2 + n_{\mathrm{sp}})}{n_{\mathrm{sp}}^2 - n_{\mathrm{sp}}} \tag{3.34}$$

Chapter 4

Investigations on connection pipes in BHE fields using monitoring data

Unpublished material not submitted for publication

4.1 Introduction

As part of the ongoing efforts to reduce carbon emissions, renewable energy sources are increasingly being used to heat and cool buildings. Geothermal energy plays a special role here, as it is suitable for heating, cooling and seasonal storage of surplus energy. One of the most common ways to harness this geothermal energy is through borehole heat exchangers (BHE) with a depth of up to 100 m (Lund and Toth, 2021). These BHE circulate water or a water-antifreeze solution within high density polyethylene (HDPE) pipes, and are connected via connection pipes to a ground source heat pump that warms up or cools down the building.

While 1-2 BHEs are often sufficient to meet the demand for single-family homes, several dozen or even hundreds of BHEs, arranged in a field, may be required for larger commercial buildings or residential towers (e.g., Luo et al., 2017; Naicker and Rees, 2020; Smith et al., 2018; Taylor et al., 1997). With new supply concepts such as low temperature heating networks, entire districts can be supplied via single or multiple, shared BHE fields (e.g. Huang et al., 2020). In many applications, a minimum spacing between the boreholes is desired to exploit a large soil volume and reduce or eliminate thermal interference between boreholes. For example, the technical guideline VDI 4640-2 (2019) and Kavanaugh and K. D. Rafferty (2014) suggest a distance of 6 m. This can result in considerable distances between the boreholes and the consumer's heat pump. These distances can be bridged by horizontal connection pipes, which are usually laid close to the surface and are connected in manifolds. While the undisturbed ground temperature is seasonally constant over most of the borehole depth, it varies at the depth of the horizontal connection pipes.

In common design practice, the heat transfer between the ground and connection pipes is usually not taken into account. In the VDI 4640-2 (2019) it is suggested to only insulate connection pipes if they are closer than 1 m to foundations or other buried infrastructure. Kavanaugh and K. D. Rafferty (2014) state though that heat transfer between connection pipes and ground can be significant for small flow rates (< 3 l/s) or long connection pipes (> 60 m), and provide a calculation approach to quantify the heat transfer between ground and pipes.

In this work, we will investigate the heat transfer along horizontal connection pipes of up to 60 m length connected to 40 BHEs in Aachen (Germany) by analysing monitoring data. After an introduction of the investigated BHE field in section 4.2, we show in section 4.3 how the heat transfer along the pipes can be calculated and the method we use to extract it from the available data. In section 4.4, a method for evaluating additional information by applying a multiple linear regression is presented. Then, in section 4.5, the results obtained with the methods from sections 4.3 and 4.4 are presented.

4.2 BHE field

The building of the E.ON Energy Research Centre (E.ON ERC) at RWTH Aachen University is supplied with heating and cooling energy by 40 BHEs of 100 m depth (Figure 4.1). The entire energy system of the building is monitored in the framework of a research project, and is therefore equipped with high-precision measurement technology. A detailed description of the BHE field and related parameters can be found in Clauser et al. (2017). Values recorded at 30 s intervals are available for the BHE inlet and outlet temperatures as well as the flow rates for all BHEs for a 12 month period starting from July 2018. The values are recorded in the three manifolds (marked A, B and C in Figure 4.1).

The temperatures are measured with Pt-1000s sensors with a limit deviation of $\pm 0.03 + 0.005|T|°\mathrm{C}$. Details on the accuracy of the flow rate measurements are not available. Figure 4.2 shows the flow rate $\dot{V}$ and the fluid temperatures $T_{\mathrm{f,in}}$ and $T_{\mathrm{f,out}}$ for the investigated period, using the example of BHE 18. The connection pipes between the manifolds and the BHEs (Figure 4.1) have a total length of 900 m if supply and return pipe are considered as one, otherwise they correspond to 1800 m of additional buried pipe. The HDPE pipes are buried without insulation at a depth between 0.94-1.54 m and have an outer diameter of 0.04 m, a wall thickness of 0.0037 m and a thermal conductivity of $0.42\,\mathrm{W\,m^{-1}\,K^{-1}}$.

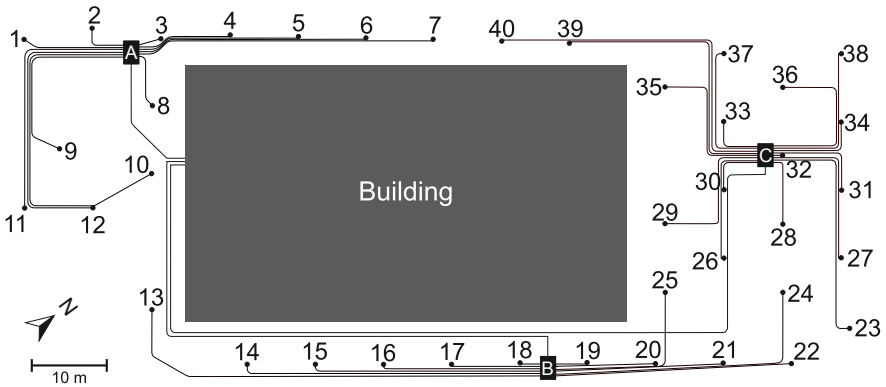

Figure 4.1 Plan view of the connection pipe network of the 40 BHEs arranged in the three manifolds A, B and C.

With the parameters plotted in Figure 4.2 and the volumetric heat capacity of the fluid ρc_{f} (equal to $3.8\,\mathrm{MJ\,m^{-3}\,K^{-1}}$) we can calculate the load Q of each BHE for each timestep t, assuming that $T_{\mathrm{f,in}}$, $T_{\mathrm{f,out}}$ and $\dot{V}$ are constant over the measuring interval of $\Delta t = 30\,\mathrm{s}$:

$$Q = (T_{\mathrm{f,in}} - T_{\mathrm{f,out}})\rho c_{\mathrm{f}} \dot{V} \Delta t. \tag{4.1}$$

Figure 4.3 shows the total monthly load of the BHEs for heating and cooling sorted by the three manifolds. The results show that there are differences of up to one GJ for some months and BHEs. The flow rates of the BHEs are generally set to the same target value, yet there

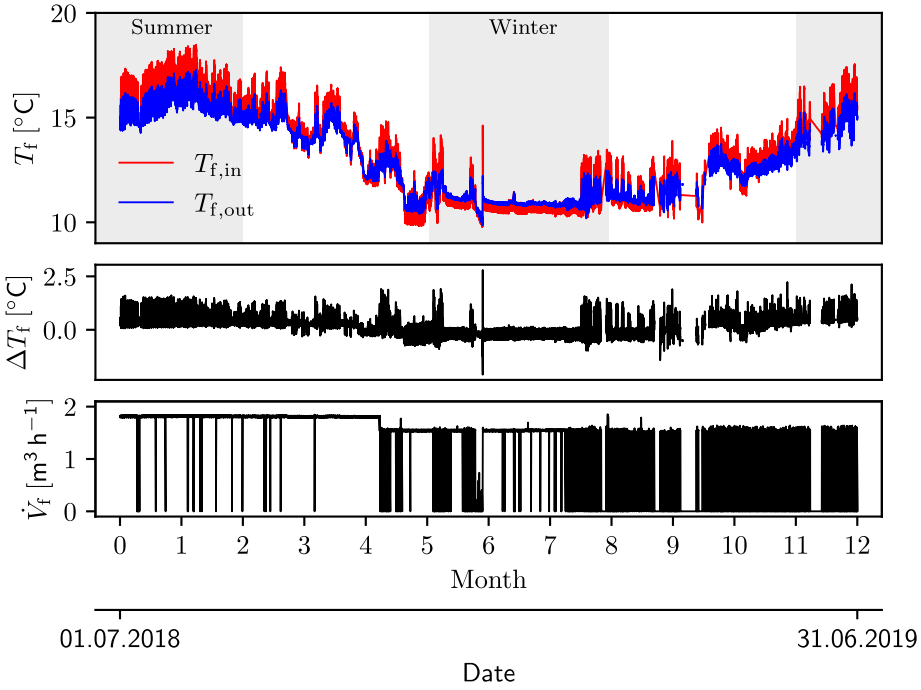

Figure 4.2 Fluid temperatures and flow rate using BHE 18 as example.

are some deviations. This becomes obvious when looking at the total, monthly circulated fluid volumes as shown in Figure 4.4.

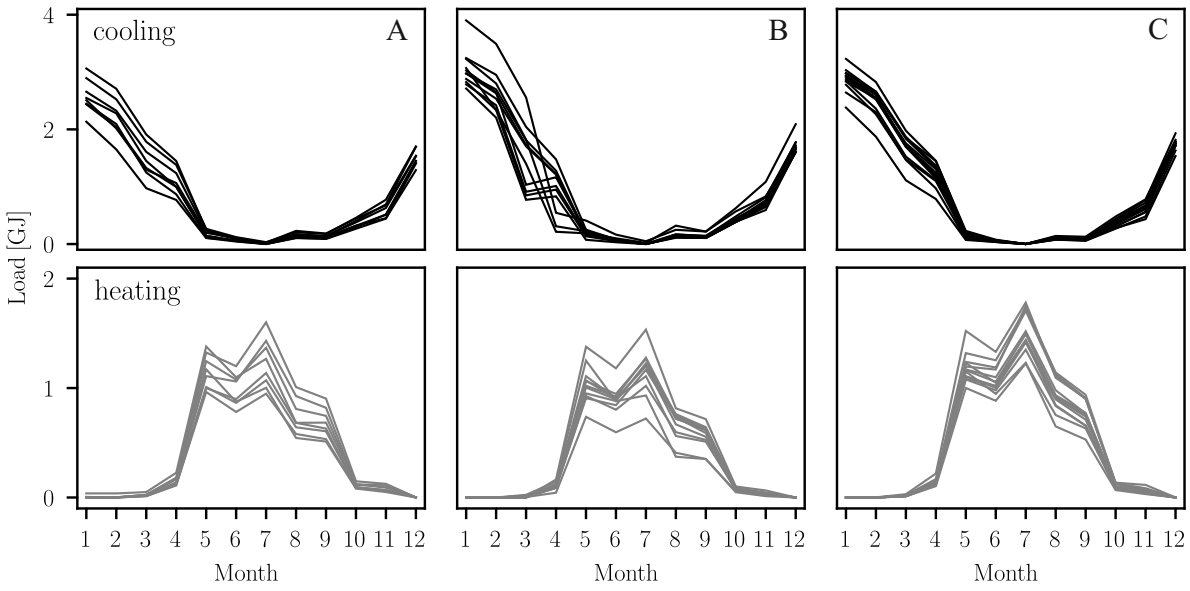

Figure 4.3 Monthly total load of all 40 BHEs.

The relation between the flow rate and heat extraction in non-linear. To somehow account for the effect of the different flow rates on the monthly loads Q_m, these are related to the monthly pumped fluid volumes V_m:

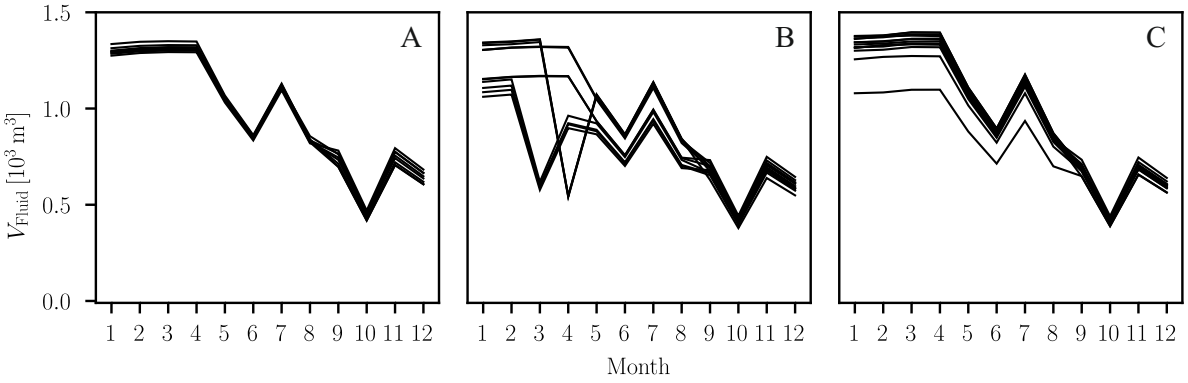

Figure 4.4 Total monthly fluid volumes for all BHEs.

$$Q'_{\mathrm{m}} = Q_{\mathrm{m}}/V_{\mathrm{m}} \tag{4.2}$$

Finally, the volume-related performances Q'_{m} can be used to determine the share χ_i of the individual BHEs in the total performance of the manifold:

$$\chi_i = 1 - \frac{Q'_i}{\frac{1}{n_{\mathrm{BHE}}} \sum_{i=1}^{n_{\mathrm{BHE}}} Q'_i} \tag{4.3}$$

The results shown in Figure 4.5 indicate that the performance of the individual BHEs differ significantly from each other in some cases, even when corrected for the varying fluid volumes.

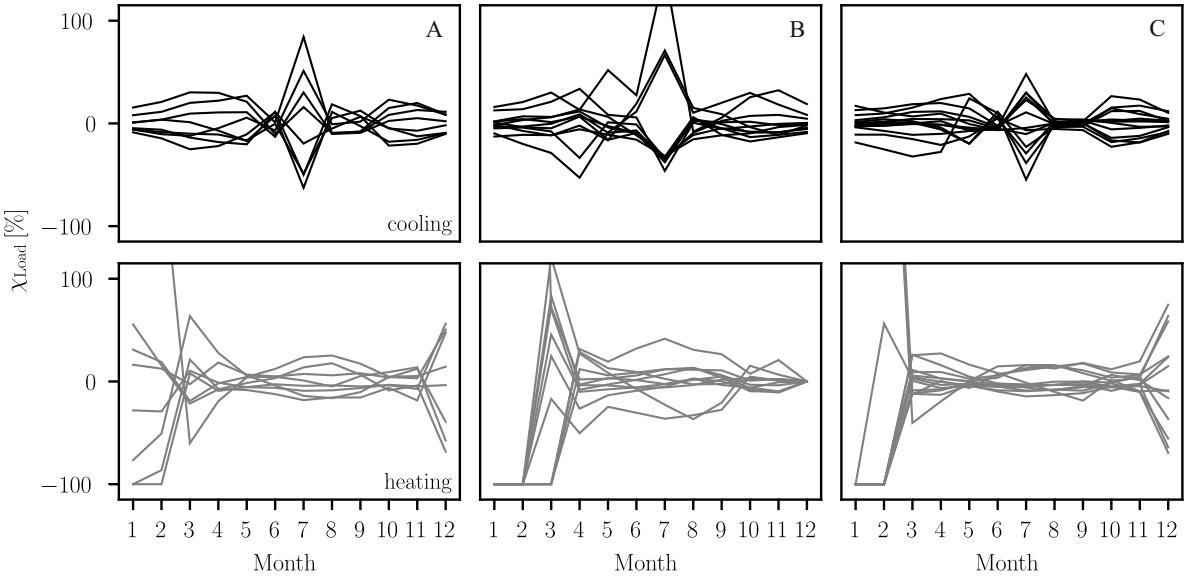

Figure 4.5 Deviation of the volume-related BHE loads from the average volume-related manifold load.

The performance of a BHE depends on many factors, such as the thermal and geometric properties of the BHE and the thermal properties of the surrounding ground. The heat flux

q_{BHE} to the BHE and thus its performance can be expressed in simplified terms as follows (M. Li et al., 2016):

$$q_{\mathrm{BHE}} = \frac{\overline{T}_{\mathrm{f}} - T_{\mathrm{s},0}}{R_{\mathrm{b}}^{*} + G}, \tag{4.4}$$

where $\overline{T}_{\mathrm{f}}$ is the mean heat carrier fluid temperature in the BHE, and $T_{\mathrm{s},0}$ the undisturbed ground temperature. The sum in the denominator defines the total thermal resistance between fluid and ground, which is a combination of the stationary borehole resistance R_{b}^{*} and the time-dependent resistance of the ground G. The borehole resistance depends on the thermal and geometric properties of the BHE, as well as the thermal properties of the heat carrier fluid and the flow state. The ground resistance, also known as the *g-function*, depends on the geometry of the BHE and the characteristic borehole time, which includes the thermal diffusivity of the ground (Eskilson, 1987).

Theoretically, any of the variables contributing to Equation 4.4 can be responsible for the observed differences in the performance or loads of the BHEs. In this study, however, we will investigate to what extent the connection pipes might be responsible for the observed deviations. Hence, the analysis is carried out under the assumption that both the properties of the BHEs and the properties of the ground are identical for all boreholes, and differences in the outlet temperatures result exclusively from the horizontal connection pipes. Since all BHEs are identical in construction, differences can only result from the grouting, whereby the position of the fluid pipes in the borehole can already affect the performance (Makasis et al., 2018). Ten of the forty boreholes were geophysically surveyed, showing no significant differences in the geology (Clauser et al., 2017).

Two sources of information are available on the connection pipes: A quantity surveying table and the installation plan shown in reduced form in Figure 4.1. The table contains the pipe lengths, cross sections and trench depths for each connection pipe. When comparing the pipe lengths for manifold A with the true-to-scale installation plan, considerable differences occur for some pipes of this manifold (Figure 4.6). Unfortunately, it could not be clarified which pipe lengths correspond to reality, so that these pipes are excluded from the analysis (BHEs 9, 10, 12). BHEs which were not in operation or which experienced measurement failures are also excluded from the analysis (BHEs 8,14,32,38,40).

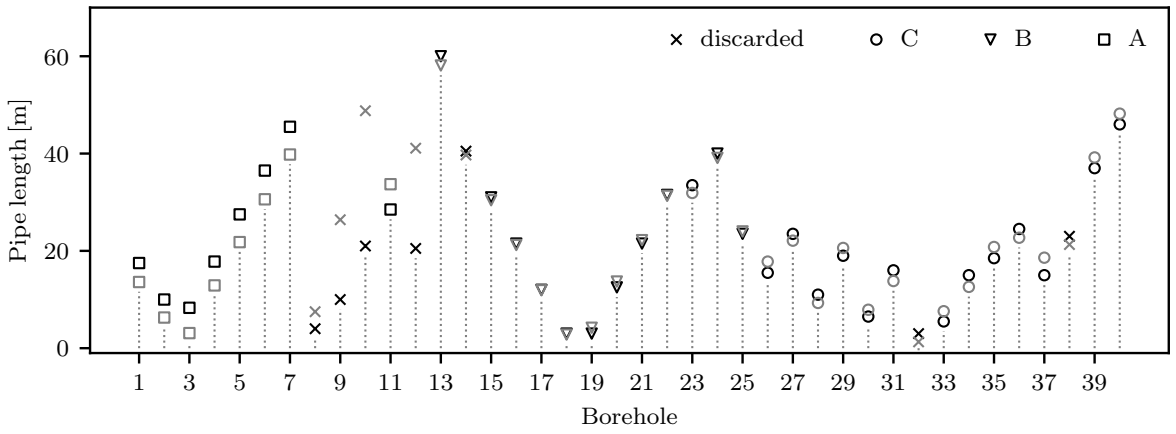

Figure 4.6 Lengths of the connection pipes from the installation plan (grey) and the quantity surveying table (black).

4.3 Heat transfer along connection pipes

4.3.1 Simplified calculation approach

The heat exchange q between a connection pipe with length l_{pipe} and the surrounding soil with the temperature T_{soil} can be described with few equations (Kavanaugh and K. D. Rafferty, 2014):

$$\Delta T = T_{\text{soil}} - \frac{T_{\text{f,in}} + T_{\text{f,out}}}{2} \tag{4.5}$$

$$q = \frac{l_{\text{pipe}}}{R_{\text{fs}}} \Delta T \tag{4.6}$$

$$T_{\text{f,out}} = T_{\text{f,in}} + \frac{q}{\dot{V} \rho c_{\text{f}}} \tag{4.7}$$

where $T_{\text{f,in}}$ and $T_{\text{f,out}}$ are fluid temperatures entering and exiting the connection pipe, $\dot{V}$ is the flow rate, ρc_{f} is the volumetric heat capacity of the fluid and R_{fs} the thermal resistance between fluid and soil. The latter is idealized as a serial connection of thermal resistances that account for the convective resistance between the fluid and the pipe and the conductive resistances of pipe and soil as shown in Figure 4.7.

The convective resistance R_{conv} can be calculated based on the dimensionless flow coefficients *Reynolds*, *Nusselt* and *Prandtl* (Gnielinski, 2013; Nusselt, 1916; Prandtl, 1905; Reynolds, 1883):

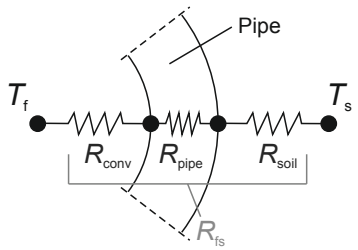

Figure 4.7 Thermal resistance model to calculate heat transfer between fluid and soil.

$$R_{\mathrm{conv}} = \frac{1}{Nu\lambda_{\mathrm{f}}\pi} \tag{4.8}$$

$$Re = \frac{u_{\mathrm{f}} d_{\mathrm{p,i}}}{\eta_{\mathrm{f}}/\rho_{\mathrm{f}}} \tag{4.9}$$

$$Pr = \frac{\eta_{\mathrm{f}} c_{\mathrm{f}}}{\lambda_{\mathrm{f}}} \tag{4.10}$$

The calculation of the Nusselt number differs depending on the flow condition. For laminar flow, the Nusselt number is defined as:

$$Nu = 4.364. \tag{4.11}$$

For turbulent flows, the following applies:

$$Nu = \frac{(\zeta/8)RePr}{1 + 12.7\sqrt{\zeta/8}(Pr^{2/3} - 1)}\left[1 + \left(\frac{d_{\mathrm{p,i}}}{l_{\mathrm{pipe}}}\right)^{2/3}\right] \tag{4.12}$$

with:

$$\zeta = (1.8\log_{10} Re - 1.5)^{-2}, \tag{4.13}$$

while for flow in the transitional range Equations 4.14 and 4.15 apply:

$$Nu = (1-\gamma)4.364 + \gamma\left\{\frac{(0.0308/8)10^4 Pr}{1 + 12.7\sqrt{0.308/8}(Pr^{2/3} - 1)}\left[1 + (\frac{d_{\mathrm{p,i}}}{l_{\mathrm{pipe}}})^{2/3}\right]\right\} \tag{4.14}$$

with:

$$\gamma = \frac{Re - 2300}{10^4 - 2300} \quad (0 \leq \gamma \leq 1) \tag{4.15}$$

Here $d_{\mathrm{p,i}}$ is the inner diameter of the pipe, u_{f} the fluid velocity, η_{f} the dynamic viscosity of the fluid, ρ_{f} the density of the fluid and λ_{f} the thermal conductivity of the fluid.

The thermal resistance of the pipe with the inner radius $r_{\mathrm{p,i}}$, the outer radius $r_{\mathrm{p,o}}$ and the thermal conductivity λ_{p} is calculated as

$$R_{\mathrm{pipe}} = \frac{\ln(r_{\mathrm{p,i}}/r_{\mathrm{p,o}})}{2\pi\lambda_{\mathrm{p}}}. \tag{4.16}$$

For the transient thermal resistance of the soil (Equation 4.18) we use a piecewise linear formulation (Kavanaugh and K. D. Rafferty, 2014), based on the thermal conductivity of the soil λ_{s} and the *Fourier* number *Fo*:

$$Fo = \frac{4\alpha_{\mathrm{s}} t}{d_{\mathrm{p,o}}^2} \tag{4.17}$$

where t is the time, α_{s} the thermal diffusivity of the soil and $d_{\mathrm{p,o}}$ the outer diameter of the pipe.

$$R_{\mathrm{soil}} = \begin{cases} (0.4343\ln(Fo) + 1.4667)/11.459/\lambda_{\mathrm{s}} & \text{for } Fo \leq 1.5 \\ (0.4343\ln(Fo) + 0.8217)/6.983/\lambda_{\mathrm{s}} & \text{for } 1.5 < Fo \leq 10 \\ (0.4343\ln(Fo) + 0.5248)/5.852/\lambda_{\mathrm{s}} & \text{for } 10 < Fo \leq 50 \\ (0.4343\ln(Fo) + 0.3979)/5.518/\lambda_{\mathrm{s}} & \text{for } Fo > 50 \end{cases} \tag{4.18}$$

The temperature of the soil T_{s} at various depths z can be approximated with sinusoidal functions. Xing's work provides an overview over several commonly used models (Xing, 2014). Here we use the formulation suggested by Phetteplace et al. (2013):

$$T_s(z,t) = T_{\mathrm{ave}} + e^{-z\sqrt{\frac{\pi}{\alpha_{\mathrm{s}} t_{\mathrm{p}}}}} T_{\mathrm{amp}} \sin\left[\frac{2\pi}{t_{\mathrm{p}}}(t - PL1) - z\sqrt{\frac{\pi}{\alpha_{\mathrm{s}} t_{\mathrm{p}}}}\right] \tag{4.19}$$

where T_{ave} is the annual average ground surface temperature, T_{amp} the amplitude of the ground surface temperature, t_{p} the period and PL1 the phase angle.

Finally Equations 4.5-4.19 can be used to calculate the heat transfer along the connection pipes at the investigated BHE installation. Rearranging Equations 4.5-4.7 to calculate the heat transfer along the connection pipe supplying the BHE and returning from the BHE leads to:

$$q_{\mathrm{supply}} = (T_{\mathrm{s}} - T_{\mathrm{f,in}}) \left(\frac{R_{\mathrm{fs}}}{l_{\mathrm{pipe}}} + \frac{1}{2\rho c_{\mathrm{f}} \dot{V}}\right)^{-1} \tag{4.20}$$

$$q_{\mathrm{return}} = (T_{\mathrm{s}} - T_{\mathrm{f,out}}) \left(\frac{R_{\mathrm{fs}}}{l_{\mathrm{pipe}}} - \frac{1}{2\rho c_{\mathrm{f}} \dot{V}}\right)^{-1}. \tag{4.21}$$

The heat transfer for the connecting pipes of one BHE thus results from the sum of Equations 4.20 and 4.21.

4.3.2 Heat transfer from measurement data

The fluid temperatures are recorded in the manifolds A, B and C (Figure 4.1). Thus, the temperatures measured are the inlet temperature of the supply connection pipe to the BHE and the outlet temperature of the return connection pipe from the BHE. Hence, the heat transfer between the connection pipes and the soil cannot be derived directly from these measurements, as they are not available at the BHE top.

This is the case in many BHE fields and therefore a method to calculate this is of general interest. To derive the heat transfer from the available data, the following procedure was developed. First, we calculate the flow rate related performance of each BHE:

$$\frac{\dot{Q}}{\dot{V}} = (T_{\mathrm{f,in}} - T_{\mathrm{f,out}})\rho c_{\mathrm{f}}. \tag{4.22}$$

Then, a reference BHE with the shortest connection pipe is identified for each manifold. For manifold A this is BHE 3 with a connection pipe length of 3.1 m; for manifold B, BHE 18 with 2.8 m connection pipe; and for manifold C, BHE 33 with 7.6 m pipe length. Next, the performance deviation of each BHE relative to the reference BHE is calculated. In addition, the length difference of the connection pipes is calculated:

$$\Delta l_{\mathrm{pipe}} = l_{\mathrm{pipe}} - l_{\mathrm{pipe,ref}} \tag{4.23}$$

Figure 4.8 shows the procedure for the example of BHE 13. This evaluation is carried out manifold by manifold, as connection pipe lengths between the building and the manifolds vary considerably (Figure 4.1), which results in different reaction times of the inlet temperatures in the manifolds to control events of the heat pump. In addition, the manifold-wise evaluation supports the assumption of identical soil properties at each BHE due to the spatial proximity. Another assumption for this analysis is that the BHEs are identical and therefore the observed performance differences are due solely to the different lengths of the connection pipes.

To support the assumption that the differences are caused the connection pipes, we take a closer look at BHE 13. This BHE is particularly suitable for this purpose because, on the one hand, it has the longest connection pipe in the entire field with $\Delta l_{\mathrm{pipe}} = 55.3\,\mathrm{m}$ and, on the other hand, the connection pipe is buried in its entire length below a grass surface. In a nearby weather station, the undisturbed ground temperature is recorded hourly at a depth of one meter also below a grass surface. The top part of Figure 4.9 shows the inlet temperature $T_{\mathrm{f,in}}$ of all BHEs in the manifold, the undisturbed soil temperature $T_{\mathrm{s,BHE}}$ at the

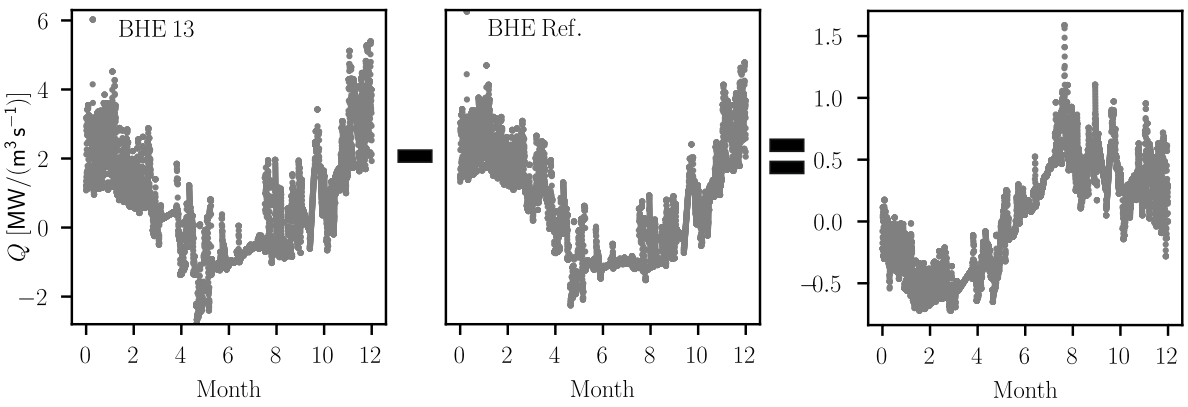

Figure 4.8 Exemplary illustration of the procedure for measurement data analysis for BHE 13: the volume flow-related performance of all BHEs (left) is offset against that of the reference BHE (center) to calculate the performance differences (right).

BHE and undisturbed ground temperature $T_{\mathrm{s,CP}}$, measured at the weather station, serving as a surrogate for the soil temperature at the connection pipe. The bottom part of Figure 4.9 shows the flow rate-related performance difference between BHE 13 and the reference BHE 18.

The thermal loads are defined according to Equation 4.1, leading to positive values for cooling loads and negative values for heating loads. The load difference ΔQ is calculated as $Q_{\mathrm{BHE13}} - Q_{\mathrm{BHE18}}$ so that for cooling $\Delta Q < 0$ indicates a worse performance of BHE 13 while $\Delta Q > 0$ indicate a better performance of BHE 13. The opposite is true for the heating case: for $\Delta Q > 0$, BHE 13 is performing worse and for $\Delta Q < 0$ it is performing better than the reference BHE 18. When the undisturbed ground temperature around the connection pipe is higher than the undisturbed ground temperature around the BHE (Months 0-5) BHE 13 is performing worse than the reference for cooling loads due to the heat gains along the connection pipe. For heating loads the contrary is correct. Here the performance of BHE 13 is greater due to the heat gains along the connection pipe. This shifts around month 5-6, when $T_{\mathrm{s,CP}}$ drops below $T_{\mathrm{s,BHE}}$, leading to heat losses along the connection pipe. This however leads to better cooling performance for this period. Even, when neglecting the change in ground temperature caused by operation, Figure 4.9 shows that attributing part of the performance differences to heat gains along the connection pipes is a plausible explanation.

Against the background of the sinusoidal temperature variations in the the ground around the connection pipes, we fit sinusoidal curves defined as:

$$A(t) = A_{\max} \sin(\omega t + \Phi) + c \tag{4.24}$$

with a period of $\omega = 365$ days with a least square algorithm to the calculated performance differences (Figure 4.9). In Equation 4.24, A is the amplitude, Φ the phase angle, t the time

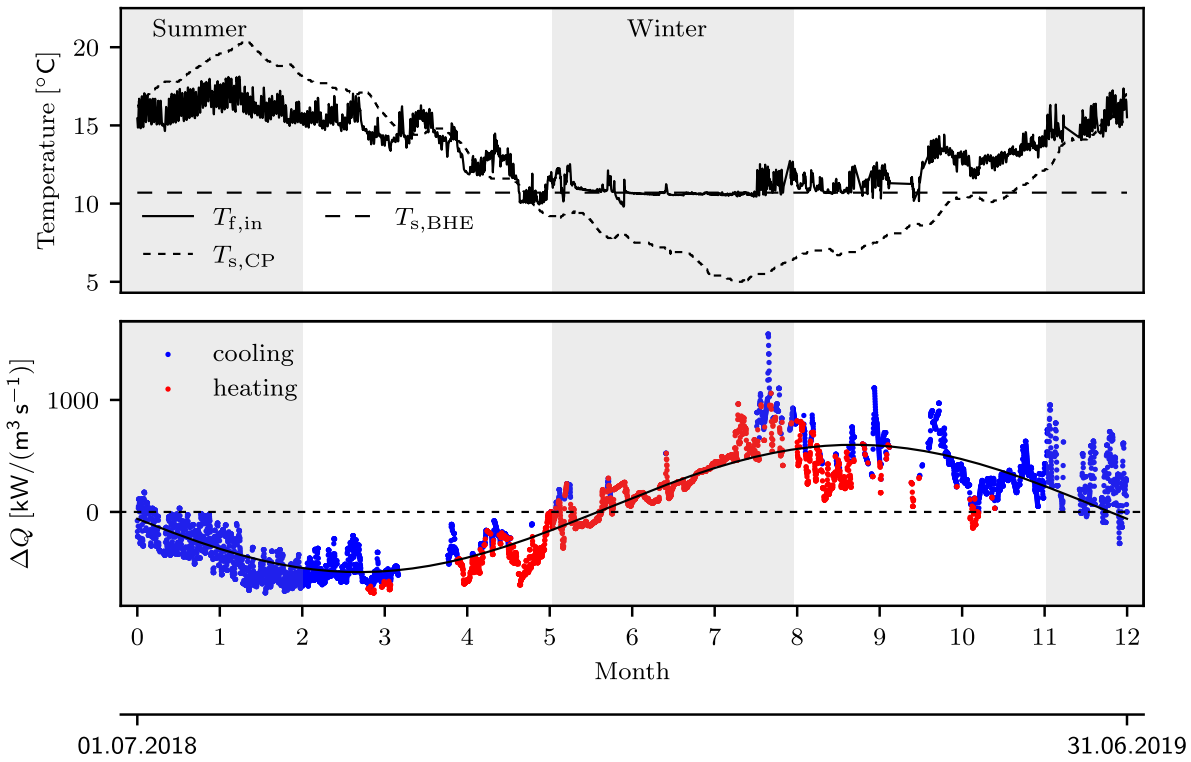

Figure 4.9 Inlet fluid temperature $T_{f,in}$ and undisturbed soil temperatures at the BHE $T_{s,BHE}$ and connecting pipe $T_{s,CP}$ (top) as well as performance difference between BHE 13 and BHE 18 (bottom - best seeing in colour).

and c the offset. Due to the fit of the sine curve, the calculated differences in performance can be described with the parameters of the sine curve, amplitude, phase and offset, for further processing and analysis. The results for all BHEs are shown in the Appendix in Figures 4.19-4.21 and Table 4.4.

4.4 Regression Analysis

In order to quantify the influence of different parameters we use a multiple regression analysis. The following data will be considered and correlated with the parameters of the sine fits described in the previous section:

- Depth of the pipes
- Surface type above the pipes
- Sun hours above the pipes
- Density of neighbouring pipes

The installation depths of the connection pipes z_{pipe} can be obtained from the quantity surveying table of the BHE field and are presented in the Appendix, Table 4.4. The surface types above the connection pipes can be derived from the combination of an aerial photograph (Figure 4.10, top) with the installation plan (Figure 4.1). Two surface types, grass and asphalt,

have been identified. By manually tracing the surfaces in the aerial photograph, a surface-type map is created with the help of graphics software. The installation plan is then cut to scale with the map (Figure 4.10, bottom). Finally, a pixel analysis along each connection pipe is used to determine the average surface type for each connection pipe.

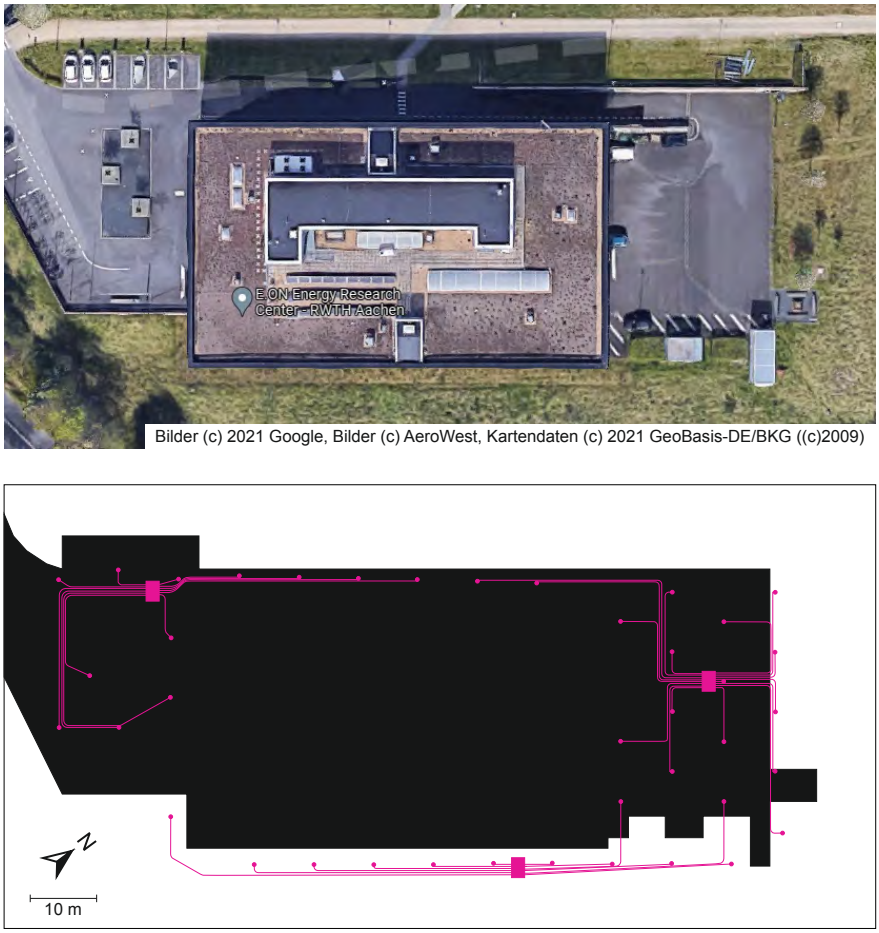

Figure 4.10 Aerial photo (top) and surface type map intersected with installation plan (bottom).

The annual sunshine hours are determined with a photogrammetric 3D-model and a sun position analysis. The 3D-model includes the E.ON ERC building as well as neighbouring buildings and vegetation to consider shading. The sun position analysis is carried out with the software *Blender* (Community, 2018) and the add-on *VI-Suite* (Southall and Biljecki, 2017). The total sunshine hours of the year are simulated based on latitude and longitude for a selected area (Figure 4.11, top). The results are finally converted into a grey-scale image and combined with the installation plan (Figure 4.11, bottom). Following the already described procedure, a pixel analysis is carried out along each connection pipe to determine the average sun hours.

Finally, the installation plan is used to create a map of connection pipe density. The installation plan is converted so that the lines of the pipes are only one pixel wide at all

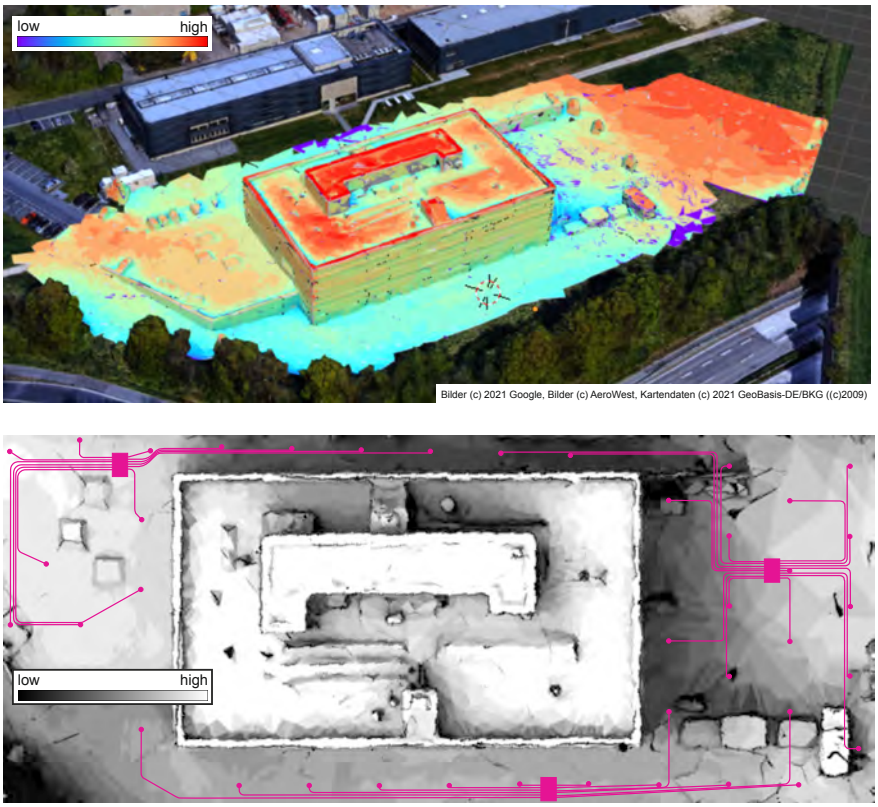

Figure 4.11 Photogrammetry model with simulated sunshine hours (top) and sunshine hour map intersected with installation plan (bottom).

points. In the next step, the sum of all inverse distances β is calculated for each pixel i of all pipes k:

$$\beta_{k,i} = \sum_{j=0}^{n_{pp}} \frac{1}{\sqrt{(x_i - x_j)^2 + (y_i - y_j)^2}} \tag{4.25}$$

where n_{pp} is the total number of all pipe pixels. The inverse distances of all pipe pixels are than averaged along each pipe to get one characteristic value for each pipe:

$$\beta_k = \frac{1}{n_p} \sum_{i=0}^{n_p} \beta_{k,i} \tag{4.26}$$

where n_p is the number of pixels for pipe k.

The results for all data are shown in the Appendix, Table 4.4. All values based on a combination of the installation plan and other data sources are normalised, as for example the pixel based inverse distances have no physical meaning anyway.

Having calculated all the required parameters, we perform a Multiple Linear Regression (MLR) with the *statsmodels* module (Seabold and Perktold, 2010) in Python with the following steps. First, we calculate the R^2 value for each variable to identify the first predictor. Then

we add each variable and see how it improves R^2. After this variable is added, we calculate the Variance Inflation Factor (VIF) to check for multi-collinearity. If the VIF is below 10, we keep the variable. Otherwise it will be excluded from the analysis. Then we repeat the procedure from the second step onwards until all variables are added to the model. The results are presented in section 4.5.2.

4.5 Results

4.5.1 Comparison between measurement and calculation

In this section we compare calculation results using section 4.3.1 with monitoring data according to section 4.3.2. We choose four representative BHEs, covering short and long connection pipes buried below gras and asphalt surface (BHEs 13, 17, 34 and 39). The trenches around the connection pipes in this installation are backfilled with sand. In the absence of more detailed information we perform one calculation with a dry sand ($\lambda = 0.4\,\mathrm{W\,m^{-1}\,K^{-1}}$, $\rho c = 1.5\,\mathrm{MJ\,m^{-3}\,K^{-1}}$) and another one with a wet sand ($\lambda = 1.5\,\mathrm{W\,m^{-1}\,K^{-1}}$, $\rho c = 1.9\,\mathrm{MJ\,m^{-3}\,K^{-1}}$) with daily averaged values for the temperatures and flow rate for BHE 13 (gras surface, $\Delta l_{\mathrm{pipe}} = 55.3\,\mathrm{m}$). The calculation for the wet sand overestimates the heat transfer clearly while the calculation with the dry sand is in perfect agreement until month 5 (Figure 4.12). One reason for the deviations from the fifth month onwards could be the operating mode of the heat pump, which starts to cycle at this point (Figure 4.2, bottom). The agreement is though considered sufficient. Based on the results for BHE 13, the calculations for the following BHEs are carried out just for the dry sand.

Figure 4.13 shows the results for BHE 17, where the connection pipe is also beneath a grass surface but is only $\Delta l_{\mathrm{pipe}} = 9.1\,\mathrm{m}$ long. Here we observe two offsets, the calculated heat transfer is generally higher (vertical offset), and the local minimum and maximum seems to be shifted by around 1 month along the x-axis for the calculation. The heat transfer between ground and connection pipes is driven by the temperature difference between the fluid and the ground. While the fluid temperatures are known from the measurements, the undisturbed ground temperature is a function of the surface temperature, the thermal diffusivity and the depth (Equation 4.19). Figure 4.14 shows the results of a sensitivity analysis on these parameters. The variation of the burial depth affects the amplitude and shift along the x-axis, referred to as phase (Figure 4.14 (a)). With increasing burial depth, the amplitude decreases and the phase is shifted to the right. The thermal conductivity (Figure 4.14 (b)) has similar effects. Here we have an increase in amplitude and a phase shift to the left with increasing thermal conductivity. The amplitude of the surface temperature has no influence on the phase but, as expected, only affects the amplitude of the undisturbed subsurface temperature and thus also the performance deviations (Figure 4.14 (c)). The mean surface temperature has no influence on amplitude or phase and only causes an offset along the vertical axis

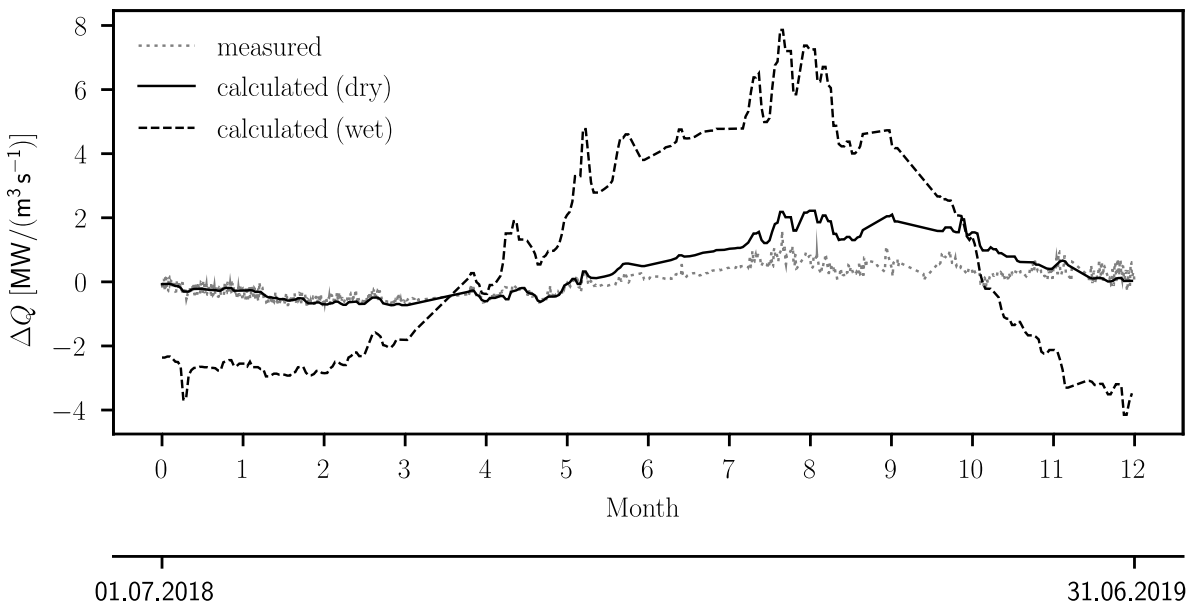

Figure 4.12 Measured performance difference and calculated performance difference for a wet and a dry sand for BHE 13 (gras surface, $\Delta l_{\mathrm{pipe}} = 55.3\,\mathrm{m}$, $z_{\mathrm{pipe}} = 1.51\,\mathrm{m}$).

(Figure 4.14 (d)). Increasing the average annual surface temperature by 30 % leads to a significant improvement in the calculation results. Whether such an assumption is justified based on the available data is questionable, since both pipes of BHEs 13 and 17 are beneath a grass surface and the calculated sunshine hours for BHE 17 are only slightly higher than for BHE 13 (Appendix, Table 4.4).

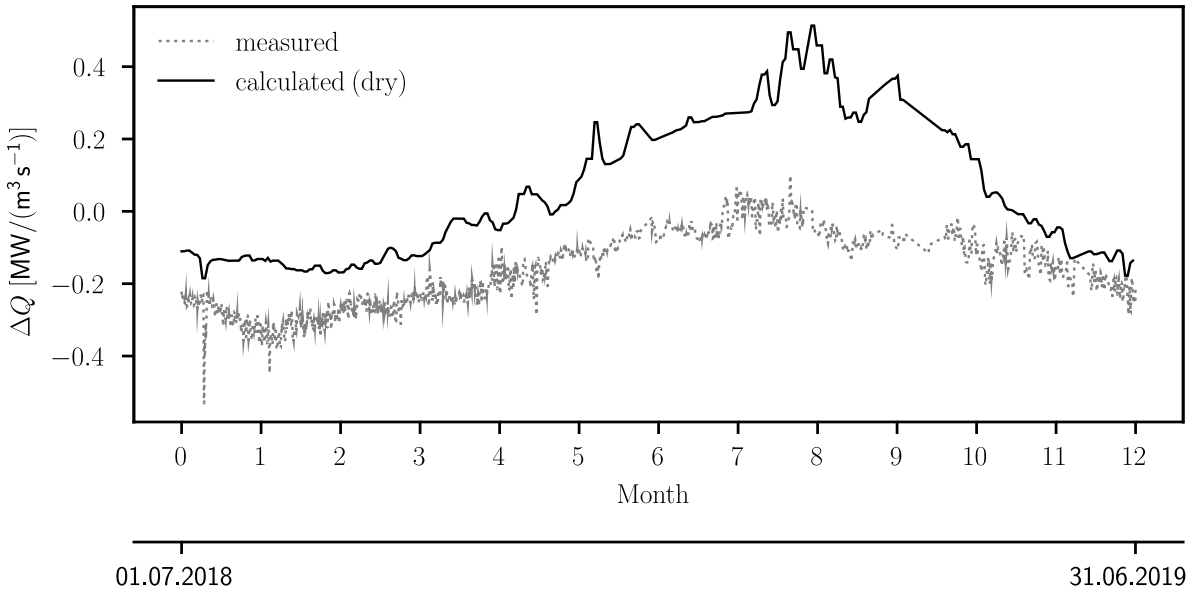

Figure 4.13 Measured performance difference and calculated performance difference for a dry sand for BHE 17 (gras surface, $\Delta l_{\mathrm{pipe}} = 9.1\,\mathrm{m}$, $z_{\mathrm{pipe}} = 1.03\,\mathrm{m}$).

The sensitivity analysis in Figure 4.14 shows the interplay of the various parameters, each of which is fraught with uncertainty. Not to mention the perhaps bold assumptions that the

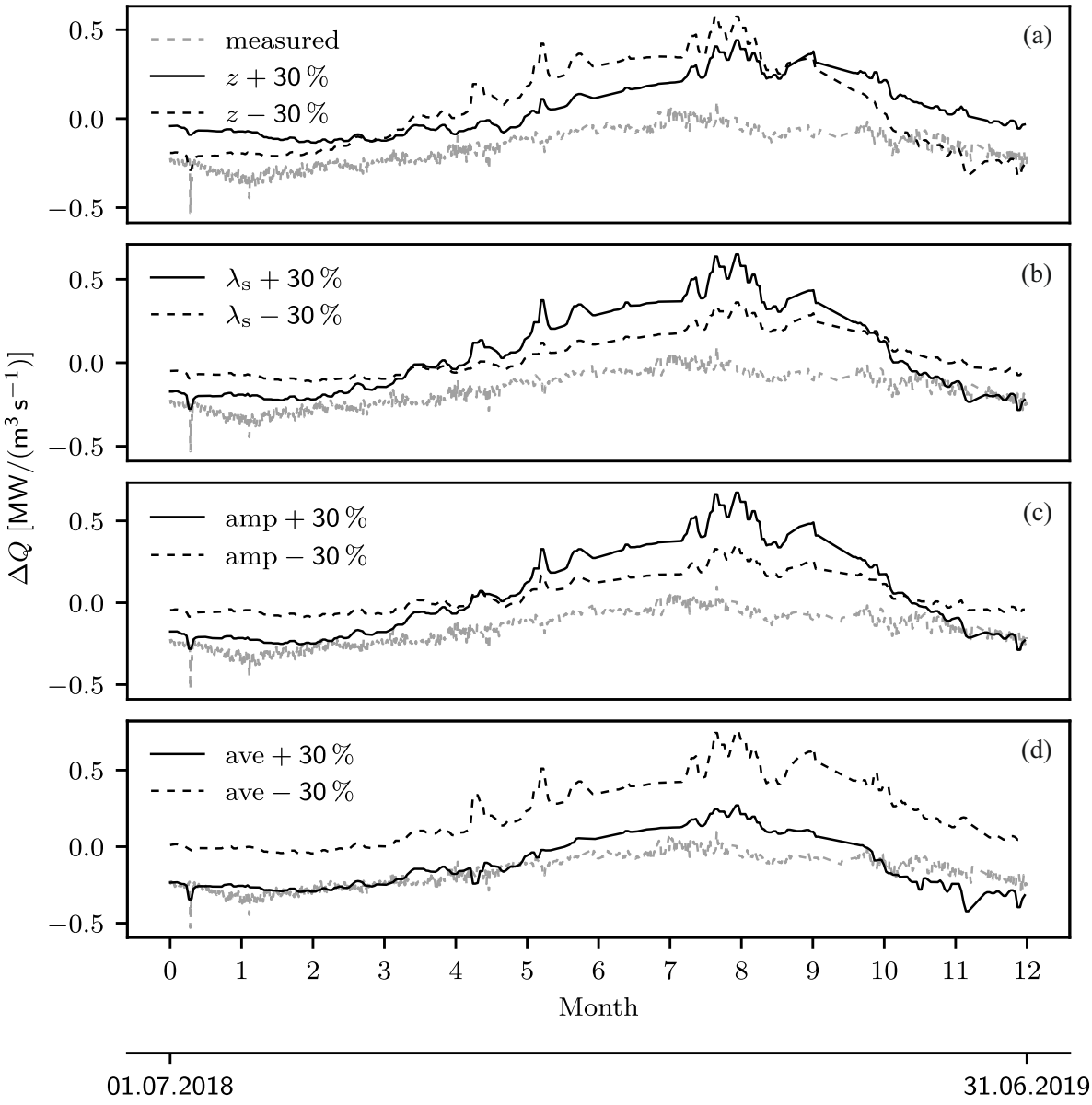

Figure 4.14 Sensitivity analysis of the parameters determining the undisturbed ground temperature on the example of BHE 17: (a) burial depth; (b) thermal conductivity; (c) amplitude of surface temperature; (d) average surface temperature.

observed differences only originate from the connection pipes, neglecting interference and changes in the soil temperature due to heat exchange.

Figure 4.15 shows the results for BHE 39 with $\Delta l_{\mathrm{pipe}} = 39.2\,\mathrm{m}$ below an asphalt surface. A more pronounced amplitude can be seen here for the calculation. Referring to Figure 4.14 this could be explained by a lower thermal conductivity, a deeper installation depth, or a decreased amplitude of the surface temperature. However, both a deeper installation depth and a lower thermal conductivity would lead to a further phase shift to the right. Due to the asphalt surface, the amplitude of the surface temperature should actually be greater than for the grass surface, as the asphalt heats up more in summer. However, the analysis of the

sunshine hours shows that the connection pipes of BHE 39 have the lowest sun hours of the entire installation (Appendix, Table 4.4). Thus, a decreased amplitude of the surface temperature would be the most likely explanation, as this would also decrease the amplitude of the calculation results without causing a further shift along the x-axis.

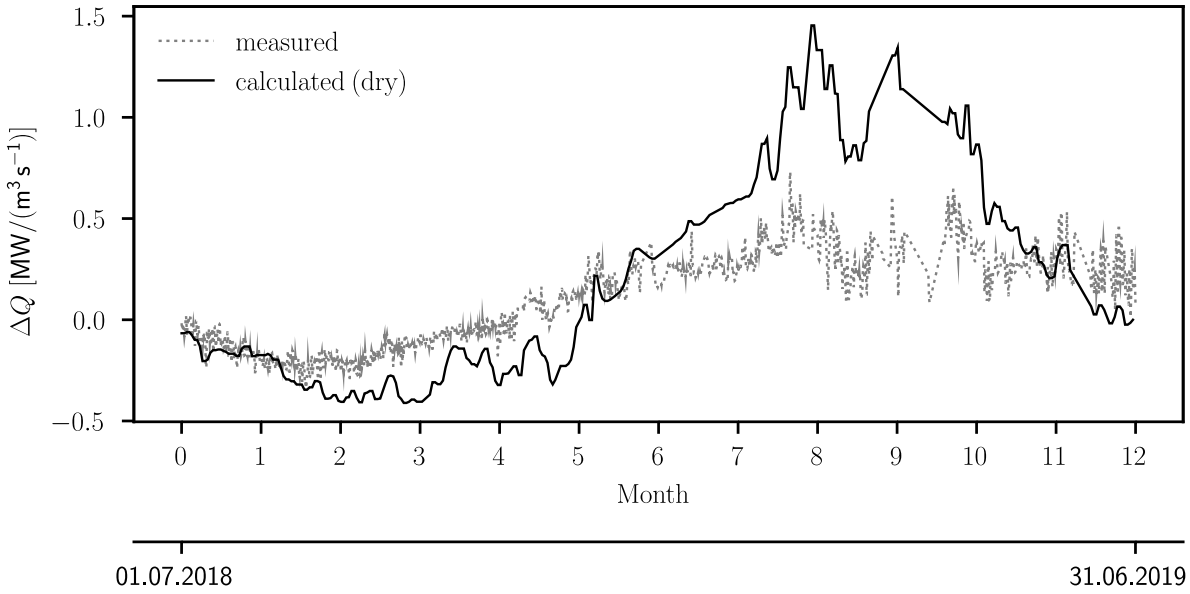

Figure 4.15 Measured performance difference and calculated performance difference for a dry sand for BHE 39 (asphalt surface, $\Delta l_{\mathrm{pipe}} = 39.2\,\mathrm{m}$, $z_{\mathrm{pipe}} = 1.45\,\mathrm{m}$).

Figure 4.16 shows the results for BHE 34 with $\Delta l_{\mathrm{pipe}} = 5.0\,\mathrm{m}$ below an asphalt surface. Here, for the first time, the calculation does not overestimate the measurements. Furthermore, the greatest deviations here occur between months 3-7, whereas for the previous BHEs it was months 7-10. The deviations in months 3-7 would be smaller if the phase in the calculation was shifted 1-2 months to the left. This would be the case with increased thermal conductivity or reduced burial depth, but both would lead to larger amplitudes. Furthermore, it would lead to larger deviations for all other months.

The comparison between calculations and observations carried out for four BHEs shows considerable differences for some cases. However, these deviations cannot be assigned to individual parameters without contradiction in most cases. On the other hand, the example of BHE 39 and the sunshine hours shows that other sources of information can contribute to the interpretation.

4.5.2 Multiple linear regression analysis

To gain further insight, we carry out an MLR as described in section 4.4. As Figures 4.19-4.21 in the Appendix show, not all BHEs have a similarly good fit of the sine function as BHE 13. Figure 4.17 shows the normalised amplitudes of the sinusoidal fits over the normalised Δl_{pipe}

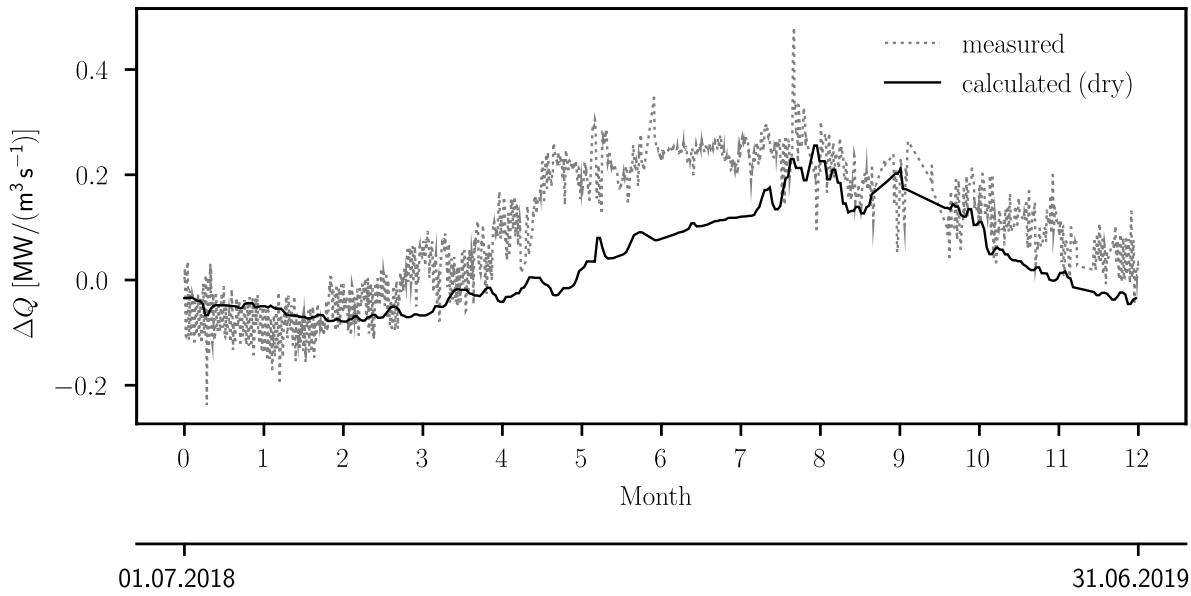

Figure 4.16 Measured performance difference and calculated performance difference for a dry sand for BHE 34 (asphalt surface, $\Delta l_{\mathrm{pipe}} = 5.0\,\mathrm{m}$, $z_{\mathrm{pipe}} = 1.23\,\mathrm{m}$).

of the connection pipes. The grey face colour is scaled with the R^2 of the sine fit, where darker values correspond to a higher R^2. The figure shows on the one hand the correlation between amplitude and pipe length and on the other hand that the poorer fits occur for rather short connection pipe lengths, at least for manifolds A and C.

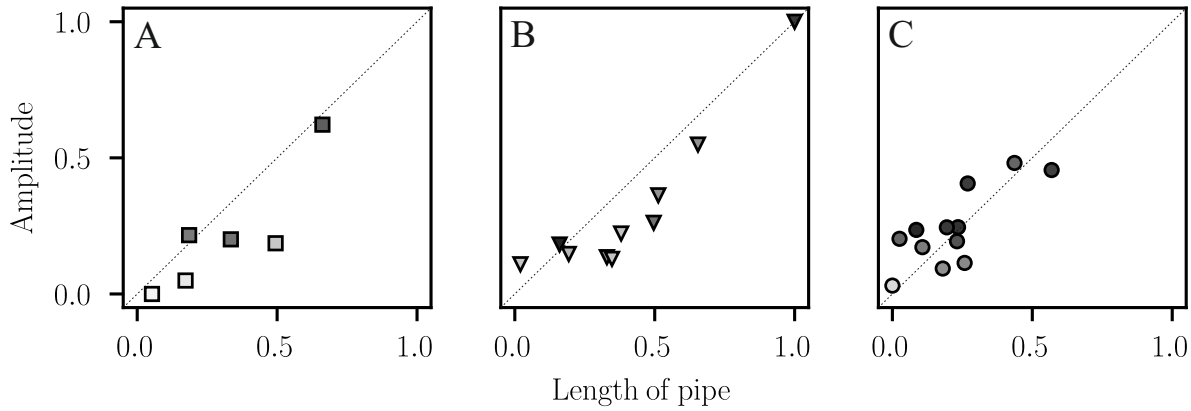

Figure 4.17 Normalised amplitudes over normalised Δl_{pipe}, grey face colour corresponds to the R^2 of the sine fit, with darker values corresponding to a higher R^2.

Tables 4.1-4.3 show the results of the stepwise MLR with amplitude, offset and phase angle as dependent variables. Each line shows the parameters of the variable added in this step. Since the coefficients of the individual variables change after the addition of further variables, the values in the tables do not necessarily correspond to those of the final equations. Furthermore, the constant added to the model is not shown in the tables, but in the final equations. When setting the amplitude as dependent variable, Δl_{pipe} was identified to be the first predictor, followed by the sun hours and surface type, which is plausible considering the governing pro-

Table 4.1 Results for MLR with amplitude as dependent variable.

Step	Variable	coeff.	std err.	t	P>|t|	R^2	Adj. R^2
1	Length	0.7964	0.093	8.600	0.000	0.733	0.723
2	Sun	0.1329	0.076	1.739	0.094	0.760	0.742
3	Surf.	-0.0568	0.049	-1.167	0.254	0.773	0.746
4	Depth	excluded due to collinearity with length					
5	Neigh.	-0.0022	0.153	-0.014	0.989	0.773	0.735

Table 4.2 Results for MLR with offset as dependent variable.

Step	Variable	coeff.	std err.	t	P>|t|	R^2	Adj. R^2
1	Surf.	-0.2051	0.102	-2.015	0.054	0.131	0.098
2	Sun	0.0446	0.164	0.273	0.787	0.133	0.066
3	Depth	0.0581	0.225	0.258	0.799	0.135	0.032
4	Length	excluded due to collinearity with depth					
5	Neigh.	0.0373	0.332	0.112	0.911	0.136	-0.008

cesses. The signs of the coefficients are also in agreement with expectations. The amplitude increases with increasing length and sun hours. For the surface type, 1 corresponds to a grass surface and 0 to an asphalt surface. The negative coefficient therefore means that the more grassy the surface, the smaller the amplitude.

The analysis also shows that the buried depth and the lengths of the pipes correlate, therefore the depth was excluded from the analysis. This makes sense considering construction process. The pipes were probably laid one on top of the other to maintain the gradient required for bleeding. Starting with the longest pipes at the bottom of the trench and then stepwise backfilling and adding other pipes. Interestingly though, the value for the neighbouring pipes (Table 4.1, Step 5) does not improve of the model. While the adjusted R^2 increases for the first three variables, it decreases after adding the neighbouring pipes. Its addition therefore only leads to an over fitting and therefore, the final Equation 4.27 only contains the first three variables and the constant. The calculation of the neighbouring pipes is based on the reduced, two-dimensional installation plan (Figure 4.1). Various depths of the pipes were not considered here. Figure 4.18 finally shows the normalized predicted amplitudes over the observed ones.

$$A = 0.8810x_{\text{length}} + 0.1507x_{\text{sun}} - 0.0568x_{\text{surf}} - 0.0575 \tag{4.27}$$

The correlations with phase angle and offset as dependent variables show that there is no linear relationship between them and the predictor variables (Tables 4.2 and 4.3). The comparisons between actual and predicted values are shown in the Appendix in Figure 4.22.

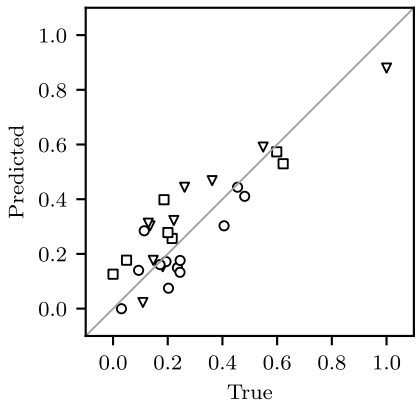

Figure 4.18 Prediction according to Equation 4.27 over observed amplitude values (normalized).

Table 4.3 Results for MLR with phase angle as dependent variable.

Step	Variable	coeff.	std err.	t	P>|t|	R^2	Adj. R^2
1	Surf.	-0.1266	0.107	-1.188	0.245	0.050	0.014
2	Depth	-0.2148	0.224	-0.959	0.347	0.082	0.012
3	Sun	-0.1130	0.174	-0.651	0.521	0.097	-0.011
4	Neigh.	-0.2180	0.337	-0.647	0.524	0.113	-0.035
5	Length	excluded due to collinearity with depth					

Although no correlations were found for phase angle and offset, the correlation between amplitude, solar radiation and surface types confirms that the observed performance differences of the BHEs are due to losses along the connection pipes.

4.6 Conclusions

Due to observed differences in performance in a BHE field, we carried out different analysis to investigate the heat transfer along connection pipes with a combined length of 900 m using monitoring data. To quantify and compare the heat losses, reference BHEs were defined and the performance differences between all other BHEs and the reference BHEs were calculated. For further statistical analyses, the performance differences were then approximated with sinusoidal curves, so they could be expressed with few parameters. Correlating these parameters with additional data revealed that the sun hours above the connection pipes were the most influential parameter on the amplitude of the deviations and that the neighbouring pipes had surprisingly no effect.

The heat gains and losses along the connecting pipes are mainly driven by the temperature difference between the heat carrier fluid and the shallow ground along the connection pipes. Theoretically, the largest beneficial gains occur for cases such as *cooling in winter*, when the underground temperature along the connection pipes is cold and the heat pump outlet temperature is warm, or *heating in summer*, when the underground temperature along the connection pipes is warm and the heat pump outlet temperature is cold. How often these cases occur depends on the type of use of the building, its insulation and the temperature set points for heating and cooling. Furthermore, it must be taken into account that, depending on the burying depth and the thermal properties of the ground, there is a phase shift in the annual temperature profile in the ground. As a result, the greatest temperature differences between the heat carrier fluid and the ground in the example shown in Figure 4.9 occur at the ends of the heating and cooling periods respectively in autumn and spring. For standard operation such as *cooling in summer* and *heating in winter*, the heat transfer along the connecting pipes has a rather negative effect in the shown example. The effect always depends on the combination of load type and ground temperature, which is determined by the climatic conditions, burial depth, surface condition and ground properties and should therefore be investigated on a case-by-case basis.

4.7 Appendix

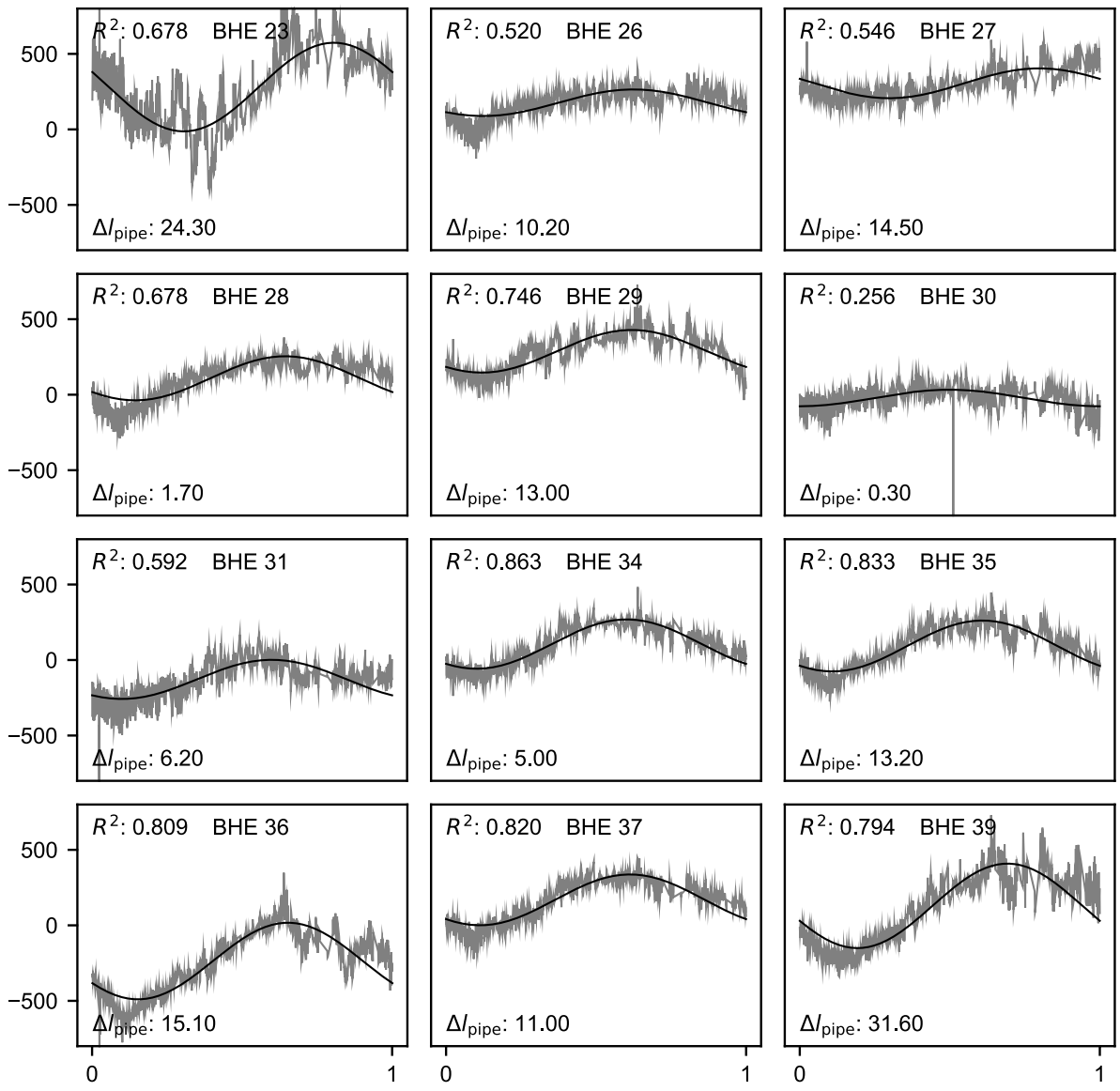

Figure 4.19 Flow rate related performance difference to the reference BHE in kW/($m^3 s^{-1}$) over the period of one year for manifold C.

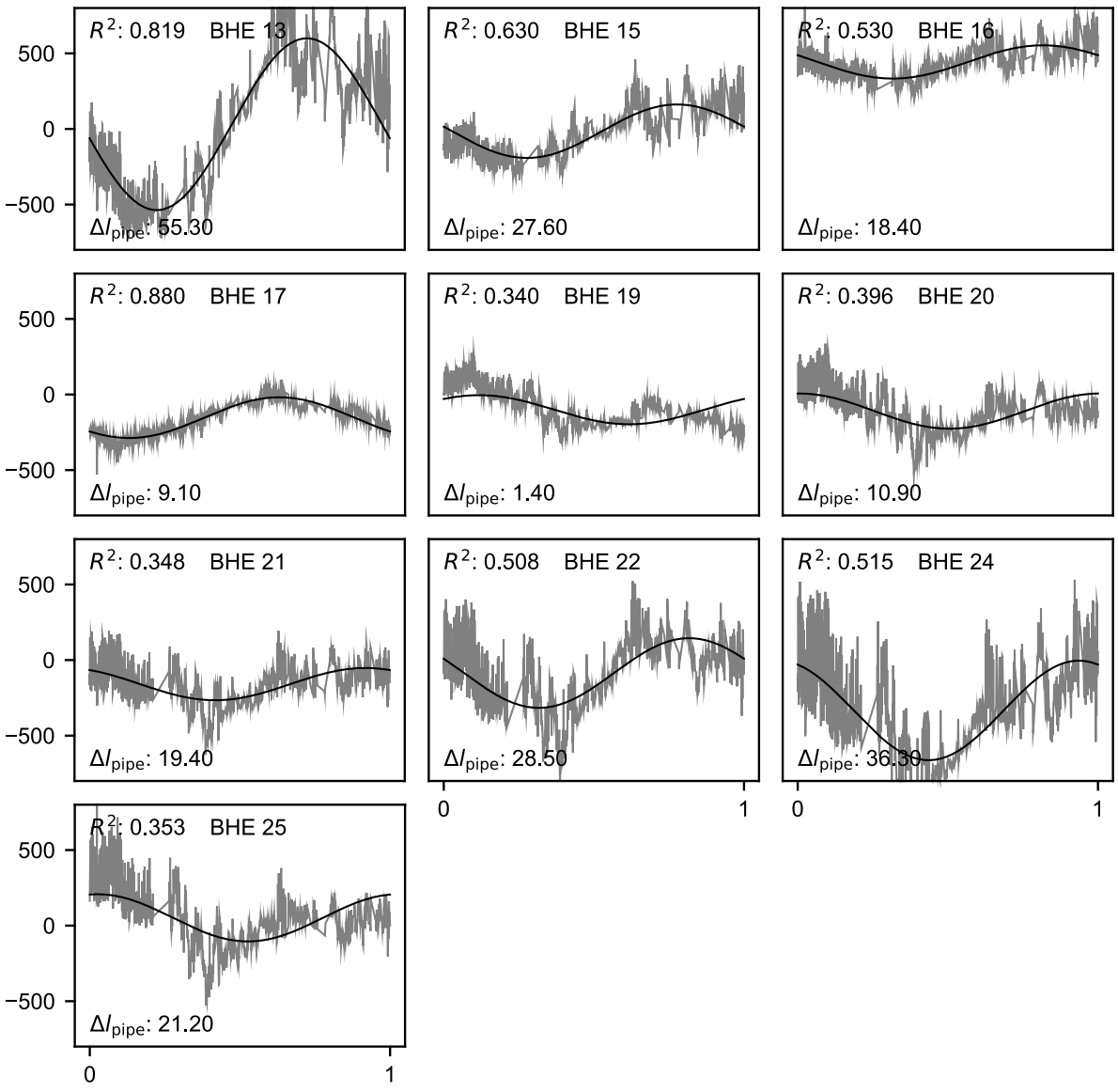

Figure 4.20 Flow rate related performance difference to the reference BHE in kW/($m^3 s^{-1}$) over the period of one year for manifold B.

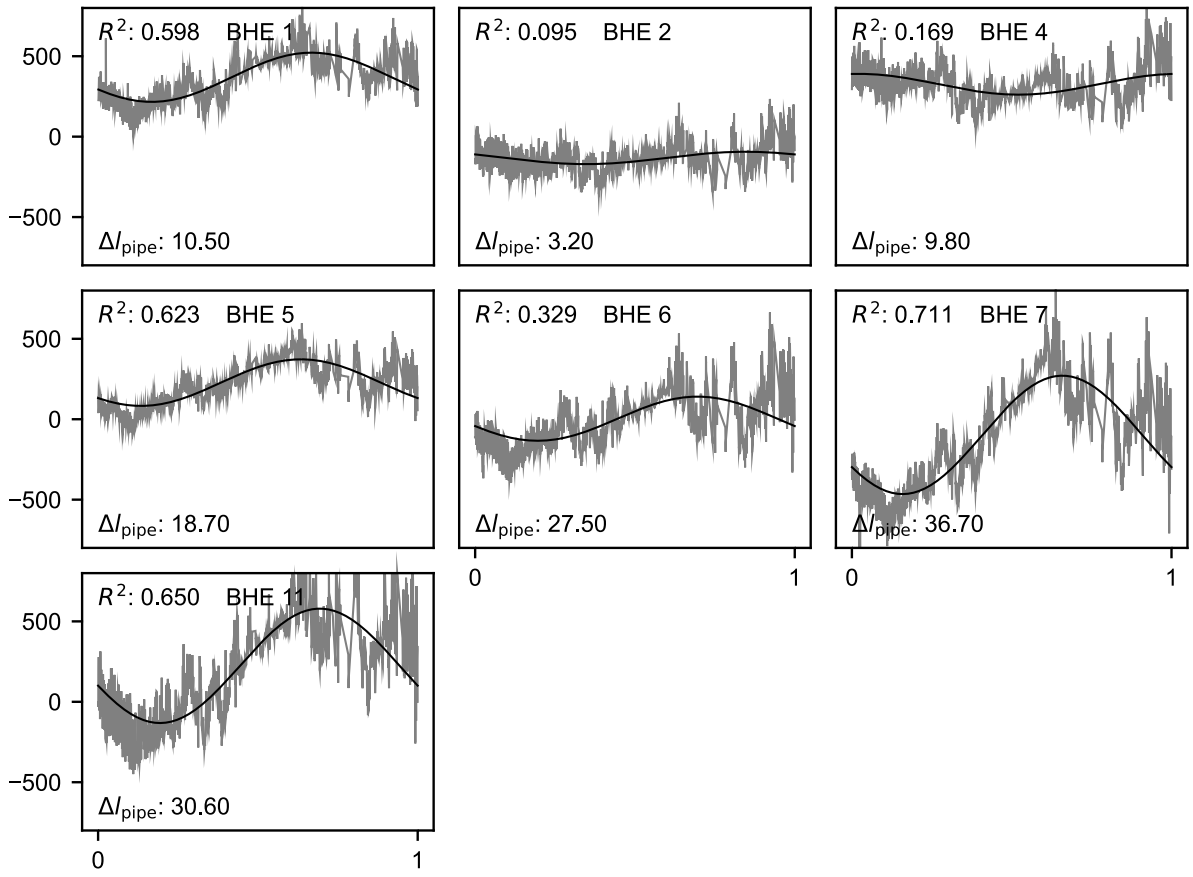

Figure 4.21 Flow rate related performance difference to the reference BHE in kW/($m^3\,s^{-1}$) over the period of one year for manifold A.

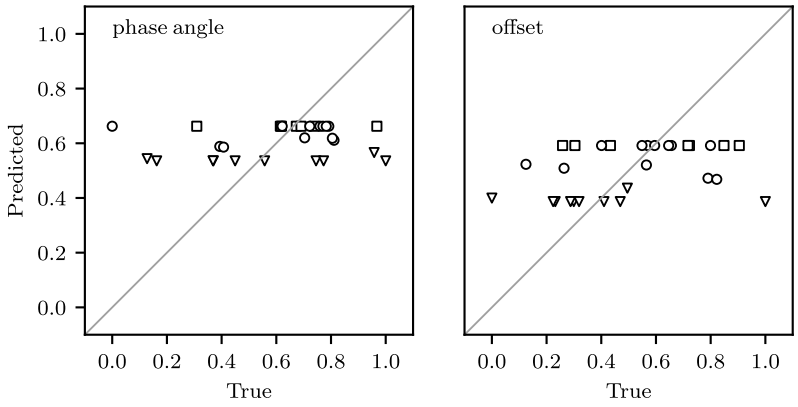

Figure 4.22 Predictions for phase angle and offset over observed values (normalized).

Table 4.4 Compilation of data used in regression analysis.

BHE	Δl_{pipe} [m]	z_{pipe} [m]	**Amp.** [kW/(m³ s⁻¹)]	**Phase angle** [rad]	**Offset** [kW/(m³ s⁻¹)]	**Surf.** [-]	**Sun** [-]	**Neigh.** [-]
1	10.5	1.26	153	0.52	369	0	1.0	0.54
2	3.2	1.18	39	-0.61	-132	0	0.91	0.44
3	0.0	1.16	-	-	-	-	-	-
4	9.8	1.26	65	1.44	326	0	0.55	0.47
5	18.7	1.36	145	0.73	228	0	0.27	0.41
6	27.5	1.45	137	0.34	3	0	0.13	0.28
7	36.7	1.54	368	0.58	-97	0	0.03	0.07
11	30.6	1.37	356	0.35	224	0	0.96	0.37
13	55.3	1.51	568	0.16	31	1	0.41	0
15	27.6	1.22	177	-0.17	-14	1	0.46	0.48
16	18.4	1.13	110	-0.42	443	1	0.50	0.59
17	9.1	1.03	135	0.75	-153	1	0.50	0.63
18	0.0	0.94	-	-	-	-	-	-
19	1.4	0.94	96	0.83	-100	1	0.45	0.67
20	10.9	1.04	116	1.54	-110	1	0.46	0.72
21	19.4	1.13	107	-1.06	-159	1	0.46	0.70
22	28.5	1.23	231	-0.42	-86	1	0.53	0.44
24	36.3	1.31	329	-1.17	-333	0.94	0.51	0.35
25	21.2	1.15	156	1.40	52	0.76	0.32	0.56
23	24.3	1.42	293	-0.34	280	0.58	0.58	0.24
26	10.2	1.24	88	0.79	176	0	0.26	0.62
27	14.5	1.32	98	-0.30	305	0.60	0.78	0.53
28	1.7	1.19	146	0.67	109	0	0.73	0.41
29	13.0	1.27	141	0.82	287	0	0.17	0.59
30	0.3	1.15	55	-1.56	-22	0	0.38	1
31	6.2	1.24	130	0.95	-128	0.41	0.84	0.83
33	0.0	1.11	-	-	-	-	-	-
34	5.0	1.23	163	0.93	106	0.35	0.89	0.88
35	13.2	1.27	169	0.89	93	0	0.18	0.79
36	15.1	1.33	254	0.62	-236	0.34	0.83	0.44
37	11.0	1.23	168	0.86	168	0	0.13	0.78
39	31.6	1.45	280	0.36	129	0	0	0.47

Chapter 5

Comparison of simulation models for connection pipes in BHE fields

Published as:

Düber S., Fuentes R., Narsilio G.A. (2023): Comparison and integration of simulation models for horizontal connection pipes in geothermal bore fields. *Geothermal Energy*, 11 (1), art. no. 15.

Düber S.: Conceptualization, Methodology, Software, Validation, Writing - Original Draft **Fuentes R.:** Writing - Review & Editing, Supervision **Narsilio G.A.:** Writing - Review & Editing, Supervision.

Abstract

The heat transfer along horizontal connection pipes in geothermal bore fields can have significant effects and should not be neglected. As practical and design-related applications require simple and efficient models, we investigate suitability of different models for the first time within this context. Three ground and three pipe models of different complexity are studied. All model combinations are coupled with a fixed ground load boundary condition on the one side, and a borehole heat exchanger (BHE) model on the other side. Models are tested under a variety of realistic conditions to evaluate performance. The investigations show that all investigated pipe models are equally suitable for the application. For the ground models, the horizontal finite line source model and the numerical 2D model produce identical results for homogeneous ground properties. The soil resistance model neglects the temperature accumulation in the ground and thus leads to considerable deviations and should be avoided. Based on the findings we propose a computationally efficient approach using a novel combination of established simple steady state models for the BHE and connection pipes. In the selected example scenario, the consideration of a 30 m connection pipe attached to the BHE leads to an increase in the BHE load by 40 % for the heating case and a reduction in the BHE load by 5 % for the cooling case.

5.1 Introduction

The exploitation of geothermal energy is becoming increasingly important in the context of global warming and the reduction of greenhouse gas emissions. Vertical borehole heat exchangers (BHE) or horizontal geothermal collectors using a ground source heat pump (GSHP) are the main installations to heat and cool buildings. In densely populated areas, BHEs are often preferred as they require much smaller footprint than horizontal systems. For the supply of commercial buildings, apartment blocks, or entire districts, systems with several dozen or even hundreds of BHEs are increasingly being installed. For example in Sweden alone the number of registered installations with 10 000 m or more total borehole length has almost quadrupled from 21 in 2015, to 76 systems in 2019, while the number of installations with 10 boreholes or more has increased by almost 40 % during the same period (Lund and Toth, 2021). In order to reduce thermal interference between the boreholes, a minimum spacing should be maintained between the BHEs in a bore field (Kavanaugh and K. D. Rafferty, 2014; VDI 4640-2, 2019). This can result in distances of several dozen meters between the BHEs and the heat pump, manifolds or header pipes. The hydraulic effects of these connection pipe networks have been investigated recently in various studies; however without in depth consideration of their thermal interference with the surrounding ground (Chen et al., 2021, 2020; M. F. Zhang et al., 2021). Luo et al. (2013) use a three-dimensional numerical model to investigate the heat loss along a single buried pipe at different depths, reporting double-digit

kW h daily heat losses depending on burial depth for an 18 m connection pipe. Tian et al. (2022) investigate the impact of burial depth, surface temperature, backfill material and flow rate on the heat loss of horizontal connection pipes connected to BHE in a sandbox experiment. In this work the inlet temperature is fixed, leading to heat gains along the connection pipes for all investigated scenarios. For practical applications in the design and optimisation of geothermal bore fields however, simpler and more efficient approaches are desirable. While numerical 3D models can accurately represent all types of heat transport and boundary conditions, some difficulties arise in the context borehole heat exchangers and horizontal connection pipes. Namely, the scale-distributed time ranges (hourly thermal loads and design periods of multiple decades) and geometries (pipe diameters of a few centimetres and BHE lengths of several 100 meters) lead to high modelling and computational efforts (M. Li et al., 2014).

Heat transfer in the near-surface ground from a combination of linear or cylindrical heat sources and sinks has been investigated in various contexts over the last century. These include buried power cables, oil or steam pipelines, pipelines for district heating networks and, increasingly in recent decades, horizontal geothermal collectors. Considering the pipe diameters and fluid temperatures, the latter are most closely related to the connection pipes investigated in this work.

Several authors have derived analytical equations for the problem of heat conduction in a semi-infinite space. While Ioffe (1972) provides a solution for transient heat conduction due to a cylinder with a fixed temperature, Thiyagarajan and Yovanovich (1974) and Martin and Sadhal (1978) provide solutions for a heat flux boundary condition at the cylinder for transient and steady state. To account for groundwater flow around the cylinder, the analytical steady state solution of Himasekhar and Bau (1987) can be applied. While the boundary condition at the ground surface is a fixed temperature for the above solutions, Chung et al. (1999) present a semi-analytical model for a buried pipe with a constant wall temperature and a convection boundary condition at the ground surface. Including the domain inside the pipe, Hastaoglu et al. (1995) propose a 3D numerical model to solve the heat transfer from a buried pipe with laminar flow and solidification of the fluid. While the works mentioned so far are formulated for single pipes, Shafagh et al. (2022) consider multiple pipes in their investigation using a 2D numerical model for the domain outside the pipes.

An early, and well known, reference on horizontal geothermal collectors is the work of Claesson and Dunand (1983). Comprehensive reviews on more recent work can be found in Y. L. Cui et al., 2019; Hou et al., 2022. Similar to simulation models for borehole heat exchangers, the spatial domain for horizontal collector models is often divided into two areas: the heat exchanger (the pipe), and the media (surrounding ground). By doing so, specifically suited

calculation models for both areas can be used to reduce the computational cost. If the ground is homogeneous and heat is only transferred through conduction, analytical solutions such as the infinite or finite line source (FLS) (Claesson and Dunand, 1983; Fontaine et al., 2011; Lamarche, 2019; Urresta et al., 2021) or ring source (H. Li et al., 2012; Xiong et al., 2015) can be used. Spatial and temporal superposition is applied in these models to account for multiple pipes and time-dependent thermal loads (Carslaw and Jaeger, 1959). As the horizontal pipes are buried at shallow depths, there are situations where transfer mechanisms other than conduction might need to be considered. Piechowski (1999) for example uses a 2D numerical ground model to account for moisture transport in the vicinity of the pipe. Another influencing factor can be the boundary condition at the surface above the pipes. Several authors consider evaporation, radiation and convection in their numerical 2D models (Bortoloni et al., 2017; Gan, 2019; Kayaci and Demir, 2018; Larwa and Kupiec, 2020). The models neglect temperature changes in the ground along the pipe axis, as it is negligible in most cases (Claesson and Dunand, 1983). Nevertheless, there are also some works in which the ground is modelled as three-dimensional, for example to investigate different pipe arrangements (Dasare and Saha, 2015; Selamat et al., 2016; Wu et al., 2010), and accounting for varying surface heat fluxes (X. Gu et al., 2022; Muñoz-Criollo et al., 2016).

Similar to the modelling of the ground, models of varying complexity are used for the pipes and fluid flow. In the simplest case, a linear temperature profile between inlet and outlet is assumed for a steady state condition (e.g., Kavanaugh and K. D. Rafferty, 2014). A more complex analytical solution considers the nonlinear temperature profile along the pipe (Van Genuchten, 1982). Assuming a homogeneous temperature field in the fluid cross-section, transient fluid flow can be modelled with one-dimensional numerical models. The coupling of the fluid models and the surrounding ground is then done through a series of thermal resistances accounting for the convective resistance from the fluid to the pipe and the conductive resistance of the pipe.

Since multiple models exist, it is hard to assess what modelling approaches to use that is suitable for a range of realistic conditions. The published literature suggests that the horizontal connection pipes can have a significant influence on the BHE operation. The level of impact may be a function of climate, depth and thermal loads; for which reliable models are needed. Depending on the conditions, the horizontal connection pipes can have a beneficial effect due to heat gains and may lead to reduced required BHE length and therefor cost. If the heat losses predominate, neglecting the horizontal pipes in the design may result in reduced efficiency of the entire system. While 3D numerical modelling or physical experiments are well suited in an academic context, simpler models are usually preferred for practical applications. Hence, the aim of this work is to identify simulation models suited to investigate heat transfer along horizontal connection pipes and to develop a computationally

efficient and simple methodology that is appropriate to capture these effects. Three ground and three pipe models are studied. All model combinations are coupled with a GSHP model. Figure 5.1 schematically shows the typical arrangement for GSHP systems and the associated models and nomenclature used in the article.

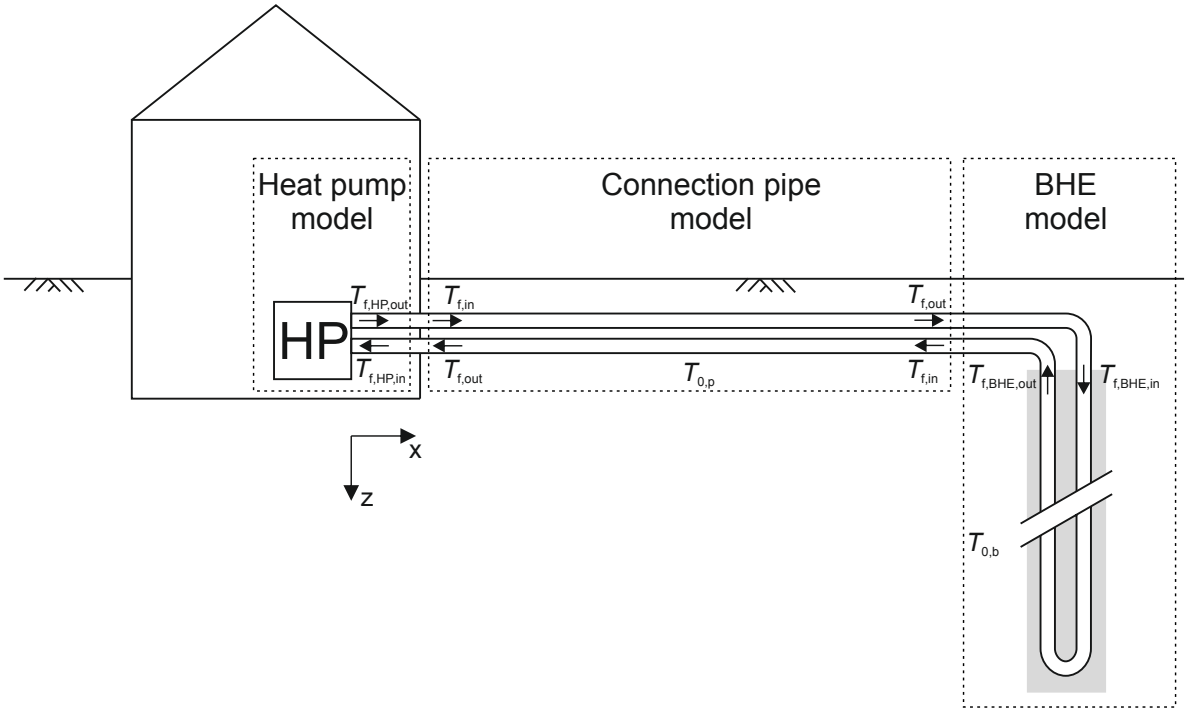

Figure 5.1 Schematic illustration of the simulated system and the coupled models

The models used for the ground and pipes are described in section 5.2 and are available through a GitHub repository. In section 5.3, the investigated scenarios are presented, followed by the results and discussion in sections 5.4 and 5.5.

5.2 Models

5.2.1 Pipe models

The one-dimensional heat transfer along a buried pipe is described by Eq. 5.1. The heat capacity of the pipe wall is neglected, and heat is exchanged with the surrounding ground:

$$\frac{\partial T_\mathrm{f}}{\partial t} + u_\mathrm{f}\frac{\partial T_\mathrm{f}}{\partial x} - \alpha_\mathrm{f}\frac{\partial^2 T_\mathrm{f}}{\partial x^2} + \phi\,(T_\mathrm{f} - T_\mathrm{s}) = 0. \tag{5.1}$$

T_f and T_s are the temperatures of the fluid and the soil, u_f is the velocity of the fluid and α_f its thermal diffusivity. The specific heat transfer coefficient ϕ is calculated based on the thermal resistance between fluid and soil R_fs, the volumetric heat capacity of the fluid ρc_f and the inner cross-sectional area of the pipe A_i:

$$\phi = \frac{1}{R_{\mathrm{fs}} A_{\mathrm{i}} \rho c_{\mathrm{f}}}. \tag{5.2}$$

R_{fs} is the sum of the convective resistance between fluid and inner pipe wall, R_{conv}, and the conductive resistance of the pipe wall, R_{p} (see Figure 5.2). The latter is calculated as

$$R_{\mathrm{p}} = \frac{\ln(r_{\mathrm{p,i}}/r_{\mathrm{p,o}})}{2\pi\lambda_{\mathrm{p}}} \tag{5.3}$$

where $r_{\mathrm{p,i}}$ is the inner radius of the pipe and $r_{\mathrm{p,o}}$ its outer radius while λ_{p} denotes its thermal conductivity (Carslaw and Jaeger, 1959).

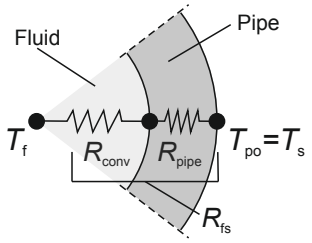

Figure 5.2 Thermal resistances between fluid and soil.

The convective resistance R_{conv} is calculated with the dimensionless flow coefficients *Reynolds*, *Nusselt* and *Prandtl* (Gnielinski, 2013):

$$R_{\mathrm{conv}} = \frac{1}{Nu \lambda_{\mathrm{f}} \pi} \tag{5.4}$$

$$Re = \frac{u_{\mathrm{f}} d_{\mathrm{p,i}}}{\eta_{\mathrm{f}}/\rho_{\mathrm{f}}} \tag{5.5}$$

$$Pr = \frac{\eta_{\mathrm{f}} c_{\mathrm{f}}}{\lambda_{\mathrm{f}}} \tag{5.6}$$

The formula for Nusselt number depends on the flow state. For laminar flow, the Nusselt number is defined as (Gnielinski, 2013):

$$Nu = 4.364. \tag{5.7}$$

For turbulent flows, the following applies:

$$Nu = \frac{(\zeta/8) RePr}{1 + 12.7\sqrt{\zeta/8}(Pr^{2/3} - 1)} \left[1 + \left(\frac{d_{\mathrm{p,i}}}{l_{\mathrm{p}}}\right)^{2/3}\right] \tag{5.8}$$

Table 5.1 Properties of the investigated pipe models

Model	axial temperatures	transient flow
1D-numerical	✓	✓
steady state	✓	x
steady state linear	x	x

with:

$$\zeta = (1.8 \log_{10} Re - 1.5)^{-2}, \tag{5.9}$$

while for flow in the transient region Equations 5.10 and 5.11 apply.

$$Nu = (1-\gamma)4.364 + \gamma \left\{ \frac{(0.0308/8)10^4 Pr}{1 + 12.7\sqrt{0.308/8}(Pr^{2/3}-1)} \left[1 + (\frac{d_{\mathrm{p,i}}}{l_{\mathrm{p}}})^{2/3} \right] \right\} \tag{5.10}$$

with:

$$\gamma = \frac{Re - 2300}{10^4 - 2300} \quad (0 \leq \gamma \leq 1). \tag{5.11}$$

Here $d_{\mathrm{p,i}}$ is the inner diameter of the pipe, l_{p} the pipe length, η_{f} the dynamic viscosity of the fluid, ρ_{f} its density and c_{f} its specific heat capacity.

The lateral heat transfer between fluid and soil is calculated with the described resistance R_{fs} in all investigated pipe models, while three approaches with differing degrees of simplification are used for the heat transfer along the pipe axis (Table 5.1).

5.2.1.1 1D numerical model

The transient fluid flow with time-dependent fluid inlet and soil temperatures as boundary conditions can be captured with a numerical model. Here we choose the Finite-Volume-Method (FVM) for the discretization of Eq. 5.1. Utilizing the upwind scheme, the fluid temperature at time step $i+1$ and cell x is calculated as:

$$T_{\mathrm{f}}(x, t_{i+1}) = T_{\mathrm{f}}(x, t_i) + \Delta t \frac{u_{\mathrm{f}}}{\Delta x} \left[T_{\mathrm{f}}(x-1, t_i) - T_{\mathrm{f}}(x, t_i) \right] + \Delta t \phi \left[T_{\mathrm{s}}(x, t_i) - T_{\mathrm{f}}(x, t_i) \right]. \tag{5.12}$$

Due to the explicit Euler scheme, the cell size Δx and the time step Δt must be chosen in a way that the CFL criterion is met: $\frac{u_{\mathrm{f}} \Delta t}{\Delta x} \leq 1$.

5.2.1.2 Steady-state analytical model

For constant inlet fluid and soil temperatures the analytical solution for Eq. 5.1 is given by Van Genuchten, 1982:

$$T_{\mathrm{f}}(x,t) = T_{\mathrm{s}} + \frac{(T_{\mathrm{f,in}} - T_{\mathrm{s}})}{2}\left\{ \exp\left[\frac{(u_{\mathrm{f}} - v)x}{2\alpha_{\mathrm{f}}}\right] \operatorname{erfc}\left(\frac{x - vt}{2\sqrt{\alpha_{\mathrm{f}} t}}\right) + \exp\left[\frac{(u_{\mathrm{f}} + v)x}{2\alpha_{\mathrm{f}}}\right] \operatorname{erfc}\left(\frac{x + vt}{2\sqrt{\alpha_{\mathrm{f}} t}}\right) \right\} \quad (5.13)$$

with

$$v = u_{\mathrm{f}}\sqrt{1 + \frac{4\phi\alpha_{\mathrm{f}}}{u_{\mathrm{f}}^2}} \quad (5.14)$$

where $\alpha_{\mathrm{f}} = \frac{\lambda_{\mathrm{f}}}{\rho c_{\mathrm{f}}}$ is the thermal diffusivity of the fluid. In our study, the pipe models are coupled with various ground models as well as a BHE model and a highly simplified, yet sufficient, GSHP model imposing a ground load boundary condition. As a result, the inlet $T_{\mathrm{f,in}}$ and ground temperatures T_{s} change in each calculation step, so that the Eq. 5.13 cannot be used as it is only valid for constant inlet fluid temperatures. To simplify matters, we assume that the pipe is completely flowed through in each calculation step and that a steady-state is reached. The steady-state solution for Eq. 5.13 reads as:

$$T_{\mathrm{f}}(x) = T_{\mathrm{s}} + (T_{\mathrm{f,in}} - T_{\mathrm{s}}) \exp\left[\frac{(u_{\mathrm{f}} - v)x}{2\alpha_{\mathrm{f}}}\right] \quad (5.15)$$

and this simpler solution is implemented in the model in this work.

5.2.1.3 Steady-state linear model

Assuming stationary conditions and a linear temperature profile along the pipe, Eq. 5.15 can be further simplified to find the outlet temperature $T_{\mathrm{f,out}}$ of the horizontal connection pipe of length l_{p}:

$$T_{\mathrm{f,out}} = T_{\mathrm{f,in}} - (T_{\mathrm{f,in}} - T_{\mathrm{s}})\frac{2\phi l_{\mathrm{p}}}{\phi l_{\mathrm{p}} + 2u_{\mathrm{f}}}. \quad (5.16)$$

To verify the correct implementation of the described pipe models, a comparative simulation was carried out with the finite element software COMSOL Multiphysics®. A single 50 m long pipe with an outer diameter of 40 mm, a wall thickness of 3.7 mm and a thermal conductivity

of $0.37\,\mathrm{W\,m^{-1}\,K^{-1}}$ was used. The fluid had a flow rate of $35\,\mathrm{m^3\,d^{-1}}$ and a temperature entering the pipe of 30 °C, while the temperature at the outer wall of the pipe is set to 15 °C. The fluid has also a thermal conductivity of $0.598\,\mathrm{W\,m^{-1}\,K^{-1}}$, a density of $998.23\,\mathrm{kg\,m^{-3}}$, specific heat capacity of $4184\,\mathrm{J\,kg^{-1}\,K^{-1}}$ and a dynamic viscosity of $1.100\,16\,\mathrm{mPa\,s}$. The results are shown in Figure 5.3 for $t = 53.8\,\mathrm{s}$, where the fluid has travelled 27 m into the pipe (left) and $t = 103.8\,\mathrm{s}$ (right), which is a sufficiently long time for steady state conditions. The numerical models (COMSOL, 1D num.) suffer from numerical diffusion, leading to a smeared temperature front compared to the analytical solution (Figure 5.3). For this example the energy absorbed by the fluid during the first $t = 103.8\,\mathrm{s}$ is 399 kJ for the transient models and 744 kJ for the steady state linear model. Once pipe is flown through, the difference in heat exchange rate between the steady state linear model and all other models is only 75 W.

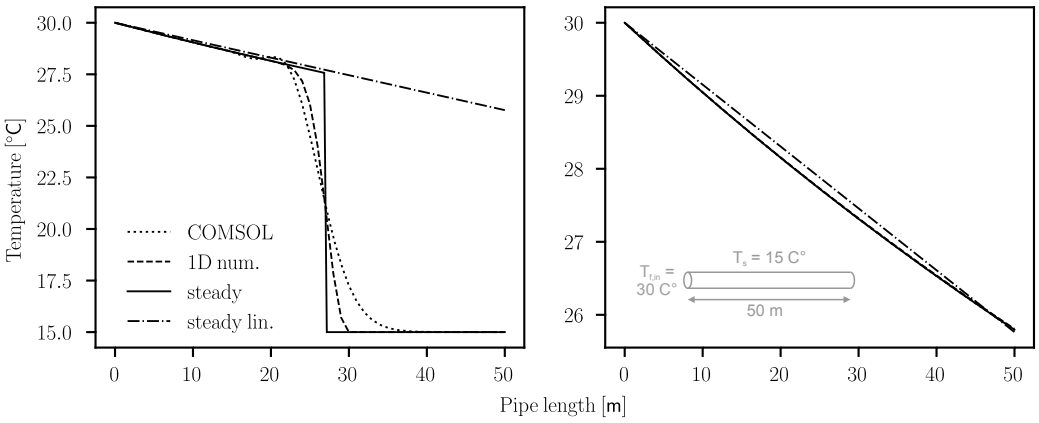

Figure 5.3 Verification of the pipe model implementation: transient case with the temperature front at the middle of a 50 m long pipe (left) and steady state case with fully flown through pipe (right).

5.2.2 Ground models

As the aim of this work is to investigate and develop simple models that are suitable for determining the heat losses along the connection pipes of BHEs, we limit the heat transfer processes in the ground to conduction, leading to Eq. 5.17 for the three-dimensional subsurface domain.

$$\frac{\partial}{\partial x}\left(\lambda\frac{\partial T}{\partial x}\right) + \frac{\partial}{\partial y}\left(\lambda\frac{\partial T}{\partial y}\right) + \frac{\partial}{\partial z}\left(\lambda\frac{\partial T}{\partial z}\right) + q_\mathrm{v} = \rho c\frac{\partial T}{\partial t} \tag{5.17}$$

Here λ is the ground thermal conductivity (assumed to be the same in all directions), ρc the volumetric heat capacity and q_v the source term. As with the pipe models, we use three different models of varying complexity as listed in Table 5.2.

Table 5.2 Investigated ground models: soil resistance model (R_s), finite line source model (FLS) and the two-dimensional numerical model with selected distinguishing features.

Model	temperature accumulation	inhomogenous ground	axial temperature field
2D numerical	✓	✓	X
FLS	✓	X	(✓)
R_s	X	X	X

5.2.2.1 2D numerical model

If heat transfer along the pipe axis is neglected, the first summand in Eq. 5.17 can be dropped and the ground described by a two-dimensional temperature field. We discretise the reduced version of Eq. 5.17 with the finite volume method. The central difference scheme is used to interpolate the temperatures on the cell walls. For adjacent cells with different thermal conductivities, the harmonic mean is applied to determine the mean thermal conductivity at the cell walls, i.e. a solution for heat transfer in media in series. We use the explicit Euler scheme for the numerical integration due to its simplicity and computational efficiency, leading to:

$$\begin{aligned} T(y,z,t_{i+1}) = T(y,z,t_i) + \frac{\Delta t}{\rho c(y,z)\Delta yz^2}\Big\{ & \lambda_y(y-1,z)T(y-1,z,t_i) \\ & - \Big[\lambda_y(y-1,z) + \lambda_y(y,z) + \Big]T(y,z,t_i) + \lambda_y(y,z)T(y+1,z,t_i) \\ & + \lambda_z(y,z-1)T(y,z-1,t_i) \\ & - \Big[\lambda_z(y,z-1) + \lambda_z(y,z) + \Big]T(y,z,t_i) + \lambda_z(y,z)T(y,z+1,t_i) \\ & + q_v(y,z,t_i)\Big\} \end{aligned} \tag{5.18}$$

with

$$\lambda_y(y,z) = \frac{2}{\frac{1}{\lambda(y,z)} + \frac{1}{\lambda(y+1,z)}} \tag{5.19}$$

and

$$\lambda_z(y,z) = \frac{2}{\frac{1}{\lambda(y,z)} + \frac{1}{\lambda(y,z+1)}} \tag{5.20}$$

where $\Delta y = \Delta z = \Delta yz$ is the regular cell size, λ the thermal conductivity and ρc the volumetric heat capacity.

5.2.2.2 Finite line source model

Lamarche (2019) has presented the general solution for the horizontal finite line source in a half space to calculate segment-to-segment temperature responses. Similarly to the work in Claesson and Javed, 2011; Lamarche, 2011 the method of images is used to account for the ground surface boundary condition (Figure 5.4). The temperature change in the ground ΔT_s at the outer wall of a single segment pipe (the horizontal line source) can be calculated as:

$$\Delta T_\mathrm{s}(t) = \frac{q}{4\pi\lambda} g(t) \tag{5.21}$$

with

$$g(t) = \int_{\frac{1}{\sqrt{4\alpha t}}}^{\infty} \frac{2\left(e^{-r^2 s^2} - e^{-r_i^2 s^2}\right)}{s^2} \left[Hs\,\mathrm{erf}(Hs) - \frac{1}{\sqrt{\pi}}\left(1 - e^{-H^2 s^2}\right)\right] ds \tag{5.22}$$

where q is the length related heat load, λ the thermal conductivity of the soil and H is the length of the line source. r denotes the distance between the line source and the surface of interest (i.e., outer pipe wall) and r_i the distance between the imagery line source and the surface of interest (Figure 5.4).

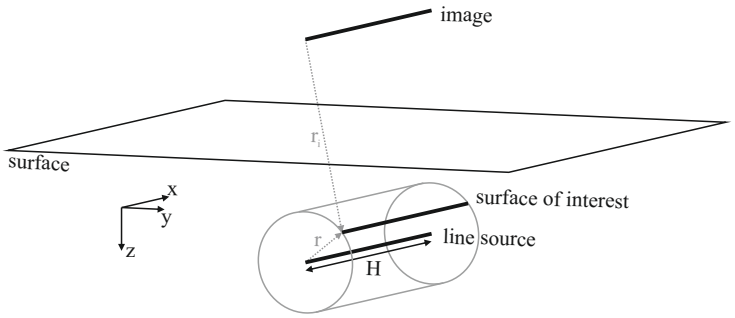

Figure 5.4 Horizontal finite line source and the method of images.

Superimposing the temperature change with the undisturbed ground temperature T_0 finally provides the ground temperature at the outer pipe wall T_s:

$$T_\mathrm{s}(t) = T_0(t) + \Delta T_\mathrm{s}(t). \tag{5.23}$$

By applying the superposition principle (Carslaw and Jaeger, 1959), time-variable thermal loads $q(t)$ can be considered as the source term (last summand in Eq. 5.17). Thus, the load profile with stepwise constant loads is transferred into load increments:

$$\Delta q(t_i) = q(t_i) - q(t_{i-1}) \tag{5.24}$$

and a summation over time applied, leading to:

$$T_{\mathrm{s}}(t_k) = T_0(t_k) + \frac{1}{4\pi\lambda} \sum_{i=1}^{k} \Delta q(t_i) \cdot g_{\mathrm{p}}(t_{k-i+1}). \tag{5.25}$$

5.2.2.3 Soil resistance model

The work of Kavanaugh and K. D. Rafferty (2014) provides a calculation template to estimate heat gain and loss in horizontal buried pipe headers. This model is identical to the FLS, but uses a different formulation for the line source. Furthermore, it does not consider temporal or spatial superposition. To include a similar model in the comparison here, we will implement Eq. 5.21-5.23, neglecting interference of multiple pipes and temperature accumulation in the ground.

To verify the implementation of the 2D numerical model and the FLS model, a comparative simulation was carried out against a full 3D finite element model implemented in the package COMSOL Multiphysics®. For this purpose, a cylindrical heat source of $10\,\mathrm{W\,m^{-1}}$ and a cylindrical heat sink of $-5\,\mathrm{W\,m^{-1}}$ with diameters of 40 mm were placed at -0.85 m from the upper boundary in a 3×3 m 2D model with thermally insulated boundaries. Figure 5.5 shows a horizontal (y) and vertical (z) temperature profile after a simulation time of 48 h. The models show good agreement. Only the horizontal section shows deviations for the area within the heat sources. However, these areas are not relevant for the coupled simulations, as the interface to the pipe model is the ground temperature at the outer radius of the pipe.

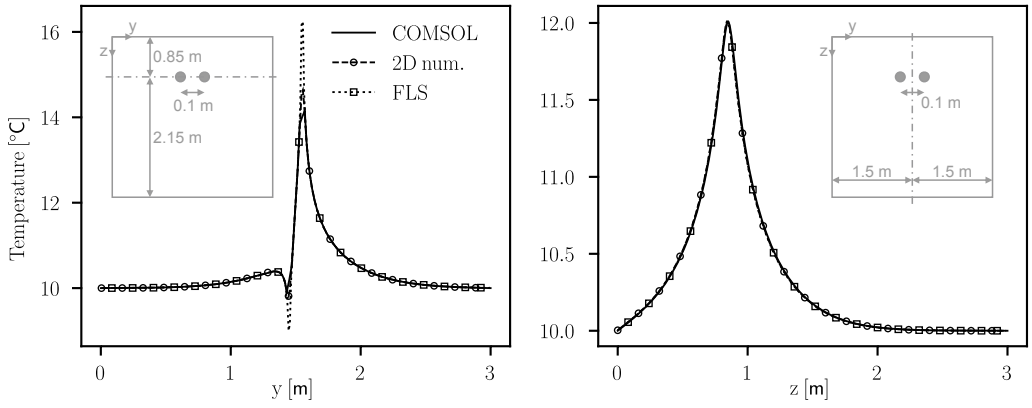

Figure 5.5 Verification of the ground model implementation: horizontal (left) and vertical (right) temperature profile.

5.2.3 Coupling of pipe and ground models

The coupling parameters between the pipe models and the ground models are the soil temperature at the pipe wall T_{s} and the heat flow between soil and pipe. Based on the soil temperature and the fluid inlet temperature $T_{\mathrm{f,in}}$, the pipe models calculate new fluid outlet

temperatures $T_{\mathrm{f,out}}$ and the fluid temperatures along the horizontal pipe. The difference between the mean fluid temperature within the pipe $\overline{T}_{\mathrm{f}}$ and the temperature at the soil-pipe wall interface T_{s} and the thermal resistance between fluid and soil R_{fs} determine the ground load:

$$q = \frac{T_{\mathrm{s}} - \overline{T}_{\mathrm{f}}}{R_{\mathrm{fs}}}. \tag{5.26}$$

The ground load serves as input for the ground models to calculate the soil temperature at the pipe wall. As the soil temperature at the pipe wall depends on the fluid temperature which also depends on the pipe wall temperature, this problem requires an iterative scheme as shown in Figure 5.6.

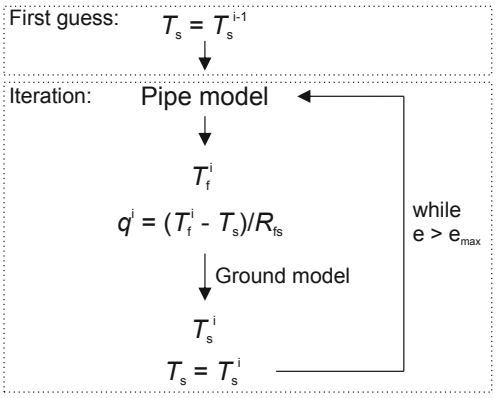

Figure 5.6 Coupling scheme between ground and pipe models.

As a first guess for the soil temperature, we use the value from the previous timestep $i-1$. After calculating a new ground temperature, this process is repeated, until an error tolerance criterion is fulfilled. The deviation of the outlet fluid temperature between two iterations is used as error criterion:

$$e = \left| \frac{T_{\mathrm{f,out}}^{\mathrm{new}} - T_{\mathrm{f,out}}^{\mathrm{old}}}{T_{\mathrm{f,out}}^{\mathrm{old}}} \right|. \tag{5.27}$$

The combination of coupled pipe and ground model will henceforth be referred to as the connection pipe model. For the investigations carried out, the various connection pipe models are coupled with a BHE model on the one side and a fixed thermal load boundary condition representing the heat pump on the other side as shown in Figure 5.1.

5.2.4 BHE model and thermal load boundary condition

For the BHE model, we use the work of Düber et al. (2022), since it is computationally efficient and can be easily coupled with the connection pipe models through its implementation in Python. The model follows the idea of Wetter and Huber (1997) of combining a

semi-numerical borehole model with a g-function ground model. The interaction of the BHEs and the consideration of time-variable loads are taken into account by spatial and temporal superposition. The borehole models utilize the thermal resistance capacity models from Bauer et al. (2011) for the horizontal heat transfer and the finite volume method for the heat transfer in vertical direction. To overcome high computational times for simulations with many time steps, the model also uses the Fast Fourier Transformation and the convolution theorem for better efficiency (Marcotte and Pasquier, 2008).

One input parameter for the simulations will be the ground load presented in the next section. To impose the load as a boundary condition on the model, we use Eq. 5.28, acting as a highly simplified heat pump model. The outlet temperature of the heat pump $T_{\mathrm{f,HP,out}}$ at time step i as is calculated as follows:

$$T_{\mathrm{f,HP,out}}(t_i) = T_{\mathrm{f,HP,in}}(t_{i-1}) - \frac{q(t_i)}{\dot{V}\rho c_{\mathrm{f}}} \tag{5.28}$$

where $\dot{V}$ is the volumetric flow rate of the fluid and ρc_{f} its volumetric heat capacity. $T_{\mathrm{f,HP,in}}(t_{i-1})$ is the fluid inlet temperature of the heat pump (Figure 5.1) and equal to the mean outlet temperature of all return horizontal connection pipes (i.e., the mean of all $T_{\mathrm{f,out}}$). $q(t_i)$ is the ground load of the current time step.

For the simulations with six BHEs considered operating in parallel (see section 5.3), we make some assumptions that allow us to isolate and analyse the effect of the thermal interference of multiple horizontal connection pipes in a shared trench. While we recognize that turns and merging of connection pipes may also exist in real projects and thus differ from this arrangement, all pipes are assumed parallel along their entire length and arranged as shown in Figure 5.7. Considering parallel operation, all supply connection pipes are assumed to be connected to the same heat pump, thus receiving the same inlet temperature $T_{\mathrm{f,HP,out}}$, while $T_{\mathrm{f,HP,in}}$ is the the mean of all $T_{\mathrm{f,out}}$ (Figure 5.1). On the other side, each pair of connection pipes is connected to an individual BHE, however the BHE models are set up to have no thermal interference between them.

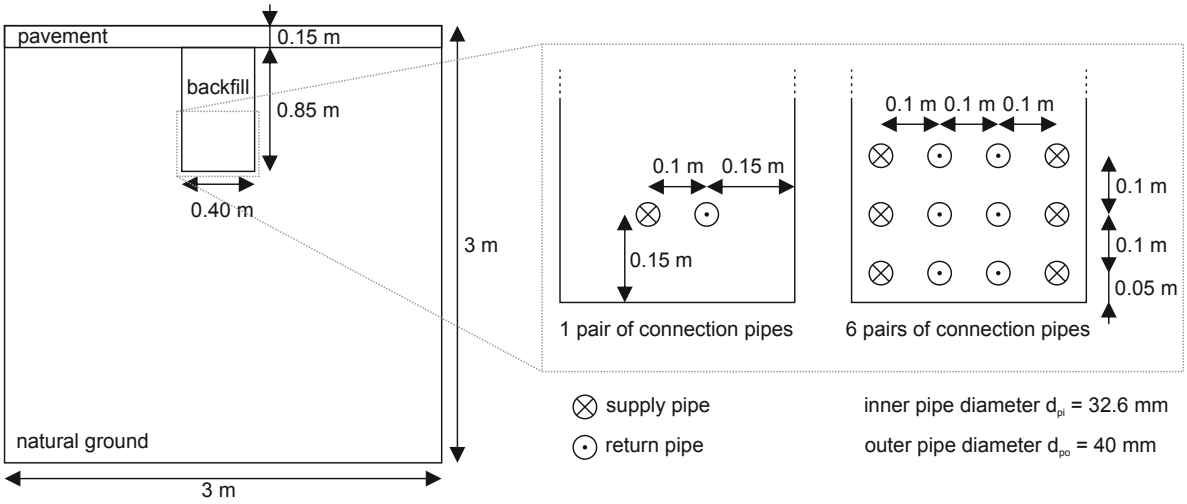

Figure 5.7 Cross-section of the trench for the heterogeneous ground model and pipe arrangement.

5.3 Scenarios

The model comparison is carried out using scenarios with horizontal connecting pipes of 30 and 60 m length and a single pair of pipes (1 BHE) or six pairs of pipes (6 BHEs) installed in a shared trench as shown in Figure 5.7.

The BHE data listed in Table 5.4 and the load profile shown in Figure 5.8 (top) are from a study from Ahmadfard and Bernier (2019). The load profile corresponds to a building located in Atlanta and is scaled down for a single BHE with factor of 1/25 and 6/25 for the simulation with 1 and 6 BHEs respectively.

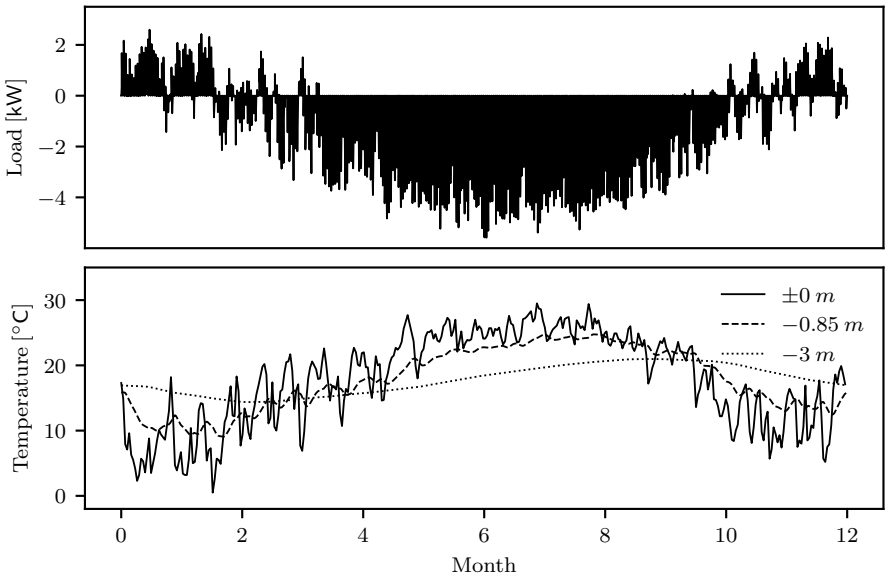

Figure 5.8 Thermal load (top) and temperatures (bottom) used as boundary conditions.

Table 5.3 Thermal properties of the trench and connection pipe.

	λ [W m^{-1} K^{-1}]	ρc [J m^{-3} K^{-1}]
Natural ground	1.5	1 800 000
Backfill	0.9	1 500 000
Pavement	1.2	1 600 000
Pipe	0.38	-

Daily values for the air temperature in Atlanta serve as temperature boundary condition at the ground surface (Figure 5.8, bottom). Temperatures at 3 m depth and the depths of the pipes have been calculated using a one-dimensional ground model with the thermal properties of the natural ground and the air temperature as surface temperature. The yearly cycle was repeated until a cyclic steady state was reached. For the numerical ground model, the temperatures at $z = \pm 0$ m and $z = -3$ m are used as boundary conditions at the top and the bottom of the model while the sides are considered thermally insulated.
In the FLS model, the temperature change due to heat exchange with the pipes is superimposed on the undisturbed temperature calculated at the depth of the pipes (e.g., -0.85 m), whereas in the soil resistance model this temperature is used as a first order boundary condition.
The inhomogeneous properties of the ground as shown in Figure 5.7 can be only considered in the 2D numerical ground model. All other models assume homogeneous conditions. For this reason we apply the material properties listed in Table 5.2 to the numerical model to simulate the inhomogeneous case and the properties of the natural ground for the whole model to simulate the homogeneous case.

The numerical ground models were discretised with a cell size of 1×1 cm and a time step of 25 s. The numerical pipe model is discretised with 11 cells for the 30 m pipe length and 22 cells for the 60 m pipe length using a 5 s time step, resulting in a CFL-number of 0.89. In the analytical steady state model, the fluid temperatures are calculated at the same points as in the numerical model, while in the linear steady state model the fluid temperature is calculated just at the outlet of the connection pipe (Figure 5.1).

Table 5.4 BHE and ground properties.

Parameter	Value	Units
Fuild properties		
Thermal conductivity	0.468	$\mathrm{W\,m^{-1}\,K^{-1}}$
Density	1026	$\mathrm{kg\,m^{-3}}$
Volumentric heat capacity	4 123 494	$\mathrm{J\,m^{-3}\,K^{-1}}$
Dynamic Viscosity	0.003 37	Pa s
BHE geometry		
Length	120	m
Diameter	0.150	m
Shank space	0.083	m
Outer diameter pipes	0.0334	m
Pipe wall thickness	0.0037	m
BHE-properties		
Thermal conductivity grout	2.0	$\mathrm{W\,m^{-1}\,K^{-1}}$
Volumetric heat capacity grout	3 900 000	$\mathrm{J\,m^{-3}\,K^{-1}}$
Thermal conductivity pipe	0.4	$\mathrm{W\,m^{-1}\,K^{-1}}$
Ground properties		
Average thermal conductivity	1.9	$\mathrm{W\,m^{-1}\,K^{-1}}$
Average volumetric heat capacity	2 052 000	$\mathrm{J\,m^{-3}\,K^{-1}}$
Undisturbed ground temperature	15.0	°C

5.4 Results

5.4.1 Fluid temperatures and BHE loads

We use the scenario with one pair of connection pipes and the 2D numerical ground model with homogeneous properties for the comparison of the pipe models. Figure 5.9 shows the calculated fluid temperatures at the heat pump for a randomly selected section of approximately 15 h during cooling operation. For both the 30 m connection pipe (Fig. 5.9, top) and the 60 m connection pipe (Fig. 5.9, bottom), the calculated fluid temperatures are similar for all pipe models. The left part of Figure 5.9, however, shows the first 30 min after the ground source heat pump starts to operate. Here, differences between the transient numerical pipe model and the two steady state models become apparent. In the numerical model, the actual travel time of the fluid through the connection pipes is considered correctly. Therefore it takes longer for the outlet temperature to change, as the fluid in the pipe, which has the same temperature as the surrounding soil, is first pushed to the outlet. This delay is exactly twice as long for 60 m pipe length as for the 30 m pipe length (Fig. 5.9, left).

To quantify the influence of the pipe models on the long term operation of the BHE and the heat pump, average fluid temperatures $\overline{T}_{\mathrm{f,HP}}$ at the heat pump and the energy exchanged between BHE and ground Q_{BHE} are investigated for a period of 5 years (Figure 5.10). The evaluation is carried out separately for heating and cooling operation. $\overline{T}_{\mathrm{f,HP}}$ is the annual average of the mean of the fluid temperatures entering and exiting the heat pump.

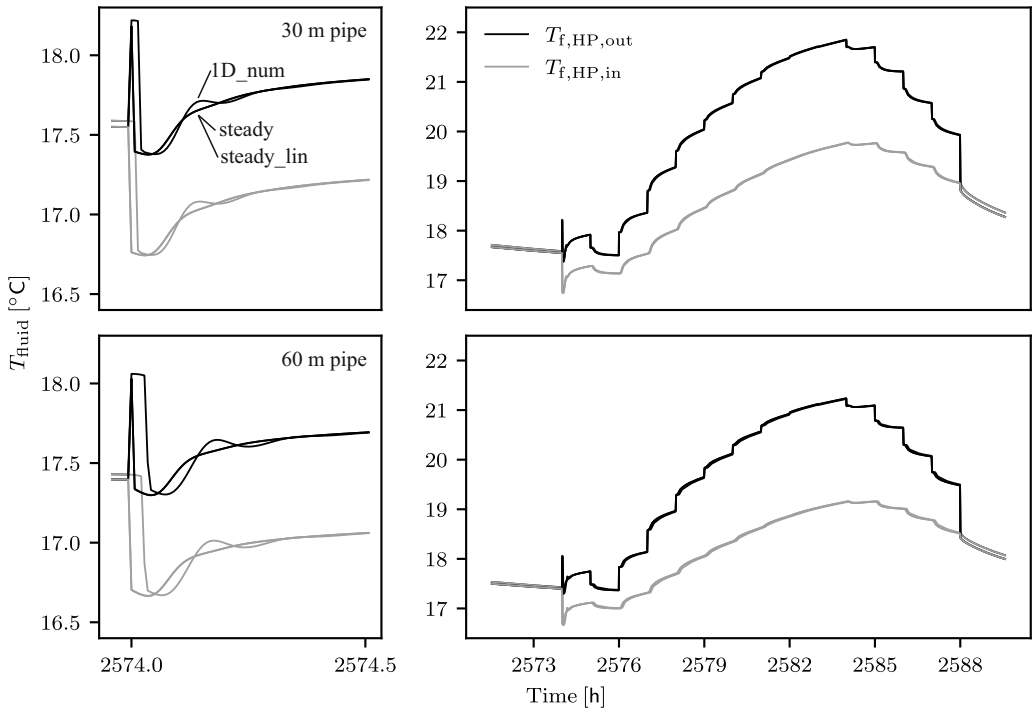

Figure 5.9 Comparison of the pipe models in combination with the 2D numerical ground model with homogenous properties for 30 m (top) and 60 m (bottom) pipe lengths.

The long term observation also reveals no relevant differences between the models in terms of temperature. For the scenarios with 60 m pipes, the average fluid temperatures for both heating and cooling are 0.2-0.3 K lower than for the 30 m pipes which are around 0.4 K lower than for the reference case with no horizontal connection pipes. These seeimingly small variations in temperature may have significant thermal energy variations implications, particularly during the 25+ years life-span of HVAC systems.

During the cooling operation, the energy injected into the ground per year through the BHE decreases from 7.7 MW h (reference case without pipes) to 7.3 MW h for the case with 30 m connection pipes and to 7.1 MW h for the case with 60 m pipes in the fifth year of operation. For heating operation, the energy extracted through the BHE increases from 0.7 MW h to just under 1 MW h for 30 m connection pipe length and to 1.2 MW h for 60 m connection pipe length. The absolute energy losses along the connection pipes are comparable for heating and cooling operation. However, comparted to the reference case, the relative increase for the heating operation is significantly higher. The evaluation of the annual average values shows that the short-term differences between the transient numerical model and the stationary models have no influence on parameters relevant for plant design. For this application, all investigated pipe models are therefore equally well suited.

A first comparison of the ground models is carried out using the scenarios with the 1D numerical pipe model and 30 m connection pipe length. Figure 5.11 shows a section of the

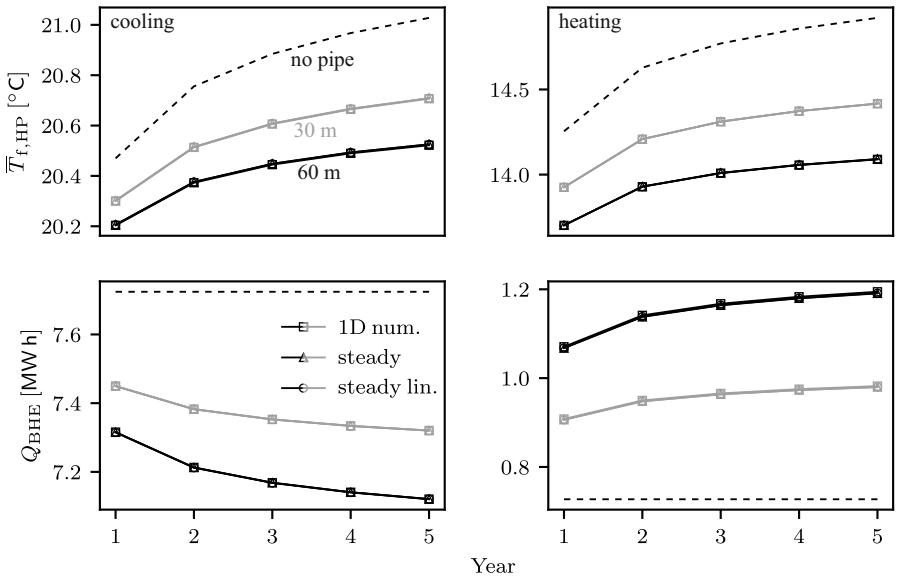

Figure 5.10 Effect of the pipe models on the annually averaged fluid temperatures (top) and on the amount of energy exchanged by BHE (bottom) separately for cooling (left) and heating (right).

calculated fluid temperatures. With the exception of the soil resistance model (R_s), the deviations between all models are relatively small. As expected, the FLS model and the numerical 2D model with homogeneous properties (2D) produce almost identical results. The difference to the numerical 2D model with inhomogeneous properties (2Di) increases with continued operation and larger loads, but remains below 0.2 K within the shown period. The fluid temperatures calculated with the soil resistance model are almost 2 K below all other models. During the first 2500 h of operation, both inlet and outlet temperatures are in any model higher than the undisturbed ground temperature around the connection pipes. This leads to a heat accumulation in the ground, resulting in higher fluid temperatures for the models accounting for heat accumulation.

Figure 5.12 shows the long-term evaluation of the ground models similar to Figure 5.10. Regardless of the pipe length no visible differences between the 2D numerical model with homogeneous properties and the FLS model for both the fluid temperatures and the exchanged energy can be observed. During cooling operation, the difference in mean fluid temperature between the inhomogeneous and homogeneous 2D models in the 5th year is about 0.05 K for both pipe lengths, while for the heating operation it is 0.2 K. The difference between 30 m and 60 m pipe is not more than 0.3 K for any ground model. The most significant deviation from all other models as well as from the reference case is produced by the soil resistance model. For example, for the 30 m pipe model, the mean fluid temperature during the cooling operation is 1 K lower as in the reference case without any pipes, while it is 1.5 K lower for the heating operation.

The difference between the homogeneous and inhomogeneous model in cooling operation is less than 0.05 MW h per year for both pipe lengths tested. Q_{BHE} calculated with the R_s

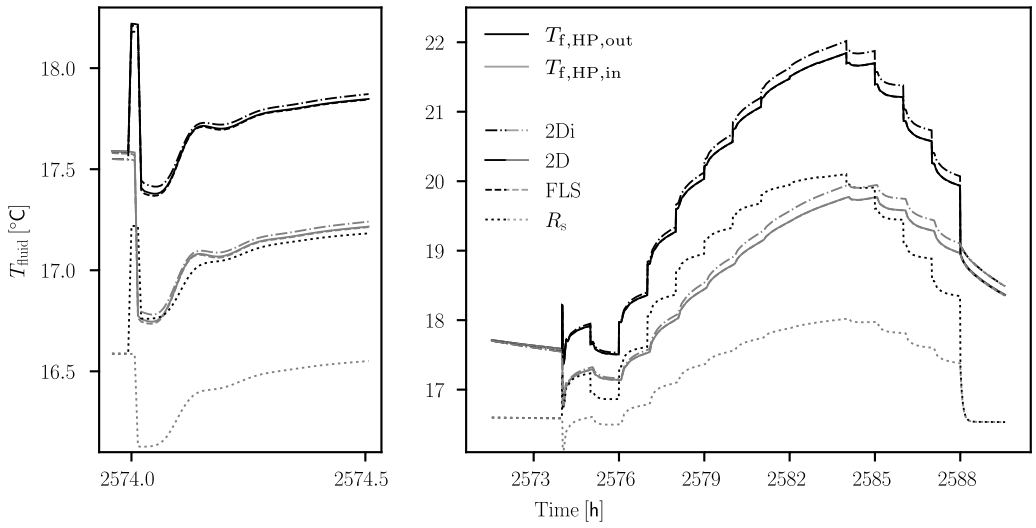

Figure 5.11 Comparison of the ground models in combination with the 1D numerical pipe model for 30 m pipe length during a day after the first 100 days of operation of the GSHP system.

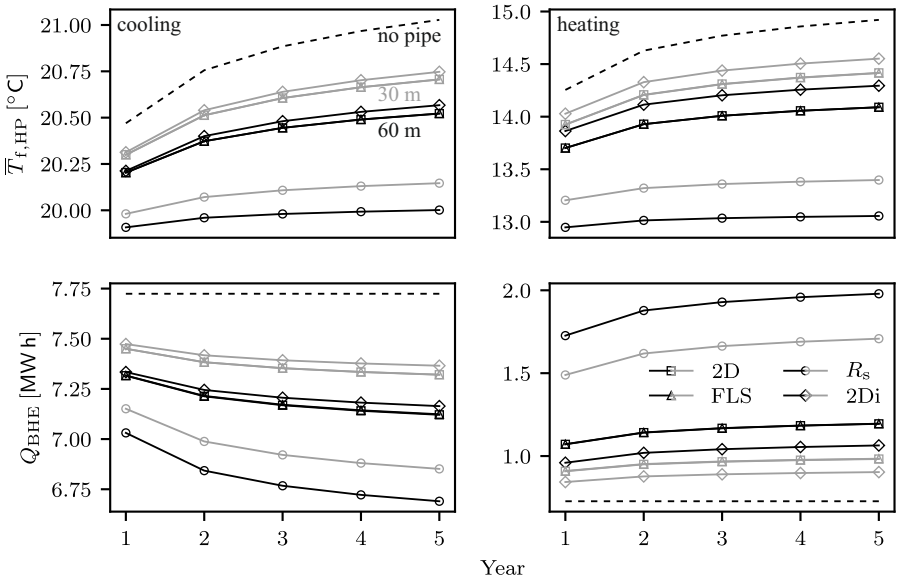

Figure 5.12 Effect of the ground models on the annually averaged fluid temperatures (top) and on the amount of energy exchanged by BHE (bottom) separately for cooling (left) and heating (right) for a 30 m (grey) and 60 m horizontal connection pipe.

model is approx. 0.5 MW h below the other models for cooling and 0.7 MW h above them for heating.

In addition to the fluid temperatures and the energy exchanged through the BHE, we can also compare the ground temperatures calculated with the different models. The comparison is made at the following events: the maximum heating and cooling load as well as the end of the heating and cooling period. Figure 5.13 shows the temperature profile along a horizontal section at the depth of the connection pipes, while Figure 5.14 shows a vertical section between the supply and return pipe.

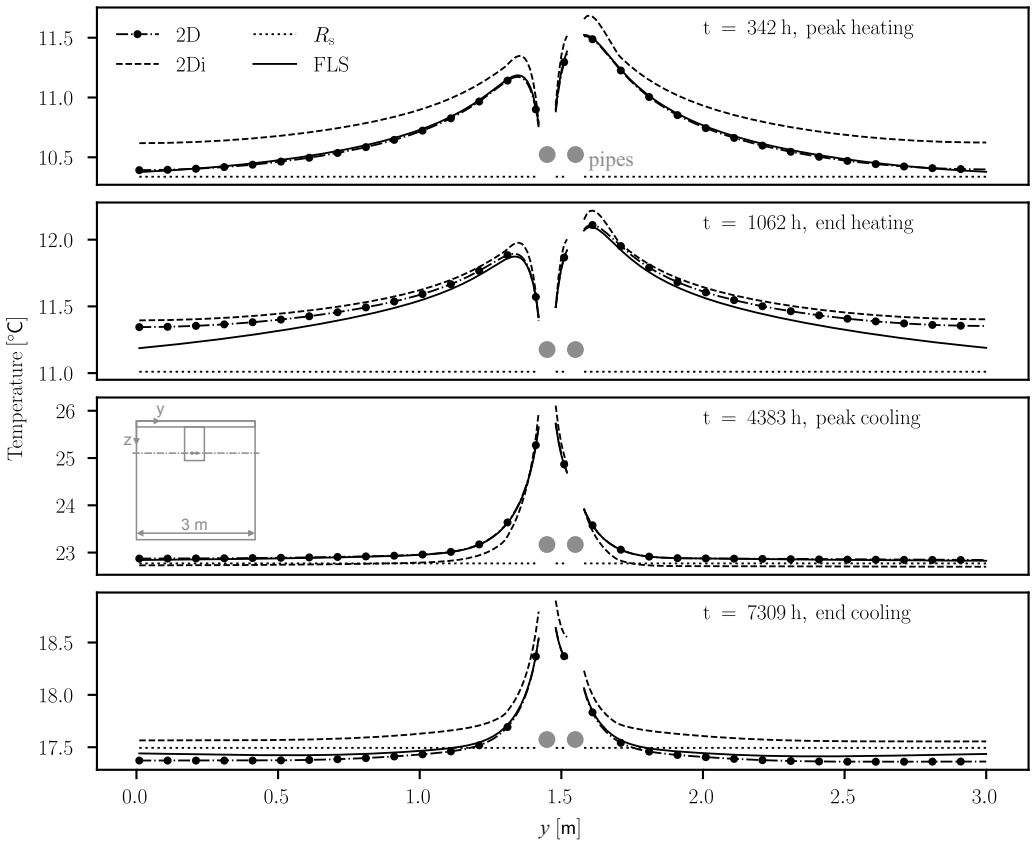

Figure 5.13 Horizontal temperature profile at the depth of the connection pipes at selected times during the first year of operation, calculated with the 1D numerical pipe model for 30 m pipe length.

Since in the soil resistance model (R_s) the ground temperature is not influenced by the pipes, it corresponds to the undisturbed ground temperature. The temperatures calculated with the FLS model and the homogeneous 2D model are largely congruent. One exception are the temperature profiles in the horizontal section at the end of the heating period (Figure 5.13, second from top). Here the temperatures diverge with increasing distance from the pipes. This indicates that the dimensions of the numerical model were chosen too small, as the temperature increase at the boundary of the model is higher than in the FLS model. For the analysis of the fluid temperatures and the BHE operation, however, this has no influence, as previously shown. The biggest change in the undisturbed ground temperature occurs within the selected times at the time of the maximum cooling load with more than 3 K (Figure 5.13, third from top).

The investigations on a single BHE with connection pipes of 30 and 60 m length have shown that there are no significant differences with regard to the average fluid temperatures and BHE loads for the different ground models, with the exception of the soil resistance model. For homogeneous soil conditions, the FLS model and the 2D numerical model deliver identical results; for the numerical model, the geometry must be sufficiently large to ensure accurate

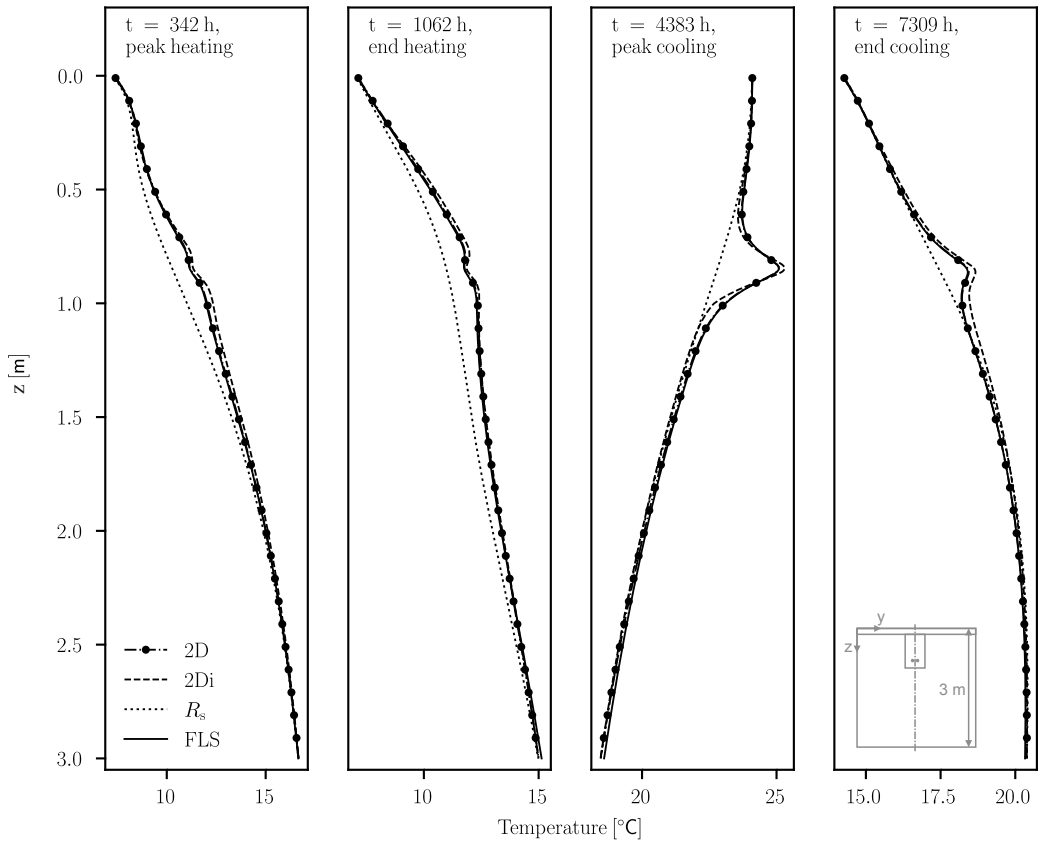

Figure 5.14 Vertical temperature profile between the supply and return pipe at selected times during the first year of operation, calculated with the 1D numerical pipe model for 30 m pipe length.

results. For the scenario with the inhomogeneous soil conditions, the calculated temperatures deviate as expected, but the influence on the average fluid temperatures and BHE loads is negligible for the parameters investigated and a design-oriented view. The results of all model combinations for one pair of connection pipes are given in 5.7.

For the scenarios with 6 BHEs, leading to 12 horizontal connection pipes in the same trench, nothing new is expected with regard to differences between the pipe models, therefore they are not discussed in more detail. Figure 5.15 shows the evaluation for the fluid temperatures at the heat pump analogous to Figure 5.11.

The heat pump inlet temperature is the average from all 6 BHE return connection pipes, the same applies for the BHE loads. Compared to the simulations with only one BHE, the difference between the homogeneous ground model and the inhomogeneous ground model is significantly lower with 6 BHEs. This is probably due to the fact that the distance of many pipes to the natural ground is smaller than in the simulation with only one BHE (Figure 5.7). Furthermore, the fluid temperatures in all models except the soil resistance model are slightly higher (0.3 K) as in the case with one pair of pipes. The comparison with the

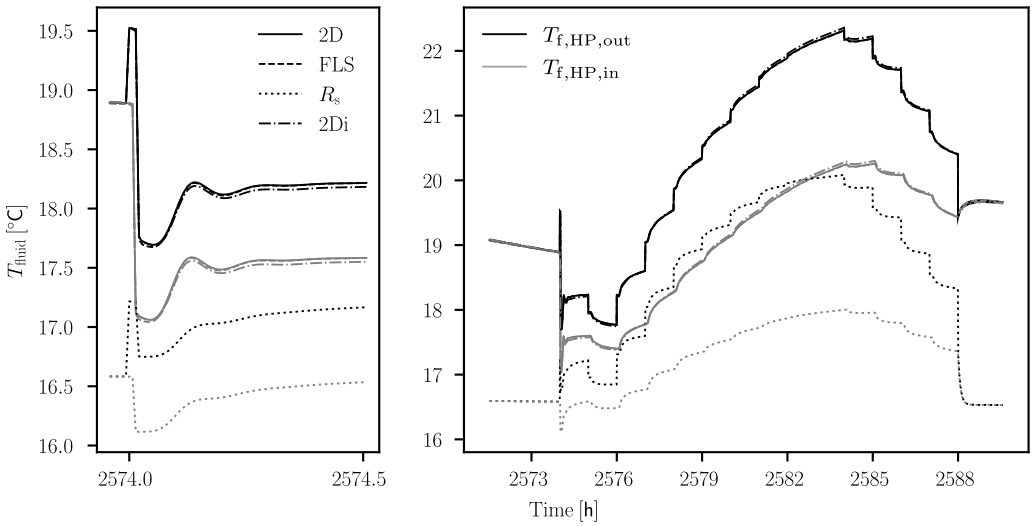

Figure 5.15 Comparison of the ground models in combination with the 1D numerical pipe model for 30 m pipe length for the connection pipes of 6 BHEs in a shared trench.

reference case (no connection pipes) in Figure 5.16 reveals that multiple pipes reduce the effect of the connection pipes.

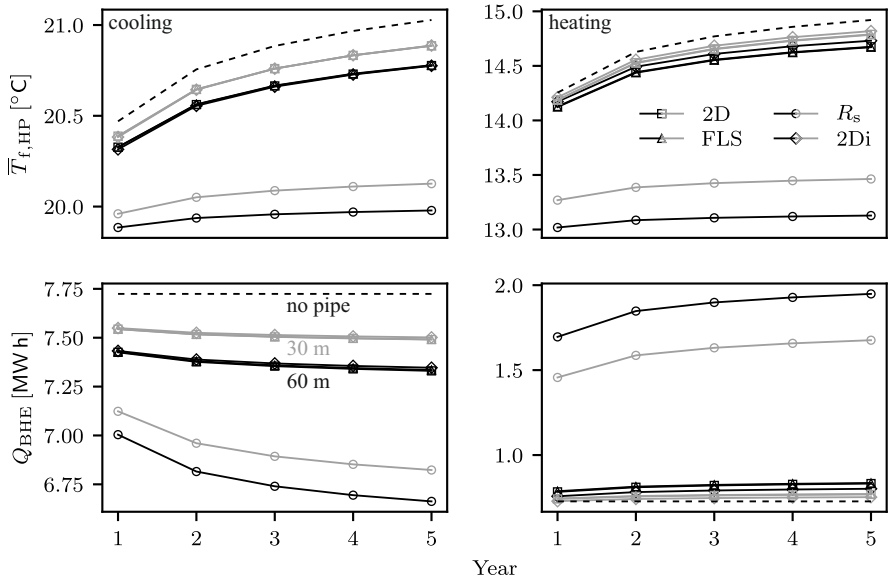

Figure 5.16 Effect of the ground models on the annually averaged fluid temperatures (top) and on the amount of energy exchanged by BHE (bottom) separately for cooling (left) and heating (right) for the connection pipes of 6 BHEs in a shared trench.

Comparing Figure 5.16 and Figure 5.12 shows that for 6 pairs of pipes the values are much closer to the reference case for all models except the soil resistance model. By placing the pipes close together, each pipe has less thermally undisturbed soil volume around it, leading to a reduced heat exchange with the surrounding soil. This is also visible in the horizontal section through the middle row of pipes in Figure 5.17: the inner return pipes are shielded

by the outer supply pipes and are influenced by them more than by the undisturbed ground temperature.

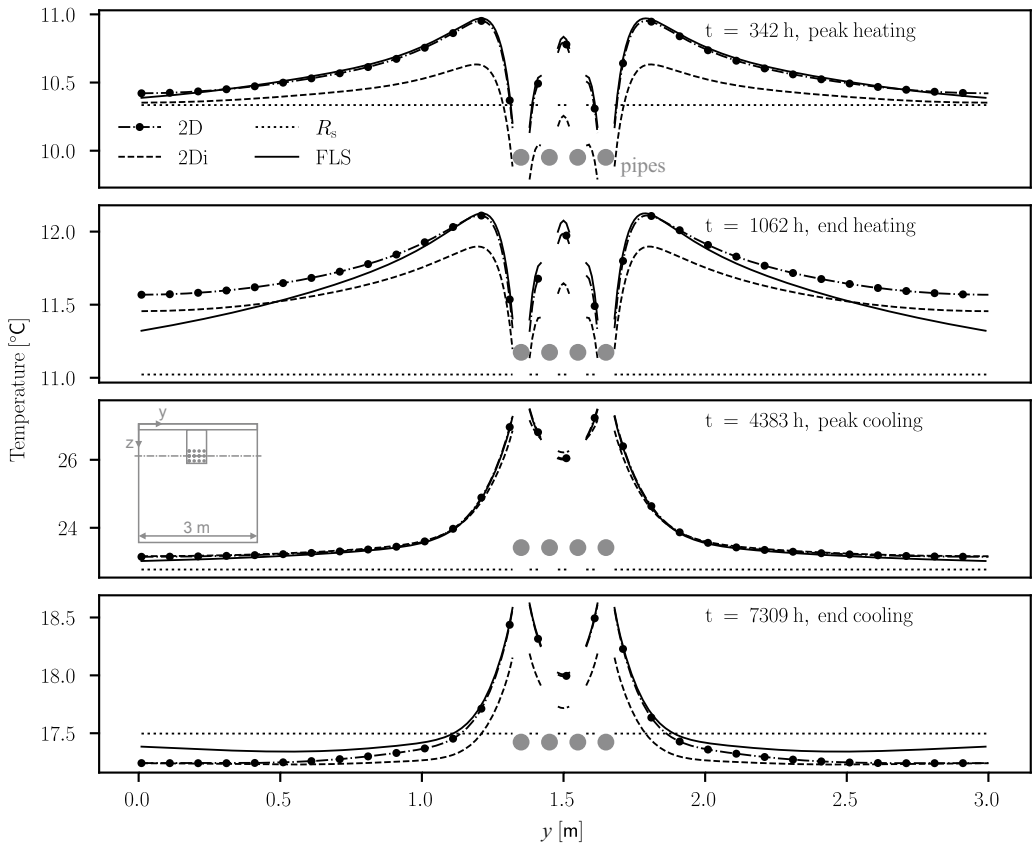

Figure 5.17 Horizontal temperature profile at the depth of the connection pipes at selected times during the first year of operation, calculated with the 1D numerical pipe model for 30 m pipe length and 6 BHEs.

Figure 5.18 shows the temperature profiles for a vertical section between the pipes. The results of all model combinations for six pairs of connection pipes are presented in Table 5.8.

The comparison of the ground models has shown that both FLS and the 2D numerical model are well suited for the application investigated in this work. Both models deliver identical results for homogeneous soil conditions for both pipe lengths investigated. Inhomogeneous soil conditions cannot be covered with the FLS model; the extent of their influence on the results depends on the actual conditions. In the example shown here, temperature accumulations occurred in the ground due to heat exchange with the connection pipes. The accumulations are not considered in the soil resistance model, leading to significant deviations that do not reflect reality. The arrangement of several connection pipes in a shared trench has shown that the heat exchange per pipe decreases significantly, leading to a reduced effect of the connection pipes on the heat pump and BHE operation altogether.

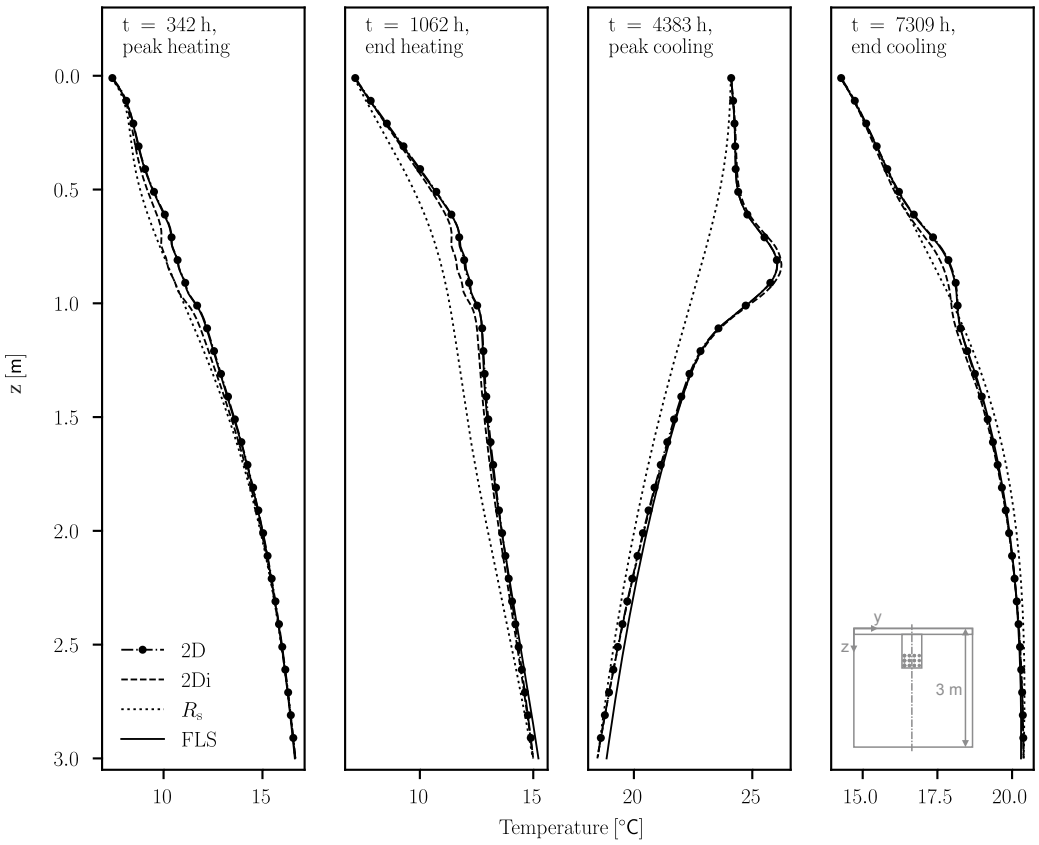

Figure 5.18 Vertical temperature profile between the supply and return pipe at selected times during the first year of operation, calculated with the 1D numerical pipe model for 30 m pipe length and 6 BHEs.

5.4.2 Computational effort

The comparison of the computational effort of the different models is carried out with the help of measured computational times where the processing unit is an Intel i7-7700K processor at 4200 MHz, 16 GB of RAM and Windows version 10. It is difficult to perform a fair and general comparison, as among the investigated models are both analytical, and thus discretization independent, and numerical models whose computational effort depends on the spatial discretization. Another influencing factor is the implementation. All models were implemented in Python to the best of our knowledge, but the authors are not professional programmers. The results shown are therefore only rough indications. Table 5.5 shows the computational times for the three pipe models in combination with the soil resistance model for a simulation time of one year at a time step of 25 s for a 60 m pipe. The computational times increase according to the complexity of the models.

The results for the different ground models are listed in Table 5.6. Again, the computational times increase with the complexity of the models. Due to the temporal and spatial superposition in the FLS model, the computational effort increases exponentially with the increasing number of time steps as well as increasing number of pipes. Comparing the times of the 1 BHE and 6 BHE simulations shows a factor of 7.5 for the soil resistance model, 24.5 for the

Table 5.5 Computational times for a one year simulation for the different pipe models in combination with the soil resistance model.

model combination	comp. time
R_s + steady lin.	200 s
R_s + steady	231 s
R_s + 1Dnum	278 s

Table 5.6 Computational times for a one year simulation for the different ground models in combination with the steady state linear pipe model.

model combination	comp. time 1 BHE	comp. time 6 BHEs
R_s + steady lin.	200 s	1563 s
FLS + steady lin.	396 s	9722 s
2D + steady lin.	6573 s	19 458 s

FLS model and 3 for 2D numerical model. If more pipes are added or the number of time steps is increased, the 2D numerical model might perform better than the FLS model in terms of efficiency.

5.4.3 Proposed model

The study has shown that the steady state pipe model and the FLS ground model are sufficient for many cases. The BHE can be modeled with a similar approach (Eskilson, 1987):

$$T_{f,BHE,in}(t) = \overline{T}_f(t) + \frac{l_b q_b(t)}{2\dot{V}\rho c_f} \tag{5.29}$$

$$T_{f,BHE,out}(t) = \overline{T}_f(t) - \frac{l_b q_b(t)}{2\dot{V}\rho c_f} \tag{5.30}$$

$$\overline{T}_f(t) = q_b(t) R_b + T_b(t) \tag{5.31}$$

$$T_b(t_k) = T_{0,b} + \frac{1}{2\pi\lambda_s} \sum_{i=1}^{k} \Delta q_b(t_i) \cdot g_b(t_{k-i+1}). \tag{5.32}$$

Here, T_b denotes the borehole wall temperature, $T_{0,b}$ the undisturbed ground temperature of the borehole and q_b the stepwise constant borehole load divided by its length l_b. $\Delta q_b(t_i) = q_b(t_i) - q_b(t_{i-1})$ defines the load increment of each time step. g_b is the borehole g-function, $\overline{T}_f$ the average of the borehole inlet and outlet fluid temperatures, $\dot{V}$ is the volume flow and ρc_f

the volumetric heat capacity of the fluid. The borehole resistance R_b is the effective thermal resistance of the BHE (Javed and Spitler, 2016).

Rewriting the equations for the steady state pipe model combined with the FLS ground model leads for the case of one pair of connection pipes to:

$$q_\mathrm{p1}(t) = \Big[T_\mathrm{f,BHE,in}(t) - T_\mathrm{s1}(t)\Big]\Big(R_\mathrm{fs} - \frac{l_\mathrm{p}}{2\dot{V}\rho c_\mathrm{f}}\Big)^{-1} \tag{5.33}$$

$$q_\mathrm{p2}(t) = \Big[T_\mathrm{f,BHE,out}(t) - T_\mathrm{s2}(t)\Big]\Big(R_\mathrm{fs} + \frac{l_\mathrm{p}}{2\dot{V}\rho c_\mathrm{f}}\Big)^{-1} \tag{5.34}$$

and:

$$T_\mathrm{s1}(t_k) = T_\mathrm{0,s1}(t_k) + \sum_{i=1}^{k} \Delta q_\mathrm{p1}(t_i) \cdot g_\mathrm{p11}(t_{k-i+1}) + \Delta q_\mathrm{p2}(t_i) \cdot g_\mathrm{p21}(t_{k-i+1}) \tag{5.35}$$

$$T_\mathrm{s2}(t_k) = T_\mathrm{0,s2}(t_k) + \sum_{i=1}^{k} \Delta q_\mathrm{p2}(t_i) \cdot g_\mathrm{p22}(t_{k-i+1}) + \Delta q_\mathrm{p1}(t_i) \cdot g_\mathrm{p12}(t_{k-i+1}). \tag{5.36}$$

Here index 1 corresponds to the supply pipe while 2 corresponds to the return pipe. q_p are the loads of the pipes divided by the pipe length l_p while $\Delta q_\mathrm{p}(t_i) = q_\mathrm{p}(t_i) - q_\mathrm{p}(t_{i-1})$ defines the load increment for each time step. T_s is the soil temperature at the outside of the the pipes. The first index at the pipes g-function g_p corresponds to the heat source and the second to the surface of interest (Figure 5.4).

The total load of the system of borehole and connection pipes Q_tot is defined as:

$$Q_\mathrm{tot}(t) = q_\mathrm{p2}(t)l_\mathrm{p} + q_\mathrm{p1}(t)l_\mathrm{p} + q_\mathrm{b}(t)l_\mathrm{b}. \tag{5.37}$$

Combining Equations 5.29-5.37 into one matrix equation leads to:

$$\boldsymbol{A} \cdot \boldsymbol{B} = \boldsymbol{C} \tag{5.38}$$

with:

$$\boldsymbol{A} = \begin{bmatrix} 0 & 0 & -g_{\mathrm{b}}(\Delta t) & 0 & 0 & 0 & 0 & 0 & 1 \\ 0 & 0 & R_{\mathrm{b}} & 0 & 0 & 0 & 0 & -1 & 1 \\ 0 & 0 & +c_3 & 0 & 0 & -1 & 0 & 1 & 0 \\ 0 & 0 & -c_3 & 0 & 0 & 0 & -1 & 1 & 0 \\ -c_1 & 0 & 0 & -1 & 0 & c_1 & 0 & 0 & 0 \\ 0 & -c_2 & 0 & 0 & -1 & 0 & c_2 & 0 & 0 \\ 1 & 0 & 0 & -g_{\mathrm{p11}}(\Delta t) & -g_{\mathrm{p21}}(\Delta t) & 0 & 0 & 0 & 0 \\ 0 & 1 & 0 & -g_{\mathrm{p12}}(\Delta t) & -g_{\mathrm{p22}}(\Delta t) & 0 & 0 & 0 & 0 \\ 0 & 0 & l_{\mathrm{b}} & l_{\mathrm{p}} & l_{\mathrm{p}} & 0 & 0 & 0 & 0 \end{bmatrix} \tag{5.39}$$

$$\boldsymbol{B} = \begin{bmatrix} T_{\mathrm{s1}}(t_i) \\ T_{\mathrm{s2}}(t_i) \\ q_{\mathrm{b}}(t_i) \\ q_{\mathrm{p1}}(t_i) \\ q_{\mathrm{p2}}(t_i) \\ T_{\mathrm{f,BHE,in}}(t_i) \\ T_{\mathrm{f,BHE,out}}(t_i) \\ \overline{T_{\mathrm{f}}}(t_i) \\ T_{\mathrm{b}}(t_i) \end{bmatrix} \tag{5.40}$$

$$\boldsymbol{C} = \begin{bmatrix} \widetilde{T}_{\mathrm{b}}(t_i) - q_{\mathrm{b}}(t_{i-1}) g_{\mathrm{b}}(\Delta t) \\ 0 \\ 0 \\ 0 \\ 0 \\ 0 \\ \widetilde{T}_{\mathrm{s1}}(t_i) - q_{\mathrm{p1}}(t_{i-1}) g_{11}(\Delta t) - q_{\mathrm{p2}}(t_{i-1}) g_{21}(\Delta t) \\ \widetilde{T}_{\mathrm{s2}}(t_i) - q_{\mathrm{p2}}(t_{i-1}) g_{22}(\Delta t) - q_{\mathrm{p1}}(t_{i-1}) g_{12}(\Delta t) \\ Q_{\mathrm{tot}}(t) \end{bmatrix} \tag{5.41}$$

and:

$$c_1 = \frac{1}{R_{\mathrm{fs}} - \frac{l_{\mathrm{p}}}{2\dot{V}\rho c_{\mathrm{f}}}} \tag{5.42}$$

$$c_2 = \frac{1}{R_{\mathrm{fs}} + \frac{l_{\mathrm{p}}}{2\dot{V}\rho c_{\mathrm{f}}}} \tag{5.43}$$

$$c_3 = \frac{l_{\mathrm{b}}}{2\dot{V}\rho c_{\mathrm{f}}}. \tag{5.44}$$

Equation 5.38 needs to be solved for $\boldsymbol{B}$ at each timestep t_i with a step size Δt. The temperatures in $\boldsymbol{C}$ are marked with a tilde as these are the initial undisturbed ground temperatures plus the temperature changes due to the previous time steps. These temperatures need to be updated according to the load increments of the current time step i for all future time steps $k > i$:

$$\widetilde{T}_{\mathrm{b}}(t_k)^{\mathrm{new}} = \widetilde{T}_{\mathrm{b}}(t_k)^{\mathrm{old}} + \Delta q_{\mathrm{b}}(t_i) \cdot g_{\mathrm{b}}(t_{k-i}) \tag{5.45}$$

$$\widetilde{T}_{\mathrm{s1}}(t_k)^{\mathrm{new}} = \widetilde{T}_{\mathrm{s1}}(t_k)^{\mathrm{old}} + \Delta q_{\mathrm{p1}}(t_i) \cdot g_{\mathrm{p11}}(t_{k-i}) + \Delta q_{\mathrm{p2}}(t_i) \cdot g_{\mathrm{p21}}(t_{k-i}) \tag{5.46}$$

$$\widetilde{T}_{\mathrm{s2}}(t_k)^{\mathrm{new}} = \widetilde{T}_{\mathrm{s2}}(t_k)^{\mathrm{old}} + \Delta q_{\mathrm{p2}}(t_i) \cdot g_{\mathrm{p22}}(t_{k-i}) + \Delta q_{\mathrm{p1}}(t_i) \cdot g_{\mathrm{p12}}(t_{k-i}). \tag{5.47}$$

For the simulation of additional BHEs and connecting pipes, the system of equations can be arbitrarily expanded. In contrast to many of the previous investigated model combinations, the proposed model requires no spatial discretization or internal iterations for the coupling, making it easy to implement and more efficient to run. The part for the horizontal pipes in the proposed model corresponds to the *FLS + steady state linear* combination. The computational time for the proposed model for the one year simulation is with just 205 s for one BHE almost halved (Table 5.6). Considering that the computational times listed in Table 5.6 do not include the computational time for the BHE model, which is in already included in the mentioned 205 s, the savings with the new formulation are even higher. For the simulation with 6 BHEs the new model needs just 10 023 s (again, including the BHEs) which is only little more than just the horizontal pipes model for this case (Table 5.6).

Figure 5.19 shows a comparison of the fluid temperatures calculated with the coupled hybrid approach used in the previous sections and the steady state model (Eq. 5.38) for a 30 m connection pipe.

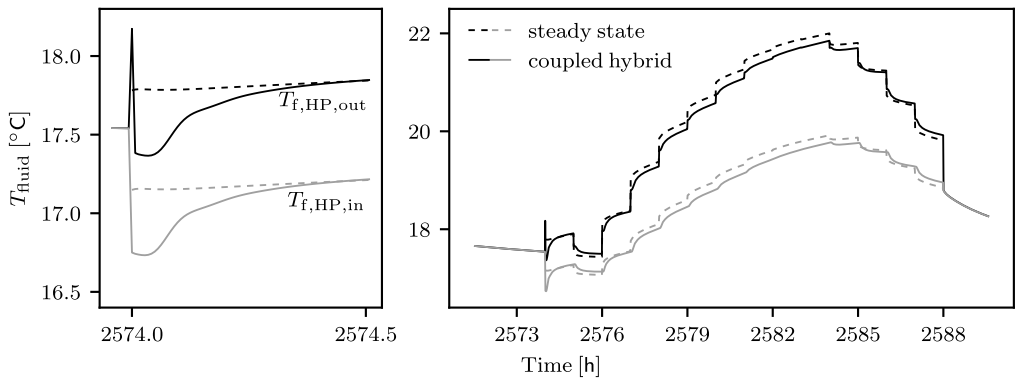

Figure 5.19 Fluid temperature calculated with the proposed steady state approach and the coupled FLS ground and steady state pipe model for a 30 m connection pipe.

The differences are caused by the heat capacity of the borehole, which is not taken into account in the steady state model. For loads that are constant over a longer period of time, both models will converge as the steady state assumption within the borehole underlying the borehole resistance approach becomes true. Figure 5.20 shows the analysis of average fluid temperatures and BHE load for the same scenario. The model is considered well suited for all scenarios where the influence of the borehole heat capacity is negligible.

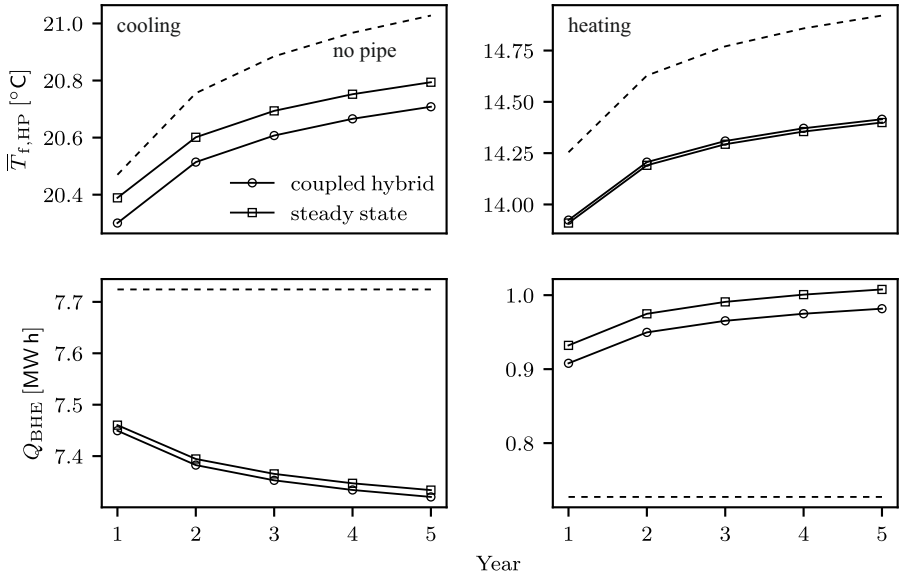

Figure 5.20 Comparison between the proposed steady state approach and the coupled FLS ground and steady state pipe model for a 30 m connection pipe.

5.5 Conclusions

In this study, three pipe models and three ground models were combined with each other to create connection pipe models for the investigation of heat losses in connection pipe networks in BHE installations. These were coupled with a BHE model and a highly simplified heat pump model. Scenarios with one and six pipe pairs with lengths of 30 and 60 m were simulated for a period of 5 years.

The steady-state pipe models with exponential and linear temperature profiles provide identical results for the investigated fluid temperatures and BHE loads. For the transient numerical pipe model, deviations occur for the short-term behaviour after control events of the heat pump. However, these have no effect on the overall assessment of BHE operation.

The numerical ground model with homogeneous properties and the FLS model provide almost identical results. The analysis of the temperature field in the ground has shown that the dimensions of the numerical model were chosen too small, which, however, did not have a

significant influence on the parameters investigated. The deviations between the two models mentioned and the numerical model with inhomogeneous properties depend on the actual properties. For the case chosen as an example here, however, it was shown that the differences between the two scenarios were rather small. The soil resistance model does not take into account temperature accumulation in the ground, nor the thermal interference of multiple pipes. This leads to significant deviations compared to the other models while overestimating the heat exchange along the connecting pipes.

Interestingly, during the simulation of six pairs of pipes in a shared trench and due to the bundled arrangement of the pipes and the thermal interference, the heat exchange per pipe with the surrounding ground decreased significantly. While the BHE heat load with one pair of 30 m pipes was increased by 40 % due to the heat transfer along the connection pipes, it was always 10 % for the case with six pairs of pipes. For the cooling loads, which are the dominant loads in the investigated scenario, the BHE load was reduced by 5 % with one pair of pipes and only 2.6 % with six pairs of pipes.

With regard to the computational effort, the steady state linear model is the most efficient of all pipe models, followed by the steady state and the 1D numerical model. The FLS model required less computational time than the 2D numerical ground model, however this is only valid for the chosen model size and discretization. Furthermore, it should be noted that for the FLS model, due to the spatial and temporal superposition, the computational effort increases exponentially with increasing number of time steps as well as with increasing number of pipes.

The proposed steady state model combines the findings from the previous comparison. By combining the well established borehole resistance approach for the BHE with a model of similar simplicity for the connection pipes, the model allows for an easy estimation of the load distribution between BHE and connection pipes for all cases in which the influence of the borehole heat capacity and short-time effects are negligible. The model can be simply extended to an arbitrary number of BHEs and connection pipes. For more complex pipe paths or inhomogeneous soil conditions, the pipe g-functions may need to be calculated numerically. However, once calculated they can be used within the proposed model for a variety of studies with different loads or thermal boundary conditions. In future work, we will use the model to investigate different climatic conditions.

5.6 Appendix

Table 5.7 Compilation of all calculation results for the simulation of one pair of connection pipes.

			1st year				2nd year				3rd year				4th year				5th year			
			T_c	T_h	Q_c	Q_h	T_c	T_h	Q_c	Q_h	T_c	T_h	Q_c	Q_h	T_c	T_h	Q_c	Q_h	T_c	T_h	Q_c	Q_h
	no pipe		20.5	14.3	7.7	0.7	20.8	14.6	7.7	0.7	20.9	14.8	7.7	0.7	21.0	14.9	7.7	0.7	21.0	14.9	7.7	0.7
2Dnum hetero	1Dnum	30 m	20.3	14.0	7.47	0.84	20.5	14.3	7.42	0.88	20.6	14.4	7.39	0.89	20.7	14.5	7.38	0.9	20.7	14.6	7.37	0.9
		60 m	20.2	13.9	7.33	0.96	20.4	14.1	7.24	1.02	20.5	14.2	7.21	1.04	20.5	14.3	7.18	1.05	20.6	14.3	7.16	1.06
	Steady	30 m	20.3	14.0	7.47	0.84	20.5	14.3	7.42	0.87	20.6	14.4	7.39	0.89	20.7	14.5	7.38	0.9	20.8	14.6	7.37	0.9
		60 m	20.2	13.9	7.33	0.96	20.4	14.1	7.25	1.01	20.5	14.2	7.21	1.04	20.5	14.3	7.18	1.05	20.6	14.3	7.17	1.06
	SteadyLin	30 m	20.3	14.0	7.47	0.84	20.5	14.3	7.42	0.87	20.6	14.4	7.39	0.89	20.7	14.5	7.38	0.9	20.8	14.6	7.37	0.9
		60 m	20.2	13.9	7.33	0.96	20.4	14.1	7.25	1.02	20.5	14.2	7.21	1.04	20.5	14.3	7.18	1.05	20.6	14.3	7.17	1.06
2Dnum homo	1Dnum	30 m	20.3	13.9	7.45	0.91	20.5	14.2	7.38	0.95	20.6	14.3	7.35	0.97	20.7	14.4	7.33	0.98	20.7	14.4	7.32	0.98
		60 m	20.2	13.7	7.32	1.07	20.4	13.9	7.21	1.14	20.4	14.0	7.17	1.17	20.5	14.1	7.14	1.18	20.5	14.1	7.12	1.19
	Steady	30 m	20.3	13.9	7.45	0.91	20.5	14.2	7.38	0.95	20.6	14.3	7.35	0.96	20.7	14.4	7.33	0.97	20.7	14.4	7.32	0.98
		60 m	20.2	13.7	7.32	1.07	20.4	13.9	7.21	1.14	20.4	14.0	7.17	1.16	20.5	14.1	7.14	1.18	20.5	14.1	7.12	1.19
	SteadyLin	30 m	20.3	13.9	7.45	0.91	20.5	14.2	7.38	0.95	20.6	14.3	7.35	0.96	20.7	14.4	7.33	0.97	20.7	14.4	7.32	0.98
		60 m	20.2	13.7	7.31	1.07	20.4	13.9	7.21	1.14	20.4	14.0	7.17	1.16	20.5	14.1	7.14	1.18	20.5	14.1	7.12	1.19
FLS	1Dnum	30 m	20.3	13.9	7.45	0.91	20.5	14.2	7.38	0.95	20.6	14.3	7.35	0.97	20.7	14.4	7.33	0.98	20.7	14.4	7.32	0.98
		60 m	20.2	13.7	7.32	1.07	20.4	13.9	7.22	1.14	20.4	14.0	7.17	1.17	20.5	14.1	7.14	1.18	20.5	14.1	7.12	1.2
	Steady	30 m	20.3	13.9	7.45	0.91	20.5	14.2	7.38	0.95	20.6	14.3	7.35	0.97	20.7	14.4	7.33	0.97	20.7	14.4	7.32	0.98
		60 m	20.2	13.7	7.32	1.07	20.4	13.9	7.21	1.14	20.4	14.0	7.17	1.16	20.5	14.1	7.14	1.18	20.5	14.1	7.12	1.19
	SteadyLin	30 m	20.3	13.9	7.45	0.91	20.5	14.2	7.38	0.95	20.6	14.3	7.35	0.97	20.7	14.4	7.33	0.97	20.7	14.4	7.32	0.98
		60 m	20.2	13.7	7.32	1.07	20.4	13.9	7.21	1.14	20.4	14.0	7.17	1.17	20.5	14.1	7.14	1.18	20.5	14.1	7.12	1.19
R_{soil}	1Dnum	30 m	20.0	13.2	7.15	1.49	20.1	13.3	6.99	1.62	20.1	13.4	6.92	1.66	20.1	13.4	6.88	1.69	20.1	13.4	6.85	1.71
		60 m	19.9	12.9	7.03	1.73	20.0	13.0	6.84	1.88	20.0	13.0	6.77	1.93	20.0	13.0	6.72	1.96	20.0	13.1	6.69	1.98
	Steady	30 m	20.0	13.2	7.15	1.49	20.1	13.3	6.99	1.62	20.1	13.4	6.92	1.66	20.1	13.4	6.88	1.69	20.1	13.4	6.85	1.71
		60 m	19.9	12.9	7.03	1.73	20.0	13.0	6.84	1.88	20.0	13.0	6.77	1.93	20.0	13.0	6.72	1.96	20.0	13.1	6.69	1.98
	SteadyLin	30 m	20.0	13.2	7.15	1.49	20.1	13.3	6.99	1.62	20.1	13.4	6.92	1.66	20.1	13.4	6.88	1.69	20.1	13.4	6.85	1.71
		60 m	19.9	12.9	7.03	1.73	20.0	13.0	6.84	1.88	20.0	13.0	6.76	1.93	20.0	13.0	6.72	1.96	20.0	13.1	6.69	1.98

Table 5.8 Compilation of all calculation results for the simulation of six pairs of connection pipes.

			1st year				2nd year				3rd year				4th year				5th year			
			T_c	T_h	Q_c	Q_h	T_c	T_h	Q_c	Q_h	T_c	T_h	Q_c	Q_h	T_c	T_h	Q_c	Q_h	T_c	T_h	Q_c	Q_h
	no pipe		20.5	14.3	7.7	0.7	20.8	14.6	7.7	0.7	20.9	14.8	7.7	0.7	21.0	14.9	7.7	0.7	21.0	14.9	7.7	0.7
2Dnum hetero	1Dnum	30 m	20.4	14.2	7.55	0.73	20.6	14.6	7.53	0.74	20.8	14.7	7.51	0.75	20.8	14.8	7.51	0.75	20.9	14.8	7.5	0.75
		60 m	20.3	14.2	7.43	0.76	20.6	14.5	7.39	0.78	20.7	14.6	7.37	0.79	20.7	14.7	7.36	0.8	20.8	14.7	7.35	0.8
	Steady	30 m	20.4	14.2	7.55	0.73	20.6	14.6	7.53	0.74	20.8	14.7	7.51	0.75	20.8	14.8	7.51	0.75	20.9	14.8	7.5	0.75
		60 m	20.3	14.2	7.43	0.76	20.6	14.5	7.39	0.78	20.7	14.6	7.37	0.79	20.7	14.7	7.36	0.8	20.8	14.7	7.35	0.8
	SteadyLin	30 m	20.4	14.2	7.55	0.73	20.6	14.6	7.53	0.74	20.8	14.7	7.51	0.75	20.8	14.8	7.51	0.75	20.9	14.8	7.5	0.75
		60 m	20.3	14.2	7.43	0.76	20.6	14.5	7.39	0.78	20.7	14.6	7.37	0.79	20.7	14.7	7.36	0.8	20.8	14.7	7.35	0.8
2Dnum homo	1Dnum	30 m	20.4	14.2	7.54	0.74	20.6	14.5	7.52	0.76	20.8	14.7	7.5	0.76	20.8	14.7	7.5	0.77	20.9	14.8	7.49	0.77
		60 m	20.3	14.1	7.43	0.78	20.6	14.4	7.38	0.81	20.7	14.6	7.35	0.82	20.7	14.6	7.34	0.83	20.8	14.7	7.33	0.83
	Steady	30 m	20.4	14.2	7.54	0.74	20.6	14.5	7.52	0.76	20.8	14.7	7.5	0.76	20.8	14.7	7.5	0.77	20.9	14.8	7.49	0.77
		60 m	20.3	14.1	7.43	0.78	20.6	14.4	7.38	0.81	20.7	14.6	7.35	0.82	20.7	14.6	7.34	0.83	20.8	14.7	7.33	0.83
	SteadyLin	30 m	20.4	14.2	7.54	0.74	20.6	14.5	7.52	0.76	20.8	14.7	7.5	0.76	20.8	14.7	7.5	0.77	20.9	14.8	7.49	0.77
		60 m	20.3	14.1	7.42	0.78	20.6	14.4	7.38	0.81	20.7	14.6	7.35	0.82	20.7	14.6	7.34	0.83	20.8	14.7	7.33	0.83
FLS	1Dnum	30 m	20.4	14.2	7.54	0.74	20.6	14.5	7.52	0.76	20.8	14.7	7.51	0.76	20.8	14.7	7.5	0.77	20.9	14.8	7.49	0.77
		60 m	20.3	14.1	7.43	0.79	20.6	14.4	7.38	0.81	20.7	14.6	7.36	0.82	20.7	14.6	7.34	0.83	20.8	14.7	7.33	0.84
	Steady	30 m	20.4	14.2	7.54	0.75	20.6	14.5	7.52	0.76	20.8	14.6	7.5	0.77	20.8	14.7	7.5	0.77	20.9	14.8	7.49	0.77
		60 m	20.3	14.1	7.43	0.79	20.6	14.4	7.38	0.81	20.7	14.5	7.36	0.83	20.7	14.6	7.34	0.83	20.8	14.7	7.33	0.84
	SteadyLin	30 m	20.4	14.2	7.54	0.75	20.6	14.5	7.52	0.76	20.8	14.6	7.5	0.77	20.8	14.7	7.5	0.77	20.9	14.8	7.49	0.77
		60 m	20.3	14.1	7.43	0.79	20.6	14.4	7.38	0.81	20.7	14.5	7.36	0.83	20.7	14.6	7.34	0.83	20.8	14.7	7.33	0.84
R_{soil}	1Dnum	30 m	20.0	13.3	7.12	1.46	20.1	13.4	6.96	1.59	20.1	13.4	6.89	1.63	20.1	13.4	6.85	1.66	20.1	13.5	6.82	1.68
		60 m	19.9	13.0	7.0	1.7	19.9	13.1	6.82	1.85	20.0	13.1	6.74	1.9	20.0	13.1	6.69	1.93	20.0	13.1	6.66	1.95
	Steady	30 m	20.0	13.7	7.11	1.17	20.1	13.4	6.95	1.59	20.1	13.4	6.89	1.63	20.1	13.4	6.85	1.66	20.1	13.5	6.82	1.68
		60 m	19.9	13.0	7.0	1.7	19.9	13.1	6.81	1.85	20.0	13.1	6.74	1.9	20.0	13.1	6.69	1.93	20.0	13.1	6.66	1.95
	SteadyLin	30 m	20.0	13.3	7.12	1.46	20.1	13.4	6.96	1.59	20.1	13.4	6.89	1.63	20.1	13.4	6.85	1.66	20.1	13.5	6.82	1.68
		60 m	19.9	13.0	7.0	1.7	19.9	13.1	6.81	1.85	20.0	13.1	6.74	1.9	20.0	13.1	6.69	1.93	20.0	13.1	6.66	1.95

Chapter 6

Effect of horizontal connection pipes in different climates

Published as:

Düber S., Fuentes R., Narsilio G. (2023): Effect of horizontal connection pipes on operation of borehole heat exchangers under different climatic conditions. *Geothermics*, 110, art. no. 102679.

Düber S.: Conceptualization, Methodology, Software, Validation, Writing - Original Draft **Fuentes R.:** Writing - Review & Editing, Supervision **Narsilio G.A.:** Writing - Review & Editing, Supervision.

Abstract

We investigate the effect of horizontal connection pipes in shallow geothermal systems attached to a borehole field for the 25 most representative climate zones across the World. For this we use a comparable 30 m connection pipe buried at 1 m depth connected to a 100 m deep borehole heat exchanger (BHE) as the unit representation of the whole system for all locations. The system is considered monovalent with weather dependent loads derived from local air temperatures. The connection pipes and BHE are modeled using thermal resistances and response functions. In the investigated reference scenario, the consideration of the connection pipes leads to an average reduction in BHE load of 34 % in tropical climates, 19 % in temperate climates, 11 % in arid and 4 % in continental climates, leading to a significant drilling cost reduction. Exceptions were the cities of Moscow and Heihe both located in continental climates and under severely colder conditions, where the BHE load increased by 13 % and 72 % due to consideration of the horizontal connection pipes, leading to a reduced efficiency or the need for additional drilling only for these cases.

6.1 Introduction

As geothermal energy use continues to grow to provide heating and cooling for the building sector, larger installations are being built with dozens of borehole heat exchangers (BHEs). In Sweden alone the number of registered installations with 10 000 m or more total borehole length has almost quadrupled from 21 in 2015, to 76 systems in 2019, while the number of installations with 10 boreholes or more has increased by almost 40 % during the same period (Lund and Toth, 2021). National guidelines suggest a minimum spacing between boreholes to reduce thermal interference (Kavanaugh and K. D. Rafferty, 2014; VDI 4640-2, 2019). Additional, the need to engage a large ground volume means that, depending on the arrangement of the boreholes, significant distances of several dozen meters between the BHEs and the heat pump, manifolds or header pipes need to be bridged with horizontal connection pipes. These pipes are typically buried in shallow depths up to 1.5 m without thermal insulation (Kavanaugh and K. D. Rafferty, 2014; VDI 4640-2, 2019). While for typical borehole depths, usually deeper than 50 m, the undisturbed ground temperature at the BHE is relatively constant throughout the year, it varies at the depth of the horizontal connection pipes, according to the local climate. The impact of this local climate on this shallow pipes with no insulation has only been very briefly studied. Luo et al. (2013) use a three-dimensional numerical model to investigate the heat loss along a single buried pipe at different depths located in Nuremberg, Germany. Losses for flowing as well as stagnating fluid are studied for different pipe depths, reporting the highest losses for stagnating fluid for heating operation in winter. Increasing the burying depth can reduce these heat losses. The

boundary conditions were derived from on-site monitoring data, however the interaction of heat pump, connection pipe and BHE as one system was not investigated.

Tian et al. (2022) study the impact of burial depth, surface temperature, backfill material and flow rate on the heat loss of horizontal connection pipes attached to a BHE in a sandbox experiment. In their experiments the undisturbed ground temperature at the BHE is 15 °C while the fluid inlet temperature is 24 °C. Different covering materials are investigated while the surface temperature above the horizontal connection pipe is between 30 and 40 °C, leading heat gains along the supply pipe, heat losses along the BHE and heat gains again along the return pipe for all investigated scenarios. The results of this test set-up with a constant fluid inlet temperature cannot be transferred to a system of heat pump, connection pipes and BHE, in which the heat pump imposes a defined load onto the ground.

In this work we investigate for the first time this effect using a 30 m connection pipe attached to a 100 m deep BHE in 25 different climate zones around the world (Figure 6.1, Table 6.1). We consider weather dependent hourly thermal loads for the full 50 year life span of a geothermal system. In section 6.2 we present our approach: a steady-state, analytical model based on response functions and thermal resistances for the system of BHE and connection pipes, how we derive the loads and boundary conditions for each location and which scenarios are investigated. In section 6.3 we first present our procedure step-by-step on the example of San Francisco before moving on to an overall analysis of all 25 locations. In section 6.4 we discuss the results, point out some limitations of the study and draw the final conclusions.

Figure 6.1 Investigated locations in 25 climate zones, see also Table 6.1.

6.2 Methodology

6.2.1 Geothermal system model

We use a combination of thermal response functions, also known as g-functions, and thermal resistances for our model of connection pipes and BHE as shown in Figure 6.2. The fluid

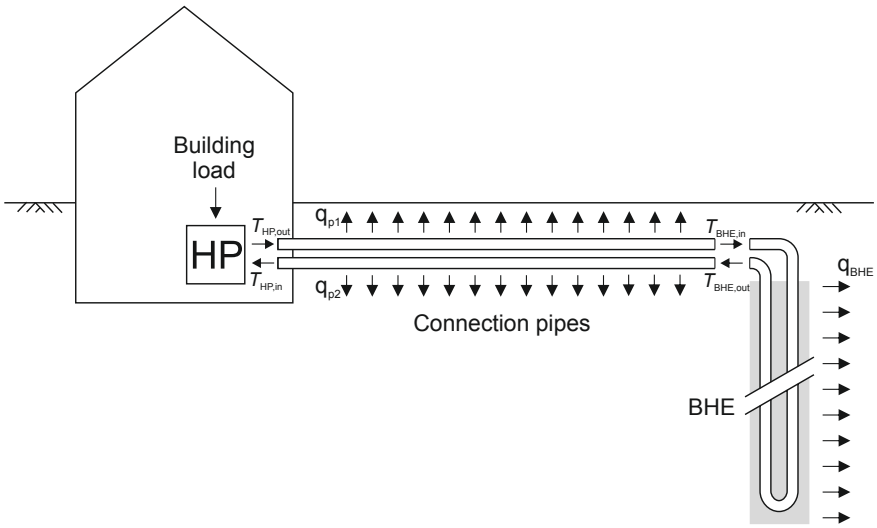

Figure 6.2 Investigated system consisting of heat pump (HP), connecting pipes and borehole heat exchanger (BHE)

temperatures at the head of the BHE $T_{\mathrm{BHE,in}}$ and $T_{\mathrm{BHE,out}}$ are calculated as following (Eskilson, 1987):

$$T_{\mathrm{BHE,in}}(t) = \overline{T}_{\mathrm{f}}(t) + \frac{l_{\mathrm{b}} q_{\mathrm{b}}(t)}{2\dot{V}\rho c} \tag{6.1}$$

$$T_{\mathrm{BHE,out}}(t) = \overline{T}_{\mathrm{f}}(t) - \frac{l_{\mathrm{b}} q_{\mathrm{b}}(t)}{2\dot{V}\rho c} \tag{6.2}$$

$$\overline{T}_{\mathrm{f}}(t) = q_{\mathrm{b}}(t) R_{\mathrm{b}} + T_{\mathrm{b}}(t) \tag{6.3}$$

$$T_{\mathrm{b}}(t_k) = T_{0,\mathrm{b}} + \frac{1}{2\pi\lambda} \sum_{i=1}^{k} \Delta q_{\mathrm{b}}(t_i) \cdot g_{\mathrm{b}}(t_{k-i+1}) \tag{6.4}$$

where T_{b} is the temperature at the borehole wall, $T_{0,\mathrm{b}}$ the undisturbed ground temperature of the borehole, q_{b} the stepwise constant borehole load divided by its length l_{b}, $\Delta q_{\mathrm{b}}(t_i) = q_{\mathrm{b}}(t_i) - q_{\mathrm{b}}(t_{i-1})$ the load increment and g_{b} the borehole g-function. $\overline{T}_{\mathrm{f}}$ is the average of the borehole inlet and outlet fluid temperatures, $\dot{V}$ is the volume flow and ρc the volumetric heat capacity of the fluid. The borehole resistance R_{b} is the effective thermal resistance of the BHE (Javed and Spitler, 2016). The g-function of the borehole is calculated with an analytical expression for the finite line source presented by Claesson and Javed (2011), as this formulation allows the calculation of the mean temperature along the borehole.

The model for the connection pipes follows the same principle. While the heat exchange between the pipes within the BHE is covered using the effective borehole resistance, it is

considered explicitly by spatial superposition (Carslaw and Jaeger, 1959) for the horizontal pipes:

$$T_{\mathrm{p1}}(t_k) = T_{0,\mathrm{p1}}(t_k) + \sum_{i=1}^{k} \Delta q_{\mathrm{p1}}(t_i) \cdot g_{\mathrm{p11}}(t_{k-i+1}) + \Delta q_{\mathrm{p2}}(t_i) \cdot g_{\mathrm{p21}}(t_{k-i+1}) \tag{6.5}$$

$$T_{\mathrm{p2}}(t_k) = T_{0,\mathrm{p2}}(t_k) + \sum_{i=1}^{k} \Delta q_{\mathrm{p2}}(t_i) \cdot g_{\mathrm{p22}}(t_{k-i+1}) + \Delta q_{\mathrm{p1}}(t_i) \cdot g_{\mathrm{p12}}(t_{k-i+1}). \tag{6.6}$$

T_{p} is the soil temperature at the outside of the the pipe and $T_{0,\mathrm{p}}$ the undisturbed ground temperature while g_{p} is the pipes g-function, calculated for a single segment according to Lamarche (2019). The supply pipe is marked with index 1 and the return pipe with index 2 (see Figure 6.2). The first numeric index at the g-functions corresponds to the heat source and the second to the surface where the temperature is evaluated. The load increment is defined as $\Delta q_{\mathrm{p}}(t_i) = q_{\mathrm{p}}(t_i) - q_{\mathrm{p}}(t_{i-1})$, where q_{p} is the length related heat load of the pipe.

Assuming a linear fluid temperature profile along the pipes, their heat load can be calculated as:

$$q_{\mathrm{p},1}(t) = \Big[T_{\mathrm{BHE,in}}(t) - T_{\mathrm{s,p1}}(t)\Big]\left(R_{\mathrm{fs}} - \frac{l_{\mathrm{p}}}{2\dot{V}\rho c}\right)^{-1} \tag{6.7}$$

$$q_{\mathrm{p},2}(t) = \Big[T_{\mathrm{BHE,out}}(t) - T_{\mathrm{s,p2}}(t)\Big]\left(R_{\mathrm{fs}} + \frac{l_{\mathrm{p}}}{2\dot{V}\rho c}\right)^{-1} \tag{6.8}$$

where l_{p} is the length of the pipe and R_{fs} the thermal resistance between the fluid and the outer side of the pipe wall. The latter is the sum of the advective resistance from the fluid to the pipe, which is in our case calculated according to Gnielinski (2013) and the conductive resistance of the pipe (Carslaw and Jaeger, 1959). The assumption of a linear temperature profile in the fluid is a simplification that can lead to errors, especially for long pipes and low fluid velocities (e.g. Lamarche (2019)). For the boundary conditions in this study however, a comparison with a 3D finite element simulation showed deviations of 0.1 K in fluid temperatures, which we consider acceptable. If required, the model can be extended to consider the non-linear fluid temperature profile by dividing the horizontal pipes into multiple segments as shown by Lamarche (2019).

Figure 6.3 shows the g-functions for the pipes and the borehole using the properties listed in Table 6.2 for a time range from 600 s to 50 years. As we assume the supply and return pipe to be buried at the same depth, as is typically the case in real projects, we get $g_{\mathrm{p11}} = g_{\mathrm{p22}}$ and $g_{\mathrm{p12}} = g_{\mathrm{p21}}$. Furthermore, the figure shows the g-function from borehole to horizontal pipe g_{bp} and vice versa, calculated with a 3D finite element model for the soil properties of the borehole. Based on the response functions we consider the pipe-borehole interference as

negligible, although the implementation in the model is straightforward.

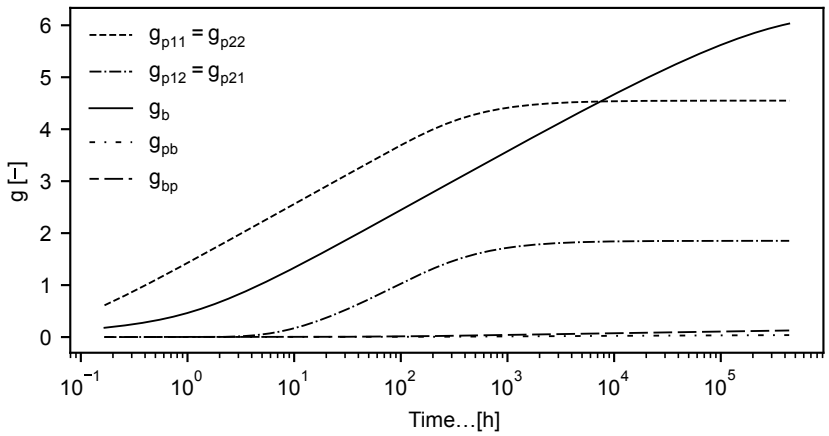

Figure 6.3 g-functions calculated according to the geometric and physical properties listed in Table 6.2.

Finally, the load of the system Q_{tot} is defined as:

$$Q_{\mathrm{tot}}(t) = q_{\mathrm{p2}}(t)l_{\mathrm{p}} + q_{\mathrm{p1}}(t)l_{\mathrm{p}} + q_{\mathrm{b}}(t)l_{\mathrm{b}}. \tag{6.9}$$

Equations 6.1-6.9 can be combined into a single matrix equation which needs to be solved for $\boldsymbol{B}$ at each timestep t_i with a step size Δt:

$$\boldsymbol{A} \cdot \boldsymbol{B} = \boldsymbol{C} \tag{6.10}$$

with:

$$\boldsymbol{A} = \begin{bmatrix} 0 & 0 & -g_{\mathrm{b}}(\Delta t) & 0 & 0 & 0 & 0 & 0 & 1 \\ 0 & 0 & R_{\mathrm{b}} & 0 & 0 & 0 & 0 & -1 & 1 \\ 0 & 0 & +c_3 & 0 & 0 & -1 & 0 & 1 & 0 \\ 0 & 0 & -c_3 & 0 & 0 & 0 & -1 & 1 & 0 \\ -c_1 & 0 & 0 & -1 & 0 & c_1 & 0 & 0 & 0 \\ 0 & -c_2 & 0 & 0 & -1 & 0 & c_2 & 0 & 0 \\ 1 & 0 & 0 & -g_{\mathrm{p11}}(\Delta t) & -g_{\mathrm{p21}}(\Delta t) & 0 & 0 & 0 & 0 \\ 0 & 1 & 0 & -g_{\mathrm{p12}}(\Delta t) & -g_{\mathrm{p22}}(\Delta t) & 0 & 0 & 0 & 0 \\ 0 & 0 & l_{\mathrm{b}} & l_{\mathrm{p}} & l_{\mathrm{p}} & 0 & 0 & 0 & 0 \end{bmatrix} \tag{6.11}$$

$$\boldsymbol{B} = \begin{bmatrix} T_{\mathrm{p1}}(t_i) \\ T_{\mathrm{p2}}(t_i) \\ q_{\mathrm{b}}(t_i) \\ q_{\mathrm{p1}}(t_i) \\ q_{\mathrm{p2}}(t_i) \\ T_{\mathrm{BHE,in}}(t_i) \\ T_{\mathrm{BHE,out}}(t_i) \\ \overline{T_{\mathrm{f}}}(t_i) \\ T_{\mathrm{b}}(t_i) \end{bmatrix} \tag{6.12}$$

$$\boldsymbol{C} = \begin{bmatrix} \widetilde{T}_{\mathrm{b}}(t_i) - q_{\mathrm{b}}(t_{i-1}) g_{\mathrm{b}}(\Delta t) \\ 0 \\ 0 \\ 0 \\ 0 \\ 0 \\ \widetilde{T}_{\mathrm{p1}}(t_i) - q_{\mathrm{p1}}(t_{i-1}) g_{11}(\Delta t) - q_{\mathrm{p2}}(t_{i-1}) g_{21}(\Delta t) \\ \widetilde{T}_{\mathrm{p2}}(t_i) - q_{\mathrm{p2}}(t_{i-1}) g_{22}(\Delta t) - q_{\mathrm{p1}}(t_{i-1}) g_{12}(\Delta t) \\ Q_{\mathrm{tot}}(t) \end{bmatrix} \tag{6.13}$$

with:

$$c_1 = \frac{1}{R_{\mathrm{fs}} - \frac{l_{\mathrm{p}}}{2\dot{V}\rho c}} \tag{6.14}$$

$$c_2 = \frac{1}{R_{\mathrm{fs}} + \frac{l_{\mathrm{p}}}{2\dot{V}\rho c}} \tag{6.15}$$

$$c_3 = \frac{l_{\mathrm{b}}}{2\dot{V}\rho c}. \tag{6.16}$$

The temperatures in $\boldsymbol{C}$ are marked with a tilde, as these are the initial undisturbed ground temperatures plus the temperature changes due to all previous time steps. After Eq. 6.10 is solved, these temperatures need to be updated according to the load increments of the current time step i for all future time steps $k > i$:

$$\widetilde{T}_{\mathrm{b}}(t_k)^{\mathrm{new}} = \widetilde{T}_{\mathrm{b}}(t_k)^{\mathrm{old}} + \Delta q_{\mathrm{b}}(t_i) \cdot g_{\mathrm{b}}(t_{k-i}) \tag{6.17}$$

$$\widetilde{T}_{\mathrm{p1}}(t_k)^{\mathrm{new}} = \widetilde{T}_{\mathrm{p1}}(t_k)^{\mathrm{old}} + \Delta q_{\mathrm{p1}}(t_i) \cdot g_{\mathrm{p11}}(t_{k-i}) + \Delta q_{\mathrm{p2}}(t_i) \cdot g_{\mathrm{p21}}(t_{k-i}) \tag{6.18}$$

$$\widetilde{T}_{\mathrm{p2}}(t_k)^{\mathrm{new}} = \widetilde{T}_{\mathrm{p2}}(t_k)^{\mathrm{old}} + \Delta q_{\mathrm{p2}}(t_i) \cdot g_{\mathrm{p22}}(t_{k-i}) + \Delta q_{\mathrm{p1}}(t_i) \cdot g_{\mathrm{p12}}(t_{k-i}). \tag{6.19}$$

To reduce the computational time introduced by Eq. 6.17-6.19, we apply the hybrid scheme presented by Düber et al. (2022) where the simulation time is split into multiple periods and the effect of past periods on future periods is evaluated utilizing the Fast-Fourier-Transform.

6.2.2 Thermal loads

To keep things simple and comparable, we consider a monovalent system with weather dependent heating and cooling loads only for all locations. The load profiles are calculated based on the hourly annual air temperatures and temperature set points (SP) for heating and cooling, assuming that heating operation starts when the air temperature drops below the set point for heating $\mathrm{SP_h}$ and cooling operation starts once it rises above the set point for cooling $\mathrm{SP_c}$. The difference between the set points and the air temperature defines the magnitude of the load at each hour of the year. To introduce some variation, we investigate five pairs of set points:

- only heating: $\mathrm{SP_h} = 15\,^{\circ}\mathrm{C}$ and $\mathrm{SP_c} = 99\,^{\circ}\mathrm{C}$
- more heating: $\mathrm{SP_h} = 20\,^{\circ}\mathrm{C}$ and $\mathrm{SP_c} = 25\,^{\circ}\mathrm{C}$
- reference: $\mathrm{SP_h} = 15\,^{\circ}\mathrm{C}$ and $\mathrm{SP_c} = 25\,^{\circ}\mathrm{C}$
- more cooling: $\mathrm{SP_h} = 15\,^{\circ}\mathrm{C}$ and $\mathrm{SP_c} = 20\,^{\circ}\mathrm{C}$
- only cooling: $\mathrm{SP_h} = -99\,^{\circ}\mathrm{C}$ and $\mathrm{SP_c} = 25\,^{\circ}\mathrm{C}$

For instance, the *reference* case with $\mathrm{SP_h} = 15\,^{\circ}\mathrm{C}$ means that air temperatures below $15\,^{\circ}\mathrm{C}$ result in heating loads while in the *more heating* case this is already the case for air temperatures below $20\,^{\circ}\mathrm{C}$. In addition, the load profiles are then scaled for each scenario using Eq. 6.1-6.4 to meet the design criteria according to the German technical guideline VDI 4640 (VDI 4640-2, 2019). This means that for heating operation the BHE inlet temperature should not drop below $0\,^{\circ}\mathrm{C}$ on a monthly average and should not drop below $-5\,^{\circ}\mathrm{C}$ at any time. For cooling operation it should not exceed the undisturbed ground temperature by more than $15\,^{\circ}\mathrm{C}$ on the monthly average and $20\,^{\circ}\mathrm{C}$ at any time.

6.2.3 Ground temperatures

Assuming a geothermal gradient of $0.03\,\mathrm{K\,m^{-1}}$ (Van Orstrand, 1939) and constant undisturbed ground temperatures at the BHEs, we calculate the temperature at the vertical center of the 100 m deep BHEs as:

$$T_{0,\mathrm{b}} = \overline{T}_{\mathrm{air}} + 1.5\,\mathrm{K} \tag{6.20}$$

where $\overline{T}_{\text{air}}$ is the mean annual air temperature. The undisturbed ground temperature at the depth of the connection pipes varies throughout the year and is calculated based on hourly ground surface temperatures. For simplicity, and to keep the number of input variables to a minimum, we assume that the surface temperatures correspond to the air temperatures already used for the calculation of the load profiles. The undisturbed ground temperature at the depth of the horizontal pipes $T_{0,\text{p}}(t)$ is calculated utilizing a response function of the ground g_{surf} (Carslaw and Jaeger, 1959) and the Fast-Fourier-Transformation (FFT) as described by Marcotte and Pasquier (2008):

$$T_{0,\text{p}} = \mathscr{F}^{-1}\left(\mathscr{F}(\Delta T_{\text{surf}}) \cdot \mathscr{F}(g_{\text{surf}})\right) + T_0 \tag{6.21}$$

with

$$g_{\text{surf}}(t) = \frac{z}{2\sqrt{\pi\alpha}} \int_0^t \frac{1}{(t-\tau)^{\frac{3}{2}}} \exp\left(-\frac{z^2}{4\alpha(t-\tau)}\right) d\tau \tag{6.22}$$

and

$$T_0(t) = \overline{T}_{\text{surf}} \operatorname{erfc}\left(\frac{z}{\sqrt{4\alpha t}}\right) \tag{6.23}$$

where $\Delta T_{\text{surf}} = T^i_{\text{surf}} - T^{i-1}_{\text{surf}}$ is the hourly surface temperature increment, t denotes the time, α the thermal diffusivity of the ground and z the depth of the connection pipes. $\mathscr{F}$ and $\mathscr{F}^{-1}$ denote the direct and inverse FFT.

6.2.4 Scenarios

To satisfy the heating and cooling loads of a building, there will be as many BHEs as needed, if the required space is available. For the sake of simplicity, we limit our analysis to just one BHE. We investigate the effect of a 30 m connection pipe on the operation of a BHE of 100 m depth for a period of 50 years for 25 locations around the world (Figure 6.1). The locations are listed in Table 6.1 and are chosen to represent 25 different climate types according to the Köppen climate classification (Koppen, 1936; Peel et al., 2007). Hourly air temperatures for a typical meteorological year (TMY) gained from the *PVGIS* web tool (Huld et al., 2012) serve as input for the calculation of the load profiles and the undisturbed ground temperatures at the connection pipes and the BHE for each location. To ensure comparability, all other parameters for the calculations are identical at all locations and shown in Table 6.2.

Table 6.1 Climate zones according to the Köppen climate classification as well as characteristic air temperatures for the investigated period.

Climate	Abbreviation	City	T_{min}	T_{max}	T_{ave}
Tropical rainforest	Af	Kuala Lumpur, Malaysia	19.7	32.7	26.0
Tropical monsoon	Am	Cairns, Queensland, Australia	10.0	33.6	21.9
Tropical savanna with dry winter char.	Aw	Bangkok, Thailand	14.8	37.8	27.7
Tropical savanna with dry summer char.	As	Mombasa, Kenya	20.9	34.6	26.1
Hot desert	BWh	Cairo, Egypt	3.3	43.0	20.7
Cold desert	BWk	Isfahan, Iran	-8.0	39.7	17.1
Hot semi-arid	BSh	Alicante, Spain	3.1	37.1	18.2
Cold semi-arid	BSk	Denver, Colorado, United States	-28.2	35.4	8.8
Humid subtropical	Cfa	Buenos Aires, Argentina	0.2	35.1	17.2
Temperate oceanic	Cfb	Auckland, New Zealand	2.0	25.1	15.1
Subpolar oceanic	Cfc	Reykjavík, Iceland	-17.1	18.1	4.0
Monsoon subtropical	Cwa	Hong Kong	5.6	33.9	22.9
Subtropical highland	Cwb	Johannesburg, South Africa	-1.9	34.6	16.0
Cold subtropical highland	Cwc	La Paz, Bolivia	-4.6	17.7	7.4
Hot-summer Mediterranean	Csa	Rome, Italy	1.2	34.3	16.5
Warm-summer Mediterranean	Csb	San Francisco, California, United States	1.8	28.2	12.8
Cold-summer Mediterranean	Csc	Balmaceda, Chile	-20.1	28.5	4.5
Hot-summer humid continental	Dfa	Chicago, Illinois, United States	-15.8	35.0	10.3
Warm-summer humid continental	Dfb	Moscow, Russia	-34.3	36.2	6.0
Subarctic	Dfc	St. Moritz, Grisons, Switzerland	-27.4	16.0	-2.2
Monsoon-influenced hot-summer humid continental	Dwa	Seoul, South Korea	-11.0	32.8	11.5
Monsoon-influenced warm-summer humid continental	Dwb	Heihe, China	-35.6	32.7	2.6
Mediterranean-influenced hot-summer humid continental	Dsa	Bishkek, Kyrgyzstan	-22.0	35.2	8.8
Mediterranean-influenced warm-summer humid continental	Dsb	South Lake Tahoe, California, United States	-15.2	29.1	5.7
Mediterranean-influenced subarctic	Dsc	Harstad, Norway	-20.9	27.4	3.2

Table 6.2 Compilation of the location-independent physical properties.

Fluid flow rate	$\dot{V}$	$35\,\mathrm{m^3\,d^{-1}}$
Fluid heat capacity	ρc	$3\,992\,340\,\mathrm{J\,m^{-3}\,K^{-1}}$
BHE length	l_b	$100\,\mathrm{m}$
BHE diameter	d_b	$0.15\,\mathrm{m}$
Effective borehole Resistance	R_b	$0.115\,\mathrm{m\,K\,W^{-1}}$
Thermal conductivity ground (BHE)	λ_s	$1.9\,\mathrm{W\,m^{-1}\,K^{-1}}$
Volumetric heat capacity ground (BHE)	ρc_s	$2.052 \times 10^6\,\mathrm{J\,m^{-3}\,K^{-1}}$
Pipe length	l_p	$30\,\mathrm{m}$
Pipe outer diameter	d_p	$0.04\,\mathrm{m}$
Pipe burying depth	z	$1\,\mathrm{m}$
Pipe spacing	s_p	$0.3\,\mathrm{m}$
Thermal resistance fluid→outer pipe wall	R_fs	$0.089\,85\,\mathrm{m\,K\,W^{-1}}$
Thermal conductivity ground (pipe)	λ_s	$1.5\,\mathrm{W\,m^{-1}\,K^{-1}}$
Volumetric heat capacity ground (pipe)	ρc_s	$1.8 \times 10^6\,\mathrm{J\,m^{-3}\,K^{-1}}$

6.3 Results

6.3.1 Detailed evaluation for San Francisco

To illustrate the procedure described in section 6.2 we present all steps on the example of San Francisco for the *reference* scenario with $SP_h = 15\,°C$ and $SP_c = 25\,°C$. Detailed results of all other scenarios are provided as supplementary material. Figure 6.4 shows the hourly air temperatures and the derived load profile according to the set points.

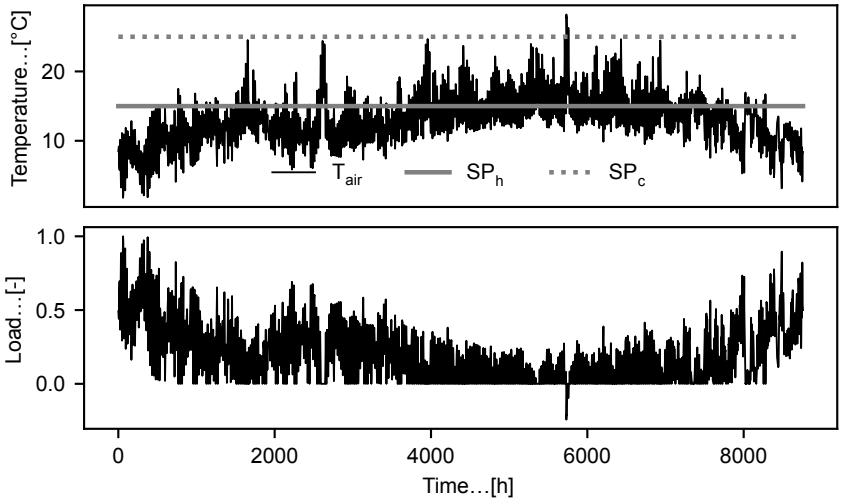

Figure 6.4 Air temperature and set points (top) and resulting normalized load profile (bottom) for the example of San Francisco.

With the help of Eq. 6.1-6.4 the load profile shown in the bottom part of Figure 6.4 is scaled up so that the critical BHE inlet temperature is reached within the design period of 50 years. Figure 6.5 shows the resulting hourly inlet temperatures of the BHE in the top and their monthly average in the bottom part. The critical minimum inlet temperatures are $-5\,°C$ for peak loads and $0\,°C$ for the monthly average. Based on the undisturbed ground temperature at the BHE (here $14.3\,°C$) the critical maximum inlet temperatures are $34.3\,°C$ for peak loads and $29.3\,°C$ for the monthly average. If the load profile from Figure 6.4 is scaled up, the minimum inlet temperature at peak loads is the first exceeded limit temperature, and thus the decisive criterion.

Figure 6.6 shows the cyclic steady state ground temperatures at 1 m depth as well as the undisturbed ground temperature at the vertical center of the BHE and the air temperature as a reference.

A selection of results from the last year of the simulation of the BHE and connection pipes is shown in Figure 6.7. The top part shows the temperature of the fluid exiting the heat pump with and without horizontal connection pipes being considered. For the case with the connection pipes, it is equal to the inlet temperature of the supply pipe $T_{\mathrm{in,CP}}$ while for the

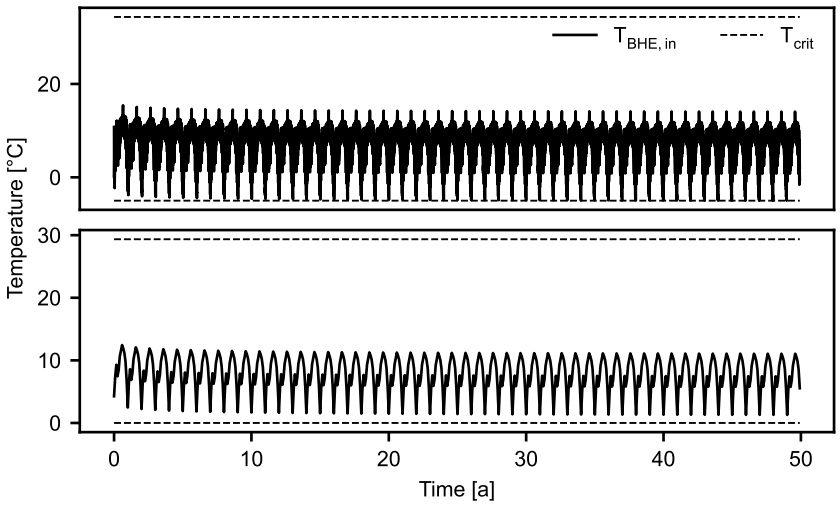

Figure 6.5 Hourly (top) and monthly (bottom) calculated BHE inlet temperatures as well as critical BHE inlet temperatures for the example of San Francisco (i.e., Warm summer Mediterranean climate).

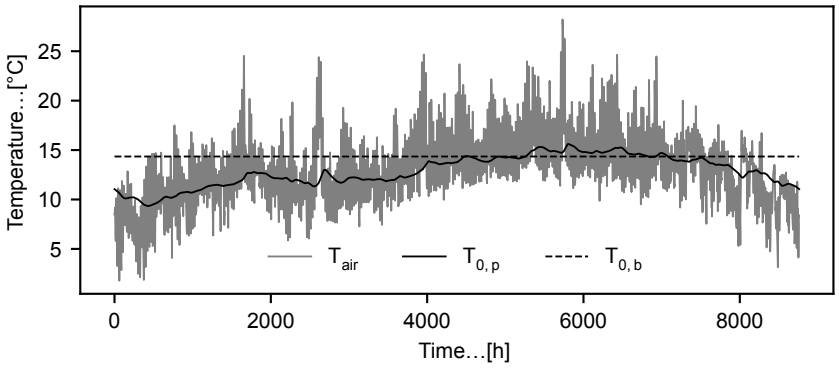

Figure 6.6 Hourly air temperature T_{air} and derived ground temperatures at the BHE $T_{0,\mathrm{b}}$ and connection pipes $T_{0,\mathrm{p}}$ for the example of San Francisco.

case without connection pipes it is equal to the inlet temperature of the BHE, here denoted as $T_{\mathrm{in,Ref}}$. The other three parts show the loads of the connection pipes and the BHE. All loads are shown in $\mathrm{W\,m^{-1}}$, revealing that the heat transfer along the connection pipes is in general lower than along the BHE. This is to be expected as the diameter of the borehole is more than triple the diameter of pipes and the higher ground temperature fluctuations at shallower depths. Indeed, another observation is that the direction of heat flow for the pipes and the BHE is not always identical due to the different ground temperatures at 1 m and at greater depths, indicating both heat losses and heat gains along the connection pipes. While for higher loads the load types are identical, we observe heat losses along the pipes for smaller loads during the heating period. However, if the entire year is considered, the heat gains clearly predominate. The load profile for San Francisco is heating dominant, with a total heating demand of 9 MW h and a cooling demand of just 0.008 MW h in the *reference* scenario. By considering the 30 m connection pipe in the simulation, the total heating load of the BHE in the 50th year is reduced by 2.2 MW h or 24.2 % due to the often

ignored contributions from the horizontal connection pipes. In the simulation without the connection pipes, the minimum BHE inlet temperature is exactly −5 °C, as this was the chosen design criteria for the scaling of the load profile. Considering the connection pipes, this value increases by 3.6 °C to −1.4 °C. The monthly averaged fluid temperatures exiting the heat pump increase from 1.3 °C to 3.6 °C within the coldest month, if the connection pipes are considered in the simulation.

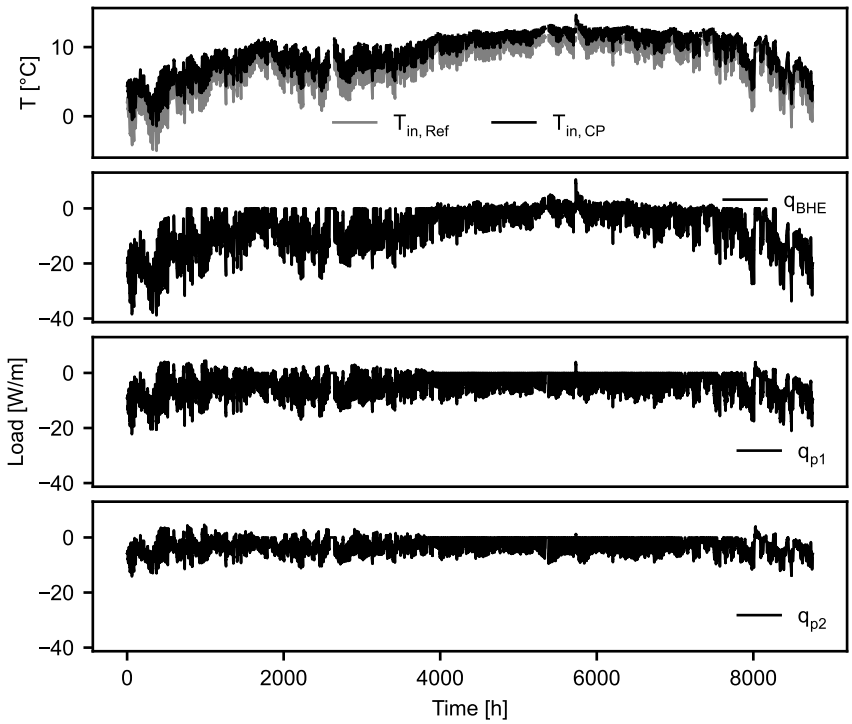

Figure 6.7 Comparison of the fluid temperature exiting the heat pump with ($T_{\mathrm{in,CP}}$) and without ($T_{\mathrm{in,Ref}}$) connection pipes (top) as well as loads of BHE and connection pipes for the example of San Francisco.

6.3.2 Evaluation for all locations

The 25 investigated locations with 5 pairs of set points add up to 125 scenarios with a 50 year simulation. Due to the amount of data we limit the analysis to the following parameters:

- change in BHE cooling and heating loads
- change in minimum and maximum fluid temperatures exiting the heat pump
- change in minimum and maximum monthly averaged fluid temperatures exiting the heat pump.

All analysis are based on the the 50th year of operation. Figure 6.8 shows the total yearly loads for all locations and scenarios. The grey bars indicate cooling and the black bars indicate heating loads. The bars are hatched in case the monthly average temperature was the decisive load scaling limit. One way of interpreting Figure 6.8 is that the loads show how

much energy can be delivered by a single BHE according to the used design criteria and load profile.

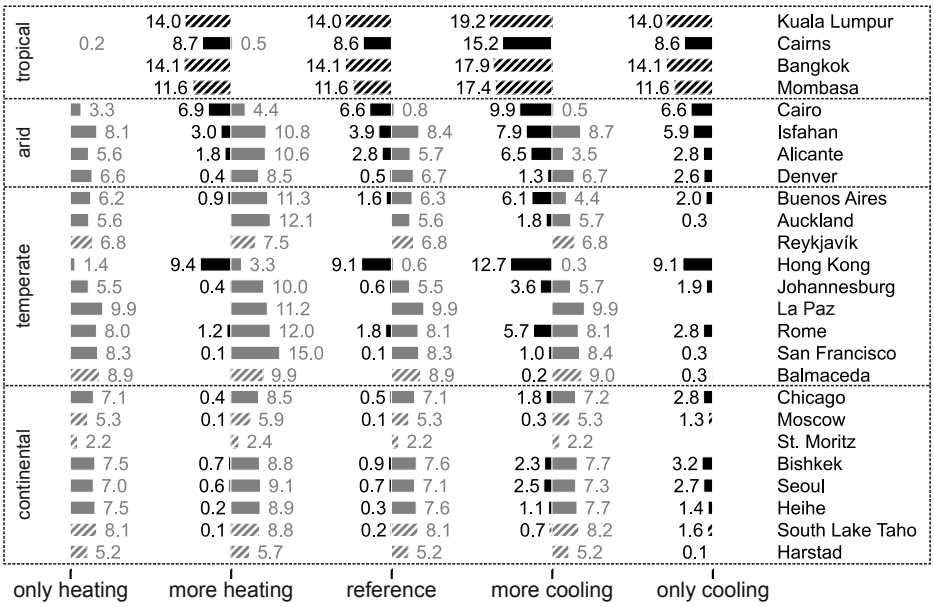

Figure 6.8 Total heating (grey) and cooling loads (black) in MW h for all scenarios. Hatched bars indicate monthly average as decisive scaling limit.

It is interesting to note that in the continental climates the monthly average fluid temperature is the decisive design criteria while it is the peak temperature for all arid climates. In the tropical climates it is the monthly average with the exception of Cairns and no trend can be observed in the temperate climates. The highest loads occur in tropical climates for the *more cooling* case, followed by heating loads in temperate and arid climates for the *more heating* case. No simulation could be carried out for St. Moritz in the continental climates. Based on our assumptions, Equation 6.20 and the TMY data (see. Table 6.1), the average undisturbed temperature at the borehole is below 0 °C. This leads to a violation of the monthly average design criteria for any heating load while the maximum air temperature results in no cooling loads (Table 6.1).

Figures 6.9-6.10 show the absolute and relative changes in BHE load when considering the connection pipes. The relative changes in Figure 6.10 are capped at 100 % as even bigger increases only occur for not decisive load types. While the relative changes give a direct impression of the effect of the connection pipes, they need to be interpreted together with Figure 6.8 and Figure 6.9.

The biggest beneficial effect occurs clearly in the tropical climates. Here, with the exception of Cairns, the connection pipes lead to a BHE load reduction of approximately 5 MW h, or around 35 %. Due to the comparatively constant temperatures in the tropical climates, the ground temperature at the depth of the connection pipes is similar to the temperature at

the depth of the BHE. The pipes can therefore be seen as an extension to the BHE with a similar temperature boundary condition.

In the arid climates and the *reference* scenario, the variance of dominant load reduction is significantly greater, ranging from 4 % for cooling loads in Denver to almost 20 % for heating loads in Cairo. In the *more heating* scenario, heating becomes the decisive load in Cairo as well and the heating load reduction for all locations ranges between 10 % and 20 %. The *more cooling* scenario is much more diverse again, with dominant cooling in Cairo and Alicante and dominant heating in Isfahan and Denver, with BHE load reductions between 3 % and 24 %.

The dominant loads within the temperate climates are heating loads with the exception of Hong Kong. In the *more heating* scenario the BHE load reduction is more than 20 % for all locations except Reykjavík and more than 15 % for 6 out of 8 locations within the *reference* scenario. The difference between the *reference* and the *more cooling* scenario is rather small for heating dominated locations as there are no big changes in the heating loads (Figure 6.8).

For the continental climates heating is the dominant load type for all locations and scenarios. However, the BHE load reduction in the *reference* scenario is more than 5 % for only 3 out of 8 locations, Chicago, South Lake Taho and Harstad. Only in the continental climates we observe an increase in the dominant load: for Moscow it is +12 % and for Heihe even +71 %. At these locations the undisturbed ground temperature in 1 m depth is below −5 °C during the coldest months, so that the assumption of a pipe without insulation may not be realistic for these conditions. Another characteristic of the continental climates is the high relative increase of the non dominant cooling loads, which is more than 100 % for almost all locations in the scenarios with heating and cooling. However, it has to be noted that these cooling loads are less than 10 % of the heating loads (Figure 6.8). Chicago, Bishkek and Seoul are exceptions for the *more cooling* scenario. For example in Soul the cooling load is 19 % of the heating load (Figure 6.8), and the consideration of the connection pipes increases the BHE cooling load by 64 % (Figure 6.10).

In addition to the change in BHE load we also take a look at the temperatures of the fluid exiting the heat pump. Figures 6.11-6.12 show the peak and monthly averaged changes in minimum and maximum fluid temperatures. As in the tropical climates the loads are cooling only for all scenarios and locations except Cairns, both minimum and maximum fluid temperatures occur during cooling operation. The peak reduction is slightly above 5 °C and around 2 °C less for the monthly average. In the arid climates the temperature change is smaller, here the maximum is a decrease of −4.8 °C in peak temperature for Cairo and the *more cooling* scenario. Interestingly, in Denver the direction of the temperature change for the peaks and monthly averages does not always coincide. For example in the *reference* scenario the peak minimum temperature is increased by 0.8 °C while the monthly averaged minimum temperature is decreased by −0.4 °C. The same can be observed for *more heating*

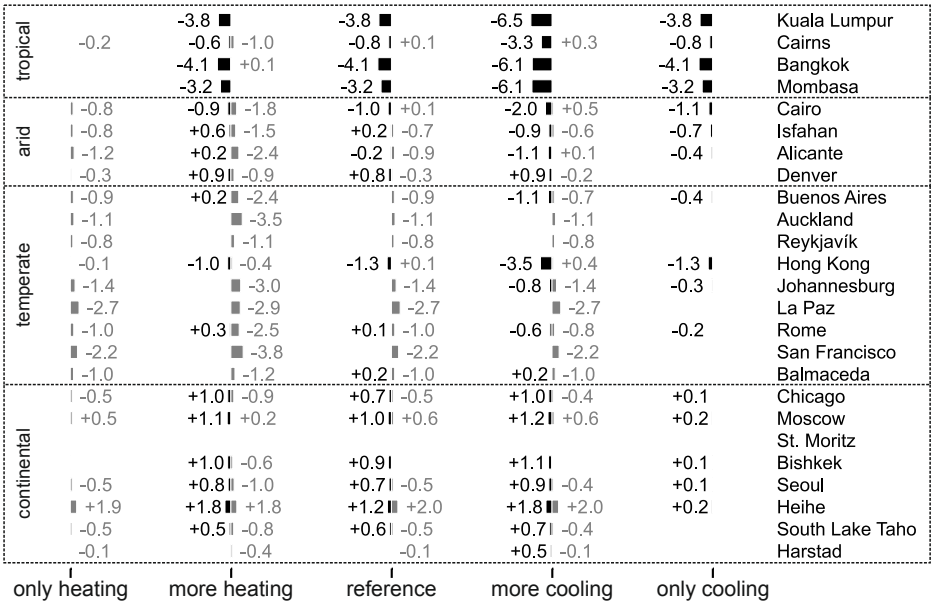

Figure 6.9 Absolute changes in BHE load in MW h in the in the 50th year. Negative values indicate a beneficial contribution by the connection pipes typically unaccounted for.

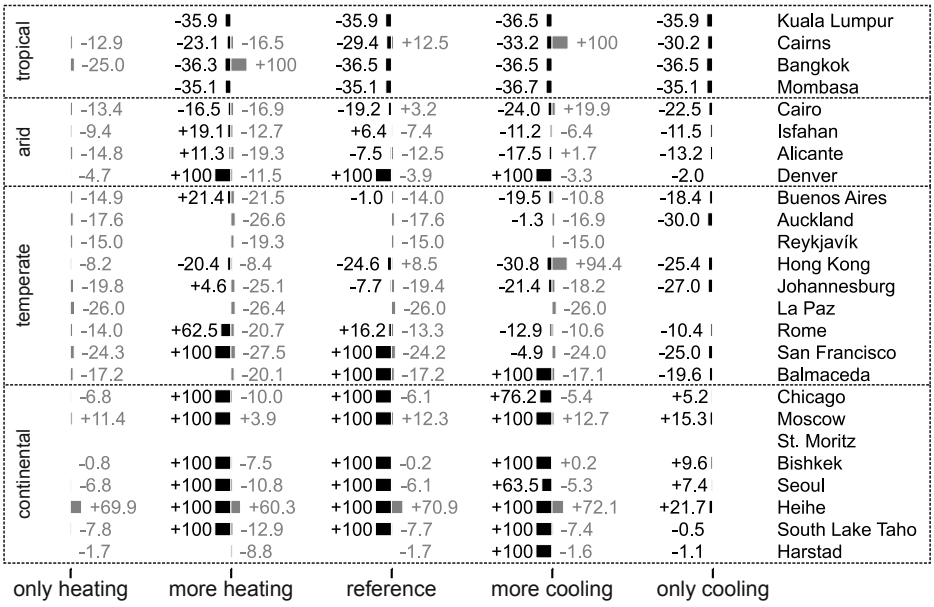

Figure 6.10 Relative changes in BHE load due to connection pipes, capped at 100 %. Deviations from Figures 6.8-6.9 occur due to calculation based on exact numbers.

scenario. However, from an operational or design point of the view the numbers are negligibly small. Similar to the loads, the temperature changes in temperate climates are in general bigger than in the arid climates but smaller than in the tropical climates. The same holds true for the continental climates, where for the dominant loads the smallest changes in fluid temperature can be observed. In Bishkek we observe again different directions of temperature change between peak and monthly averaged temperatures.

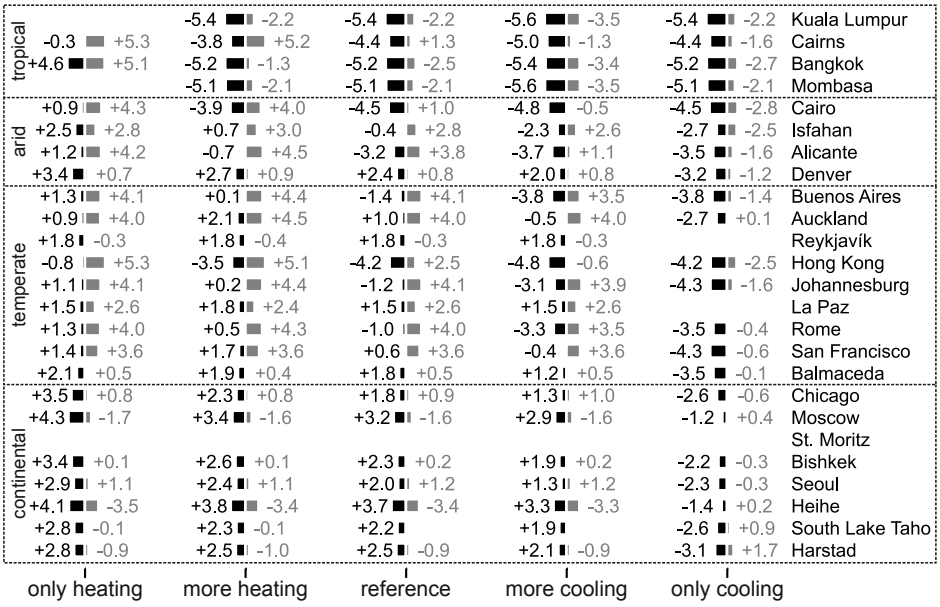

Figure 6.11 Absolute change in minimum (grey) and maximum (black) fluid temperatures exiting the heat pump.

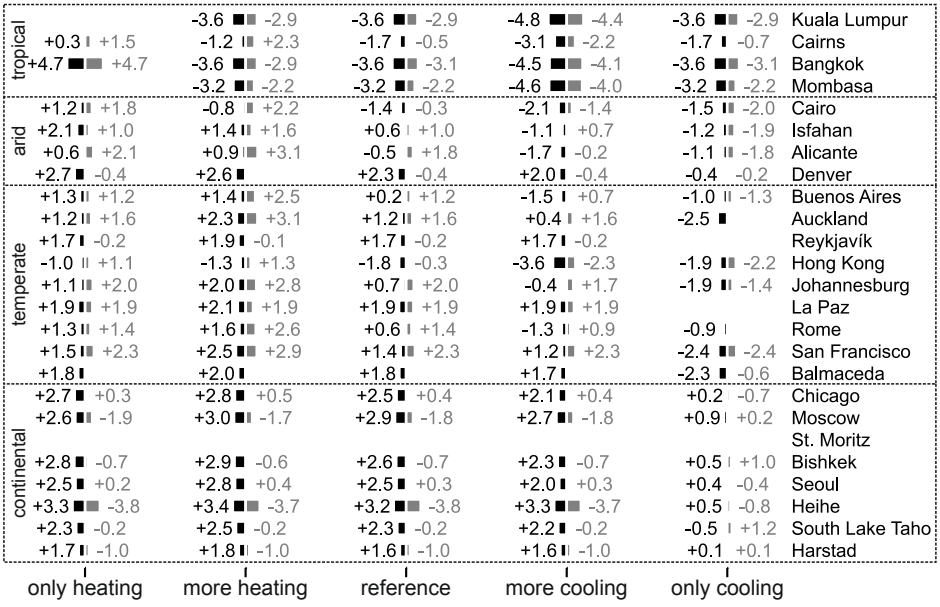

Figure 6.12 Absolute change in monthly averaged minimum (grey) and maximum (black) fluid temperatures exiting the heat pump.

6.4 Discussion and conclusions

In this study we investigate the effect of a 30 m connection pipe attached to a BHE of 100 m depth in 25 climate zones. To produce comparable results, we have made a number of (reasonable) assumptions: the load is weather dependent only and derived from hourly air temperatures for a typical typical meteorological year; the ground temperatures are derived from the same hourly air temperatures and the ground surface temperature is assumed to be

identical to the air temperature; the ground is single-phase and heat is transferred only by conduction; the system is monovalent; the loads are scaled to meet the design criteria of the German VDI 4640 guideline (VDI 4640-2, 2019); the ground, BHE and pipe properties are identical for all locations.

Depending on the location, some of the assumptions are more realistic than others. For example in locations where the frost depth is deeper than 1 m, an uninsulated connection pipe might not be buried at that depth. The temperature limits used for the scaling of the load may also be different in colder regions. The extent to which the limitation of heat transfer to conduction only applies, depends on the local conditions. The assumption that the surface temperature is identical to the air temperature neglects effects such as transpiration, solar radiation or surface coverage. The direction and extent to which these effects influence the results can only be determined on a case-by-case basis. For example, the insulating effect of a snow cover can be beneficial for cold air temperatures in winter. In spring, when the system is still in heating mode, it can be disadvantageous by delaying the warming of the ground. Solar radiation will increase the ground surface temperature, which is good for heating in winter but bad for cooling in summer. Connection pipes of considerable length are required in fields of multiple boreholes, which supply commercially used buildings, apartment blocks or entire districts. Here, the assumption of an only weather dependent load as well as the monovalent system may be challenged. Installing multiple pairs of pipes in a shared trench will reduce the heat exchange per pipe with the ground. Also, the chosen locations may not be representative accurately of other locations in the same climate type.

Taking into account the assumptions and limitations mentioned above, some conclusions can nevertheless be drawn. The connection pipes have a beneficial effect and reduce the dominating BHE load in almost all cases.

The biggest reduction occurs in the tropical climates, followed by the temperate, arid and continental climates. The same trend can be observed regarding the fluid temperatures. Here, however the absolute changes are in most cases too small to have a significant effect on the heat pump efficiency.

The reduced BHE loads however show that the consideration of the pipes in the design can lead to an either increased capacity of the system or reduced borehole length and therefore installation cost. The amount of reduction due to the pipes depends on the combination of load, climate, pipe depth and spacing as well as the properties of the surrounding ground, to just name a few of them. The results also show that even within the same climate type, different results can manifest, e.g., Cairns in the tropical climates. It is therefore advisable to calculate potential savings for each individual case. Site-specific boundary conditions, such as the surface conditions above the horizontal pipes, can then also be taken into account more accurately. For homogeneous ground conditions around the pipes and heat transfer through conduction, this can be done efficiently with the proposed model.

Chapter 7

Utilization of horizontal connection pipes in existing BHE fields

Published as:

Düber S., Fuentes R., Narsilio G. (2024): Exploiting heat gains along horizontal connection pipes in existing borehole heat exchanger fields. *Geothermics*, 118, art. no. 102912.

Düber S.: Conceptualization, Methodology, Software, Validation, Writing - Original Draft **Fuentes R.:** Writing - Review & Editing, Supervision **Narsilio G.A.:** Writing - Review & Editing, Supervision.

Abstract

This study investigates three options for utilising the additional capacity of borehole heat exchanger (BHE) fields through gains along horizontal connection pipes, whose contribution is routinely ignored. The analysis considers thermal load profiles with different heating to cooling ratios and finds that the effect of horizontal pipes becomes more significant with unbalanced loads. The study explores the potential of extended operation, increased loads and an optimised operating strategy to exploit the idle capacity gain from the horizontal connection pipes. It is shown that for the scenarios investigated, the BHE field operational time can be extended by more than 25 years without violating the critical fluid temperatures in the design phase. Alternatively, the thermal load can be increased by up to 26 %. In addition, the study highlights the potential of an optimised operating strategy involving adjustments to the number of BHEs operated to reduce power consumption and therefore reducing operating costs in existing systems by utilising heat gains from the horizontal connection pipes.

7.1 Introduction

Apartment blocks, commercial buildings or entire neighborhoods are increasingly being supplied with geothermal energy for heating and cooling. Shallow borehole heat exchangers (BHEs) with a typical depth of around 100 m are widely used in this context. Several BHEs are arranged in a borehole field to meet the energy needs of these large consumers. In Sweden alone the number of registered installations with 10 000 m or more total borehole length has almost quadrupled from 21 in 2015, to 76 systems in 2019, while the number of installations with 10 boreholes or more has increased by almost 40 % during the same period (Lund and Toth, 2021). To reduce the thermal interference in these borehole fields, a minimum distance between the individual boreholes should be maintained (VDI 4640-2, 2019). Depending on the arrangement of the boreholes, significant distances of several dozen meters between the BHEs and manifolds, header pipes or the consumers must be bridged with horizontal connection pipes. While these pipes are typically buried at shallow depths without thermal insulation, their thermal interaction with the ground is usually not considered in the design (Kavanaugh and K. D. Rafferty, 2014; VDI 4640-2, 2019).

Research on horizontal pipes and BHEs is limited. However, modelling of heat transfer around buried pipes has been extensively studied in various contexts, including buried power cables, pipelines, district heating networks and, more recently, horizontal geothermal heat exchangers. Similar to the vertical boreholes, a variety of analytical solutions exist based on the line or cylinder source theory utilizing the method of images to take into account the ground surface (e.g. Ingersoll (1948)). The general solution for an arbitrarily oriented finite line source in a semi-infinite body was presented by Marcotte and Pasquier (2009). Following the work of

Claesson and Javed (2011) and Cimmino and Bernier (2014) on vertical boreholes, Lamarche (2019) presented the general form for the segment-to-segment response for horizontal pipes, which eliminates the double integral in the work of Marcotte and Pasquier (2009). More recent works on horizontal ground heat exchangers also consider heat transfer mechanisms other than conduction using numerical models. The Piechowski (1999) finite difference model and the Gan (2019) finite volume model include mass transfer due to moisture content. The Gan (2013) finite volume model also includes freezing.

The effect of horizontal pipes in BHE installations has been studied only very briefly. Recent studies have examined the hydraulic effects of the connection pipes, but without in depth consideration of their thermal interference with the surrounding ground (Chen et al., 2021, 2020; M. F. Zhang et al., 2021). Luo et al. (2013) investigate the heat loss along a single buried pipe at different depths for flowing and stagnant fluid, and report the highest losses for stagnant fluid for heating operation in winter. Tian et al. (2022) investigate the effect of burial depth, surface temperature, backfill material and flow rate on the heat loss of horizontal connection pipes attached to a BHE in a sandbox experiment. The whole system of heat pump, connection pipes and BHE under different climatic conditions is investigated by Düber et al. (2023). In contrast to the previous work, their study shows that the horizontal connection pipes have a positive effect in many applications, reducing the thermal load of the BHE and increasing the capacity of the whole system. They show that considering the connection pipes in the design can reduce the required depth of the vertical boreholes and therefore the cost.

In this work, we investigate how the extra capacity of connection pipes, not considered at the design stage, can be used in plants already in operation. Three optimisation options are investigated: *longer operation*, *higher loads* and an *optimised operating strategy* to reduce the electricity consumption of the heat and circulation pump. The study is based on a mixed-use university building in Germany, which is supplied with heating and cooling energy by 40 BHEs 100 m deep (Clauser et al., 2017).

In section 7.2 we present a detailed description of the system of connection pipes and boreholes as well as the load profiles studied. Our modelling approach is presented in section 7.3, where we first introduce the model for the connection pipes and BHEs, followed by our approach for the optimised operation strategy investigations. Finally, section 7.4 presents the results and some discussions, followed by conclusions in section 7.5.

7.2 Scenario

The study is based on the example of the E.ON ERC building in Aachen, Germany. The building houses laboratories, conference rooms and offices. A field of 40 2U-type BHEs with a depth of 100 m supplies the building with heating and cooling energy. The BHEs are operated in parallel and are grouped into three manifolds A, B and C (Figure 7.1). The connection

pipes between the BHEs and the manifolds are buried at depths between 0.94 m and 1.54 m and are between 1.3 m (BHE 32) and 58.1 m (BHE 13) in length. The total length of all (supply and return pair of) connection pipes is 899 m, giving an average length per BHE of 22.5 m. This means that if the distance between the BHE and the manifold is 30 m, the length of the connecting pipe is here counted as 30 m, even though the supply and return pipe are each 30 m long. The properties of the BHEs, pipes and ground are listed in Table 7.1.

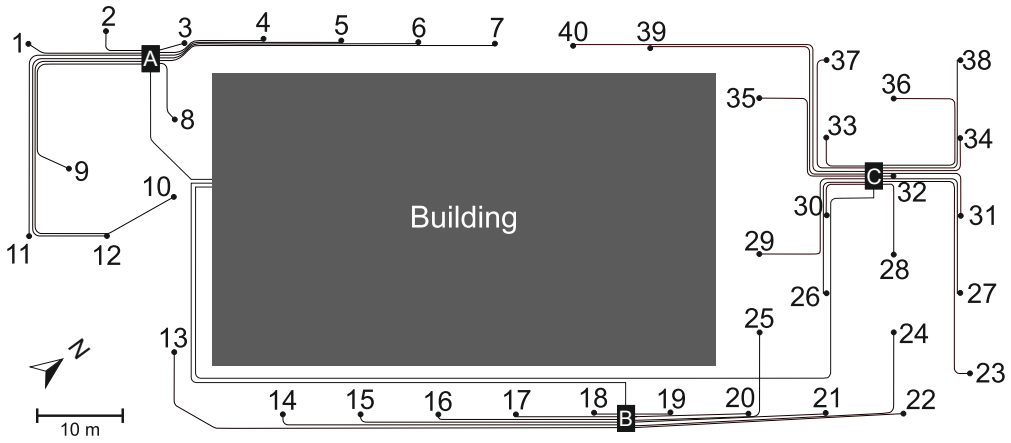

Figure 7.1 Plan view of the connection pipe network of the 40 BHEs arranged in the three manifolds A, B and C.

Figure 7.2 shows the hourly ground thermal load of the BHE field over a one year period, derived from measured flow rates and fluid temperatures. The load is cooling dominant, with a cooling/heating ratio of 3.14. To introduce some variation representing other building types or use, we investigate 5 different load profiles with cooling/heating ratios between 0.1 and 10. We also perform the analysis with hourly load profiles as well as monthly averaged profiles, which are often used in engineering practice during the design phase. All load profiles are based on the profile shown in Figure 7.2. To generate profiles with cooling/heating ratios of $0.1, 0.32, 1.0, 3.14$ and 10, the measured profile is shifted towards heating or cooling until the desired ratio is reached. This is done by incrementally increasing or decreasing by 10 W all values not equal to 0 of the initial load profile with c/h = 3.14 until the desired c/h ratio is reached. It is then scaled as described in Düber et al. (2023) to meet the design criteria of the German technical guideline VDI 4640 (VDI 4640-2, 2019), which states that for heating operation the BHE inlet temperature should not fall below 0 °C on a monthly average and should not fall below −5 °C at any time. In cooling mode, it should not exceed the undisturbed ground temperature by more than 15 °C on a monthly average and 20 °C at any time. The range of load ratios may represent different building uses and plants. Here, the g-function of the BHE field is calculated using the *pygfuntcion* toolbox (Cimmino and Cook, 2022) with the equal inlet temperature boundary condition and single segment BHEs which corresponds to our model as will be shown later in section 7.3. The design period for the scaling of the load profiles is assumed to be 50 years. Figure 7.3 shows all load profiles. To

ensure that the monthly profiles have the same cooling/heating ratio as the hourly profiles, the profile in Figure 7.2 was first averaged monthly and then shifted until the desired ratio was achieved.

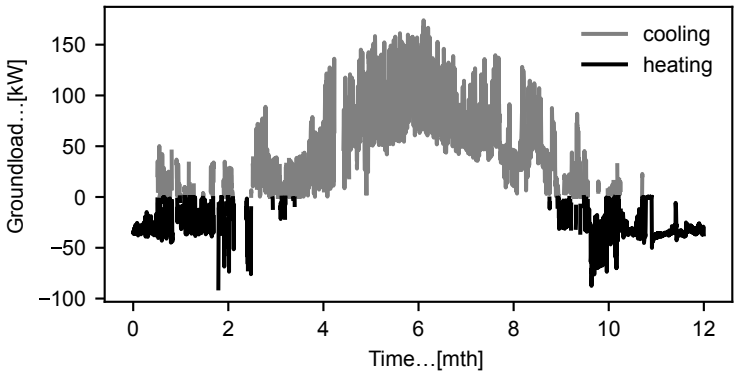

Figure 7.2 Actual hourly ground load of the BHE field derived from measurements.

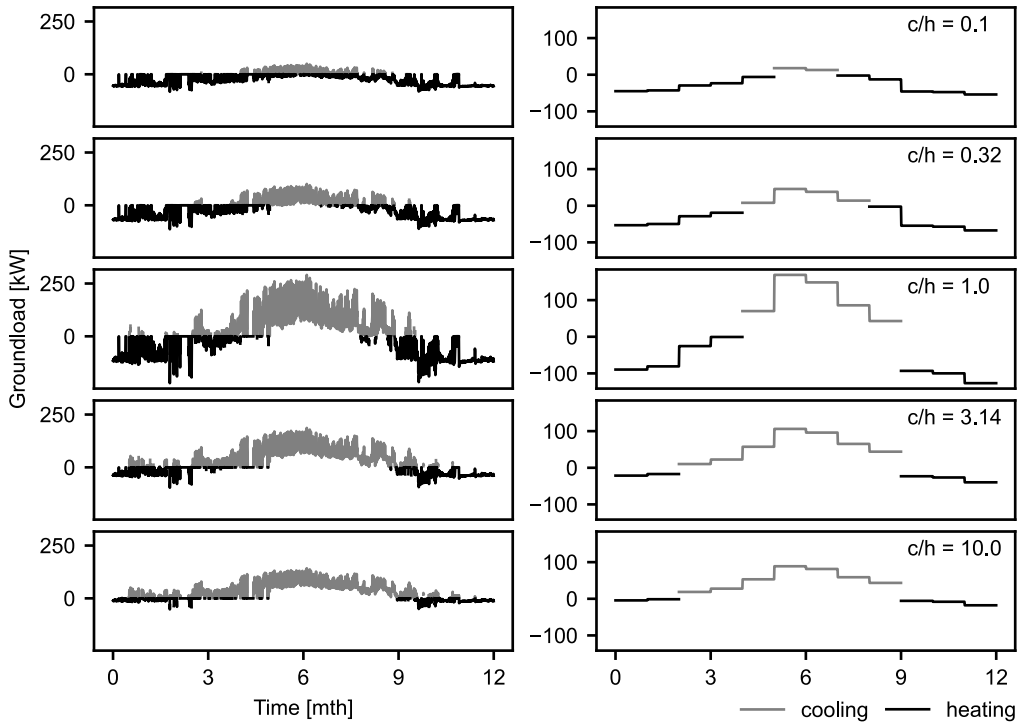

Figure 7.3 Hourly (left) and monthly (right) load profiles with cooling/heating ratios (c/h) ranging from 0.1 to 10.

When scaling the load profiles, the monthly average fluid temperature was the critical limit for all unbalanced load profiles. Only for the hourly profile with a cooling/heating ratio = 1.0 was the maximum fluid temperature during cooling the decisive limit. However, for the monthly averaged profile with the same ratio, it was again the monthly averaged fluid temperature, this time during heating operation.

Table 7.1 BHE and ground properties of the BHE field (Clauser et al. (2017) and documents from the construction phase).

Domain	Parameter	Value	Units
Fluid	Thermal conductivity	0.43	$\mathrm{W\,m^{-1}\,K^{-1}}$
Fluid	Density	1045	$\mathrm{kg\,m^{-3}}$
Fluid	Volumetric heat capacity	3 800 000	$\mathrm{J\,m^{-3}\,K^{-1}}$
Fluid	Dynamic Viscosity	0.0035	$\mathrm{Pa\,s}$
Fluid	Flow rate per BHE	1.5	$\mathrm{m^3\,h^{-1}}$
BHE	Length	100	m
BHE	Diameter	0.152	m
BHE	Shank space	0.04	m
BHE	Outer diameter pipes	0.032	m
BHE	Pipe wall thickness	0.0029	m
BHE	Thermal conductivity grout	2.0	$\mathrm{W\,m^{-1}\,K^{-1}}$
BHE	Volumetric heat capacity grout	1 000 000	$\mathrm{J\,m^{-3}\,K^{-1}}$
BHE	Thermal conductivity pipe	0.3	$\mathrm{W\,m^{-1}\,K^{-1}}$
BHE	Borehole thermal resistance	0.089	$\mathrm{m\,K\,W^{-1}}$
h. pipe	Length	1.3 - 58.1	m
h. pipe	Depth	0.94 - 1.54	m
h. pipe	Outer diameter	0.04	m
h. pipe	Wall thickness	0.0037	m
h. pipe	Thermal conductivity	0.38	$\mathrm{W\,m^{-1}\,K^{-1}}$
h. pipe	Pipe thermal resistance	0.0989-0.0999	$\mathrm{m\,K\,W^{-1}}$
Ground BHE	Thermal conductivity	2.3	$\mathrm{W\,m^{-1}\,K^{-1}}$
Ground BHE	Volumetric heat capacity	2 300 000	$\mathrm{J\,m^{-3}\,K^{-1}}$
Ground BHE	Undisturbed temperature	11.0	°C
Ground h. pipe	Thermal conductivity	2.0	$\mathrm{W\,m^{-1}\,K^{-1}}$
Ground h. pipe	Volumetric heat capacity	2 000 000	$\mathrm{J\,m^{-3}\,K^{-1}}$
Ground h. pipe	Undisturbed temperature	0.5 - 23.9	°C

7.3 Model and methods

We use the model recently introduced in Düber et al. (2023) for the system of BHEs and connection pipes. It is based on thermal resistances for the pipes and BHEs and thermal response functions, also known as g-functions (Eskilson, 1987), for the ground around the BHEs and pipes. In the previous work we used the horizontal finite line source presented by Lamarche (2019) to calculate the g-functions for the horizontal pipes. Here, we use a 3D-numerical model to calculate the pipe g-functions. This allows us to take into account the different paths of the pipes as well as the impact of the building embedding into the ground (Figure 7.1). For the sake of simplicity we make the following assumptions that differ from the actual conditions at the building: the ground surface is flat, the ground is homogeneous and the building is embedded 3 m into the ground over its entire footprint. To reduce the modelling effort, we neglect the thermal interference of horizontal pipes belonging to different manifolds. The minimum distance between connection pipes of different manifolds is about 10 m (BHE 23 and 24, see Figure 7.1), while the maximum burial depth is 1.54 m. With this arrangement, the effects of mutual interference are dominated by the effects of the ground surface, even over long observation periods. This allows us to use individual models for each manifold, resulting in fewer elements and less computation for each model.The spatial discretisation of each model was verified with a grid independence test. Figure 7.4 shows the numerical model for manifold C. Since g-functions in essence capture changes in temperature (from the far-field or undisturbed ground temperature), rather then using the actual ground temperature, the initial temperature of the model is directly set to 0 °C. The boundaries of the model are set to have a constant temperature boundary condition of 0 °C. By choosing these values, the induced temperature change by heat injection along different pipes can be directly converted to the respective g-function without subtraction of undisturbed ground temperatures. Only the (boundary) faces where the building is embedded in the ground are considered to be thermally insulated (i.e., the portion of the upper boundary face with the building footprint). Considering supply and return pipe individually results in $(12 \cdot 2)^2 = 576$ g-functions for manifold A, $(12 \cdot 2)^2 = 576$ g-functions for manifold B and $(16 \cdot 2)^2 = 1024$ g-functions for manifold C (Figure 7.5). Taking into account the $40^2 = 1600$ borehole g-functions adds up to a total number of 3776 g-functions considered in the model. The g-functions for the boreholes are calculated with the finite line source as presented by Claesson and Javed (2011).

The g-functions derived as described above serve as input parameters for the model presented in Düber et al. (2023). Here, the initial temperature at the BHEs is assumed to be constant as $T_{0,\mathrm{b}} = 11\,°\mathrm{C}$. Unlike the common approach of considering a constant undisturbed ground temperature in vertical BHEs, the undisturbed ground temperatures for the horizontal pipes varies throughout the year and are calculated according to Phetteplace et al. (2013):

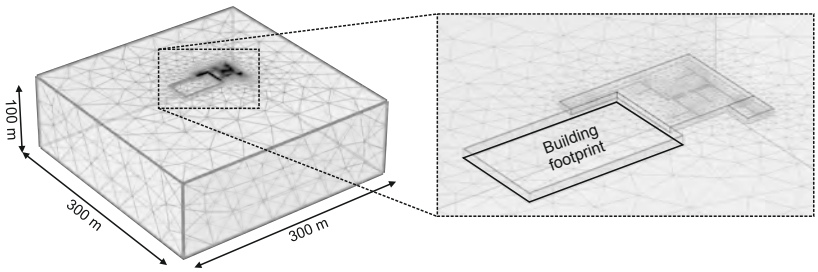

Figure 7.4 Numerical model for calculation of g-functions for manifold C.

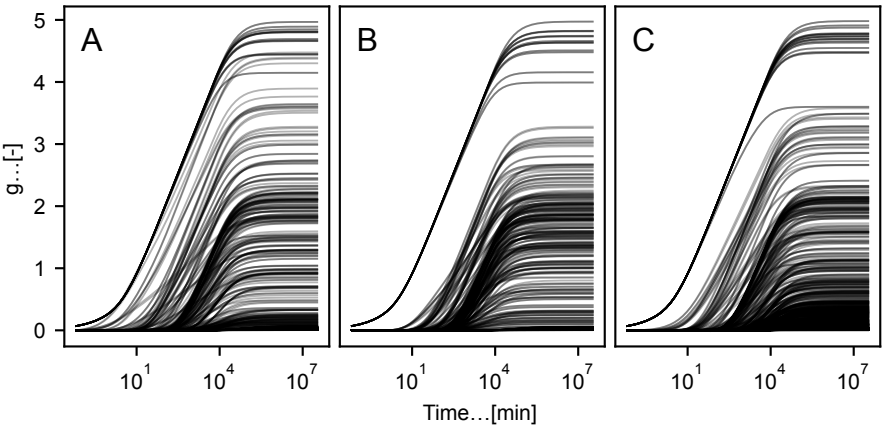

Figure 7.5 G-functions for the horizontal pipes for manifolds A, B and C.

$$T_s(z,t) = T_{\text{ave}} + e^{-z\sqrt{\frac{\pi}{\alpha_s t_p}}} T_{\text{amp}} \sin\left[\frac{2\pi}{t_p}(t-\Phi) - z\sqrt{\frac{\pi}{\alpha_s t_p}}\right] \tag{7.1}$$

where T_{ave} is the average annual ground surface temperature, T_{amp} the amplitude of the ground surface temperature, t_p is the period of soil temperature cycle and t is the time. z is the depth at which the temperature is evaluated and α_s is the thermal diffusivity of the ground. The constants for Equation 7.1 were derived from data from a nearby weather station as $T_{\text{ave}} = 12.2\,°\text{C}$, $T_{\text{amp}} = 15.8\,°\text{C}$ and $\Phi = 106\,\text{d}$. The resulting temperatures at the horizontal pipes are shown in Figure 7.6.

The electricity consumers in a geothermal system are the circulation pump and the ground source heat pump. In section 7.4.4 we assume active heating and cooling and try to reduce the total electricity demand with an optimised operating strategy. The idea is to not operate all BHEs at all times and therefore reduce the electricity demand of the circulation pump. This idea has already been explored by various authors outside the context of the horizontal connection pipes, partly in a modified form (e.g. Hackel and Pertzborn (2011), Hecht-Méndez et al. (2013), Zarrella et al. (2017), Stoffel et al. (2022)). While the investigations on longer operation time and higher loads (sections 7.4.2 and 7.4.3) use the ground loads presented

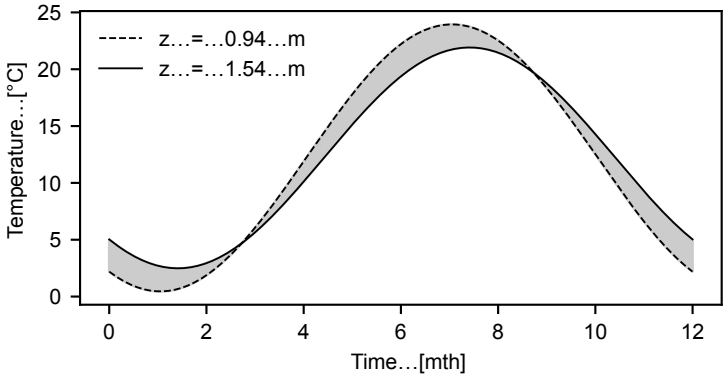

Figure 7.6 Range of undisturbed ground temperatures at the horizontal connection pipes which are buried between 0.94 m and 1.54 m below the surface starting on the first of January.

in the previous section, the analysis of an optimised operation strategy requires building loads and models for the heat pump and the circulation pump. Here, the ground load Q_{g} is calculated based on the building load Q_{b}, the temperature of the fluid exiting the BHE field and entering the heat pump $T_{\mathrm{in,HP}}$ and the coefficient of performance (COP) of the heat pump. For cooling loads we get:

$$Q_{\mathrm{g}} = Q_{\mathrm{b}} \frac{\mathrm{COP_c}(T_{\mathrm{in,HP}}) + 1}{\mathrm{COP_c}(T_{\mathrm{in,HP}})} \tag{7.2}$$

and for heating loads,

$$Q_{\mathrm{g}} = Q_{\mathrm{b}} \frac{\mathrm{COP_h}(T_{\mathrm{in,HP}}) - 1}{\mathrm{COP_h}(T_{\mathrm{in,HP}})}. \tag{7.3}$$

The COP is calculated based on manufacturer data (using Envision NKW150 as example only) shown in the left part of Figure 7.7. For the inter- and extrapolation of the only pointwise available data we use the *scipy.interpolate.interp1d* function with a quadratic spline interpolater (Virtanen et al., 2020). To calculate the electricity consumption of the circulation pump, we use the same interpolation method on manufacturer data (using Wilo ChronoLine-IL-E 65 as example only) which is shown in the right part of Figure 7.7. It is also assumed that all BHEs are hydraulically balanced and have a flow rate of $1.5\,\mathrm{m^3\,h^{-1}}$ regardless of the length of the individual connection pipe. It should be noted that the heat pump data shown in Figure 7.7 does not correspond to the heat pump in the actual 20 yr old building, but to a contemporary GSHP, an assumption used here for our theoretical analysis.

For the optimised operating strategy, we divide the operating period of the BHE field into smaller periods of one month for which we want to determine the optimal number of BHEs in operation so that the electricity consumption is minimised. We have chosen an optimisation period of one month, or 12 control events per year, because the effort involved in switching

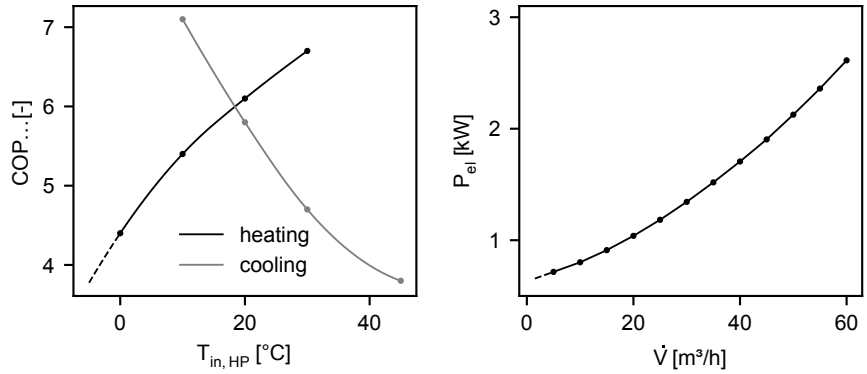

Figure 7.7 Heat pump data (left) and circulation pump data (right) used for the model. Dashed lines indicate extrapolation.

the BHEs on and off seems justifiable, even if the the task is undertaken manually without an automated control system or programmable BMS (building management system). To calculate the optimal number of BHEs for each period, we set up two models, a *simulation model* and a *prediction model*. The simulation model is the model already described, which is used for all analyses in this work. The predictor model is another instance of the same model, but with a coarser time step to reduce the computational effort.

The inputs for the predictor model are the average building load $\overline{Q}_\mathrm{b}$ of the period and the temperatures at the boreholes $T_{0\mathrm{b}}$ and the horizontal pipes $T_{0\mathrm{p}}$. The predictor model simulates the period for all cases from 1 to 40 BHEs in operation (i.e., using only 1, or only 2, or up to 40 BHEs at a time to satisfy the load in that period of time), using the described heat pump and circulation pump models. The optimal number of BHEs is selected based on the total electricity consumption P_tot and the critical fluid temperatures. This means that the number of BHEs is selected so that the critical fluid temperatures are maintained and the total power consumption is as low as possible. To ensure the most efficient selection of BHEs, the BHEs are first ordered according to their borehole wall temperatures. This depends on the average load of the period. If the load of the period is a building cooling load, the boreholes are sorted in ascending order starting with the coldest borehole, since it would have more capacity to reject heat to the ground than other BHEs. If it is a building heating load, the order is reversed and sorting starts with the warmest borehole. A flowchart of the described procedure is shown in Figure 7.8.

Figure 7.9 shows the results of the predictor model for a period of heating operation. The bottom part shows the electricity consumption of the heat pump P_HP, the circulation pump P_circ and the sum of both P_tot as a function of the number of BHEs in operation.

The top part shows the corresponding inlet fluid temperature of the BHE field. As the number of BHEs increases, the power consumption of the circulation pump increases while the power consumption of the heat pump decreases, resulting in an overall optimum of 5 kW with 8 BHEs in operation. As the load for the period shown is a heating load, the fluid

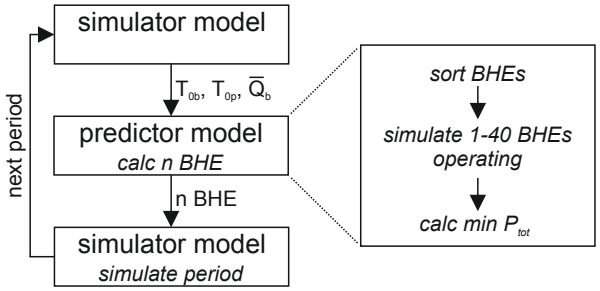

Figure 7.8 Procedure to calculate the optimal number of BHEs operating for each period.

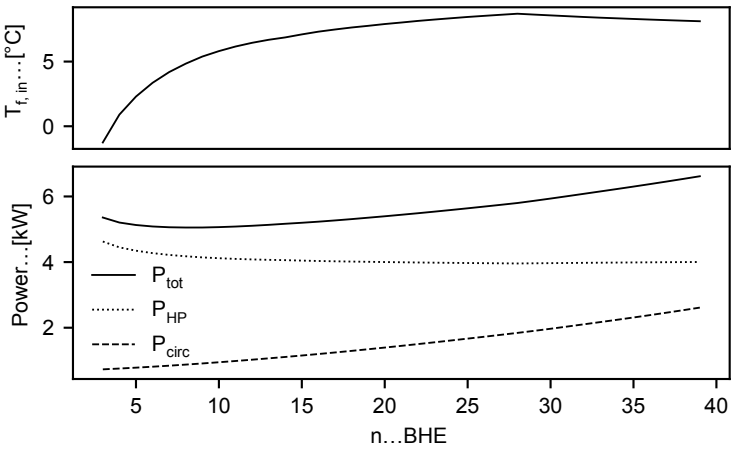

Figure 7.9 Exemplary results of the predictor model.

temperature increases as the number of BHEs increases. However, from 28 BHEs onwards we can see that it decreases slightly. This is due to the order of the BHEs. In the period prior to the current period of simulation, heating was also needed, and only 12 BHEs were in operation. By sorting the BHEs according to their borehole wall temperatures, these 12 BHEs are the least favourable for this period and are therefore only selected when 28 or more BHEs are required. Again, the optimum selection in terms of power consumption is 8 BHEs operating in this case.

To ensure comparability with the previous investigations on longer operation and higher loads (without heat pump model and ground load as boundary condition), the building loads are calculated so that the exact same ground loads occurs when using the heat pump model and building loads as boundary condition. Therefore we simulate the BHE field with 40 BHEs, including the connection pipes, with the specified ground loads (Figure 7.3). Based on the fluid temperatures and the heat pump data (Figure 7.7, left) we calculate the corresponding building load for each ground load profile.

7.4 Results and discussions

7.4.1 Effect of horizontal pipes

To give a first impression of the effect of the horizontal pipes, we simulate the BHE field at a constant cooling load of 120 kW for a period of 50 years. Figure 7.10 shows the results for a simulation with our simulation model where the thermal conductivity of the horizontal pipes is set to zero (no pipes) and a simulation with the *pygfunction* toolbox as reference (pygfunc). Simulations with our model considering the pipes were performed with a constant undisturbed ground temperature around the pipes (pipes, $T_0 = \text{const.}$) and with varying ground temperatures (pipes, $T_0 = f(t)$).

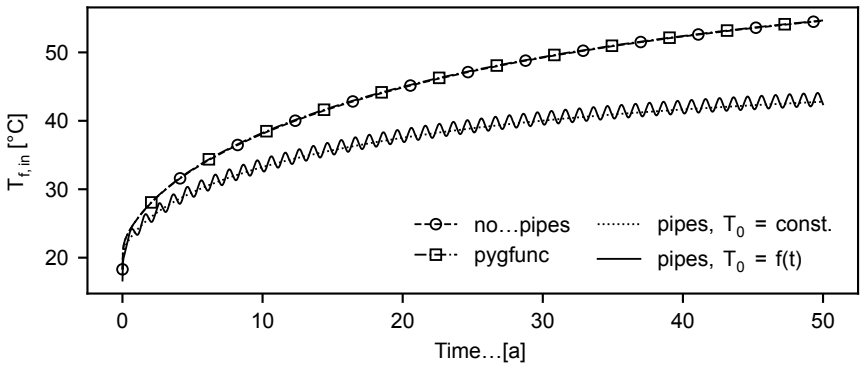

Figure 7.10 Development of the fluid temperature entering the BHE field at a constant load of 120 kW with and without consideration of the horizontal connection pipes.

The inclusion of the horizontal pipes leads to a difference in the fluid temperature entering the BHE field of more than 10 °C at the end of the period. The effect of the seasonal temperature variations around the horizontal pipes on the fluid temperature is rather small, resulting in a peak-to-peak amplitude of about 2 °C in this case. However, for the load profiles shown in Figure 7.3, the effect of the horizontal pipes is less dramatic (Table 7.2). To demonstrate this, we simulate all scenarios with and without consideration of the horizontal pipes. Figure 7.11 shows the results for the hourly load profile on the example of the c/h = 3.14 scenario where the temperature difference at peak loads is just 2 °C in the last year.

For the sake of clarity, we restrict the plots for all other cases to the envelopes of the fluid temperatures entering the BHE field. Figure 7.12 shows the results for the hourly and monthly load profiles.

The results show that the more unbalanced the load profile, the greater the effect of the horizontal connection pipes (see also Tables 7.2 and 7.3). This is independent of whether the load profile is heating or cooling dominant. For unbalanced cooling-dominant profiles, the heat accumulates in the ground leading to a steady increase in fluid temperatures until eventually a steady state is reached. If the horizontal pipes are considered in the simulation, the capacity of the whole system is greater, leading to a slower temperature rise and possibly

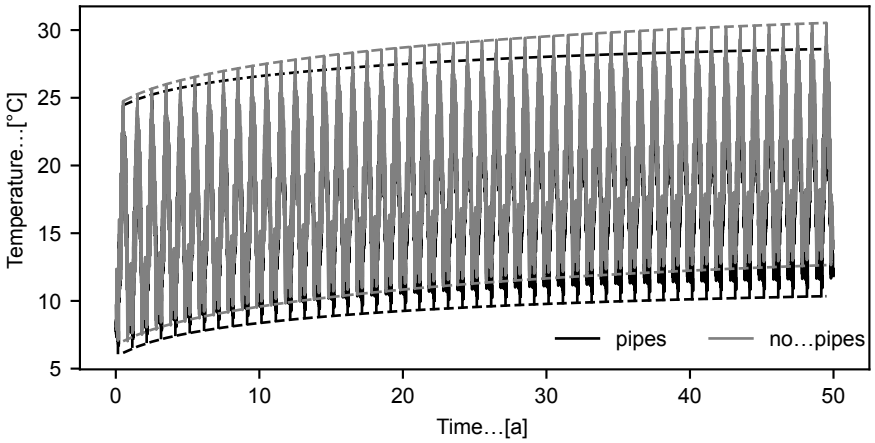

Figure 7.11 Fluid temperatures entering the BHE field with and without consideration of the horizontal connection pipes for the c/h = 3.14 hourly load profile.

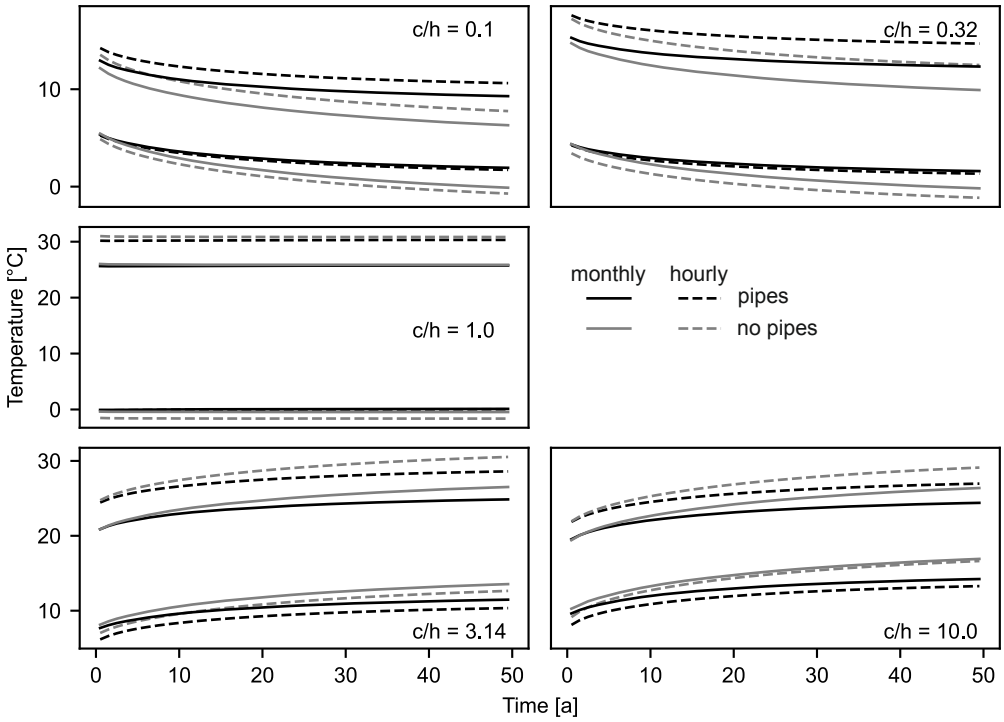

Figure 7.12 Envelopes of the fluid temperatures entering the BHE field for all c/h ratios and monthly and hourly load profiles.

earlier reached state state. The same applies to the heating loads, except that the ground is cooling instead of heating. Interestingly, in the case of balanced loads, the effect of the horizontal pipes is hardly noticeable. This is a special case that rarely occurs in practice.

Table 7.2 shows the average fluid temperature entering the BHE field for the design period of 50 years with and without consideration of the horizontal pipes. The biggest difference with 1.7 °C occurs in the c/h = 0.1 scenario, both for hourly and monthly profiles, while

the smallest effect can be observed for the balanced monthly profile (c/h = 1.0) with just 0.3 °C.

Table 7.2 Average fluid inlet temperature [°C] of the BHE field for operational period of 50 years with and without consideration of the horizontal connection pipes.

	hourly profile		monthly profile	
c/h ratio	no pipes	pipes	no pipes	pipes
0.1	4.6	6.3	4.5	6.2
0.32	5.8	7.2	5.7	7.2
1.0	11.0	11.5	11.0	11.3
3.14	17.6	16.7	17.4	16.3
10.0	19.1	18.0	18.9	17.4

Table 7.3 shows the relative share of the load covered by the BHEs, taking into account the horizontal pipes. The dominant BHE thermal loads are reduced between 6 % (monthly profile, c/h = 3.14) and 19.3 % (hourly profile, c/h = 0.1). Load increases for the BHEs result exclusively for the non-dominant loads.

Table 7.3 Load share [%] covered by the BHEs for the different load profiles separated for cooling and heating operation.

	hourly profile		monthly profile	
c/h ratio	heating	cooling	heating	cooling
0.1	80.7	172.8	82.1	182.6
0.32	89.2	132.0	91.2	137.0
1.0	95.5	98.8	97.2	99.6
3.14	118.9	93.3	123.6	94.0
10.0	174.1	89.7	214.7	92.8

7.4.2 Longer operation

All load profiles have been scaled to reach the critical fluid inlet temperatures within the design period of 50 years, without consideration of the horizontal pipes. Based on technical guidelines, the BHE field can theoretically not be operated at the design loads after the 50-year period because the fluid temperatures will be either too high or too low. However, as shown in the previous section, the consideration of horizontal pipes leads to slower heat accumulation or depletion in the case of unbalanced load profiles. In this section we investigate how much longer the BHE field can operate with the same load profile by taking into account the horizontal connection pipes. Figure 7.13 shows the results for the monthly profiles for an additional 25 years of operation or a total of 75 years of operation. Here, we plot the envelopes of the monthly averaged fluid temperatures entering the BHE field, as these were

the decisive design criteria when scaling the loads (section 7.2). Without the consideration of the pipes, the fluid temperatures reach the critical limit exactly after 50 years. Considering the pipes however, the fluid temperatures do not reach the critical limits even after 75 years for the same load profiles for all cases. In fact, the BHE field is almost in a steady state after this time, with negligible temperature accumulation. Figure 7.14 shows the results for the hourly load profiles. The results are almost identical, only the absolute temperatures are slightly shifted.

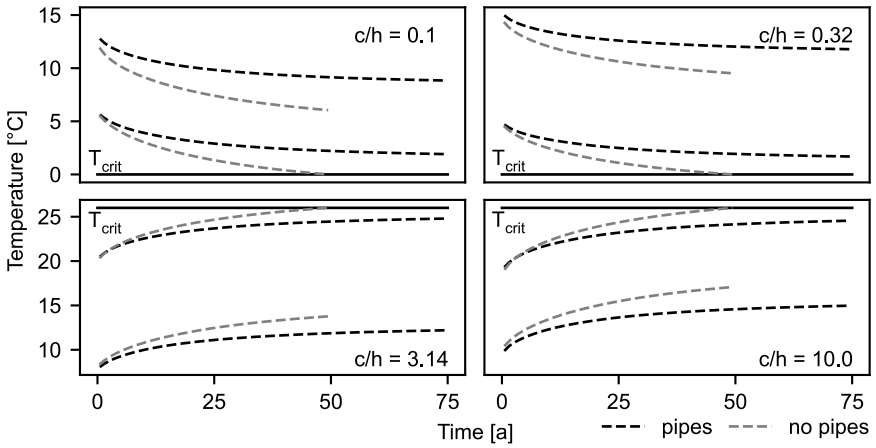

Figure 7.13 Envelopes of the monthly averaged inlet temperature of the BHE field with and without consideration of the connection pipes for the monthly load profiles.

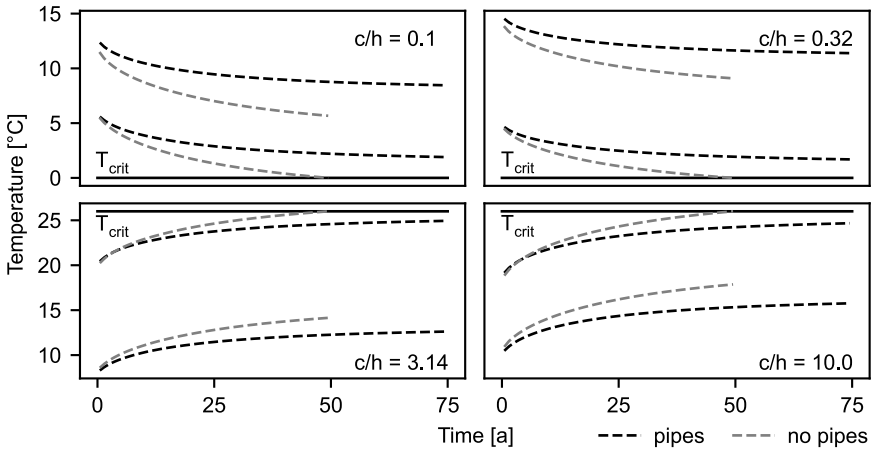

Figure 7.14 Envelopes of the monthly averaged inlet temperature of the BHE field with and without consideration of the connection pipes for the hourly load profiles.

7.4.3 Increased load

The increased capacity of the BHE field due to the consideration of the horizontal pipes will also allow higher loads within the same temperature limits. As our model only considers heat transfer through conduction, we can use the linear relation between temperature change

and thermal load to calculate the the possible load increase directly. The results in Table 7.4 roughly coincide with the reduced BHE loads in Table 7.3, where the biggest reductions were observed for the unbalanced heating dominant profiles, followed by the unbalanced cooling dominant scenarios.

Table 7.4 Factors by which the load profiles can be multiplied until the critical fluid temperatures are reached considering the horizontal pipes.

c/h ratio	hourly profile	monthly profile
0.1	1.26	1.26
0.32	1.22	1.22
1.0	1.04	1.07
3.14	1.12	1.13
10.0	1.15	1.16

Figure 7.15 shows an example of the results for the monthly load profiles. By considering the horizontal pipes, the load profile can be increased according to the factors in Table 7.4 so that at the end of the design period the exact same monthly average fluid temperatures are achieved as without considering the pipes.

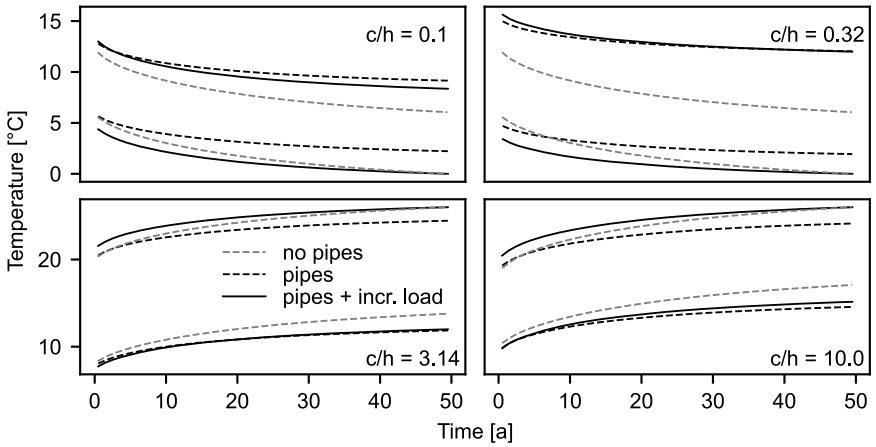

Figure 7.15 Envelope of the monthly averaged fluid temperatures entering the BHE field for the monthly load profiles including the increased load profiles according to Table 7.4

7.4.4 Optimised operation

The previous sections have shown that neglecting the horizontal pipes in the design leads to an oversized system that allows for higher loads or longer operational times. In this section, we investigate whether the oversized system can be used more efficiently by applying an optimised operating strategy.

Figure 7.16 shows detailed results for the second year of operation for the c/h = 3.14 case and the monthly load profile. The top part shows the fluid temperature entering the BHE field for

the case with all BHEs operating and the optimal number of BHEs operating. The middle part shows the corresponding COP while the bottom part shows the electricity consumption of the heat and circulation pump. By not running all BHEs, the fluid temperatures decrease during heating (first two and last three months, see also Figure 7.3) and increase during cooling. This results in a reduced COP of the heat pump and therefore increased electricity consumption, which is however compensated by the reduced electricity consumption of the circulation pump. For the period shown here the total electricity consumption if all BHEs are on at all times is 78 755 kW h while for the optimised number of BHEs operating it is just 69 211 kW h which corresponds to a reduction of 12 %.

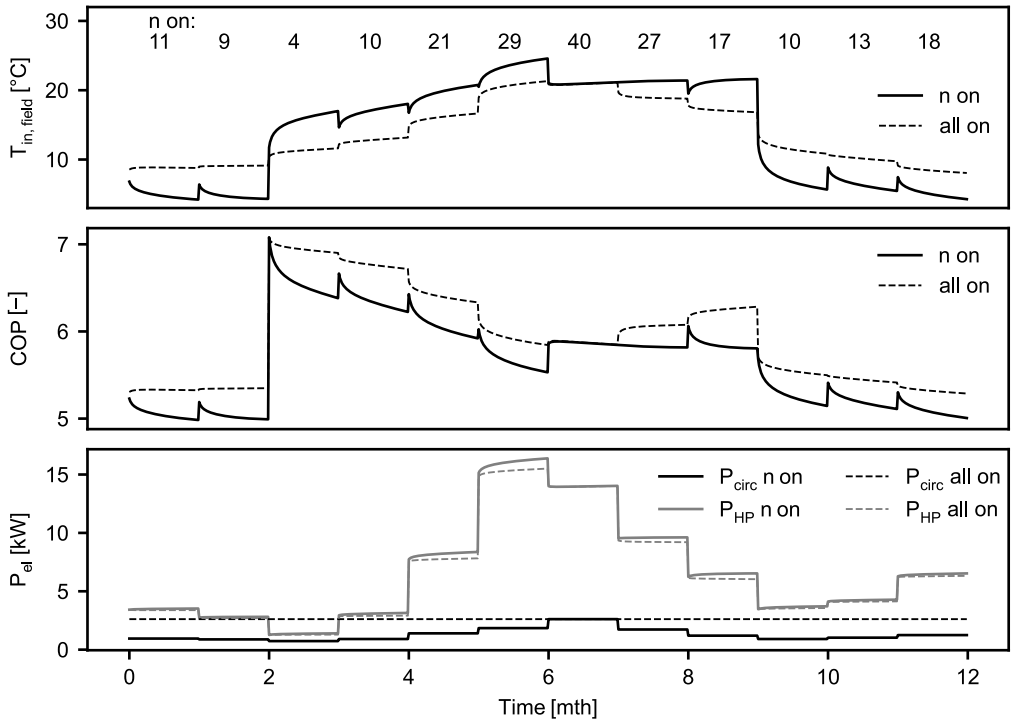

Figure 7.16 Detailed results for the second year of the c/h = 3.14 case with monthly loads.

For better clarity we limit the analysis for all cases and the full 50 year period to annual values as shown in Figure 7.17. The left column shows the monthly averaged temperatures entering the BHE field of the month with the highest respectively lowest fluid temperature. The *no pipes* curves correspond to the scenario where the horizontal pipes are neglected, while the *pipes* curves show the fluid temperatures with consideration of the horizontal pipes. The *pipes, n on* curves finally show the fluid temperatures with some BHEs operating. The operation with less BHEs exploits the temperature reserve induced by the horizontal pipes, while staying within the temperature limits at all times. The right column of Figure 7.17 shows the average annual electricity demand. The potential electricity savings are summarised in Table 7.5.

The proposed operating strategy works well with the monthly load profiles. The average monthly load used as input to the predictive model corresponds exactly to the load used

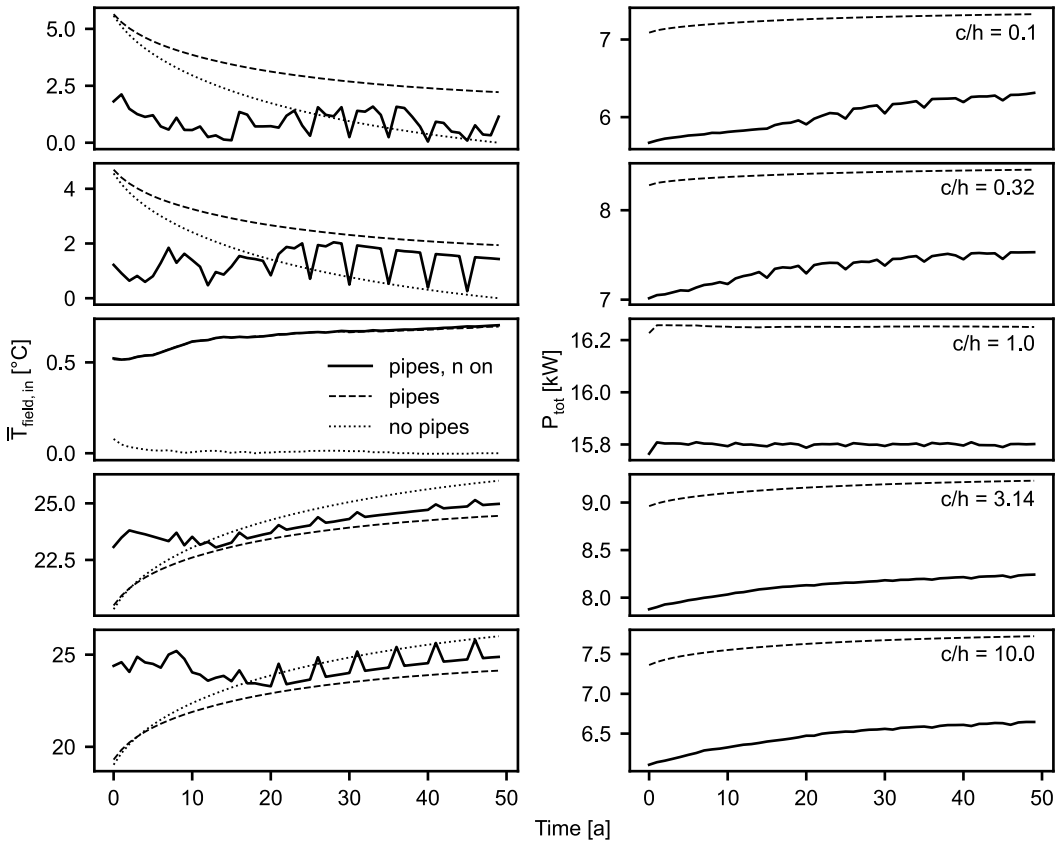

Figure 7.17 Monthly averaged fluid inlet temperatures of the critical month (left) and total electricity consumption (right) for the monthly load profiles and the optimised operating strategy.

Table 7.5 Electricity savings with optimised operation strategy and the monthly load profiles.

c/h ratio	electricity reduction %
0.1	17
0.32	12
1.0	3
3.14	11
10.0	15

later in the simulator model. Therefore, the predictive model is able to predict the fluid temperatures sufficiently accurately with significantly fewer calculation steps. However, applying the same approach to the hourly load profiles will result in temperature overshoots and even increased electricity consumption in some cases. Using a monthly average of the hourly load profile for the predictor model underestimates the BHE demand, especially when both heating and cooling loads are averaged. This is shown in the top part of Figure 7.18 on the example of the c/h = 3.14 scenario.

The critical temperatures are particularly violated during the third month, where both heating and cooling loads occur (compare Figure 7.3). Table 7.6 a) summarises the results

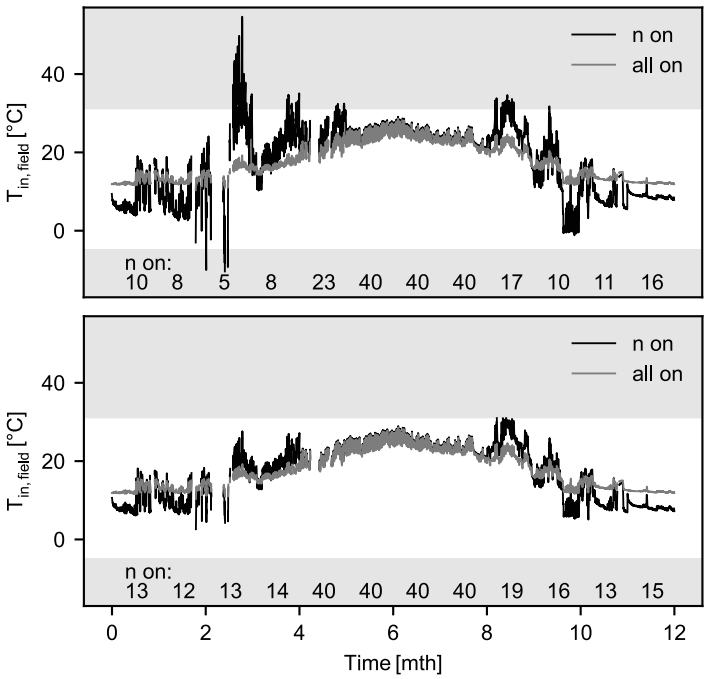

Figure 7.18 Fluid inlet temperature of the BHE field for a one year period with all BHEs operating and the optimised operating strategy based on monthly averaged loads (top) and monthly averaged dominant loads (bottom). Range of critical fluid temperatures highlighted in grey.

for all other c/h ratios. For the c/h = 1.0 scenario, the optimised operating strategy results even in an increased electricity consumption of 3 %, while the for the c/h = 10.0 scenario the critical fluid temperatures are violated during 14.1 % of the operational hours. In order to avoid underestimating the absolute loads by averaging heating and cooling loads within one month, we adjusted the input of the predictor model. Instead of using the average load of the whole month, we average heating and cooling loads within the month separately and use the dominant average as input for the predictor model. Exemplary results are shown in the bottom part of Figure 7.18, note the increased number of BHEs operating most months. The results listed under b) in Table 7.6 show that the temperature constrain violations are greatly reduced and the electricity reduction is increased in most cases. In a final approach to prevent any temperature violations, we implemented a function in the simulation model, that activates two additional BHEs if 90 % of the critical fluid temperature is reached. The results are listed under c) in Table 7.6. For the unbalanced load profiles, the temperature violations could be reduced by one order of magnitude with just 1-4 additional control events (switching on additional BHEs) per year, while for the balanced profile the number of control events almost doubled.

Figure 7.19 finally shows the results for the hourly load profiles in the same way as in Figure 7.17, here for the prediction based on the monthly average of the dominant load type (Table 7.6 c)).

Table 7.6 Electricity reduction [%], operating hours [%] in which the critical fluid temperatures were exceeded and average number of control events per year.

	elect. reduction			temp. violation			control events		
c/h ratio	a)	b)	c)	a)	b)	c)	a)	b)	c)
0.1	10	12	12	5.0	0.004	0.0	12	12	13
0.32	8	9	9	2.7	0.05	0.004	12	12	13
1.0	−3	2	2	7.2	0.4	0.009	12	12	23
3.14	9	9	13	2.3	0.15	0.003	12	12	15
10.0	11	13	13	14.1	0.1	0.001	12	12	16

[a)] prediction based on monthly average
[b)] prediction based on monthly average of dominant load type
[c)] prediction based on monthly average of dominant load type + additional control events

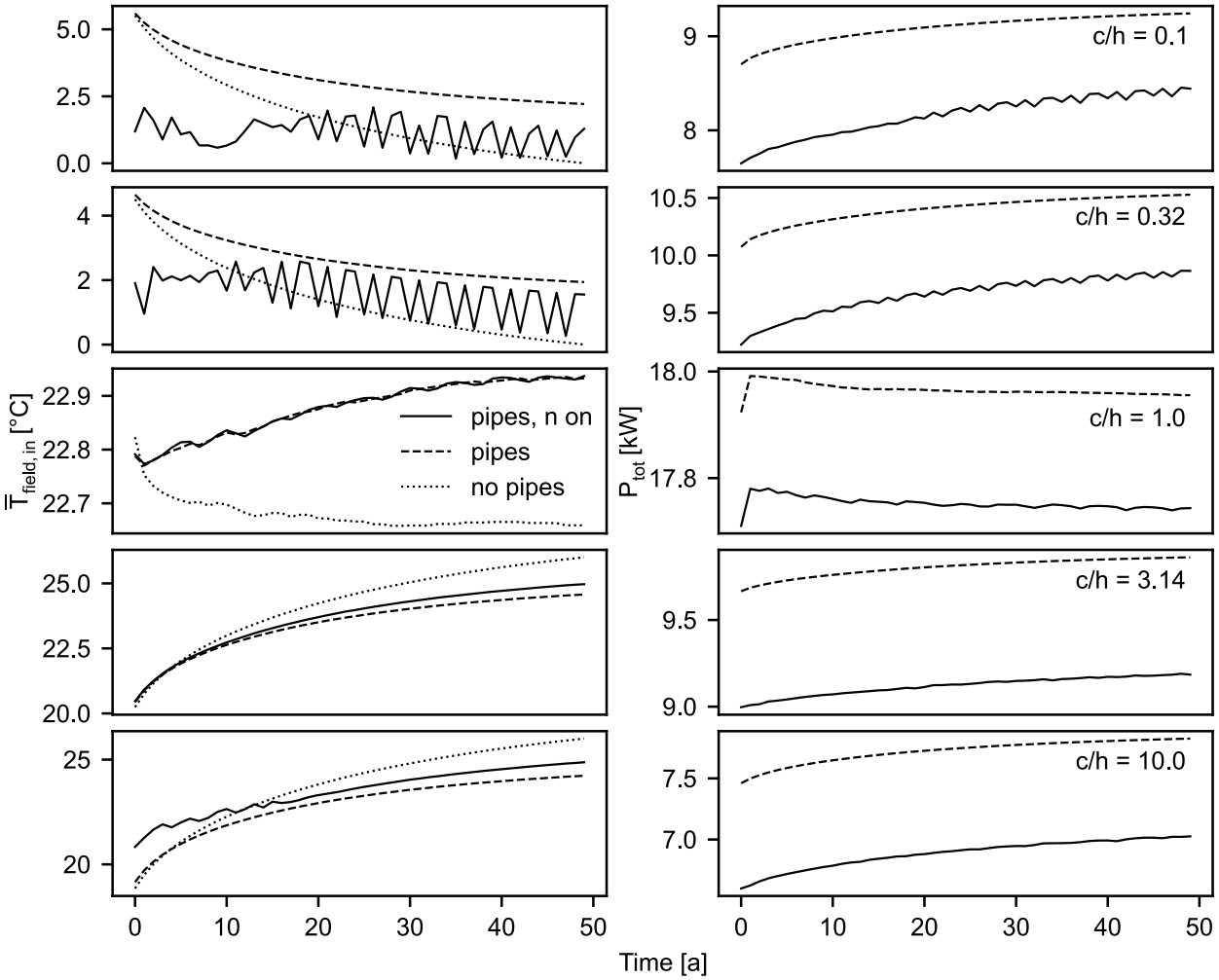

Figure 7.19 Monthly averaged fluid inlet temperatures of the critical month (left) and total electricity consumption (right) for the hourly load profiles and the optimised operating strategy.

7.5 Conclusions

We investigated three ways to utilise the additional capacity of BHE fields due to the gains along horizontal connection pipes. The analysis with load profiles with different heating to cooling ratios showed that the more unbalanced the load profile, the greater the effect of the horizontal pipes. In fact, the effect of the pipes in combination with the perfectly balanced profile was almost negligible.

The German technical guideline VDI 4640 VDI 4640-2 (2019) requires that borehole heat exchangers are designed to ensure that the temperature of the fluid does not exceed certain limits during the operating period, which is typically 50 years. The investigations on longer operation revealed that even after 75 years of operation the critical temperatures were not reached for all scenarios, due to the additional gains along the connection pipes. Prolonging the (efficient) operation of existing BHE fields with a constant load profile is therefore a valid option to utilise the capacity gain from the connecting pipes.

Instead of extended operation, the thermal load can be increased (or conversely, the number of BHEs can be decreased in a new built situation). For the case c/h = 0.1, the load profile could be increased by 26 %, while for the case c/h = 1.0 it was only 4 %. The question here is to what extent this is possible in practice. With monovalent design, the BHE field is designed for the given building load, which is rather constant for many types of use and cannot be increased. If a BHE field is used mainly for cooling, the building loads may increase steadily due to climate change. In this case, the additional reserves provided by the connection pipes could ensure efficient operation. In a bivalent system, the share of geothermal energy can be increased according to the capacity reserve.

The investigations into the optimised operating strategy are based on the assumption that the number of BHEs operated and the flow rate of the circulation pump can be adjusted as required and that the energy demand for the optimisation period can be predicted with sufficient accuracy. By adjusting the number of BHEs operated on a monthly basis, the power demand could be reduced by up to 13 %. However, it was found that the critical fluid temperatures for the hourly load profiles were exceeded, but this occurred in less than 1 % of the operating hours. If the above conditions for an optimised operating strategy are met, it is a valid possibility to use the heat gains along the connection pipes to reduce operating costs in existing systems.

Finally, the results can be summarized as:

- Horizontal connection pipes (of considerable length) that were neglected in the design phase of a BHE field lead to additional heat exchange capacity.
- The effect of horizontal connecting lines is greatest with unbalanced load profiles, as the soil near the surface regenerates thermally more quickly.

- Unbalanced load profiles lead to temperature accumulation in the ground and at the BHE. This process is slowed down by taking the connecting pipes into account and the system can be operated in the intended temperature range for longer.
- The additional heat exchange along the connection pipes means that the thermal loads can be increased while maintaining the desired temperature range.
- The additional capacity due to the connection pipes theoretically leads to an oversized system. In this case, electrical energy can be saved under certain conditions by means of an optimised operating strategy.

As stated above, each of the investigated options has its requirements. The *longer operation* is most relevant for unbalanced load profiles with heat accumulation/depletion. The *higher loads* option is only applicable, if the actual loads can be adjusted, while the *optimised operation* requires control over individual BHEs and total flow rate as well as predictable loads. Under suitable boundary conditions, the options can also be combined as required.

Chapter 8

Using thermal response factors with variable thermal properties

Published as:

Düber S., Fuentes R., Narsilio G. (2024): Using thermal response factors with time dependent thermal properties. *Geothermics*, 119, art. no. 102957.

Düber S.: Conceptualization, Methodology, Software, Validation, Writing - Original Draft **Fuentes R.:** Writing - Review & Editing, Supervision **Narsilio G.A.:** Writing - Review & Editing, Supervision.

Abstract

This paper presents a simple and fast methodology to consider changing thermal properties in, for example, the design of shallow geothermal systems, by using thermal response factors. The simulation period is split into multiple sections according to the changes in thermal properties. By transforming the temperature response from one section to the next and subsequent superposition, any changes in the thermal conductivity properties of the media through which heat travels can be taken into account. The method is verified by numerical simulation and its efficiency is demonstrated in an application example. Results show that even though the computational effort increases exponentially with the variation of thermal parameters in time, the computational time is significantly shorter than comparable numerical simulations.

8.1 Introduction

Thermal response factors, also known as g-functions (Eskilson, 1987), are one of the main methods for designing shallow geothermal systems such as borehole heat exchangers, energy piles or horizontal geothermal collectors. The g-functions describe the dimensionless, time-dependent thermal resistance of the ground and allow the calculation of temperature changes due to heat conduction (Ingersoll et al., 1954):

$$\Delta T(t) = \frac{q}{2\pi\lambda} \cdot g(t). \tag{8.1}$$

Here λ is the thermal conductivity of the ground, q the thermal load, and g is the g-function of the heat exchanger, depending on its geometry and a dimensionless time. Starting from the infinite line source (Ingersoll et al., 1954), more and more analytical approaches have been developed in recent years to calculate the g-functions. For borehole heat exchangers and energy piles, the heat source radius (Man et al., 2010), finite length and surface effects (Rivera et al., 2016; Zeng et al., 2002), groundwater flow (Molina-Giraldo et al., 2011), layered soil types (Abdelaziz et al., 2014) and more realistic interaction between multiple boreholes (Cimmino and Bernier, 2014) can now be considered. Approaches for horizontal collectors can also take into account different geometries such as the slinky heat exchanger (H. Li et al., 2012) and the finite length of the pipes (Lamarche, 2019).

All of the approaches described above assume though that the thermal properties of the ground are constant over time. This assumption is generally justified in many cases, especially for deeper systems. However, it may be too simplistic for e.g., horizontal geothermal collectors or even energy piles, since the thermal properties may vary because of ground moisture content fluctuations due to seasonal changes or climate change (Leong et al., 1998). In these

cases, time-demanding, more complex, numerical models are necessary to obtain an accurate response (Gan, 2019; Piechowski, 1999).

This paper fills this gap and presents a simple method to account for changing thermal properties using the thermal response factor method. The methodology is presented in detail in section 8.2, followed by a verification and application example in section 8.3, and finishing with conclusions in section 8.4. A Python implementation of the proposed method is available online (Düber, 2023).

8.2 Methodology

The proposed method works with any type of g-function, but for illustration purposes, we use here a single buried pipe, for which the g-function is calculated using the horizontal finite line source (HFLS) as shown in Eq. 8.2. For more details on the derivation of Eq. 8.2, we refer the reader to the work of Lamarche (2019).

$$g(t) = \int_{\frac{1}{\sqrt{4\alpha t}}}^{\infty} \frac{\left(e^{-r^2 s^2} - e^{-(r^2+4z^2)s^2}\right)}{Hs^2} \left[Hs\,\mathrm{erf}(Hs) - \frac{1}{\sqrt{\pi}}\left(1 - e^{-H^2 s^2}\right)\right] ds. \tag{8.2}$$

Here α denotes the thermal diffusivity of the ground, t the time, H the length of the line source, z its depth and r the horizontal distance where the temperature is evaluated. The temperature change $\Delta T(t)$ due to a time-varying thermal load $q(t)$ is calculated using the g-function method and the superposition principle (Carslaw and Jaeger, 1959) as:

$$\Delta T(t_k) = \frac{1}{2\pi\lambda} \sum_{i=1}^{k} \Delta q(t_i) \cdot g(t_{k-i+1}) \tag{8.3}$$

where $\Delta q(t_i) = q(t_i) - q(t_{i-1})$ is the load increment, λ is the thermal conductivity of the ground and g the g-function according to Equation 8.2.

Neither Equation 8.3 nor the formulation of the g-function account for time dependent thermal properties of the ground. It means that, applying Equation 8.3 for a constant load $q(t)$ for $t_{\mathrm{start}} \leq t \leq t_{\mathrm{c}}$ results in a $\Delta T(t)$ as shown in the top part of Figure 8.1.

However, in reality, the thermal properties of the ground can change. Hence, if the thermal diffusivity α of the ground changes instantaneously at $t = t_{\mathrm{c}}$, this change will only affect the temperature decay for $t > t_{\mathrm{c}}$, as shown conceptually in the bottom part of Figure 8.1.

As the temperatures for $t > t_{\mathrm{c}}$ have been calculated using Equation 8.3 for α_1, we suggest that there is no need to recalculate them for α_2. In fact, we propose that the change of α only causes a compression or stretching of the already calculated temperature change along the time axis. Hence, we can write for $t > t_{\mathrm{c}}$:

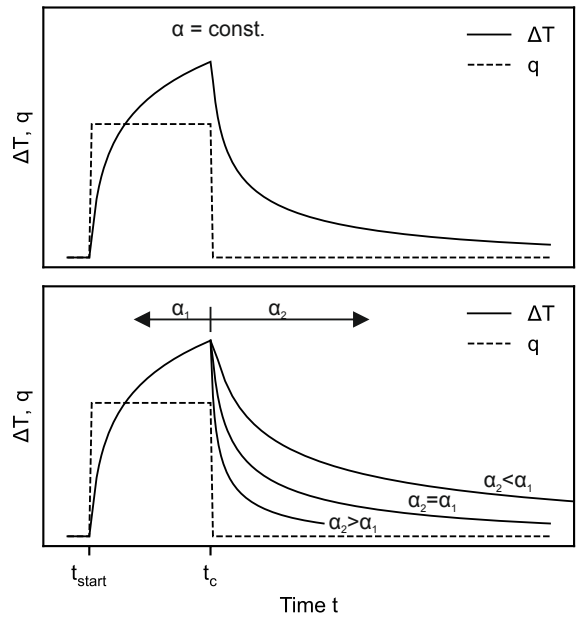

Figure 8.1 Temperature change ΔT according to a constant load q between t_{start} and t_{c} for a typically assumed constant thermal parameter α of the heat transfer medium (top) and for the case when α changes for $t > t_{\mathrm{c}}$ (bottom).

$$\Delta T(\alpha_2, t) = \Delta T(\alpha_1, t\frac{\alpha_1}{\alpha_2} - t_{\mathrm{c}}(\frac{\alpha_1}{\alpha_2} - 1)). \tag{8.4}$$

The factor $\frac{\alpha_1}{\alpha_2}$ accounts for a time stretching/compression of the temperature curve while $t_{\mathrm{c}}(\frac{\alpha_1}{\alpha_2} - 1)$ corrects for the thereby introduced offset.

Figure 8.2 shows conceptually what happens if the thermal property reduces from α_1 to α_2 at time $t = t_{\mathrm{c}}$ (see solid line). The temperature will grow faster from $t = t_{\mathrm{c}}$ until the time when $q = 0$, from which it will start a normal decay. The resulting curve is the superposition of the ΔT calculated using Equation 8.3 for α_1, from $t = t_{\mathrm{start}}$ to $t = t_{\mathrm{c}}$, plus the same temperature response transformed for $t > t_{\mathrm{c}}$, plus one calculated for α_2 from $t = t_{\mathrm{c}}$ onward.

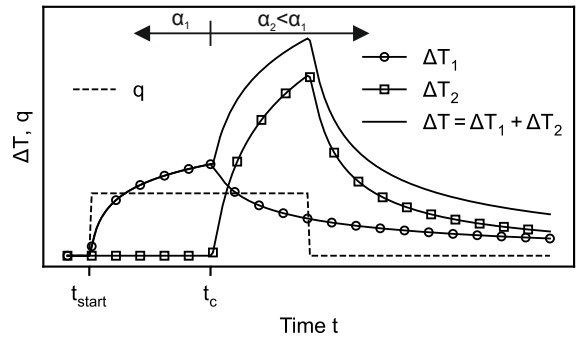

Figure 8.2 Temperature change for a constant load with changing α at t_{c} as the sum of ΔT_1 and ΔT_2.

The method described can be used for any type of thermal load profile and for any variation in thermal conductivity or heat capacity. For an efficient implementation, we use the Fast

Fourier Transform (FFT) as presented by (Marcotte and Pasquier, 2008), which replaces the summation over time in Equation 8.3 with a single multiplication in the Fourier domain:

$$\Delta T = \mathscr{F}^{-1}\left(\mathscr{F}\left(\frac{\Delta q}{2\pi\lambda}\right)\cdot\mathscr{F}(g)\right) \tag{8.5}$$

where $\mathscr{F}$ is the direct and $\mathscr{F}^{-1}$ the inverse FFT. To ensure that Equation 8.4 can be applied for any change in α, the simulation period must be extended. An increase in α results in a compression of the temperature response along the time axis, as can be seen in the bottom part of Figure 8.1. To ensure that the transformed temperature response covers the entire simulation period, the maximum time $t_{\max}$ must be increased to $t'_{\max}$ as:

$$t'_{\max} = \max(\{f(\alpha_j) : j = 1, \ldots, n\}) \tag{8.6}$$

with:

$$f(\alpha_j) = \frac{1}{\alpha_j}\left(\sum_{i=j}^{n-1}\alpha_i t_{\mathrm{c},i+1} - \sum_{i=j+1}^{n}\alpha_i t_{\mathrm{c},i} + \alpha_n t_{\max}\right) \tag{8.7}$$

where n stands for the number of changes in α and $t_{\mathrm{c},i}$ for the times at which α changes. Finally, the implementation follows the flowchart presented in Figure 8.3.

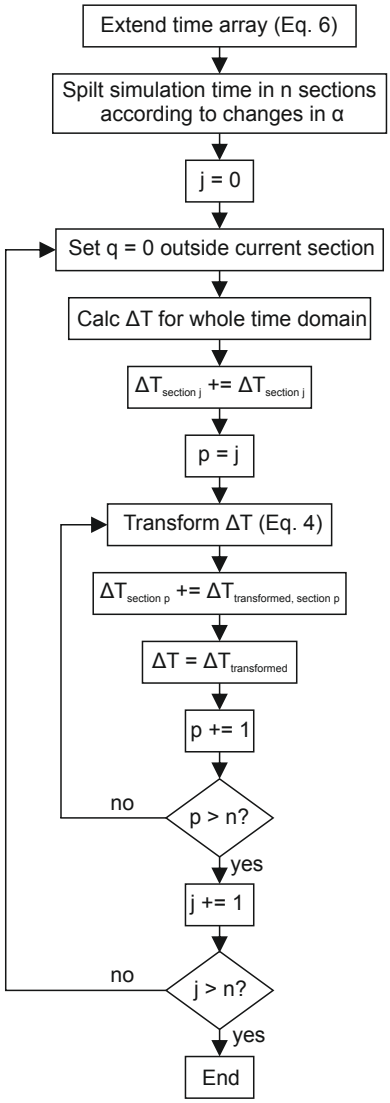

Figure 8.3 Flowchart for the algorithm to account for arbitrary variations of α.

8.3 Verification and application

To verify the described approach, we compare it to a simulation using a 2D numerical finite volume model. The numerical model is spatially discretised with 600×600 cells each 10×10 mm in size. The temperatures on the cell walls are calculated using the central difference scheme while the explicit Euler scheme is used for the numerical integration. All parameters and boundary conditions are listed in Table 8.1. A large value was chosen for the length of the line source to minimise the influence of the finite length, which is not considered in the 2D numerical model. The radius in Table 8.1 denotes the horizontal distance from the line source where the temperature is evaluated. Using two thermal property changes over the calculation period, the results in Figure 8.4 show perfect agreement between the numerical simulation and our approach. The numerical simulation took 181 s on a standard personal

computer, while the computational time for the analytical approach was just 1.5 s.

Table 8.1 Parameters used for verification simulation.

Parameter	Symbol	Value	Units
HFLS length	H	500	m
HFLS depth	z	0.85	m
Radius	r	0.2	m
Thermal load	q	30	$\mathrm{W\,m^{-1}}$
Thermal conductivity	λ	1.0 for $t < t_{c,1}$ 2.0 for $t_{c,1} \leq t < t_{c,2}$ 1.5 for $t \geq t_{c,2}$	$\mathrm{W\,m^{-1}\,K^{-1}}$
Volumetric heat capacity	ρc	1 000 000	$\mathrm{J\,m^{-3}\,K^{-1}}$
Simulation time	$t_{\max}$	35	h
Time step	Δt	12.5	s
Time of change 1	$t_{c,1}$	41 675	s
Time of change 2	$t_{c,2}$	83 337.5	s

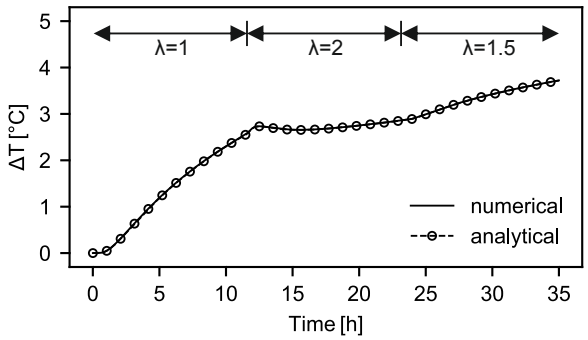

Figure 8.4 Comparison of the proposed method with a numerical finite volume simulation.

To show how the method performs for a realistic scenario, we consider a single pipe of a horizontal geothermal collector buried 1.2 m below the surface exposed to the hourly load profile shown in Figure 8.5. The load profile is derived from measurements of an operating geothermal system in Germany, all other parameters are given in Table 8.2.

For the ground it is assumed that the thermal properties change seasonally due to a change in the water content of the ground. The ground water content over central-western Europe can be approximated with a sinusoidal curve (Van der Linden et al., 2019). Here we assume for the thermal conductivity λ a value of $1.0\,\mathrm{W\,m^{-1}\,K^{-1}}$ for the dry and $2.2\,\mathrm{W\,m^{-1}\,K^{-1}}$ for the fully saturated case. The volumetric heat capacity ρc is considered to be $1.5\,\mathrm{MJ\,m^{-3}\,K^{-1}}$ for the dry and $2.2\,\mathrm{MJ\,m^{-3}\,K^{-1}}$ for the fully saturated case, resulting in the profile shown in Figure 8.6. For the design or simulation of a real geothermal system, these values would ideally have to be measured. To understand the importance of ground property variations,

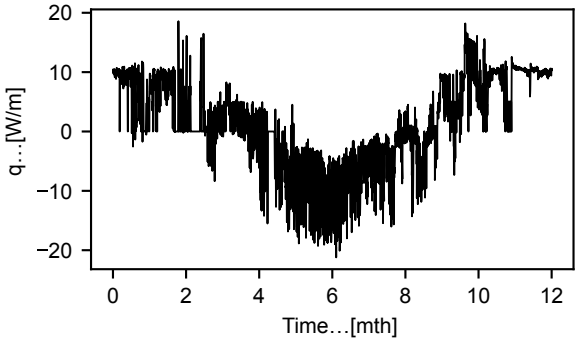

Figure 8.5 Hourly load profile used for the application example.

Table 8.2 Parameters used for the application example.

Parameter	Symbol	Value	Units
HFLS length	H	20	m
HFLS depth	z	1.2	m
Radius	r	0.02	m
Thermal conductivity	λ	see Figure 8.6	
Volumetric heat capacity	ρc	see Figure 8.6	
Simulation time	$t_{\max}$	8760	h
Time step	Δt	1200	s

we approximate the profile of the thermal properties with daily, monthly and three-monthly averages, resulting in 4, 12 and 365 values for α in the simulation. As we are only interested in the effect of the changes in the thermal properties, we neglect the course of the undisturbed ground temperature and restrict the analysis to the temperature change at the outside of the pipe introduced by the heat exchanger.

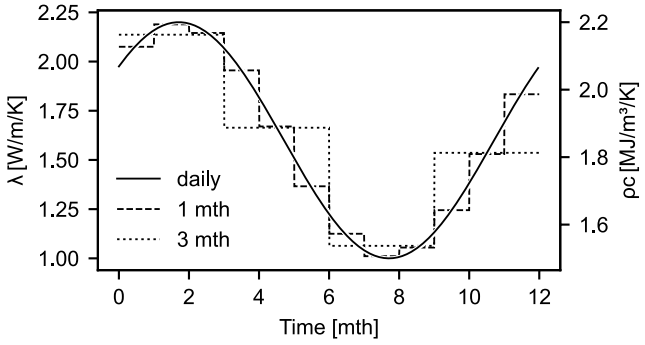

Figure 8.6 Sinusoidal approximation of annual profile of the thermal properties. Daily, monthly and 3 monthly averaged values used as input for the simulation.

The top part of Figure 8.7 shows the results for the simulation with averaged thermal properties ($\lambda = 1.6\,\mathrm{W\,m^{-1}\,K^{-1}}$, $\rho c = 1.85\,\mathrm{MJ\,m^{-3}\,K^{-1}}$) for the whole simulation period as

reference. The lower parts show the temperature difference introduced by considering the different time resolution for changes in thermal properties. For the scenarios with 4 and 12 different values of α, the changes are clearly visible compared to the smooth curve for 365 values of α. The temperature difference introduced by the change in thermal properties is more than 2 °C, which is almost half of the temperature change caused by the heat exchanger when considering averaged properties (Figure 8.7, top).

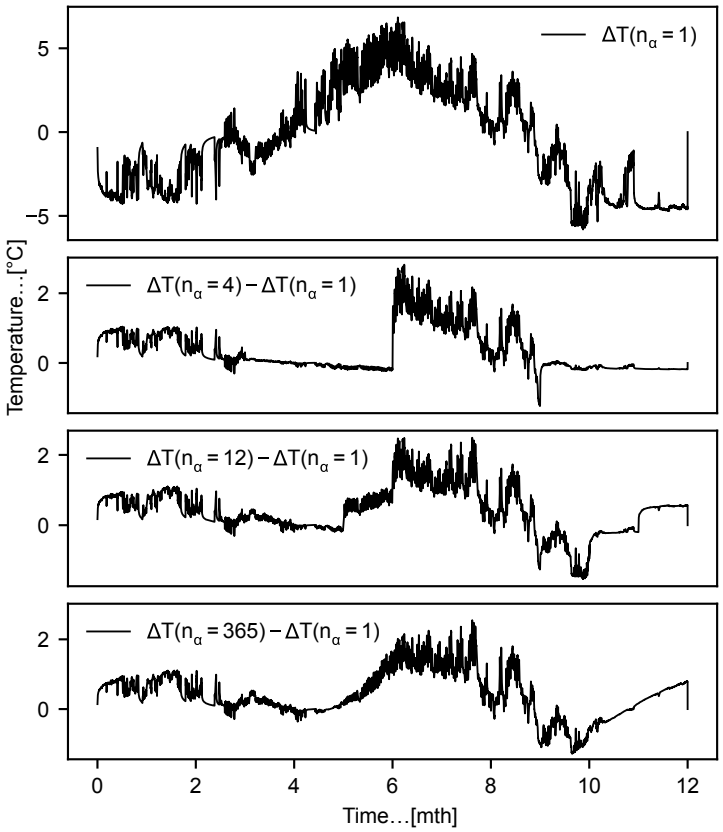

Figure 8.7 Results of the application example with n_α values for α for the simulation period.

Finally, Table 8.3 shows the computational times of the proposed method compared to a 2D numerical model consisting of 1124 triangular elements simulated with the finite element software COMSOL Multiphysics^{TM}. The computational times of the proposed method increase exponentially with the number of changes in α. This is because for each change, the response has to be transformed (Equation 8.4) for all subsequent values of α. However, even with daily updated values the total computation time is still only 44.8 s, clearly superior to the numerical simulation.

Table 8.3 Computational times [s] depending on the number of values for α.

n_α	proposed method	2D numerical model
1	0.017	162
4	0.065	335
12	0.31	341
365	44.8	404

8.4 Conclusions

The use of thermal response factors is widespread in the simulation of shallow geothermal systems. While the thermal properties of the ground are rightly assumed to be constant for the simulation of borehole heat exchangers, typically 100 m or deeper, they can vary closer to the surface for a number of reasons over the life-time operation. This change, caused, for example, by varying groundwater levels or moisture content, can be relevant for systems such as horizontal geothermal collectors or shorter energy piles.

The proposed approach is a simple, yet efficient, method to account for changing thermal properties using the response factor method. One limitation is that the change in thermal properties is homogeneous, which is a simplification of the actual conditions. By dividing the simulation domain into several sections according to the changes in thermal properties and applying the superposition principle, arbitrary variations in thermal properties can be considered. The computational effort increases exponentially with the number of changes, but it is still considered superior to numerical simulations in many cases.

Chapter 9

Summary and future work

When constructing large geothermal fields with dozens or hundreds of BHEs, the distances between the boreholes and the manifolds or the building must be bridged by horizontal connection pipes. The heat transfer along these near-surface pipes is usually not considered in the thermal design. One of the advantages of BHEs, with a typical depth of around 100 m, is the constant temperature in the ground at this depth throughout the year. In contrast, the connection pipes are laid closer to the surface at a depth of 1-2 m in a frost-free zone, depending on the climate. At this depth, the ground temperature follows the annual air temperature profile with a time lag and damped amplitude. This results in different ground temperatures along the horizontal connection pipes and the BHEs depending on the season and climate. According to the operating state of the system (heating or cooling), heat gains or losses may occur along the connection pipes. The simulation and consequences of these effects are the subject of this work.

Chapter 3 presents a method for the efficient simulation of BHE fields with small time steps. In the approach presented, heat transfer in the soil is modelled using thermal response functions. Time-varying loads are considered by superposition of temperature responses due to load increments within this method. This results in an exponential increase in computational time for a linear increase in the number of time steps. To significantly minimise this computational expense, the presented method divides the simulation time into several periods. The thermal influence of previous periods on subsequent periods is calculated using the convolution theorem and FFT. This reduces the summation of the temperature responses of each load increment to a single array multiplication and significantly reduces the computational time. For example, the computational time of the investigated BHE field with 40 BHEs and approximately 1 million time steps was reduced from 873 h to 14 h. Furthermore, equations were derived and validated to calculate the optimal number of periods for any number of time steps based on the measured computation times.

In Chapter 4, the heat transfer along horizontal connection pipes is investigated using monitoring data from an operating BHE field. Since the fluid temperatures are only recorded in the manifolds, the heat transfer along the connection pipes cannot be derived directly from the measured data. Therefore, a method is developed to determine the heat gains and losses along the pipes using reference BHEs. The results are compared with a simplified

calculation approach, which in some cases shows significant deviations. The reasons for these deviations cannot be clearly identified. On the one hand, the calculation approach neglects the temperature accumulation in the ground, and on the other hand, the calculation of the undisturbed ground temperature at the pipes is subject to uncertainties due to the available data. For further analysis, the heat gain profiles of the individual connection pipes are approximated with sinusoidal curves. To gain further insight into the decisive factors influencing the heat transfer along the connection pipes a multiple linear regression analysis is performed. The result shows that the hours of sunshine above the pipes have the greatest influence. Further analysis is difficult due to the many uncertainties in the data. For example, it is unclear to what extent the tabulated burial depths correspond to reality. Nevertheless, the analysis shows the effect of the horizontal connection pipes based on monitoring data of an operating system as well as a methodology to determine the heat transfer based on inlet and outlet temperatures in the manifolds.

In Chapter 5, different simulation models for the horizontal connection pipes and the surrounding ground are implemented and compared. The results are used to formulate a simplified analytical model based on thermal resistances and response functions. By using response functions for the heat transfer in the ground, the method of dividing the simulation time into multiple periods developed in Chapter 3 is applied again to reduce the computational time. The new model is then used in Chapter 6 to investigate the influence of horizontal connection pipes under different climatic conditions. Air temperatures for a typical meteorological year from 25 climate zones were used to derive the ground temperatures along the connection pipes and boreholes and to determine the thermal loads of the building. To ensure comparability, a number of factors were ignored, such as different construction methods in different climates, surface coverage, different burial depths and heat transfer processes other than conduction. Despite the assumptions and simplifications made, it could be shown that in almost all climate zones the connection pipes had a positive effect and could reduce the required borehole length or increase the capacity of the system. A clear trend was observed: the smaller the amplitude in the annual air temperature profile, the greater the BHE thermal load reduction due to the connection pipes.

The study in Chapter 6 shows potential savings that can be achieved if the horizontal connection pipes are considered at the design stage. Using the BHE field at the E.ON ERC as an example, the following Chapter 7 examines how the capacity gain resulting from the horizontal pipes, which were neglected in the design phase, can be used in already operational fields. Load profiles with different cooling to heating ratios were investigated and it was found that the more unbalanced the load profile, the greater the positive effect of the connection pipes. The unbalanced load profiles result in a temperature accumulation in the ground around the BHEs. The ground continues to heat up or cool down over several years until either a thermal equilibrium is reached or the critical fluid temperatures of the heat pump are reached preventing further operation. Along the horizontal pipes however, the thermal

regeneration of the ground happens faster than at the BHEs, due to the shallow burial depth. This increases the positive effects of the connection pipes for such load profiles. In the scenarios studied, the operational time of the BHE field could be extended by over 25 years without violating the critical design temperatures. Alternatively, the load could be increased by up to 26 % resulting in the same temperatures as planned in the design. In addition, an operational optimisation study showed that up to 13 % of the electrical energy of the circulation pump could be saved by controlled partial operation of the field. However, in order to actually implement the operating strategy tested in the simulation, it is necessary to have control over all BHEs and the circulation pump, as well as an accurate prediction of the expected thermal loads. This optimisation strategy may work well in monovalent systems, where the entire building thermal load is supplied by the geothermal system. Therefore, the system needs to be designed for peak loads, even if these only occur for a few hours or days of a year. For any other time with lower loads, the system is oversized accordingly. A comparable effect is achieved by neglected horizontal connection pipes in the design phase. If the loads during the operation correspond to those from the design phase, the system is oversized and partial operation can lead to energy savings.

In Chapter 8, a new method to account for time-varying thermal conductivity properties using the response function method is presented. Especially in the shallow ground, variations in water content can lead to varying thermal properties. This can be relevant for heat transfer along horizontal connection pipes in BHE fields. Other applications include the simulation of horizontal geothermal collectors, buried power cables or other pipelines. Even energy geostructures with shallow embedment depths, such as energy pile foundations, can experience changes in groundwater level as a result of climate change or seasonal variations. The presented method is again based on the temporal superposition of temperature responses. It takes advantage of the fact that a change in thermal conductivity properties only stretches or compresses the temperature response along the time axis. This means that temperature responses for different thermal properties can be transformed with a factor and then superimposed. The method is superior to numerical methods in terms of computational time while delivering the accuracy of exact analytical solutions. However, a limitation is that the change in thermal conductivity is homogeneous, i.e. it occurs simultaneously throughout the considered space or half-space.

In Chapter 5, a numerical pipe model was coupled with the hybrid BHE model from Chapter 3 to model the transient fluid flow in both the connection pipes and the BHE. However, for all subsequent investigations in Chapters 6 and 7, the steady-state model based on thermal resistances was used. On the one hand, the steady-state model was chosen because of its better computational efficiency. On the other hand, the combinations of borehole, pipe, and flow properties as well as the hourly load profiles were consistent with the steady-state assumption.

Finally, the question arises as to whether technical guidelines and national codes should be adapted to take account of heat transfer along the horizontal connection pipes in borehole heat exchanger fields. The following points should be noted:

- Heat exchange along the connection pipe reduces the thermal load on the borehole heat exchanger in many scenarios and can therefore lead to a reduced depth or number of boreholes required. This can potentially lower costs and make borehole heat exchangers more attractive.
- If neglected in the design phase, the connection pipes lead to hidden capacity reserves. This can be advantageous if the thermal loads in operation are higher than planned, as the system can then still be operated efficiently due to the additional capacity.
- The bundling of many connection pipes in a shared trench considerably reduces the heat exchange per pipe due to the thermal interaction; this must be taken into account when considering the connection pipes.
- The effects of the horizontal connection pipes in natural cooling still need to be investigated.

If the above points are taken into account, it may be worthwhile to consider heat transfer along the connection pipes when designing borehole heat exchanger systems. However, their effect needs to be verified by simulation to avoid under-dimensioning. In individual cases, specific boundary conditions such as installation depth, surface conditions above the pipes and properties of the backfill material can also be taken into account. These simulations can be carried out using the calculation models developed in this work.

Further research is needed to investigate the effects of the horizontal connection pipes for natural cooling operation. In the investigations in this thesis all cooling operation was considered active, i.e. involving a heat pump. This means that the heat pump imposes the load profile on the connection pipes and BHEs as long as the critical temperatures are not violated. The case of natural cooling, where the heat pump remains switched off, has not been considered. In that case, the available cooling capacity depends on the temperature difference between the heat source (the building) and the heat sink (the ground). As a result of the cooling operation, the ground heats up and the cooling capacity decreases. The steady-state model from Chapter 5 cannot model natural cooling in its current form, as it uses the ground load as an input parameter. However, this case can easily be investigated with other model combinations presented in the same Chapter. Future work can use these models to extend the results from Chapter 6 and 7 to scenarios with natural cooling.

In order to ensure comparability, the investigations in Chapter 6 were based on weather-dependent loads as they are often found in residential buildings. Other types of building use, or the provision of process heat for industrial processes, may result in different load profiles, e.g. heating in summer or cooling in winter. Extending the analysis of Chapter 6 to such load profiles would be desirable and can be done with the presented models. In addition, further aspects that have so far been neglected could be analysed in more in-depth studies.

As a first step, the temporally variable heat conduction properties of the near-surface ground could be analysed using the method from Chapter 8. Depending on the climate and location, it may also be sensible to consider other heat transfer mechanisms. The cited publications on geothermal collectors provide an initial indication of the expected effects.

As a result of climate change, extreme weather events such as droughts and heavy rainfall are becoming more frequent. These events also affect the water content in the soil at greater depths, impacting vertical geothermal systems like BHEs or energy piles. It is reasonable to investigate the extent to which such events and the associated changes in ground properties can lead to inefficient operation or even failure of these systems. The method described in Chapter 8 is suitable for an initial assessment.

Bibliography

Abdelaziz, S. L., Ozudogru, T. Y., Olgun, C. G., and Martin, J. R. (2014): Multilayer finite line source model for vertical heat exchangers, in: *Geothermics* 51, pp. 406–416, ISSN: 0375-6505, DOI: https://doi.org/10.1016/j.geothermics.2014.03.004.

Ahmadfard, M. and Bernier, M. A. (2019): A review of vertical ground heat exchanger sizing tools including an inter-model comparison, in: *Renewable & Sustainable Energy Reviews* 110, pp. 247–265, ISSN: 1364-0321, DOI: 10.1016/j.rser.2019.04.045.

Alberty, J., Carstensen, C., and Funken, S. A. (1999): Remarks around 50 lines of Matlab: short finite element implementation, in: *Numerical algorithms* 20.2-3, pp. 117–137.

Bahmani, M. H. and Hakkaki-Fard, A. (2022): A hybrid analytical-numerical model for predicting the performance of the Horizontal Ground Heat Exchangers, in: *Geothermics* 101, ISSN: 03756505, DOI: 10.1016/j.geothermics.2022.102369.

Bau, H. H. (1984): Convective heat losses from a pipe buried in a semi-infinite porous medium, in: *International Journal of Heat and Mass Transfer* 27.11, pp. 2047–2056, ISSN: 00179310, DOI: 10.1016/0017-9310(84)90191-1.

Bauer, D., Heidemann, W., Müller-Steinhagen, H., and Diersch, H.-J. G. (2011): Thermal resistance and capacity models for borehole heat exchangers, in: *International Journal of Energy Research* 35.4, pp. 312–320.

Bernier, M. A. (2001): Ground-coupled heat pump system simulation, in: *ASHRAE Transactions* 107, pp. 605–616.

Bernier, M. A., Pinel, P., Labib, R., and Paillot, R. (2004): A multiple load aggregation algorithm for annual hourly simulations of GCHP systems, in: *Hvac&R Research* 10.4, pp. 471–487, ISSN: 1078-9669, DOI: Doi10.1080/10789669.2004.10391115.

Bilke, L., Fischer, T., Naumov, D., Lehmann, C., Wang, W., Lu, R., Meng, B., Rink, K., Grunwald, N., Buchwald, J., Silbermann, C., Habel, R., Günther, L., Mollaali, M., Meisel, T., Randow, J., Einspänner, S., Shao, H., Kurgyis, K., Kolditz, O., and Garibay, J. (2022): OpenGeoSys, version 6.4.3, If you use this software, please cite it using these metadata., DOI: 10.5281/zenodo.7092676.

Bortoloni, M., Bottarelli, M., and Su, Y. H. (2017): A study on the effect of ground surface boundary conditions in modelling shallow ground heat exchangers, in: *Applied Ther-*

mal Engineering 111, pp. 1371–1377, ISSN: 1359-4311, DOI: 10.1016/j.applthermaleng.2016.05.063.

Bose, J. E. (1985): Design/data manual for closed-loop ground-coupled heat pump systems, in: *ASHRAE*.

Carslaw, H. S. and Jaeger, J. C. (1959): Conduction of Heat in Solids, in: *Oxford University*.

Chen, S., Cai, W. L., Witte, F., Wang, X. R., Wang, F. H., Kolditz, O., and Shao, H. B. (2021): Long-term thermal imbalance in large borehole heat exchangers array - A numerical study based on the Leicester project, in: *Energy and Buildings* 231, ISSN: 0378-7788, DOI: ARTN11051810.1016/j.enbuild.2020.110518.

Chen, S., Witte, F., Kolditz, O., and Shao, H. B. (2020): Shifted thermal extraction rates in large Borehole Heat Exchanger array - A numerical experiment, in: *Applied Thermal Engineering* 167, ISSN: 1359-4311, DOI: ARTN11475010.1016/j.applthermaleng.2019.114750.

Christodoulides, P., Vieira, A., Lenart, S., Maranha, J., Vidmar, G., Popov, R., Georgiev, A., Aresti, L., and Florides, G. (2020): Reviewing the Modeling Aspects and Practices of Shallow Geothermal Energy Systems, in: *Energies* 13.16, ISSN: 1996-1073, DOI: 10.3390/en13164273.

Chung, M., Jung, P. S., and Rangel, R. H. (1999): Semi-analytical solution for heat transfer from a buried pipe with convection on the exposed surface, in: *International Journal of Heat and Mass Transfer* 42.20, pp. 3771–3786, ISSN: 0017-9310, DOI: Doi10.1016/S0017-9310(99)00046-0.

Cimmino, M. (2015): The effects of borehole thermal resistances and fluid flow rate on the g-functions of geothermal bore fields, in: *International Journal of Heat and Mass Transfer* 91, pp. 1119–1127, ISSN: 0017-9310, DOI: https://doi.org/10.1016/j.ijheatmasstransfer.2015.08.041.

Cimmino, M. and Bernier, M. A. (2014): A semi-analytical method to generate g-functions for geothermal bore fields, in: *International Journal of Heat and Mass Transfer* 70, pp. 641–650.

Cimmino, M. and Cook, J. C. (2022): pygfunction 2.2 : New Features and Improvements in Accuracy and Computational Efficiency, in: *Research Conference Proceedings, IGSHPA Conference 2022*, International Ground Source Heat Pump Association, pp. 45–52, DOI: 10.22488/okstate.22.000015.

Claesson, J. and Dunand, A. (1983): Heat extraction from the ground by horizontal pipes: a mathematical analysis.

Claesson, J. and Eskilson, P. (1987): Conductive heat extraction by a deep borehole. Analytical studies, in: *Department of Mathematical Physics and Building Technology, Sweden*.

Claesson, J. and Javed, S. (2011): An analytical method to calculate borehole fluid temperatures for time-scales from minutes to decades, English, in: vol. 117, PART 2, ASHRAE, pp. 279–288, ISBN: 9781936504121.

Claesson, J. and Javed, S. (2012): A load-aggregation method to calculate extraction temperatures of borehole heat exchangers, in: *ASHRAE Transactions* 118.1, pp. 530–540.

Clauser, C., Michalski, A., Müller, D., Fütterer, J., and Stinner, F. (2017): Exergetisch optimierte Betriebsführung der Wärme- und Kälteversorgung eines Gebäudes unter Nutzung eines dynamischen Regelungssystems und flexibler Einbindung eines vollständig überwachten Erdwärmesondenfeldes : Endbericht, tech. rep., Aachen: Institute for Energy Efficient Buildings and Indoor Climate.

Community, B. O. (2018): Blender - a 3D modelling and rendering package, Blender Foundation, Stichting Blender Foundation, Amsterdam.

COMSOL AB, Stockholm, Sweden (n.d.): COMSOL Multiphysics, version 6.1, URL: www.comsol.com.

Cui, Y., Zhu, J., Twaha, S., and Riffat, S. (2018): A comprehensive review on 2D and 3D models of vertical ground heat exchangers, in: *Renewable and Sustainable Energy Reviews* 94, pp. 84–114, ISSN: 13640321, DOI: 10.1016/j.rser.2018.05.063.

Cui, Y. L., Zhu, J., Twaha, S., Chu, J. Z., Bai, H. Y., Huang, K., Chen, X. J., Zoras, S., and Soleimani, Z. (2019): Techno-economic assessment of the horizontal geothermal heat pump systems: A comprehensive review, in: *Energy Conversion and Management* 191, pp. 208–236, ISSN: 0196-8904, DOI: 10.1016/j.enconman.2019.04.018.

Dasare, R. R. and Saha, S. K. (2015): Numerical study of horizontal ground heat exchanger for high energy demand applications, in: *Applied Thermal Engineering* 85, pp. 252–263, ISSN: 1359-4311, DOI: 10.1016/j.applthermaleng.2015.04.014.

Diao, N., Li, Q., and Fang, Z. (2004): Heat transfer in ground heat exchangers with groundwater advection, in: *International Journal of Thermal Sciences* 43.12, pp. 1203–1211, ISSN: 12900729, DOI: 10.1016/j.ijthermalsci.2004.04.009.

Diao, N. R., Zeng, H. Y., and Fang, Z. H. (2004): Improvement in Modeling of Heat Transfer in Vertical Ground Heat Exchangers, in: *HVAC&R Research* 10.4, pp. 459–470, ISSN: 1078-9669, DOI: 10.1080/10789669.2004.10391114.

Diersch, H.-J. G. (2013): FEFLOW: finite element modeling of flow, mass and heat transport in porous and fractured media, Springer Science & Business Media.

Diersch, H.-J. G., Bauer, D., Heidemann, W., Rühaak, W., and Schätzl, P. (2010): Finite element formulation for borehole heat exchangers in modeling geothermal heating systems by FEFLOW, in: *WASY Software FEFLOW White Paper* 5, pp. 5–96.

Dinh, B. H., Go, G. H., and Kim, Y. S. (2021): Performance of a horizontal heat exchanger for ground heat pump system: Effects of groundwater level drop with soil-water thermal characteristics, in: *Applied Thermal Engineering* 195, ISSN: 1359-4311, DOI: ARTN11720310.1016/j.applthermaleng.2021.117203.

Düber, S. (2018): Semi-analytisches Werkzeug zur Dimensionierung von Erdwärmesonden, in: *35. Baugrundtagung, Forum für junge Geotechnik-Ingenieure, Beiträge der Spezialsitzung*, Essen: DGGT, pp. 211–220.

Düber, S. (2022): Hybrid simulation model for borehole heat exchangers, Available at https://github.com/GUT-Aachen/Hybrid-BHE-Simulation-Model, version 1.0.0.

Düber, S., Fuentes, R., and Narsilio, G. A. (2023): Effect of horizontal connection pipes on operation of borehole heat exchangers under different climatic conditions, in: *Geothermics* 110, p. 102679, ISSN: 0375-6505, DOI: https://doi.org/10.1016/j.geothermics.2023.102679.

Düber, S., Ziegler, M., and Fuentes, R. (2022): Development and validation of a computationally efficient hybrid model for temporal high-resolution simulations of geothermal bore fields, in: *International Journal for Numerical and Analytical Methods in Geomechanics* 46.14, pp. 2792–2813, DOI: https://doi.org/10.1002/nag.3427.

Düber, S. (2023): varprop_gfunc, version 1.0.0, Available at https://github.com/GUT-Aachen/varprop_gfunc, version 1.0.0, DOI: https://doi.org/10.5281/zenodo.10209359.

Erol, S. and François, B. (2018): Multilayer analytical model for vertical ground heat exchanger with groundwater flow, in: *Geothermics* 71, pp. 294–305, ISSN: 0375-6505, DOI: https://doi.org/10.1016/j.geothermics.2017.09.008.

Eskilson, P. (1987): Thermal analysis of heat extraction boreholes [Ph. D. thesis], in: *Lund, Sweden: University of Lund*.

Eskilson, P. and Claesson, J. (1988): Simulation model for thermally interacting heat extraction boreholes, in: *Numerical heat transfer* 13.2, pp. 149–165.

Farouk, B. and Shayer, H. (1988): Natural Convection Around a Heated Cylinder in a Saturated Porous Medium, in: *Journal of Heat Transfer* 110.3, pp. 642–648, ISSN: 0022-1481 1528-8943, DOI: 10.1115/1.3250540.

Fontaine, P. O., Marcotte, D., Pasquier, P., and Thibodeau, D. (2011): Modeling of horizontal geoexchange systems for building heating and permafrost stabilization, in:

Geothermics 40.3, pp. 211–220, ISSN: 0375-6505, DOI: 10.1016/j.geothermics.2011.07.002.

Gan, G. (2019): A numerical methodology for comprehensive assessment of the dynamic thermal performance of horizontal ground heat exchangers, in: *Thermal Science and Engineering Progress* 11, pp. 365–379, ISSN: 2451-9049, DOI: 10.1016/j.tsep.2019.04.013.

Gan, G. (2013): Dynamic thermal modelling of horizontal ground-source heat pumps, in: *International Journal of Low-Carbon Technologies* 8.2, pp. 95–105, ISSN: 1748-1317 1748-1325, DOI: 10.1093/ijlct/ctt012.

Gautschi, W. and Cahill, W. F. (1964): Handbook of mathematical functions.

Gnielinski, V. (2013): G1 Durchströmte Rohre, in: *VDI-Wärmeatlas*, Berlin, Heidelberg: Springer Berlin Heidelberg, pp. 785–792, ISBN: 978-3-642-19981-3.

Gu, X., Makasis, N., Motamedi, Y., Narsilio, G. A., Arulrajah, A., and Horpibulsuk, S. (2022): Geothermal pavements: field observations, numerical modelling and long-term performance, in: *Géotechnique* 72.9, pp. 832–846, DOI: 10.1680/jgeot.20.P.296, eprint: https://doi.org/10.1680/jgeot.20.P.296.

Gu, Y. and O'Neal, D. L. (1998): Development of an equivalent diameter expression for vertical U-tubes used in ground-coupled heat pumps, English, in: vol. 104, 2, ASHRAE, ASHRAE, Atlanta, GA, United States, pp. 347–355.

Habibi, M. and Hakkaki-Fard, A. (2018): Evaluation and improvement of the thermal performance of different types of horizontal ground heat exchangers based on techno-economic analysis, in: *Energy Conversion and Management* 171, pp. 1177–1192, ISSN: 0196-8904, DOI: 10.1016/j.enconman.2018.06.070.

Hackel, S. and Pertzborn, A. (2011): Effective design and operation of hybrid ground-source heat pumps: Three case studies, in: *Energy and Buildings* 43.12, pp. 3497–3504, ISSN: 0378-7788, DOI: 10.1016/j.enbuild.2011.09.014.

Hastaoglu, M. A., Negiz, A., and Heidemann, R. (1995): Three-dimensional transient heat transfer from a buried pipe Part III. Comprehensive model, in: *Chemical Engineering Science* 50.16, pp. 2545–2555.

Hecht-Méndez, J., Paly, M. de, Beck, M., and Bayer, P. (2013): Optimization of energy extraction for vertical closed-loop geothermal systems considering groundwater flow, in: *Energy Conversion and Management* 66, pp. 1–10, ISSN: 01968904, DOI: 10.1016/j.enconman.2012.09.019.

Hellström, G. (1991): Ground heat storage : thermal analyses of duct storage systems, English, PhD thesis, Lund University Box 117, 221 00 LUND: Lund University, ISBN: 91-628-0290-9.

Hellström, G. and Sanner, B. (1994): Software for dimensioning of deep boreholes for heat extraction, in: *Proc. Calorstock* 94, pp. 195–202.

Himasekhar, K. and Bau, H. H. (1987): Thermal convection associated with hot/cold pipes buried in a semi-infinite, saturated, porous medium, in: *International journal of heat and mass transfer* 30.2, pp. 263–273.

Hou, G., Taherian, H., Song, Y., Jiang, W., and Chen, D. (2022): A systematic review on optimal analysis of horizontal heat exchangers in ground source heat pump systems, in: *Renewable and Sustainable Energy Reviews* 154, ISSN: 13640321, DOI: 10.1016/j.rser.2021.111830.

Huang, J., Fan, J., and Furbo, S. (2020): Demonstration and optimization of a solar district heating system with ground source heat pumps, in: *Solar Energy* 202, pp. 171–189, ISSN: 0038-092X, DOI: https://doi.org/10.1016/j.solener.2020.03.097.

Huber, A. (2005): Erdwärmesonden für Direktheizung. Phase 1: Modellbildung und Simulation, in: *Schlussbericht. Bundesamt für Energie (BFE), Bern.*

Huld, T., Müller, R., and Gambardella, A. (2012): A new solar radiation database for estimating PV performance in Europe and Africa, in: *Solar Energy* 86.6, pp. 1803–1815, ISSN: 0038-092X, DOI: https://doi.org/10.1016/j.solener.2012.03.006.

Ingersoll, L. R. (1948): Theory of the ground pipe heat source for the heat pump, in: *Heating Piping and Air Conditioning* 20, pp. 119–122.

Ingersoll, L. R., Zobel, O. J., and Ingersoll, A. C. (1954): Heat Conduction: With Engineering, Geological, and Other Applications, New York: McGraw-Hill.

Ioffe, I. A. (1972): A problem of transient heat conduction in a semibounded body with an internal cylindrical heat source, in: *Journal of engineering physics* 23.2, pp. 1051–1054.

Javed, S. and Claesson, J. (2011): New Analytical and Numerical Solutions for the Short-term Analysis of Vertical Ground Heat Exchangers, in: *Ashrae: Transactions 2011, Vol 117, Pt 1* 117, pp. 3–12, ISSN: 0001-2505.

Javed, S. and Spitler, J. D. (2016): Calculation of borehole thermal resistance, in: *Advances in Ground-Source Heat Pump Systems*, pp. 63–95, ISBN: 9780081003114, DOI: 10.1016/b978-0-08-100311-4.00003-0.

Javed, S. and Spitler, J. D. (2017): Accuracy of borehole thermal resistance calculation methods for grouted single U-tube ground heat exchangers, in: *Applied Energy* 187, pp. 790–806, ISSN: 0306-2619, DOI: 10.1016/j.apenergy.2016.11.079.

Kavanaugh, S. P. (1985): Simulation and experimental verification of vertical ground-coupled heat pump systems, PhD thesis, Oklahoma State University 601 North Willis St. Stillwater, OK 74078: Oklahoma State University.

Kavanaugh, S. P. and Rafferty, K. D. (2014): Geothermal heating and cooling: design of ground-source heat pump systems, ASHRAE.

Kayaci, N. and Demir, H. (2018): Numerical modelling of transient soil temperature distribution for horizontal ground heat exchanger of ground source heat pump, in: *Geothermics* 73, pp. 33–47, ISSN: 0375-6505, DOI: 10.1016/j.geothermics.2018.01.009.

Keller, J., Rath, V., Bruckmann, J., Mottaghy, D., Clauser, C., Wolf, A., Seidler, R., Bücker, H. M., and Klitzsch, N. (2020): SHEMAT-Suite: An open-source code for simulating flow, heat and species transport in porous media, in: *SoftwareX* 12, p. 100533, DOI: 10.1016/j.softx.2020.100533.

Al-Khoury, R., BniLam, N., Arzanfudi, M. M., and Saeid, S. (2020): A spectral model for a moving cylindrical heat source in a conductive-convective domain, in: *International Journal of Heat and Mass Transfer* 163, ISSN: 00179310, DOI: 10.1016/j.ijheatmasstransfer.2020.120517.

Al-Khoury, R. and Bonnier, P. G. (2006): Efficient finite element formulation for geothermal heating systems. Part II: transient, in: *International journal for numerical methods in engineering* 67.5, pp. 725–745.

Kim, M.-J., Lee, S.-R., Yoon, S., and Jeon, J.-S. (2018): An applicable design method for horizontal spiral-coil-type ground heat exchangers, in: *Geothermics* 72, pp. 338–347, ISSN: 03756505, DOI: 10.1016/j.geothermics.2017.12.010.

Koppen, W. (1936): Das geographische system der Klimate, in: *Handbuch der klimatologie*, p. 46.

Laferrière, A., Cimmino, M., Picard, D., and Helsen, L. (2020): Development and validation of a full-time-scale semi-analytical model for the short-and long-term simulation of vertical geothermal bore fields, in: *Geothermics* 86, p. 101788.

Lamarche, L. (2011): Analytical g-function for inclined boreholes in ground-source heat pump systems, in: *Geothermics* 40.4, pp. 241–249, ISSN: 0375-6505, DOI: https://doi.org/10.1016/j.geothermics.2011.07.006.

Lamarche, L. (2013): Short-term behavior of classical analytic solutions for the design of ground-source heat pumps, in: *Renewable Energy* 57, pp. 171–180, ISSN: 09601481, DOI: 10.1016/j.renene.2013.01.045.

Lamarche, L. (2015): Short-time analysis of vertical boreholes, new analytic solutions and choice of equivalent radius, in: *International Journal of Heat and Mass Transfer* 91, pp. 800–807, ISSN: 00179310, DOI: 10.1016/j.ijheatmasstransfer.2015.07.135.

Lamarche, L. (2019): Horizontal ground heat exchangers modelling, in: *Applied Thermal Engineering* 155, pp. 534–545, ISSN: 1359-4311, DOI: 10.1016/j.applthermaleng.2019.04.006.

Lamarche, L. and Beauchamp, B. (2007): A new contribution to the finite line-source model for geothermal boreholes, in: *Energy and Buildings* 39.2, pp. 188–198, ISSN: 03787788, DOI: 10.1016/j.enbuild.2006.06.003.

Larwa, B. and Kupiec, K. (2020): Heat transfer in the ground with a horizontal heat exchanger installed - Long-term thermal effects, in: *Applied Thermal Engineering* 164, ISSN: 1359-4311, DOI: ARTN11453910.1016/j.applthermaleng.2019.114539.

Lazzarotto, A. (2015): Developments in Ground Heat Storage Modeling, PhD thesis, KTH Royal Institute of Technology.

Leong, W. H., Tarnawski, V. R., and Aittomäki, A. (1998): Effect of soil type and moisture content on ground heat pump performance: Effet du type et de l'humidité du sol sur la performance des pompes à chaleur à capteurs enterrés, in: *International Journal of Refrigeration* 21.8, pp. 595–606.

Li, C. F., Mao, J. F., Peng, X., Mao, W., Xing, Z. L., and Wang, B. (2019): Influence of ground surface boundary conditions on horizontal ground source heat pump systems, in: *Applied Thermal Engineering* 152, pp. 160–168, ISSN: 1359-4311, DOI: 10.1016/j.applthermaleng.2019.02.080.

Li, H., Nagano, K., and Lai, Y. X. (2012): A new model and solutions for a spiral heat exchanger and its experimental validation, in: *International Journal of Heat and Mass Transfer* 55.15-16, pp. 4404–4414, ISSN: 0017-9310, DOI: 10.1016/j.ijheatmasstransfer.2012.03.084.

Li, M. and Lai, A. C. K. (2012): New temperature response functions (G functions) for pile and borehole ground heat exchangers based on composite-medium line-source theory, in: *Energy* 38.1, pp. 255–263, ISSN: 03605442, DOI: 10.1016/j.energy.2011.12.004.

Li, M. and Lai, A. C. K. (2013): Analytical solution to heat conduction in finite hollow composite cylinders with a general boundary condition, in: *International Journal of Heat and Mass Transfer* 60, pp. 549–556, ISSN: 00179310, DOI: 10.1016/j.ijheatmasstransfer.2013.01.029.

Li, M., Li, P., Chan, V., and Lai, A. C. K. (2014): Full-scale temperature response function (G-function) for heat transfer by borehole ground heat exchangers (GHEs) from

sub-hour to decades, in: *Applied Energy* 136, pp. 197–205, ISSN: 0306-2619, DOI: 10.1016/j.apenergy.2014.09.013.

Li, M., Zhu, K., and Fang, Z. (2016): Analytical methods for thermal analysis of vertical ground heat exchangers, in: *Advances in Ground-Source Heat Pump Systems*, pp. 157–183, ISBN: 9780081003114, DOI: 10.1016/b978-0-08-100311-4.00006-6.

Liao, Q., Zhou, C., Cui, W., and Jen, T. C. (2012): New correlations for thermal resistances of vertical single U-Tube ground heat exchanger, in: *Journal of Thermal Science and Engineering Applications* 4.3.

Liu, X. (2005): Development and experimental validation of simulation of hydronic snow melting systems for bridges, Oklahoma State University.

Loveridge, F. and Powrie, W. (2013): Temperature response functions (G-functions) for single pile heat exchangers, in: *Energy* 57, pp. 554–564, ISSN: 0360-5442, DOI: https://doi.org/10.1016/j.energy.2013.04.060.

Lund, J. W. and Toth, A. N. (2021): Direct utilization of geothermal energy 2020 worldwide review, in: *Geothermics* 90, ISSN: 0375-6505, DOI: ARTN10191510.1016/j.geothermics.2020.101915.

Luo, J., Rohn, J., Bayer, M., and Priess, A. (2013): Modeling and experiments on energy loss in horizontal connecting pipe of vertical ground source heat pump system, in: *Applied Thermal Engineering* 61.2, pp. 55–64, ISSN: 13594311, DOI: 10.1016/j.applthermaleng.2013.07.022.

Luo, J., Zhao, H., Jia, J., Xiang, W., Rohn, J., and Blum, P. (2017): Study on operation management of borehole heat exchangers for a large-scale hybrid ground source heat pump system in China, in: *Energy* 123, pp. 340–352, ISSN: 0360-5442, DOI: https://doi.org/10.1016/j.energy.2017.01.136.

Makasis, N., Narsilio, G. A., Bidarmaghz, A., and Johnston, I. W. (2018): Ground-source heat pump systems: The effect of variable pipe separation in ground heat exchangers, in: *Computers and Geotechnics* 100, pp. 97–109, ISSN: 0266-352X, DOI: https://doi.org/10.1016/j.compgeo.2018.02.010.

Man, Y., Yang, H., Diao, N., Liu, J., and Fang, Z. (2010): A new model and analytical solutions for borehole and pile ground heat exchangers, in: *International Journal of Heat and Mass Transfer* 53.13-14, pp. 2593–2601.

Marcotte, D. and Pasquier, P. (2008): Fast fluid and ground temperature computation for geothermal ground-loop heat exchanger systems, in: *Geothermics* 37.6, pp. 651–665.

Marcotte, D. and Pasquier, P. (2009): The effect of borehole inclination on fluid and ground temperature for GLHE systems, in: *Geothermics* 38.4, pp. 392–398, ISSN: 03756505, DOI: 10.1016/j.geothermics.2009.06.001.

Martin, W. and Sadhal, S. S. (1978): Bounds on transient temperature distribution due to a buried cylindrical heat source, in: *International Journal of Heat and Mass Transfer* 21.6, pp. 783–789.

Minaei, A. and Maerefat, M. (2017a): A new analytical model for short-term borehole heat exchanger based on thermal resistance capacity model, in: *Energy and Buildings* 146, pp. 233–242.

Minaei, A. and Maerefat, M. (2017b): Thermal resistance capacity model for short-term borehole heat exchanger simulation with non-stiff ordinary differential equations, in: *Geothermics* 70, pp. 260–270, ISSN: 03756505, DOI: 10.1016/j.geothermics.2017.06.011.

Mogensen, P. K. (1983): Fluid to duct wall heat transfer in duct system heat storages, in.

Molina-Giraldo, N., Blum, P., Zhu, K., Bayer, P., and Fang, Z. (2011): A moving finite line source model to simulate borehole heat exchangers with groundwater advection, in: *International Journal of Thermal Sciences* 50.12, pp. 2506–2513.

Monzó, P., Mogensen, P., Acuña, J., Ruiz-Calvo, F., and Montagud, C. (2015): A novel numerical approach for imposing a temperature boundary condition at the borehole wall in borehole fields, in: *Geothermics* 56, pp. 35–44, ISSN: 03756505, DOI: 10.1016/j.geothermics.2015.03.003.

Mottaghy, D. and Dijkshoorn, L. (2012): Implementing an effective finite difference formulation for borehole heat exchangers into a heat and mass transport code, in: *Renewable Energy* 45, pp. 59–71, ISSN: 0960-1481, DOI: https://doi.org/10.1016/j.renene.2012.02.013.

Muñoz-Criollo, J. J., Cleall, P. J., and Rees, S. W. (2016): Factors influencing collection performance of near surface interseasonal ground energy collection and storage systems, in: *Geomechanics for Energy and the Environment* 6, Themed Issue on Selected Papers Symposium of Energy Geotechnics 2015 — Part I, pp. 45–57, ISSN: 2352-3808, DOI: https://doi.org/10.1016/j.gete.2016.04.001.

Naicker, S. S. and Rees, S. J. (2020): Long-term high frequency monitoring of a large borehole heat exchanger array, in: *Renewable Energy* 145, pp. 1528–1542, ISSN: 0960-1481, DOI: https://doi.org/10.1016/j.renene.2019.07.008.

Naldi, C. and Zanchini, E. (2019): A new numerical method to determine isothermal g-functions of borehole heat exchanger fields, in: *Geothermics* 77, pp. 278–287, ISSN: 03756505, DOI: 10.1016/j.geothermics.2018.10.007.

Negiz, A., Hastaoglu, M. A., and Heidemann, R. A. (1993): Three-dimensional transient heat transfer from a buried pipe—I. Laminar flow, in: *Chemical engineering science* 48.20, pp. 3507–3517.

Nusselt, W. (1916): Die Oberflächenkondensation des Wasserdampfes, VDI, URL: https://books.google.de/books?id=m8fwjgEACAAJ.

Oppelt, T., Riehl, I., and Gross, U. (2010): Modelling of the borehole filling of double U-pipe heat exchangers, in: *Geothermics* 39.3, pp. 270–276, ISSN: 03756505, DOI: 10.1016/j.geothermics.2010.06.001.

Ozudogru, T. Y., Olgun, C. G., and Senol, A. (2014): 3D numerical modeling of vertical geothermal heat exchangers, in: *Geothermics* 51, pp. 312–324, ISSN: 03756505, DOI: 10.1016/j.geothermics.2014.02.005.

Pan, A., McCartney, J. S., Lu, L., and Tian, Y. (2020): A novel analytical multilayer cylindrical heat source model for vertical ground heat exchangers installed in layered ground, in: *Energy* 200, ISSN: 03605442, DOI: 10.1016/j.energy.2020.117545.

Pasquier, P. and Lamarche, L. (2022): Analytic expressions for the moving infinite line source model, in: *Geothermics* 103, ISSN: 03756505, DOI: 10.1016/j.geothermics.2022.102413.

Pasquier, P. and Marcotte, D. (2012): Short-term simulation of ground heat exchanger with an improved TRCM, in: *Renewable energy* 46, pp. 92–99.

Pasquier, P. and Marcotte, D. (2014): Joint use of quasi-3D response model and spectral method to simulate borehole heat exchanger, in: *Geothermics* 51, pp. 281–299, ISSN: 03756505, DOI: 10.1016/j.geothermics.2014.02.001.

Pasquier, P., Zarrella, A., and Labib, R. (2018): Application of artificial neural networks to near-instant construction of short-term g-functions, in: *Applied Thermal Engineering* 143, pp. 910–921, ISSN: 1359-4311, DOI: 10.1016/j.applthermaleng.2018.07.137.

Peel, M. C., Finlayson, B. L., and McMahon, T. A. (2007): Updated world map of the Köppen-Geiger climate classification, in: *Hydrology and Earth System Sciences* 11.5, pp. 1633–1644, DOI: 10.5194/hess-11-1633-2007.

Phetteplace, G., Bahnfleth, D., Mildenstein, P., Overgaard, J., Rafferty, K., Wade, D. W., et al. (2013): District heating guide, in: *Atlanta, ASHRAE*.

Philippe, M., Bernier, M. A., and Marchio, D. (2009): Validity ranges of three analytical solutions to heat transfer in the vicinity of single boreholes, in: *Geothermics* 38.4, pp. 407–413.

Piechowski, M. (1999): Heat and mass transfer model of a ground heat exchanger: Theoretical development, in: *International Journal of Energy Research* 23.7, pp. 571–588, ISSN: 0363-907x.

Prandtl, L. (1905): Über flüssigkeitsbewegung bei sehr kleiner reibung. verhandlungen des iii. internationalen mathematiker-kongresses, heidelberg, in: *LPGA* 2, pp. 575–584.

Priarone, A. and Fossa, M. (2016): Temperature response factors at different boundary conditions for modelling the single borehole heat exchanger, in: *Applied Thermal Engineering* 103, pp. 934–944, ISSN: 13594311, DOI: 10.1016/j.applthermaleng.2016.04.038.

Reynolds, O. (1883): XXIX. An experimental investigation of the circumstances which determine whether the motion of water shall be direct or sinuous, and of the law of resistance in parallel channels, in: *Philosophical Transactions of the Royal society of London* 174, pp. 935–982.

Rezaei, A., Kolahdouz, E. M., Dargush, G. F., and Weber, A. S. (2012): Ground source heat pump pipe performance with Tire Derived Aggregate, in: *International Journal of Heat and Mass Transfer* 55.11-12, pp. 2844–2853, ISSN: 00179310, DOI: 10.1016/j.ijheatmasstransfer.2012.02.004.

Rivera, J. A., Blum, P., and Bayer, P. (2016): A finite line source model with Cauchy-type top boundary conditions for simulating near surface effects on borehole heat exchangers, in: *Energy* 98, pp. 50–63, DOI: 10.1016/j.energy.2015.12.129.

Ruiz-Calvo, F., De Rosa, M., Monzó, P., Montagud, C., and Corberán, J. M. (2016): Coupling short-term (B2G model) and long-term (g-function) models for ground source heat exchanger simulation in TRNSYS. Application in a real installation, in: *Applied Thermal Engineering* 102, pp. 720–732, ISSN: 1359-4311, DOI: https://doi.org/10.1016/j.applthermaleng.2016.03.127.

Schulte, D. O., Ruhaak, W., Welsch, B., and Sass, I. (2016): BASIMO - borehole heat exchanger array simulation and optimization tool, in: *European Geosciences Union General Assembly 2016* 97, pp. 210–217, ISSN: 1876-6102, DOI: 10.1016/j.egypro.2016.10.057.

Seabold, S. and Perktold, J. (2010): statsmodels: Econometric and statistical modeling with python, in: *9th Python in Science Conference*.

Selamat, S., Miyara, A., and Kariya, K. (2016): Numerical study of horizontal ground heat exchangers for design optimization, in: *Renewable Energy* 95, pp. 561–573, ISSN: 0960-1481, DOI: 10.1016/j.renene.2016.04.042.

Shafagh, I., Shepley, P., Shepherd, W., Loveridge, F., Schellart, A., Tait, S., and Rees, S. J. (2022): Thermal energy transfer around buried pipe infrastructure, in:

Geomechanics for Energy and the Environment 29, ISSN: 23523808, DOI: 10.1016/j.gete.2021.100273.

Sharqawy, M. H., Mokheimer, E. M., and Badr, H. M. (2009): Effective pipe-to-borehole thermal resistance for vertical ground heat exchangers, in: *Geothermics* 38.2, pp. 271–277, ISSN: 0375-6505, DOI: https://doi.org/10.1016/j.geothermics.2009.02.001.

Shi, Y., Xu, F., Li, X., Lei, Z., Cui, Q., and Zhang, Y. (2022): Comparison of influence factors on horizontal ground heat exchanger performance through numerical simulation and gray correlation analysis, in: *Applied Thermal Engineering* 213, ISSN: 13594311, DOI: 10.1016/j.applthermaleng.2022.118756.

Shirazi, A. S. and Bernier, M. A. (2013): Thermal capacity effects in borehole ground heat exchangers, in: *Energy and Buildings* 67, pp. 352–364, ISSN: 03787788, DOI: 10.1016/j.enbuild.2013.08.023.

Smith, D. C., Elmore, A. C., and Thompson, J. (2018): The effect of seasonal groundwater saturation on the effectiveness of large scale borehole heat exchangers in a karstic aquifer, in: *Geothermics* 75, pp. 164–170, ISSN: 0375-6505, DOI: https://doi.org/10.1016/j.geothermics.2018.05.001.

Southall, R. and Biljecki, F. (2017): The VI-Suite: a set of environmental analysis tools with geospatial data applications, in: *Open Geospatial Data, Software and Standards* 2.1, p. 23, ISSN: 2363-7501, DOI: 10.1186/s40965-017-0036-1.

Spitler, J. D. (2000): A design tool for commercial building loop heat exchangers, in: *Fourth International Heat Pumps in Cold Climates Conference, Aylmer, Québec.*

Spitler, J. D. and Bernier, M. A. (2016): Vertical borehole ground heat exchanger design methods, in: *Advances in Ground-Source Heat Pump Systems*, pp. 29–61, ISBN: 9780081003114, DOI: 10.1016/b978-0-08-100311-4.00002-9.

Stoffel, P., Kümpel, A., and Müller, D. (2022): Cloud-Based Optimal Control of Individual Borehole Heat Exchangers in a Geothermal Field, in: *Journal of thermal science* 31.5, pp. 1253–1265, ISSN: 1993-033X, DOI: 10.1007/s11630-022-1639-0.

Sutton, M. G., Nutter, D. W., and Couvillion, R. J. (2003): A Ground Resistance for Vertical Bore Heat Exchangers With Groundwater Flow, in: *Journal of Energy Resources Technology* 125.3, pp. 183–189, ISSN: 0195-0738 1528-8994, DOI: 10.1115/1.1591203.

Tang, F. and Nowamooz, H. (2020): Outlet temperatures of a slinky-type Horizontal Ground Heat Exchanger with the atmosphere-soil interaction, in: *Renewable Energy* 146, pp. 705–718, ISSN: 09601481, DOI: 10.1016/j.renene.2019.07.029.

Taylor, H. E., Stiles, L. F., and Hemphill, W. (1997): Technical description of the Stockton College geothermal HVAC retrofit, in.

Thiyagarajan, R. and Yovanovich, M. M. (1974): Thermal Resistance of a Buried Cylinder With Constant Flux Boundary Condition, in: *Journal of Heat Transfer* 96.2, pp. 249–250, ISSN: 0022-1481, DOI: 10.1115/1.3450174.

Thomson, W. and Kelvin, W. T. B. (1872): Reprint of papers on electrostatics and magnetism, Macmillan.

Tian, X., Mao, R., Pei, P., Wu, H., Ma, H., Hu, C., and Zhang, Z. (2022): Experimental study on temperature control optimization of ground source heat pump horizontal headers, in: *Energy and Buildings* 277, ISSN: 03787788, DOI: 10.1016/j.enbuild.2022.112541.

Treeck, C. A. van, Frisch, J., Weck-Ponten, S., Fichter, E., Ziegler, M., Düber, S., Derksen, J., Juarez, O., Blankenbach, J., Becker, R., Laska, M., and Hein, N. (2020): GeTIS - Geothermisches Informationssystem zur Bemessung, Modellierung, Bewertung und Genehmigung vernetzter geothermischer Energiesysteme auf Gebäude- und Stadtquartiersebene : Schlussbericht : Laufzeit des Vorhabens: 01.01.2016 bis 31.12.2019, tech. rep. 03ET1357A, Aachen: RWTH Aachen University, p. 329, DOI: 10.2314/KXP:1738225658.

Urresta, E., Moya, M., Campana, C., and Cruz, C. (2021): Ground thermal conductivity estimation using the thermal response test with a horizontal ground heat exchanger, in: *Geothermics* 96, ISSN: 0375-6505, DOI: ARTN10221310.1016/j.geothermics.2021.102213.

Van der Linden, E., Haarsma, R., and Schrier, G. (2019): Impact of climate model resolution on soil moisture projections in central-western Europe, in: *Hydrology and Earth System Sciences* 23, pp. 191–206, DOI: 10.5194/hess-23-191-2019.

Van Genuchten, M. T. (1981): Analytical solutions for chemical transport with simultaneous adsorption, zero-order production and first-order decay, in: *Journal of Hydrology* 49.3, pp. 213–233, ISSN: 0022-1694, DOI: https://doi.org/10.1016/0022-1694(81)90214-6.

Van Genuchten, M. T. (1982): Analytical solutions of the one-dimensional convective-dispersive solute transport equation, 1661, US Department of Agriculture, Agricultural Research Service.

Van Orstrand, C. E. (1939): Observed Temperatures in the Earth's Crust, in: *Internal Constitution of the Earth*, New York and London: McGaw-Hill Book Company, Inc., pp. 125–151.

VDI 4640-2 (2019): Thermal use of the underground - Part 2: Ground source heat pump systems, Berlin: Beuth Verlag.

Virtanen, P., Gommers, R., Oliphant, T. E., Haberland, M., Reddy, T., Cournapeau, D., Burovski, E., Peterson, P., Weckesser, W., Bright, J., van der Walt, S. J., Brett, M., Wilson, J., Millman, K. J., Mayorov, N., Nelson, A. R. J., Jones, E., Kern, R., Larson, E., Carey, C. J., Polat, I., Feng, Y., Moore, E. W., VanderPlas, J., Laxalde, D., Perktold, J., Cimrman, R., Henriksen, I., Quintero, E. A., Harris, C. R., Archibald, A. M., Ribeiro, A. H., Pedregosa, F., van Mulbregt, P., and SciPy 1.0 Contributors (2020): SciPy 1.0: Fundamental Algorithms for Scientific Computing in Python, in: *Nature Methods* 17, pp. 261–272, DOI: 10.1038/s41592-019-0686-2.

Wei, J. P., Wang, L., Jia, L., and Cai, W. J. (2016): A new method for calculation of short time-step g-functions of vertical ground heat exchangers, in: *Applied Thermal Engineering* 99, pp. 776–783, ISSN: 1359-4311, DOI: 10.1016/j.applthermaleng.2016.01.105.

Wetter, M. and Huber, A. (1997): Vertical borehole heat exchanger EWS Model, in: *TRNSYS type* 451.

Wołoszyn, J. and Gołaś, A. (2013): Modelling of a borehole heat exchanger using a finite element with multiple degrees of freedom, in: *Geothermics* 47, pp. 13–26, ISSN: 03756505, DOI: 10.1016/j.geothermics.2013.01.002.

Wu, Y. P., Gan, G. H., Verhoef, A., Vidale, P. L., and Gonzalez, R. G. (2010): Experimental measurement and numerical simulation of horizontal-coupled slinky ground source heat exchangers, in: *Applied Thermal Engineering* 30.16, pp. 2574–2583, ISSN: 1359-4311, DOI: 10.1016/j.applthermaleng.2010.07.008.

Xing, L. (2014): Estimations of undisturbed ground temperatures using numerical and analytical modeling, Oklahoma State University.

Xiong, Z. Y., Fisher, D. E., and Spitler, J. D. (2015): Development and validation of a Slinky(TM) ground heat exchanger model, in: *Applied Energy* 141, pp. 57–69, ISSN: 0306-2619, DOI: 10.1016/j.apenergy.2014.11.058.

Yang, W., Xu, R., Wang, F., and Chen, S. (2020): Experimental and numerical investigations on the thermal performance of a horizontal spiral-coil ground heat exchanger, in: *Renewable Energy* 147, pp. 979–995, ISSN: 09601481, DOI: 10.1016/j.renene.2019.09.030.

Yavuzturk, C. and Spitler, J. D. (1999): A short time step response factor model for vertical ground loop heat exchangers, in: *ASHRAE transactions* 105.2, pp. 475–485.

Yavuzturk, C., Spitler, J. D., Rees, S. J., et al. (1999): A transient two-dimensional finite volume model for the simulation of vertical U-tube ground heat exchangers, in: *ASHRAE transactions* 105.2, pp. 465–474.

Zarrella, A., Emmi, G., and De Carli, M. (2017): A simulation-based analysis of variable flow pumping in ground source heat pump systems with different types of borehole heat exchangers: A case study, in: *Energy Conversion and Management* 131, pp. 135–150, ISSN: 0196-8904, DOI: 10.1016/j.enconman.2016.10.061.

Zarrella, A., Scarpa, M., and De Carli, M. (2011): Short time step analysis of vertical ground-coupled heat exchangers: The approach of CaRM, in: *Renewable Energy* 36.9, pp. 2357–2367.

Zeng, H. Y., Diao, N. R., and Fang, Z. H. (2002): A finite line-source model for boreholes in geothermal heat exchangers, in: *Heat Transfer—Asian Research: Co-sponsored by the Society of Chemical Engineers of Japan and the Heat Transfer Division of ASME* 31.72, pp. 558–567.

Zhang, M. F., Gong, G. C., and Zeng, L. W. (2021): Investigation for a novel optimization design method of ground source heat pump based on hydraulic characteristics of buried pipe network, in: *Applied Thermal Engineering* 182, ISSN: 1359-4311, DOI: ARTN11606910.1016/j.applthermaleng.2020.116069.

Zhang, W., Yang, H., Lu, L., and Fang, Z. (2013): The analysis on solid cylindrical heat source model of foundation pile ground heat exchangers with groundwater flow, in: *Energy* 55, pp. 417–425, ISSN: 0360-5442, DOI: https://doi.org/10.1016/j.energy.2013.03.092.

Zhao, Z., Lin, Y.-F., Stumpf, A., and Wang, X. (2022): Assessing impacts of groundwater on geothermal heat exchangers: A review of methodology and modeling, in: *Renewable Energy* 190, pp. 121–147, ISSN: 09601481, DOI: 10.1016/j.renene.2022.03.089.

Zubair, S. M. and Chaudhry, M. A. (1996): Temperature solutions due to time-dependent moving-line-heat sources, in: *Heat and Mass Transfer* 31.3, pp. 185–189, ISSN: 0042-9929, DOI: Doi10.1007/Bf02333318.

Publications

The following publications are part of this work:

Düber, S., Ziegler, M., & Fuentes, R. (2022): Development and validation of a computationally efficient hybrid model for temporal high-resolution simulations of geothermal bore fields. *International Journal for Numerical and Analytical Methods in Geomechanics*, 46(14), 2792-2813.

Düber S., Fuentes R., Narsilio G.A. (2023): Comparison and integration of simulation models for horizontal connection pipes in geothermal bore fields. *Geothermal Energy*, 11 (1), art. no. 15.

Düber S., Fuentes R., Narsilio G. (2023): Effect of horizontal connection pipes on operation of borehole heat exchangers under different climatic conditions. *Geothermics*, 110, art. no. 102679.

Düber S., Fuentes R., Narsilio G. (2024): Exploiting heat gains along horizontal connection pipes in existing borehole heat exchanger fields. *Geothermics*, 118, art. no. 102912.

Düber S., Fuentes R., Narsilio G. (2024): Using thermal response factors with time dependent thermal properties. *Geothermics*, 119, art. no. 102957.